SELF-ASSEMBLY OF THREE-DIMENSIONAL NUCLEIC ACID NANOSTRUCTURES

by

LUVENA LE-YUN ONG

S.B. Chemical-Biological Engineering
Massachusetts Institute of Technology, 2010

Submitted to the Harvard-MIT Division of Health Sciences and Technology
in partial fulfillment of the requirements for the degree of

DOCTOR OF PHILOSOPHY IN MEDICAL ENGINEERING AND MEDICAL PHYSICS

at the

MASSACHUSETTS INSTITUTE OF TECHNOLOGY

June 2016

© Massachusetts Institute of Technology 2016. All rights reserved.

Signature of Author: Signature redacted
Harvard-MIT Division of Health Sciences and Technology
April 1, 2016

Certified by: Signature redacted
Peng Yin, Ph.D.
Professor of Systems Biology

Accepted by: Signature redacted
Emery N. Brown, M.D., Ph.D.
Director, Harvard-MIT Program in Health Sciences and Technology
Professor of Computational Neuroscience & Health Sciences and Technology

MASSACHUSETTS INSTITUTE
OF TECHNOLOGY
JUN 22 2016
LIBRARIES
ARCHIVES

Dedication

To my parents Sing Cheong and Siu-Wah Ong
for their sacrifices, encouragement, and love.

Self-assembly of three-dimensional nucleic acid nanostructures

by

Luvena Ong

Submitted to the Harvard-MIT Division of Health Sciences and Technology
on April 1, 2016,
in partial fulfillment of the requirements for the degree of
Doctor of Philosophy in Medical Engineering and Medical Physics

Abstract

Patterning complex 3D features at the nanoscale offers potential applications for a wide range of fields from materials to medicine. While numerous methods have been developed to manipulate nanoscale materials, these methods are typically limited by their difficulty in creating arbitrary 3D patterns. Self-assembly of nucleic acids has emerged as a promising method for addressing this challenge due to the predictability and programmability of the material and its structure. While a diversity of DNA nanostructures have been designed by specifying complementarity rules between strands, creation of 3D nanostructures requires careful design of strand architecture, and patterns are often limited to a volume of $25 \times 25 \times 25$ nm^3.

Here, we address the challenges in structural DNA nanotechnology by developing a modular DNA "brick" approach. These bricks are short, single-stranded oliogomers that can self-assemble in a single-pot reaction to a prescribed 3D shape. Using this modular approach, we demonstrate high efficiency in 3D design by generating 100 distinct, discrete 3D structures from a library of strands. We also created long-range ordering of channels, tunnels, and pores by growing micron-sized 3D periodic crystals made from DNA bricks. Finally, we applied this approach to control over 30,000 unique component strands to self-assemble into cuboids measuring over 100 nm in each dimension. These structures were further used to pattern highly complex cavities. Together, this work represents a simple, modular, and versatile method for 3D nanofabrication. This unique patterning capability of DNA bricks may enable development of new applications by providing a foundation for intricate and complex control of an unprecedented number of independent components.

Thesis Supervisor: Peng Yin, Ph.D.
Title: Professor of Systems Biology

Acknowledgments

I've been fortunate to have a number of positive influences during my graduate studies. Through these incredible mentors, colleagues, and friends, I learned not only how to be a better scientist but more importantly a better person.

First and foremost, I would like to thank my advisor Peng Yin. I remember when I first stumbled upon his paper on dynamically assembled structures, I was simultaneously confused and intrigued by DNA nanotechnology. I had never heard of anything like this field, but I was curious enough to schedule a meeting with Peng to learn more. That first meeting I had with Peng was particularly memorable. I'd never met anyone so enthusiastic and optimistic about the prospects of the technology on which s/he was working. I left the meeting being incredibly excited about working in his lab. The summer rotation was amazing. Even though I was completely new, Peng had generously given me my own independent project and freedom to work and explore. With support from the lab, I learned so much during that rotation. Immediately, I was convinced that this was the place to nurture my scientific curiosity and skills. I am especially appreciative of the experience I've had in Peng's lab and of his mentorship. Through his infectious enthusiasm, he has molded an environment where innovation and creativity flows freely and is allowed to develop and grow. Since I've been in the lab, he's given me numerous opportunities and support to pursue a range of projects and ideas. Thank you for being open to taking risks, for always giving constructive feedback, for entrusting confidence in me, and for being understanding. I am indebted to Peng for providing me with such a invaluable and unique experience.

I would also like to thank my committee members, Jagesh Shah and William Shih, who have been very supportive and willing to share their excitement for this work. Thank you for all the insightful feedback and interesting ideas. William has also served as a collaborator on numerous projects and shares an office wall with Peng. I am particularly grateful for his openness in discussing experiments and willingness to share his philosophy and outlook on science and life. These conversations have served as a source of inspiration for guiding my future path.

During my Ph.D., I was lucky to be exposed to different mentoring styles and perspectives on science through the many brilliant postdocs who have trained me. When I first joined the lab, Dave Zhang showed me the fundamental concepts and DNA techniques that I would later use in nearly every project on which I worked. Later, Yonggang Ke and Xi Chen taught me everything they respectively knew about structural DNA nanotechnology and nucleic acid detection. They were very giving with their time and always kept an open ear to my ideas, regardless of how naïve my suggestions were. It was through their mentorship that I grew my capability of thinking, analyzing, and communicating science and learned how to craft a cohesive scientific story. I am thankful for their patience, time, and teaching. I'm especially grateful to Yonggang who has been my unofficial co-advisor throughout the latter half of my graduate studies. Yonggang conceived of the DNA bricks platform and generously shared his work and time with me, even as he transitioned to a professorship at Georgia Tech. Without him, this thesis certainly would not have been possible. I am very honored to have worked so closely with such expertise.

I've also had the fortune of working with numerous talented collaborators, including Wei Sun, Bryan Wei, Josie Kishi, Max Scheible, and Jie Song. Thank you for all the stimulating discussions and lessons. Additionally, I'm grateful for the many teammates without whom the large-scale DNA bricks project would not have been successful: Omar Yaghi, Casey Grun, Nikita Hanikel, Bei Wang, and Allen Zhu. I have greatly enjoyed working with them and am inspired by their motivation, curiosity, and positive attitude. Along with their impressive scientific capabilities, I'm excited to see what the future holds for them and have no doubt that it will be bright. Thank you for being special, for keeping me organized, and for teaching me what it means to be a mentor and a friend.

The Molecular Systems Laboratory has always been a very dynamic and stimulating environment with a large number of visiting fellows and students. I've truly enjoyed my experience here and am excited to have learned and improved my research skills at the forefront of DNA nanotechnology. I admire the talents of my coworkers and cherish the many friendships I've made during this time. I would particularly like to thank Juanita Lara for sharing her warmth, thoughtfulness, and love of culture, food, and music with me; Joanne Ho for sharing her strength, unique perspective, and interests; Cameron Mhyrvold for the continuous stream of cute animal videos and images; Nicolas Garreau de Loubresse for his humor and for being "vegetarian"; Mario Teichmann, Aishu Sukumar, Joanna Robaszewski, Danielle Pastuszak, Sarit Agasti, Sungwook Woo, and Jongmin Kim for the memorable movie nights and outings; my German family: Ralf Jungmann, Jo Wöhrstein, Maximilian Strauß, Florian Schüder, and Thomas Schlichthärle for all the fun late nights and weekends in lab, for teaching me German language and culture, and for exposing me to unusual music ranging from classic 80s pop to bizarre electronica. I would especially like to thank Ralf, as he is a role model scientist manifesting both kindness and humility. Thank you to my wonderful labmates who have made the past six years seem so short: Maier Avendano, Brian Beliveau, Nikhil Gopalkrishnan, Dongran Han, Rizal Hariadi, Ninning Liu, Sinem Saka, Hiroshi Sasaki, Tom Schaus, Jie Shen, Jesse Silverberg, Feng Xuan, Mingjie Dai, Josie Kishi, Yu Wang, Weidong Xu, Mengmeng Zhang, Anita Chandrahas, Frederic Vigneault, Justin Werfel, Mael Manesse, Harish Soundararajan, Alex Green, Weili Wang, John Sadowski, Adam Marblestone, Pascal Pieters, Tony Cho, Tianyang Cao, Zhiyu Zhou, Michelle Vhudzijena, Ryosuke Iinuma, Amy Guan, Verena Schüller. Our lab would certainly not be functioning without the help of our awesome administrative assistants: Elizabeth Haney, Jaclyn Aliperti, Ashley Ferreira, Danielle Pastuszak, Elena Chen, and Annabelle Jones. I'm thankful for everything they do and for their help with the everyday things in lab.

The open lab space at the Wyss has also led to numerous friendships. I had the privilege of working alongside these top-rate scientists and people. Thank you especially to Nandhini Ponnuswamy, Leo Chou, and Rasmus Sørensen for all the experimental and computer help, for always putting a smile on my face, and for being the best adopted big siblings ever :)! Also, I am thankful for Bhavik Nathwani for sharing so many egg yolks, Jaeseung Hahn for sharing so many desserts, Marika Ziezack for sharing so many food and drink adventures, as well as Maartje Basting, Steve Perrault, Shelley Wickham, Anne Louise Kodal, Sarah Helmig, Debbie Huber, Simone Hendrikson, Bas Nijholt, Mathias Vinter, Bas Rosier, Sjors Wijnands, Keith Pardee, Nadia Cohen, Peter Nguyen, Dan Goodman, Frank Poeljwik, Jonathan Scheimann, Alex Chavez, Su Vora, John Min, Charles Fracchia, Mikro Palla, Leon Liu, Steph Hays, Andy Shumaker, Matt Mattozzi, Jeff Way, Avi Robinson-Mosher, Bryan Hassell, Katie Spina, Andries van der Meer, Samira Musah, Mohammed Khan, Aileen Li, Basma Hashmi, Juani Feliz, and many others in the Shih, Silver, Church, Collins, and Ingber labs for the rich conversations and fun times. I am also especially appreciative of the many people who have kept the Wyss running smoothly and who have given me kind words of encouragement: Susan Kelley, Jeannie Nisbet, Jodi Saia, Jermaine Reid, Alison Reggio, Luz Sosa, Joel Rivera-Cardona, Ed Doherty, Ayis Antoniou, Martin Montoya, Fettah Kosur, Garry Cuneo, Jean Lai, Ngawang Sherpa, Lily Kim, Jessica McDonough, Sami, Carlos Estrada, and Julio Velazquez.

I am lucky to have the opportunity of studying at a place as rich and resourceful as MIT and Harvard and in a program as unique as HST. I am grateful to have had an immersive experience in medical classes and a clerkship at Mount Auburn hospital. I thank my advisor Elazer Edelman for his help in navigating graduate school. I would like to acknowledge the HST administrators and director for help in guiding me through the milestones: Julie Greenberg, Laurie Ward, Traci Anderson, Joe Stein, and Emery Brown. Thank you to all the instructors and organizers, especially those at Mount Auburn hospital Mary Hewitt, Nathaniel Price, Alexandra Chabrerie, Roger Mark, Magdalena Espinoza, Brinda Kamat, Nathalie Bloch, Matthew Fickie, and Prudence Lam for giving me an unparalleled medical and clinical experience. During my graduate studies, I had the fortune of participating in a few opportunities outside the Boston community, including Clubes de Ciencia, International Biocomplexity Summer School, and the US-Turkey Advanced Institute on Global Healthcare Challenges. I would also like to acknowledge my funding sources that opened me to new experiences: NSF Graduate Research Fellowship, MIT Ida M. Green Fellowship, ALIFE Student travel grant, MIT GSC Travel Grant, Amgen Scholar Alumni Travel Grant, and DNA Student Travel Grant.

Another aspect that sets HST apart is its supportive community. I am thankful for Laura Tanenbaum for being so supportive through our time in transport and ICM, Justin Lo for sharing his musical talent, and Kay Furman, Pavitra Krisnaswamy, Dan Day, James Dahlman, Alex German, Jon Sellon, Kelvin Ng, Jean-Phillipe Coutu, Kendall Clement, Jacob Sargent, Nuria Oliva, Britni Crocker, and Mie Kunio for their camaraderie. Graduate school certainly would not have been the same without the LMA lunch group/Biophysics Breakfast Club: Stephanie Yaung, George Xu, Luis Barrera, Hanlin Tang, James Kath, Thomas Graham, with guest appearances by Helen Hou, Mingjie Dai, Drago Guggiana-Nilo, Sandeep Koshy and Vikram Juneja. It's been an awesome three years of weekly Wednesday lunches. Thank you for being the ultimate graduate student support network, the highlight of my work week, and the best lunch buddies :). Of particular note, Stephanie was seated one bay away from me in lab, and we navigated through graduate school together. I am so grateful to have such an incredible friend with an open ear and compassionate heart to keep my spirits up.

Before starting graduate school, I had the fortune of working in a number of research laboratories. I am grateful to Sangeeta Bhatia for gifting me one of the most defining experiences during my undergraduate, for serving as my role model, and for giving me thoughtful direction. During my time as a UROP in her lab, I had the privilege of working closely with Geoffrey von Maltzahn and Alice Chen. They are amongst not only the best scientists but also the best people I've met. Thank you for the endless guidance, kindness, and encouragement. I would also like to thank Nate Reticker-Flynn, Kartik Trehan, Meghan Shan, Kelly Stevens, Robert Schwartz, and Kevin Lin for the wonderful times in lab and Sue Kangiser for helping with all my graduate application materials. I would especially like to thank Nate and Kartik, who were my unofficial mentors. Geoff, Alice, Nate, and Kartik significantly influenced my decision to go to graduate school and are constant sources of inspiration for me. I also had the privilege of working in Gordana Vunjak-Novakovic's laboratory at Columbia University. During that summer, I had an incredible experience training with Danny Freytes who taught me a number of skills that carried with me through graduate school. I am especially thankful for Gordana's incredible support and generosity that extended beyond my time working in her laboratory. Throughout my studies, Gordana always gave me the most insightful and wise advice. I am also very appreciative of my other mentors Young Seok Song, Keping Qian, Leping Shen, M. Ian Phillips, Andrew Lieberman, and Minghui Chai for cultivating my interest in research, as well as my undergraduate advisor Alan Hatton for supporting my career path. I would also like to thank my instructors at HMS, MIT, and the University of Michigan for sharing their passions, opening my mind, and nurturing my creativity, especially Shiv Pillai, Rick Mitchell, Jose Gomez-Marquez, Jean-Francois Hamel, MIT Glassblowing Lab, Jay Pastorello, Peggy Adler, H. Don Cameron, Julen Etxabe, and Kathleen Nolta.

I'm blessed to have the support of many friends during my graduate studies. They were always there to keep me balanced and to remind me of the important things in life. Thank you Alan Leung, Cassie Liu, Eugenio de Hoyos, Mary-Jane Tsang Mui Ching, Jessica Chen, Christie Sze, Jen Gillman, Hattie Chung, Jennifer Lai, Jonathan Lansey, Daniel Martin-Alarcon, Claire Redin, and Wanwisa Sørensen for the breakfast, lunch, and dinner dates. Thank you Wendy Hom, Andrew Tse, Paul Jang, Brian Choi, and Kenneth Ng for the fun annual new year adventures. Thank you Cookie Club bakers Cameron Mhyrvold, Crystal Rawlings, Elaine Oberlick, Deepali Ravel, and Alina Chen for sharing your sweet tooth and love of optimizing. Thank you roommates David Colognori, Vincent Liu, and Kendall Huang for the fun dinner parties and boardgames nights. Thank you LMRT UROP alums Jayanthi Jayakumar, Sarah Han, Semmie Kim, Peter Fung, Daniel Kim, Omar Abudayyah, and Razaz Mageid for keeping the parties going outside of lab and undergrad. Thank you WILG alums Veena Venkatachalam, Sarah Harrison, Rachel Price, Caroline Lowenthal, Alex Piotrowski, Farah Alibay, Minwah Leung, Yuki Jung, Jen Paek, Kathleen Fleming, Sabine Langkau, Emily Conn, Vidya Ganapati, and Sara Sheehan for inspiring me with your positive strength. I'd especially like to thank Jen and Kathleen for continuing the crazy fun times outside our late nights in the dungeon and Sabine, Emily, Vidya, and Sara for being so sweet and supportive and for extending our mischievous explorations from around campus to around the nation and world. In a wonderful coincidence, a number of friends from my small hometown moved to the area. Thank you Elise Novitski, Anjuli Jain-Figueroa, Grace Lee, Joshua Cregger, honorary townie Akshaya Verghese, and occasional weekend visitors Indira Jain-Figueroa, Chenan Zhang, Michael Lee, and Ankita Mohanty for keeping me grounded. Thank you my dear pen-pals Wendy Mu and Esther Ho for constantly surprising and brightening my day. I am especially appreciative of Mary Xu and Diana Cai who are pillars in my life. Thank you for being amazing, for always being there to give me a hug, for sharing some chocolate or a warm meal when I most need it, and for being my Boston family :). I would certainly be lost without them. I am thankful for all my wonderful friends who have enriched my life and helped make Boston home for me.

I am very grateful to have my very best friend and favorite travel buddy Jack Lu. We have explored the world together and had many happy and fond memories together with Nanobot, Happy, Berri, Gumbo, Gumdrop, and Bobo. Thank you for always being there to give me the most needed words of comfort, support, and encouragement through my time in Boston. Regardless of the ups or downs of life, he reminds me of the bigger picture of life and challenges me to grow more resilient, to have more strength, to be more courageous, and to give more freely. I can't be more appreciative or grateful of having someone as great in my life and a companion with whom I can always share delicious food, smiles, and laughter :).

Most of all, I have would like to thank my family. I certainly would not have had any of these opportunities without the love and encouragement of my family. I'd like to extend my gratitude to my Aunt, Uncle, Carmen, and Kariona Lam for sharing their home and caring for me so well every Thanksgiving, Christmas, and any other random time I show up. I always enjoyed filling my belly and felt most relaxed when I visited. My brothers Payton and Peijie are the best brothers any sister could ask :). Thank you for coming all the way to Boston to help me move twice times. Thank you for cooking food for me at the crack of dawn or after an exhausting long day's work. I couldn't have had more fun growing up with or be any luckier to have the two of them. I cannot even begin to describe how appreciative I am of my wonderful parents Sing Cheong and Siu-Wah Ong. My parents raised us to look beyond superficial achievements and value ourselves for our character. They showed us that growing passions and carving our own paths required hard work, perseverance, and focus. They gently fostered our inquisitiveness, gave endless encouragement and belief for our every endeavor, and provided infinite care, comfort, and support when we struggled. They instilled in us a sense of integrity and taught us how to share and love without expectation. For all this, I have everything to thank for my parents.

While the acknowledgments above are certainly incomplete, I am very grateful for everyone for the impact they've made in my life and for making my time in graduate school particularly memorable. Thank you for inspiring me to be a better person and a lifelong learner and for making this journey amazing! :) I hope that I can now enter the world, fully embracing my responsibilities, creating improvement in society, and demonstrating reciprocity for all the extraordinary gifts and times I've received from the MIT, Harvard, and Boston community and beyond.

Contents

Dedication 3

Abstract 5

Acknowledgments 7

1 History of structural DNA nanotechnology 21

1.1 Challenges in manipulating nanoscale materials . . . 21
1.2 DNA as a structural and logic code . . . 21
  1.2.1 Structure of DNA . . . 22
  1.2.2 Branched DNA . . . 22
1.3 Structural DNA nanotechnology . . . 22
  1.3.1 Tiling approaches . . . 22
  1.3.2 DNA origami . . . 26
  1.3.3 Single-stranded tiles . . . 28
1.4 Dynamic DNA nanotechnology . . . 28
1.5 The promise of structural DNA nanotechnology . . . 31
  1.5.1 Materials development . . . 31
  1.5.2 Biophysical studies . . . 31
  1.5.3 Medical applications . . . 32
1.6 Challenges of structural DNA nanotechnology . . . 34
1.7 Scope of thesis . . . 34

2 Modular 3D DNA nanostructure assembly 35

2.1 Abstract . . . 35
2.2 Introduction . . . 35
2.3 Materials and Methods . . . 37
2.4 Results . . . 38
  2.4.1 Design of DNA-brick structures and a 3D "molecular canvas" . . . 38
  2.4.2 Optimization and characterization of DNA-brick cuboid structures . . . 41
  2.4.3 Structures of different sizes . . . 49

2.4.4 Complex shapes made from a 10×10×10 voxel 3D canvas . . . 50
2.4.5 Shapes made by carving the 10×10×10 voxel 3D canvas . . . 55
2.4.6 Generality of DNA brick self-assembly . . . 56
2.5 Discussion . . . 59
2.6 Acknowledgments . . . 60
2.7 Author Contributions . . . 61
2.8 Supplementary Data . . . 61
2.8.1 Analysis of different sized DNA brick cuboids . . . 62
2.8.2 Custom shapes made from a 3D molecular canvas . . . 64
2.8.3 Agarose gels of shapes . . . 66
2.8.4 3D carving . . . 68
2.8.5 Generality of modular DNA-brick self-assembly . . . 69

3 DNA Brick Crystals with Prescribed Depth 71
3.1 Abstract . . . 71
3.2 Introduction . . . 71
3.3 Materials and Methods . . . 72
3.4 Results . . . 74
3.4.1 Design and assembly of DNA brick crystals . . . 74
3.4.2 One-dimensional DNA-bundle crystals (Z-crystals) . . . 76
3.4.3 One-dimensional X-crystals . . . 76
3.4.4 Two-dimensional DNA-multilayer crystals (ZX-crystals) . . . 76
3.4.5 Two-dimensional DNA-forest crystals (XY-crystals) . . . 80
3.4.6 Crystal growth mechanism . . . 84
3.4.7 Yield and quality analysis . . . 89
3.4.8 Patterning gold nanoparticles . . . 93
3.5 Discussion . . . 95
3.6 Acknowledgments . . . 96
3.7 Author contributions . . . 96
3.8 Supplementary Materials . . . 96
3.8.1 Cryo-EM images of the XY-32H×64B-pore crystal and the XY-32H×128B-pore crystal . . . 96
3.8.2 AFM images of the XY-32H×64B-pore crystal and the XY-32H×128B-pore crystal 98

4 Towards large scale DNA assemblies 99

4.1 Abstract 99
4.2 Introduction 99
    4.2.1 Sequence space 101
    4.2.2 Thermodynamic analysis of brick interaction 103
    4.2.3 Brick design 103
4.3 Materials and Methods 105
4.4 Results 106
    4.4.1 Design optimization 107
    4.4.2 Variants of the 13-nt 6H×6H×104B structure 113
    4.4.3 Assembly optimization 114
    4.4.4 Structure characterization 118
    4.4.5 Design Software 120
    4.4.6 Shape Design 120
    4.4.7 Discrete symmetric structures 124
4.5 Discussion 126
4.6 Acknowledgments 127
4.7 Author contributions 128
4.8 Supplementary materials 128
    4.8.1 Particle size measurement distribution 128
    4.8.2 Feature testing of the 30H×30H×260B canvas structure 130
    4.8.3 Gel electrophoresis of large shape designs 131
    4.8.4 3D models of large shapes 132

5 Perspectives and Outlook **133**
5.1 Summary 133
5.2 Revisiting the promise 135
5.3 Conclusions 135

References **137**

List of Figures

Figure 1-1 DNA as a structural code 23

Figure 1-2 Multi-stranded DNA tiles 25

Figure 1-3 DNA origami 27

Figure 1-4 Single-stranded DNA tiles 29

Figure 1-5 Dynamic DNA systems 30

Figure 1-6 Applications of structural DNA nanotechnology 33

Figure 2-1 Design of DNA brick structures 40

Figure 2-2 Comparison of the self-assembly of a 4H×12H×120B cuboid with three sets of random sequences 41

Figure 2-3 Design of 48nt boundary bricks 42

Figure 2-4 A 6H×6H×64B cuboid with 48nt boundary bricks or 16nt boundary bricks 43

Figure 2-5 Design and TEM images of the 6H×10H×128B cuboid 44

Figure 2-6 Optimization of assembly conditions of the 6H×10H×128B cuboid 45

Figure 2-7 TEM analysis of the purified 6H×10H×128B cuboid 46

Figure 2-8 Assembling a 4H×4H×128B cuboid at different concentrations 47

Figure 2-9 Agarose gel electrophoresis and TEM images of 6H×10H×64B dimers 48

Figure 2-10 Cuboid DNA-brick structures 49

Figure 2-11 DNA bricks and derivatives for making the 3D canvas 51

Figure 2-12 Shapes made from a 3D “molecular canvas” 54

Figure 2-13 Schematics of structural reconfiguration from a 2D SST canvas 55

Figure 2-14 Structural reconfiguration from a 3D cuboid 56

Figure 2-15 Generality of DNA brick self-assembly 57

Figure 2-16 Design of a 6H×10H×64B-A cuboid 58

Figure 2-17 TEM and agarose gel electrophoresis of 3H×3H, 4H×4H, 6H×6H, 6H×10H, 8H×12H, 4H×24H, and 12H×12H cuboids 62

Figure 2-18 Workflow of designing 3D shapes 64

Figure 2-19 3D shape editing interface 65

Figure 2-20 Agarose gel electrophoresis of shapes 1–17 66

Figure 2-21 Agarose gel electrophoresis of shapes 18–100 67

Figure 2-22 Agarose gel electrophoresis analysis for 3D carving 68

Figure 2-23 Agarose gel electrophoresis of other modular DNA brick assemblies 69

Figure 3-1 Design of DNA brick crystals. 75
Figure 3-2 One-dimensional DNA crystals 77
Figure 3-3 Two-dimensional multilayer ZX-crystals 79
Figure 3-4 Two-dimensional DNA-forest XY-crystals. 81
Figure 3-5 Formation mechanism of the XY-4H×4H×32B-tube crystal 83
Figure 3-6 Boundary analysis of the XY-32H×64B-pore crystal and of hierarchically assembled 2D lattices 85
Figure 3-7 Annealing and time-lapse analysis of the ZX-4H×20H×32B crystal. 87
Figure 3-8 Annealing and time-lapse analysis of the XY-32H×64B-pore crystal. 88
Figure 3-9 Isothermal assembly and time-lapse analysis of the ZX-6H×4H×96B crystal 90
Figure 3-10 Deposition density analysis of the ZX-6H×4H×96B crystal. 90
Figure 3-11 FRET quenching of the ZX-6H×6H×64B cuboid crystal 92
Figure 3-12 Defect analysis of the XY-32H×64B-pore crystal 94
Figure 3-13 Gold nanoparticles patterned using DNA brick crystals. 95
Figure 3-14 Cryo-EM images of the XY-32H×64B-pore crystal and the XY-32H×128B-pore crystal 97
Figure 3-15 AFM images of the XY-32H×64B-pore crystal and the XY-32H×128B-pore crystal . 98

Figure 4-1 Domain sequence match analysis for varying numbers of randomly assigned domains 102
Figure 4-2 Detailed schematic for the 13-nt brick structure 104
Figure 4-3 Gel electrophoresis of a 6H×6H×(8-domain) structure with domains of length 8-nt, 13-nt, and 18.5-nt 108
Figure 4-4 Band intensity percentages and rate of change at varying times during structure assembly 110
Figure 4-5 Characterization of a 6H×6H×104B structure composed of 8-nt versus 13-nt DNA bricks 112
Figure 4-6 Gel electrophoresis of a 6H×6H×104B structure composed of variations of the 13-nt DNA bricks 113
Figure 4-7 Annealing ramp optimization 114
Figure 4-8 Assembly efficiency of the 30H×30H×260B cuboid across different reaction times . 115
Figure 4-9 Range of temperature formation 117
Figure 4-10 Assembly of DNA cuboids across scales 119
Figure 4-11 Process flow diagram and features of Nanobricks, a DNA brick shape design software 120
Figure 4-12 Complex shapes from a 30H × 30H × 20H canvas. 123
Figure 4-13 Discrete symmetric structures composed of 6H×6H×104B units 125

Figure 4-14 Gel electrophoresis of a tetramer comprised of 36H×36H×312B units 126
Figure 4-15 Histogram of measured edge lengths for the 36H×36H×312B particles 129
Figure 4-16 Feature testing of the 30H×30H×260B canvas structure. 130
Figure 4-17 Gel electrophoresis of large shape designs 131
Figure 4-18 3D view of Shapes A–D 132

Figure 5-1 Summary of DNA bricks 134

List of Tables

Table 2-1 Statistics of 3H×3H, 4H×4H, 6H×6H, 6H×10H, 8H×12H, 4H×24H, and 12H×12H cuboids 63

Table 4-1 Average hybridization energies and melting temperatures at 5 nM strand concentration 104

Table 4-2 Optimal formation temperature for isothermal assembly of different sized cuboids at 5 nM strand concentration 105

CHAPTER 1

History of structural DNA nanotechnology

In this chapter, we briefly discuss the motivation behind creating DNA structures. Particularly, we will discuss existing methods of manipulating matter on the nanoscale; describe why DNA is a good building material; what DNA nanotechnology is; and some history and recent advances in the field focused on the structural aspects. We then summarize the scope of this thesis and how our work builds upon and extends the field of DNA nanotechnology towards addressing some challenges in nanofabrication.

1.1 Challenges in manipulating nanoscale materials

Nanotechnology describes the study and creation of materials on the nanoscale (1-100 nanometers). Unique electronic, optical, mechanical, and biological properties and functions arise on the nanoscale, such as structural color or superhydrophobicity [1]. Because these properties offer promising opportunity for creating more efficient devices or smarter therapeutics, nanotechnology has a huge potential for impacting fields ranging from materials to medicine. This excitement has given rise to the development of a number of techniques to better synthesize and control different nanomaterials. Nanofabrication methods are typically categorized into "top-down" and "bottom-up" approaches. Conventional top-down approaches, such as lithography, can be used to pattern arbitrary patterns in a high throughput manner [2]; however, obtaining complex 3D features requires multi-step processes [3, 4]. Typical bottom-up approaches, such as self-assembly of block-copolymers, offer the advantage of high feature resolution across large surfaces and low costs , but achieving both 3D complex features and nanometer resolution remains difficult [5]. For both methods, there are often preferred materials for patterning and post-patterning functionalization must be used [6, 7]. While these methods have proliferated and improved over the years, creating arbitrary 3D patterns on the nanoscale still remains challenging. Because nucleic acids are programmable, their self-assembly offer the potential of addressing these fabrication challenges, allowing for facile, rational design of complex 2D and 3D patterns.

1.2 DNA as a structural and logic code

DNA is widely known to be the "blue-print" of life. James Watson and Francis Crick's publication of the structure of DNA in 1953 ushered in a new era of biology focused on elucidating underlying molecular mechanisms [8–10]. With the establishment of the central dogma of biology, DNA became synonymous with its biological function as a genetic material. Only in the recently has interest in using DNA for other means arisen.

In 1982, Nadrian Seeman describes how nucleic acids can be programmed to self-assemble into particular topologies [11]. The fundamental insight that DNA is a programmable molecule catapulted the field of DNA nanotechnology and opened up a wide-array of directions, pursing the vision of using DNA to spatially and temporally manipulate matter. Since then, a large number of developments in structural and dynamic systems have been made [12, 13]. In this section, we will describe the structure of linear DNA and then describe the underlying concepts for creating novel DNA motifs.

1.2.1 Structure of DNA

DNA adopts a number of different structural forms depending on the local environment, but it is most typically found in its B-form in physiological or hydrated conditions. In this form, the molecule contains two anti-parallel, complementary strands that follow Watson-Crick base-pairing rules, where adenine (A) hydrogen bonds with thymine (T) and guanine (G) with cytosine(C) (Fig. 1-1A). The hydrophobicity of the bases result in DNA forming a right-handed double helix structure with a 2 nm diameter and a pitch of 3.5 nm, giving 10.5 bp/turn [14]. These length scales make DNA a material inherently capable of nanoscale resolution construction. Ultimately, the complementarity rules drives the underlying function of designed DNA systems, enabling researches to specify how different strands should interact through careful sequence design.

The double helix is held together by both the hydrogen bonding interactions of the base-pairs and π-π interactions of the base-stacks. Numerous thermodynamic models have been developed to estimate the hybridization energies [15], which are important to consider when designing stable structures. Due to the asymmetrical orientation of the basepairs, the resulting double helix contains a major and minor groove. Accounting for these groove differences is also important when creating unstrained structures.

1.2.2 Branched DNA

To go beyond linear DNA and create complex DNA structures, we must be able to form stable junctions and branches. In nature some branched structures exists such as Holliday junctions that form during recombination; however, these Holliday junctions have mobile branch points due to the sequence symmetry present in the arms. To create an immobile four-arm junction, each of the arms is designed to contain a set of unique sequences (Fig. 1-1C, complementarity indicated by matching colors) [16]. From these four arms, we can derive four strand species that can be designed to fold into the designed junction. Seeman posits that these junctions can be used to create higher order structures through "sticky-end" interaction, where single-stranded segments on the ends of the junctions can hybridize with other free sticky ends (Fig. 1-1C). This concept of DNA programmability and branched topology from careful assignment of strand complementarity, strand architecture, and sequence design underlies the field of structural DNA nanotechnology.

1.3 Structural DNA nanotechnology

As implied by the name, structural DNA nanotechnology focuses on using nucleic acids as a building material to create thermodynamically stable nanoscale features for patterning, placing, and/or positioning functional molecules. A number of RNA structures have also been created, but often these are much smaller in size and exploit the non-canonical hybridization that RNA can undergo, such as kissing loop or tetraloop and receptor interactions [17–19]. In this section we will focus on the development of nanostructures with designed Watson-Crick base-pairing interactions. We will discuss two categorical methods for forming DNA nanostructures: tiling or origami.

1.3.1 Tiling approaches

The first synthetic DNA nanostructures developed used a modular tilling approach. While the example structure above demonstrated the ability to create immobile branches, the overall form is still floppy and capable of adopting a number of different conformations (Fig. 1-1B), making this structure difficult for use

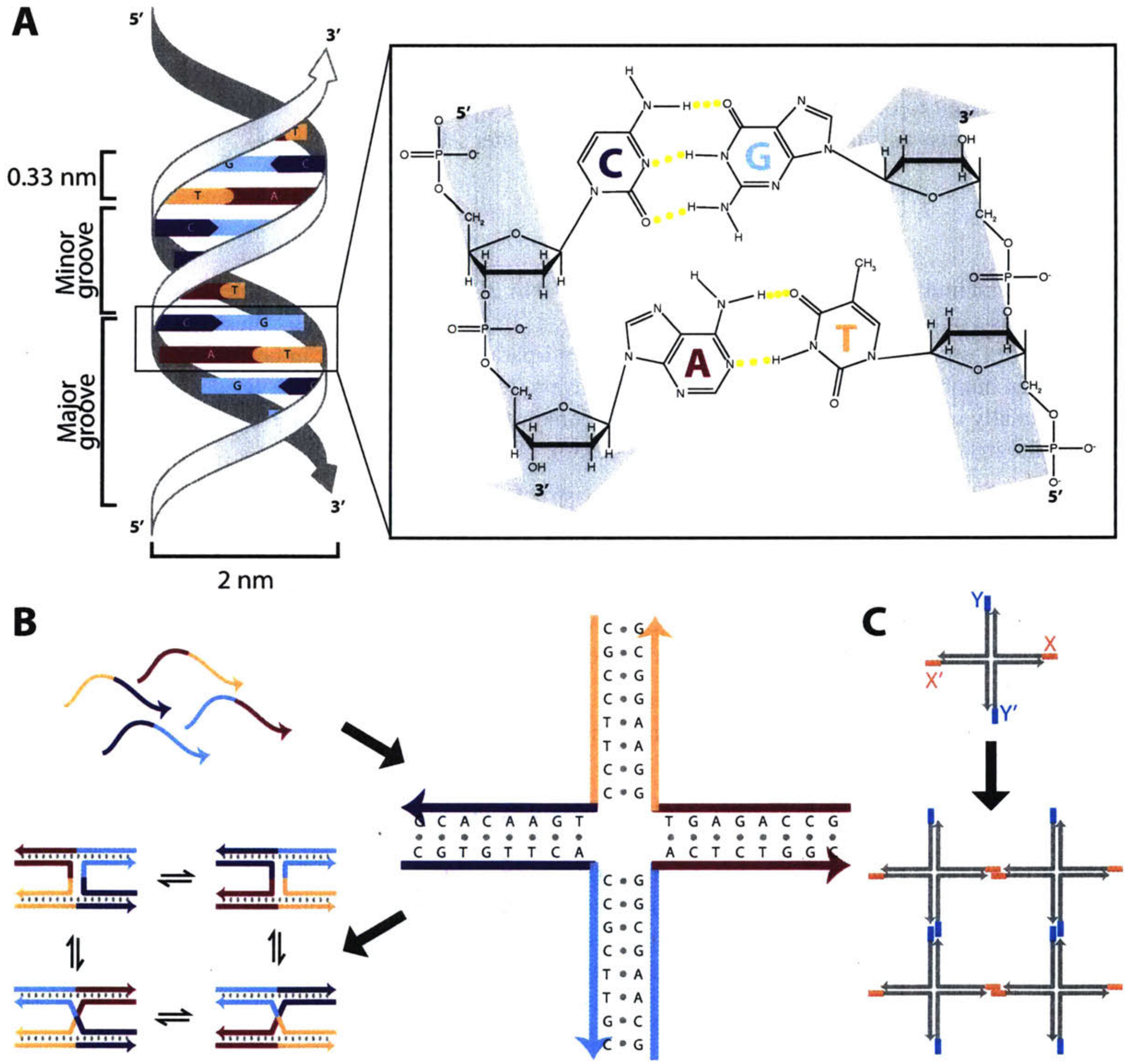

Figure 1-1: DNA as a structural code. **(A)** Schematic showing B-form DNA. Dimension of the diameter and the rise per base-pair are shown. Major and minor grooves are labelled. Inset shows the molecular structure of the Watson-Crick basepairs and how hydrogen bonding occurs. Arrows indicate the 3' end of the helix. **(B)** Schematic of a stable four-arm junction assembly. Colored domains indicate sequence complementarity. Unique sequences are designed for each arm to avoid symmetry and mobility of the branch junction. Flexibility of the junction is shown in the bottom left where structure can adopt antiparallel and parallel crossover orientations. **(C)** Four-arm junctions with complementary single-stranded "sticky-ends" can be used to assemble higher order lattices. Sticky ends are colored in blue and orange and marked by domains X and Y, which are respectively complementary to X' and Y'.

in creating rigid features necessary for precise positioning. Thus, a number DNA tiles consisting of multiple strands that would self-assemble to form a unit with a rigid core and display sticky ends were developed (Fig. 1-2). These tiles were designed such that they contain long binding domains in the core and short sticky-ends, so the structure can assemble hierarchically to first form the rigid core. These single-stranded ends could then interact cooperative to form stable arrays. Later, a single-stranded tiling approach would simplify each unit to only the functional sticky ends. Progress for multi-stranded tiles are described below and we will discuss advances in single-stranded tiles in a later section.

Lattices

One of the first multi-stranded tiles used to form large DNA 2D lattices were the double crossover tiles (DX), which consists of two juxtaposed 4-arm junctions (Fig. 1-2A). While double-helix tiles come in many forms, the two types used for lattice construction contain anti-parallel helices and can be designed with either an odd or even number of half-turns between the crossovers (termed DAO and DAE). By designing sticky ends that minimally interact, Winfree et al. was able to demonstrate the formation of 2-tile and 4-tile 2D lattices that would grow to microns in size [20] (Fig. 1-2B,C).

These DX tiles are just one of many used to construct arrays, tubes, and ribbons [12]. Other tile motifs include Holliday junction rhombus-like motifs [21], triple crossover complexes [22, 23], 4×4 tiles [24], tensegrity triangles [25], three-point star motifs [26], six-helix bundle tiles [27], double-double crossover tiles [28], triple crossover tiles [29], 4-, 8-, and 12- helix tiles [30], paranemic (PX) tiles [31], DX parallelograms [31], and two-stranded weave tiles [32]. Although the tile type used can tune the lattice pattern of final structure, many of these patterns produced are not arbitrary and have a small repeating unit.

To create more complex patterns, Rothemund, et al. used algorithmic self-assembly to program four or six DX tiles to perform XOR logic commands and pattern Sierpinski triangles on a growing lattice (Fig. 1-2D) [33].

A breakthrough came in 2009 when Seeman's group demonstrated the construction of a 3D DNA crystal [34]. By using tensegrity tiles composed of seven strands, they grew crystals that reached hundreds of microns in size and that were capable of diffracting X-rays (Fig. 1-2E). While these crystals attained a new level of precision and rigidity, their cavity size was quite small, measuring 103 nm^3, limiting the type of guest molecules that can be hosted for structure determination. Further, similar to many of the other multi-stranded tiles, these require high strand purity and stoichiometric control.

Finite structures

Some of the earliest finite-sized constructions are small polyhedra that use single-duplex edges with completely unique sequences [35–37]. Shih, et al. created a larger octahedron using a 1.7 kilobase scaffold strand and 5 helper strands to form DX and PX struts [38]. Designing such shapes is challenging due to the need for carefully designed sequences. For the most part, multi-stranded DNA tiles have been used to create infinite 2D or 3D crystals out of few component strands. Researchers have also focused on using tiles to create polyhedra by promoting curvature in the tiles. For example, Mao's group modified their 3-point star DNA tile and developed a new 5-point star motif to allow for flexibility [39, 40]. Through tuning the strand concentrations, they could assemble polyhedra of different sizes, including a large buckyball structure that contains 60 tiles (Fig. 1-2F).

While an impressive diversity of structures can be assembled from this tiling approach, the overall addressability of these structures are often quite limited due to the use of few unique tiles. Researchers have used seed structures and strands to nucleate and grow ribbons with fixed widths [41–43]. Groups have created finite fully addressable arrays by programming unique sticky ends for each tile or introducing overall symmetry in the structure [44–46]; however, these require multistep processes that can be difficult to scale if very large structures are desired and shape complexity is often limited in these designs. Further, these sticky ends require well-designed sequences to minimize errors and defects that occur during structure growth. Progress towards truly arbitrary shapes was made to create more addressable structures through incorporation of a long scaffold strand.

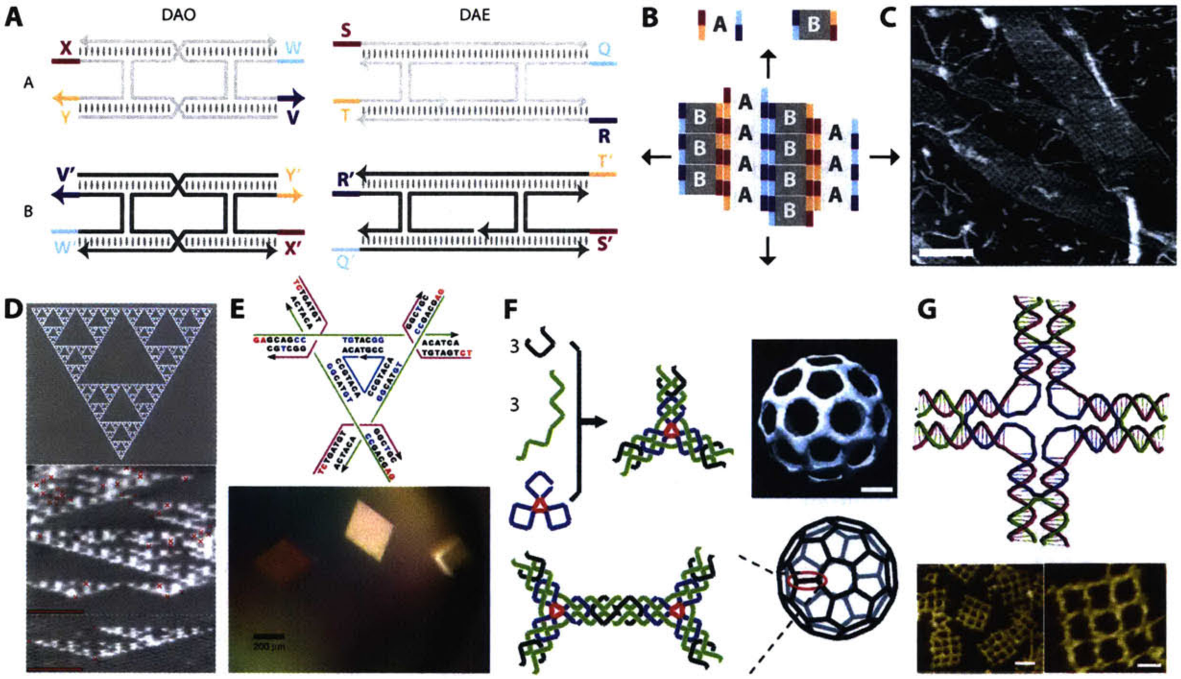

Figure 1-2: Multi-stranded DNA tiles. A few different examples showing the diversity of tiles used and the structures they can assemble. **(A)** Two types of double-helix tiles that can be used to create large lattices: DAO (double crossover, antiparallel, odd number of half-turns) and DAE (double crossover, antiparallel, even number of half-turns) tiles. Each of these type types have two forms A and B, which contain sticky ends that are complementary to one another, as indicated by matching color and coordinated domain names. **(B)** The A and B tiles shown in (A) can assemble to form large 2D lattices by sticky end hybridization. **(C)** An AFM image of a lattice assembled from A and B DAE tiles. Scale bar measures 300 nm. **(D)** Sierpinski triangle lattice assembled from six unique DAO tiles. Scale bar measures 100 nm. **(E)** 3D DNA crystal assembled from a 7-strand tensegrity triangle. Scale bar measures 200 μm. **(F)** Buckyball assembled from 60 three-point star motifs. Scale bar measures 20 nm. **(G)** 16-tile finite assembly made from the multi-step assembly of 4×4 tiles. Left shows a 2-step assembly procedure containing completely unique sticky ends (scale bar measures 50 nm). Right shows the product of a 4-step assembly to minimize sequence design (scale bar measures 20 nm). Portions of this figure were adapted with permission from refs. [20, 33, 34, 39, 45, 47]

1.3.2 DNA origami

In 2006, Paul Rothemund brought DNA nanotechnology to a new level of complexity through his invention of DNA origami [48]. Previously, DNA structures were typically made from a small number of components using the tiling based methods described above. In this seminal work, Rothemund demonstrated the formation of abitrarily-designed complex ~5 MDa 2D DNA nanostructures that span approximately a 100 nm × 100 nm area. These DNA origami structures consisted of a long single-stranded "scaffold" strand derived from M13 bacteriophage genome and numerous complementary synthetic "staple" oligomers that ranged between 32–48 nt. To create a desired shape, the scaffold strand would be used to rasterize pattern. Following, staple strands would be designed to be complementary to nonadjacent segments of the scaffold, thereby holding together different parts of the scaffold to create the overall 2D shape (Fig. 1-3A,B).

The structures can be formed by annealing the circular scaffold strand and in the presence of 100 fold excess of staple strands in a single-pot reaction. Because each of the staple strands can be independently addressed, the overall structures would have a 6 nm spatial resolution. In additional to the landmark structural demonstration, the work shows that sequences did not need to be carefully designed and that the staple oligomers, unlike strands used in the tilling approach, do not need to be purified for successful structure formation. The origami approach also differs from tilling approaches in that staple component strands hybridize only with the scaffold strand.

3D origami

Some of the first attempts at creating 3D structures create single-layer sheets that contained hinge connections so the scaffold could fold to a hollow form [49, 50]. Although these forms potentially allow for control over access to the inside of the structure, arbitrary 3D structures are difficult to pattern using this strategy. Development of 3D origami soon followed when Shih and coworkers demonstrated numerous shapes containing a honeycomb-like lattice [51]. To create these structures, the scaffold strand was carefully routed layer by layer through the structural form. Staple strands were then designed to hold the different layers of scaffold together. Using this approach, the group was able to assemble numerous structures on a honeycomb lattice (Fig. 1-3C). Later solid form DNA origami structures with square, hexagonal, and hybrid lattices were assembled [52, 53].

Curved structures

In addition to the 2D and 3D structures described above, researchers have also developed bent, twisted, and curved DNA origami structures [54, 55]. These strained structures were created by careful deletion or insertion of basepairs to create the appropriate torque. Using these methods, DNA bundles with a minimum 6 nanometer radius of curvature, hollow DNA spheres, and nanoflasks were assembled (Fig. 1-3D).

Wire-framed structures

Recently, two groups demonstrated the capability to create origami wire-framed structures [56, 57]. Polyhedral meshes are capable of modeling any arbitrary shape without fixing the structures to any particular lattice, making such an approach to approximating shape highly desirable. These groups were able to identify an algorithm that would allow them to route the scaffold easily through any shape. As a result, they created both 2D quasi-crystalline patterns and 3D models of arbitrary shapes, including a snub cube (Fig.

1-3E). Although the the hollow nature of these polyhedral meshes enabled assembly at lower salt conditions, the openness of the structure also resulted in floppiness.

Multimerization

Structures of larger sizes can be assembled by treating either the tiles or origami structures as monomeric building blocks [58–62]. Often this is a two-step process where the monomers are first assembled then are mixed together to form the larger structures. Polymerization of the monomers is often achieved either by designing complementary surfaces for base-stacking interactions to hold structures together or through designed sticky-end interactions. An impressive demonstration of 3D self-assembly enabled multimerize perpendicular to the helical axis through shape complementary and base-stacking interactions (Fig. 1-3F). This method was used to create both infinite and finite assemblies (trimers were demonstrated) that can be reconfigured depending on the solution $MgCl_2$ concentration [61].

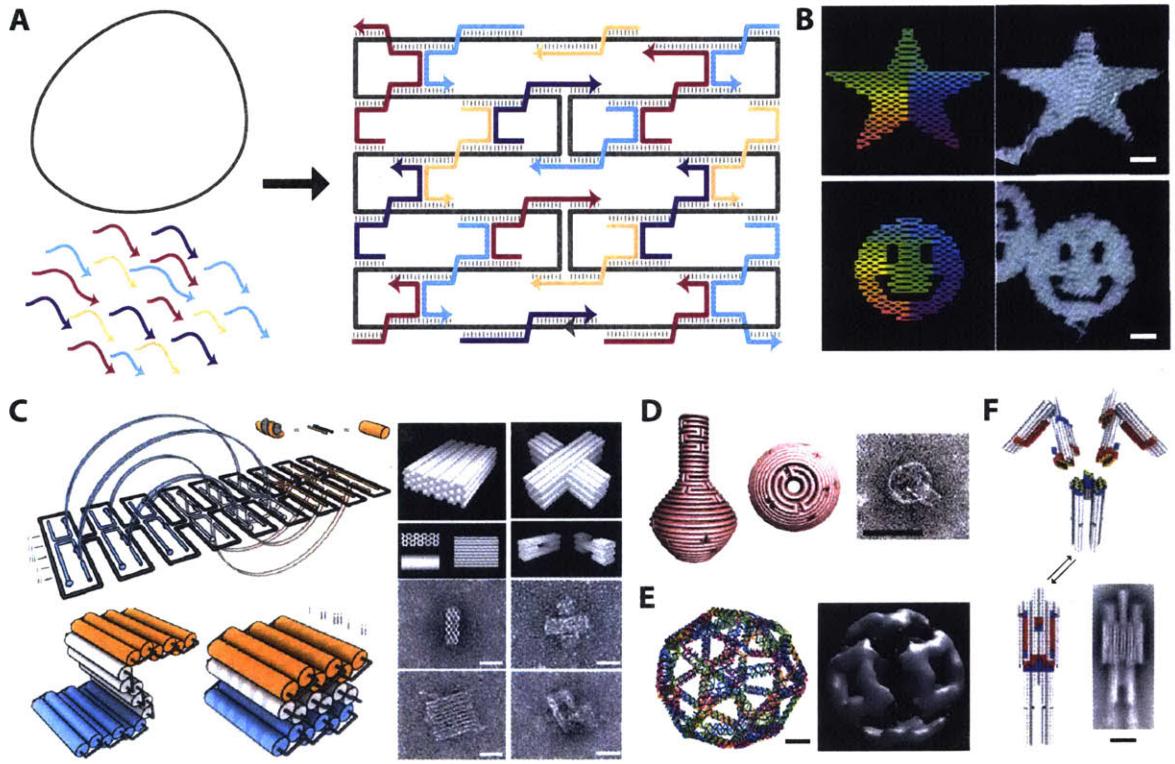

Figure 1-3: DNA origami. A few examples of DNA origami structures. **(A)** Schematic depicting the concept of DNA origami. A circular scaffold strand assembles to a prescribed shape through complementary interactions with short oligomeric staples. **(B)** 2D DNA origami with left panel showing designs and right panel showing AFM images. Scale bar measures 25 nm. **(C)** 3D DNA origami has a layered scaffold routing held together by staple strands. Left shows two designed structures and associating TEM micrographs. Scale bars measures 20 nm. **(D)** DNA nanoflask designed with complex curvature. Scale bar measures 50 nm. **(E)** A wireframe DNA origami of a snub cube containing 24 vertices and 60 edges. Scale bar measures 10 nm. **(F)** 3 different DNA origami parts self assemble to create an origami man. Scale bar measures 25 nm. Portions of this figure were adapted with permission from refs. [48, 51, 55, 57, 61].

1.3.3 Single-stranded tiles

While traditional tiling approaches enable modularity in design, the shape complexity is limited and control over dimensions often require nucleating strands or seed structures. In contrast, DNA origami approach addresses this challenges in creating structures of designed shape and size; however, each arbitrary design requires careful scaffold routing and redesign of staple strands. Thus, single-stranded tiles (SST) were developed as a simple method to utilize the advantages of both tiling and origami techniques for modular size and shape control [63, 64].

An SST consists of a single-stranded 42-nt oligomer split into 4 separate binding domains across two helices. When incorporated in a structure, the tiles adopt a U-shape conformation and interact with 4 different strands on neighboring helices. These SSTs differ from traditional tiles in that they reduce the form factor to only the functional sticky ends, are floppy when unbound, contain roughly equal binding energies throughout, and use single half-crossovers.

To create fixed width ribbons, Yin, et al. used tiles with unique sequences in each row and bounded the structure with half-tiles. They demonstrated formation of ribbons and tubes from 4- to 20-helices wide. Similarly, to specify tube diameters, the group used connecting tiles that were complementary to opposing edges of the original ribbons. It was hypothesized that tubes of designed dimensions rather than extended lattices or tubes with $i \cdot n$ diameter, where n is the the designed diameter and i is an integer greater than 1, were formed due to the intrinsic curvature of the structure and kinetic trapping of closed tubes [63].

The ability to demonstrate defined 1D structures using a modular SST approach enabled the group later to extend this work to defined arbitrary 2D structures. By utilizing a similar tile architecture and implementing completely random domain sequences, Yin's group created 2D rectangular canvases (Fig. 1-4) [64]. Because of the modular architecture of SST structures, the group could easily pattern a number of shapes by simply including the desired strands. Following this work, numerous other single-stranded tile motifs with different binding domain lengths, linker lengths, and strand architecture have been explored to create flatter structures or to control assembly temperatures [65, 66]. These SST structures demonstrate that shapes as large and complex as M13 origami structures can be assembled from modular components. This scaffold-free approach also enabled component reuse and rapid shape and size changes without the need to redesign sequences. Further, development of the single-stranded tile approach debunked a number of notions about tile-based assemblies. Particularly, the method demonstrated that structures could form without perfect stoichiometry, purification, or carefully designed sequences.

1.4 Dynamic DNA nanotechnology

The other half of DNA nanotechnology involves creation of dynamic devices and systems. While our focus in this thesis and chapter is on the structural aspects of DNA nanotechnology, we will summarize a few key findings in this field. The foundation of dynamic DNA nanotechnology is the concept of strand displacement, where one strand replaces another in a hybridized duplex through the branch migration process (Fig. 1-5A). Using strand displacement, scientists have created various DNA circuits [67–70], catalytic pathways [68, 71], and walkers [68, 72, 73].

Structural and dynamic DNA nanotechnology has also been combined to create structures with mechanical functions. Some of the earliest work consists used DNA tiles to create switches [74–76]. Molecular tweezers that can be controlled through a single strand displacement have also been invented [77] (Fig. 1-5B). Hinged components enabled opening and closing of hollow DNA structures [49, 78–80]. Recently, more complex structural reconfigurations using strand displacement mechanisms have been developed using

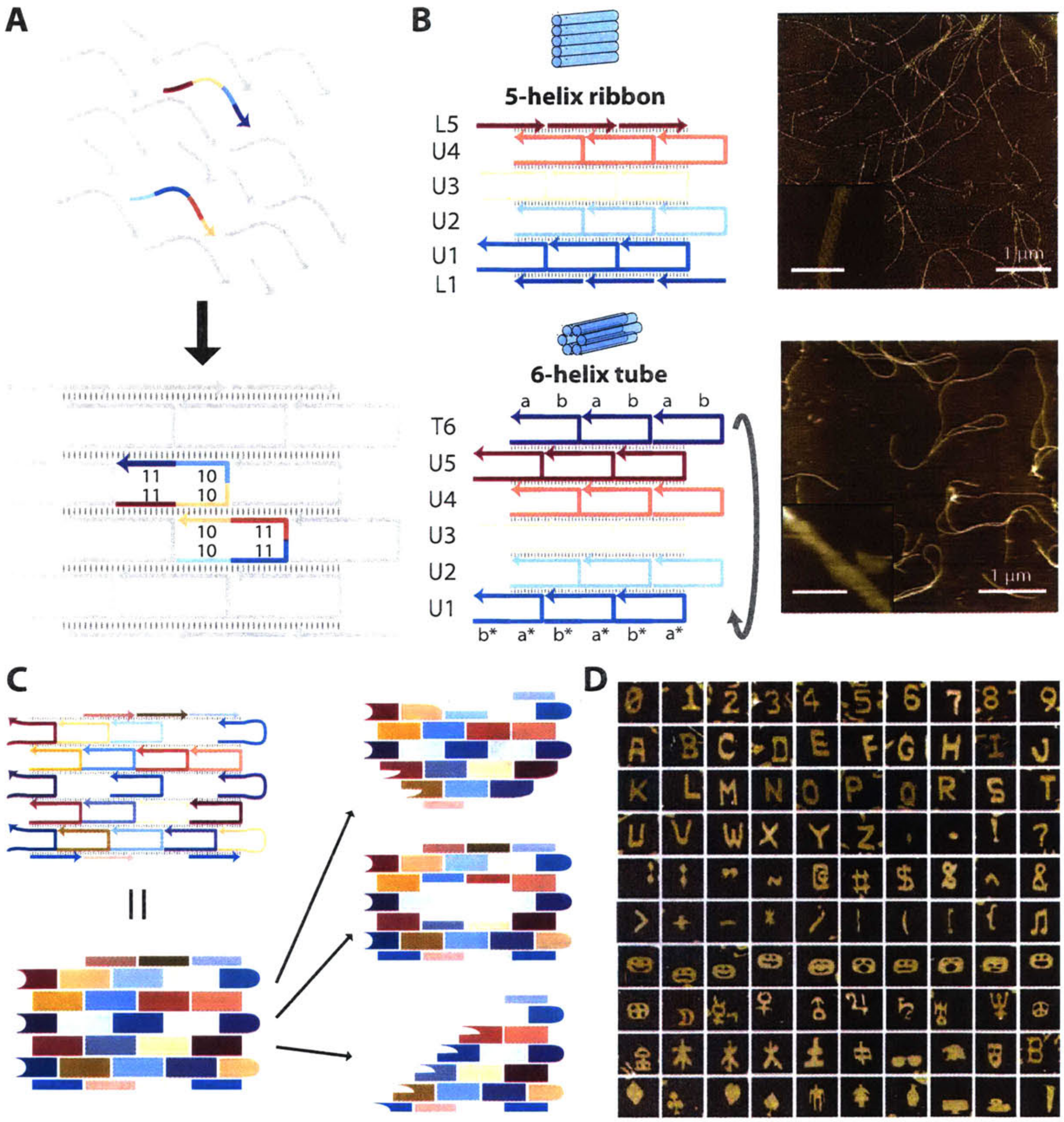

Figure 1-4: Single-stranded DNA tiles (SST). (A) Schematic of SST assembly. Each strand contains 4 binding domains of length 10 or 11 nt. Colors are used to highlight the different domains on two strands. The SST is incorporated into a structure in a U-shaped motif, and the highlighted architecture is repeated throughout the whole of the structure. **(B)** Assembly of 1D DNA nanostructures. Similarly colored strands represent the same species. The 5-helix ribbon (top) contains half strands, and a 6-helix tube (bottom) contains a transversing tile with complementary faces on the two sides of the ribbon (T6). Left shows AFM images of the respectively designed structures. Inset scale bar measure 50 nm. **(C)** Assembly of 2D DNA nanostructures. Different strand species are indicated by the different colors. Strands can be represented as tiles. By modular inclusion of these tiles, different shapes can be assembled. **(D)** AFM image of different SST structures. The edge of each image measures 150 nm. Portions of this figure were adapted with permission from refs. [63, 64].

DNA origami structures [75, 81, 82, 82, 83]. Of particular note, Yan's group demonstrated the formation of catenane derived from DNA origami Möbius strip [82]. Separately, Castro's group has created larger scale molecular devices that mimic macroscopic mechanical devices such as kinematic joints and sliders by programming DNA to fold into origami structures with single-stranded connectors that constrain motions [84] (Fig. 1-5C).

In addition to designing DNA structures that have mechanical functions, groups have also focused on controlling assembly pathways. Yin, et al. showed that assembly pathways can be specified to create target structures. In this work, component strands are initially trapped in a metastable hairpin conformation. Only upon presentation of a triggering strand are the hairpins opened to expose free single-stranded ends, allowing for strands to interact in a pre-defined order to assemble a final structure [63] (Fig. 1-5D).

As DNA nanotechnology progresses, we'll likely see a convergence of the two parts to achieve a rich interplay of structural and dynamic functions.

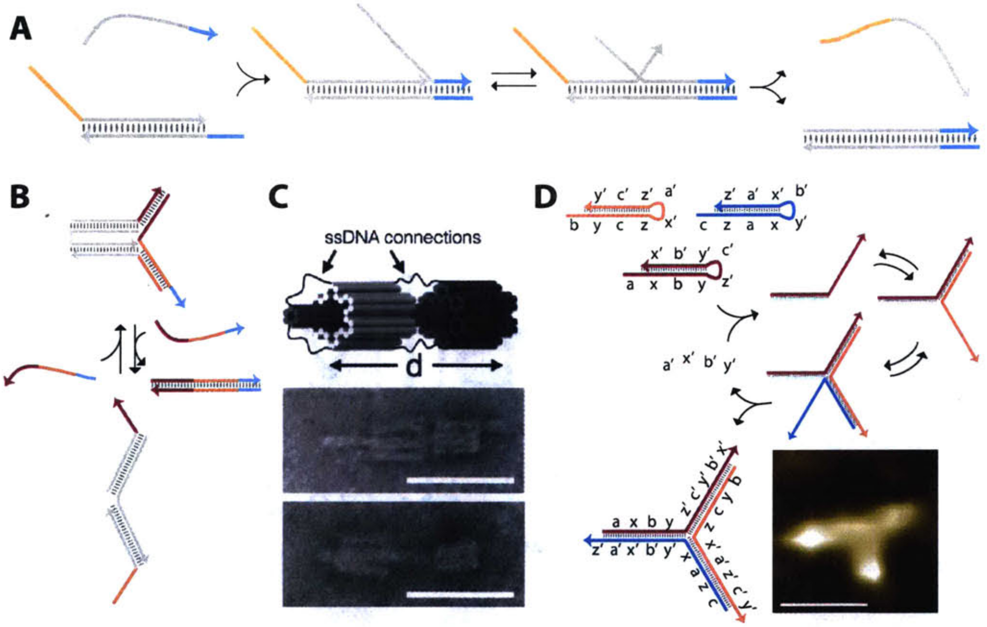

Figure 1-5: Dynamic DNA systems. **(A)** Schematic of strand displacement. Matched colored segments indicate sequence complementarity. The displacing strand can bind a free single-stranded "toehold" to cause branch migration to occur, eventually displacing the original incumbent strand. **(B)** Schematic of molecular tweezers. Introduction of a triggering strand can control opening and closing of the tweezers. **(C)** DNA origami mechanical slider containing single-stranded connectors. TEM images show an open and a closed conformation. Scale bars measure 50 nm. **(D)** Dynamic self assembly of a three-arm junction. Initial monomers are in a metastable hairpin conformation. Upon addition of a triggering strand (light blue), the hairpins can sequentially open and hybridize to the growing structure. Eventually the trigger strand is displaced off irreversibly. Matching domains is indicated by numbers. Scale bars in AFM image measures 10 nm. Portions of this figure were adapted with permission from refs. [68, 84].

1.5 The promise of structural DNA nanotechnology

Since the construction of the large arrays, DNA nanostructures have been used to pattern molecules. The original intention of Seeman's interest in creating DNA-based lattices was to pattern proteins for structural determination. The development of a diversity of structures and especially of the DNA origami method spawned a number of new applications. Because of the versatility and parallelized construction offered by DNA nanotechnology, these structures have been utilized across a variety of disciplines, such as in materials and biological sciences, leveraging the capability for a diversity of matter to be controlled through conjugation with DNA. A multitude of these applications rely on using DNA nanostructures displaying sticky ends at specific locations as scaffolds for arranging and manipulating functional moieties containing complementary strands. We will discuss a few key results in this section.

1.5.1 Materials development

Due to the intrinsic nanometer resolution of the component molecule, DNA structures have been used to organize a variety of inorganic materials including metal nanoparticles [85, 86], quantum dots [87–89], chromophores [90], nanodiamonds [91], polymers [92], and carbon nanotubes [93], with the goals of create efficient energy antennae or unique electronic, plasmonic, or photonic properties. Studies have demonstrated the assembly of chains of gold nanoparticles spaced <10 nm apart or patterned with multiple particle types [94, 95]. A group led by Liedl showed that chiral AuNP chains exhibiting different optical properties can be formed using DNA origami as a scaffold [86] (Fig. 1-6A). Yan's laboratory also demonstrate the patterning of gold nanorods in different angular configurations on a 2D origami substrate [85]. To create long range ordering, researchers have also focused on organizing DNA origamis on a SiO_2 surfaces [96, 97] and on using these oriented origami to further arrange nanoparticles [98]. Although these approaches are promising for future device fabrication, a number of challenges still exists to fully integrate DNA nanostructures with top-down approaches, including defect control, solution compatibility, and tighter and more precise particle positioning. Because many of these studies use open-form DNA nanostructures, positioned particles have the flexibility to rotate, causing deviations in alignment. Recently, Dietz and co-workers demonstrated the capability of positioning molecules down to smaller than one nanometer resolution using a hinged origami structure [99].

The DNA nanostructures have also served as molds, masks, or templates for other patterning purposes [100]. Liu, et al. showed that "Y"-shaped DNA origami can be metallized to transfer its pattern to a gold substrate [101]. The Yin lab also demonstrated that metal nanoparticles can be cast into unique forms using DNA origami as molds [102] (Fig. 1-6B). The group has also demonstrated patterning of graphene substrates and inorganic oxides using DNA structures as masks and templates [103, 104] For many of these applications, template rigidity may pose problems, as these DNA structures may deform to cause defects in the pattern transfer. Additionally, the transferred patterns often have limited resolution at sharp corners and edges.

1.5.2 Biophysical studies

The resolution and addressability of DNA nanostructures offer an attractive platform for studying both molecular and cellular biophysics. Towards pursuing Seeman's vision of using crystals for protein structure determination, Turberfield's lab showed that a DNA tile lattice could be used to obtain cryoEM projection maps of proteins [105]. Douglas, et al. used 6-helix bundles to align proteins for NMR structure determination [106]. While high resolution maps of DNA origami structures have been determined [107], difficulties in positioning proteins rigidly in specific orientations still hinders the ability obtain high resolution protein maps.

In addition to protein structure determination, scientists have used DNA structures to study protein functions on a single molecule level [108]. Seeman's group used DNA origami structures to nucleate the growth of amyloid fibers [109]. Researchers have also used structures to position different proteins for studying or improving flux through enzymatic pathways and protein cascades [110–113]. Aldaye, et al. used RNA lattices produced *in* vivo to increase hydrogen output in bacteria [114] (Fig. 1-6C). These studies highlight the unique advantage of DNA scaffolds to provide exquisite control of the spatial organization of proteins and protein pathways for obtaining insight to their function on a single molecule level. Recently, researchers have used structures to study the collective behavior of molecular motors [115–118]. Finally, these structures are also being used to study cellular mechanics. By positioning ligands with specific spacing apart, researchers could regulate expression levels through receptor-mediated activation [119] (Fig. 1-6D). These studies show that DNA structures have much potential for as a research tool for elucidating both molecular functions *in* vitro, because creating useful functional devices and technologies requires a stronger understanding of the underlying molecular and cellular mechanisms.

1.5.3 Medical applications

One of the most appealing uses of structural DNA nanotechnology is in medical applications because of the biocompatibility of DNA and its genetic function. A number of the dynamic systems offer potential for medical use due to the ability to perform computation using specific sequences to detect genetic alterations or specific cell surface markers [120–122]. In general, efforts have been focused on developing *in vitro* molecular diagnostics or drug delivery and therapeutics ultimately intended for *in vivo* usage.

Early molecular diagnostics used DNA nanostructures as platforms for detecting the binding of target molecular species. For example, Ke, et al. created DNA origami probes that could create distinguishable patterns on the structure's surface upon detection of different variants of RNA species [30]. While the probe could distinguish single nucleotide variants, the readout relies upon AFM, making it difficult to scale. Other groups have focused on creating fluorescent barcodes to uniquely label molecular species [123, 124]. An interesting development was arrangement of fluorophores on a DNA origami substrate to create hundreds of distinct barcodes [124]; however, use of these structures in a diagnostics setting, labelling in a mixed pool hundreds of species, has yet to be demonstrated. More recently, interest has grown in creating DNA origami nanopores for sequencing purposes [125, 126] (Fig. 1-6E). While translocation events are detectable, much work has yet to be completed to demonstrate single base calls.

A number of therapeutic applications have also been developed. Researchers are using DNA origami structures as adjuvants for immunotherapy [100, 127]. Anderson's group conjugated siRNA to the corners of a DNA tetrahedron and showed delivery to tumor sites [128]. The ability to create shapes and hollow forms also offer potential for controlling drug payloads within the structure [78, 80]. Douglas, et al. implemented AND logic gates to show targeted delivery of a clamshell DNA origami structure containing antibody fragments [78] (Fig. 1-6F). Later, Bachelet's group expanded the computational capacity by using more structures and showed controlled targeting in cockroaches [129]. While promising, these systems still require extensive *in vivo* testing and optimization to demonstrate or improve structure stability [130], circulation times, targeted delivery, and cellular uptake.

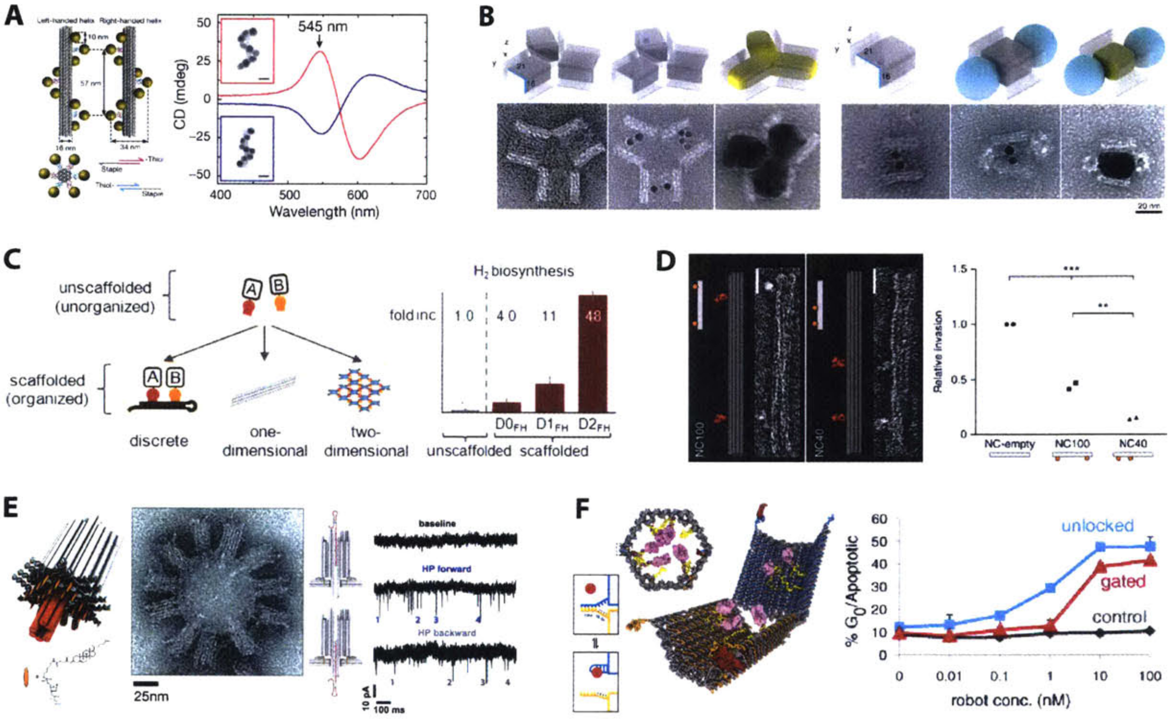

Figure 1-6: Applications of structural DNA nanotechnology. **(A)** Gold nanoparticles arranged in a chiral manner using DNA origami rods. Circular dichroism spectra are shown for left- (red) and right- (blue) handed helical patterns. Scale bars measure 20 nm. **(B)** Schematics (top) and TEM images of cast silver nanoparticles (left) and quantum dot-silver composites (right) from initial gold seeds. **(C)** Increased hydrogen production relative to unscaffolded structures were measured. Ferredoxin/MS2 and hydrogenase/PP7 proteins were scaffolded onto discrete (D0), one-dimensional (D1), and two-dimensional (D2) scaffolds. **(D)** DNA rod scaffolded with ephrin ligands spaced 40 or 100 nm apart were tested for *in* vitro efficacy. Matrix invasion differences of breast cancer cells MDA-MB-231 relative to ephrin-free DNA rods were measured. **(E)** DNA origami nanopore decorated with cholesterol for integration into the lipid bilayer of unilamellar vesicles. TEM images shown in middle. Translocation of a DNA hairpin was studied and showed both forward and backwards motion (right). **(F)** DNA origami clamshell with aptamer lock-and-key mechanism and loaded with anti-CD33 and anti- CDw328/Siglec-7 Fab fragments was tested for concentration effects on cell cycle distribution in NKL cells after 3 days. This figure were adapted with permission from refs. [78, 86, 102, 114, 119, 126].

1.6 Challenges of structural DNA nanotechnology

While DNA nanotechnology enables a number of the promising applications described above, the applications are also limited by the our capability to create diverse patterns of varying sizes, mechanical properties, and increased stability. Currently, our patterning capability is limited to a volume of 25 × 25 × 25 nm^3, dictated by the length of the origami scaffold. By having a truly scalable means of producing structures, we can potentially achieve a higher degree of addressability. This may open up possibilities for manipulating larger or more components for 3D spatial patterning. Additionally, structure stability is still limited in many of the larger complexes. Solutions that are suitable for use in biological or materials development applications have relatively low salinity and are not compatible with conditions necessary for keeping compact DNA nanostructure intact, because the tightly packed DNA helices require high salt concentrations to shield the repulsion from the negatively-charged phosphate backbone. Lastly, rigidity of these structures may be of concern. 2D forms distort and hollow structures collapse easily, resulting in deviations from the intended pattern. A possible solution is to create multi-layered structures to reenforce the fragile parts.

1.7 Scope of thesis

In this thesis, we focus the development of a method for assembling DNA structures and on addressing the challenge of creating large scale 3D DNA nanostructures. This DNA bricks platform is a 3D extension of the single-stranded tiles described above. While applications will be briefly discussed within these chapters, our work is fundamental and builds upon the development and understanding of DNA structural architectures.

In chapter 2, we describe the development of the 3D DNA bricks method. This approach allows us to create discrete 3D structures in a modular manner. We demonstrate both additive and subtractive methods of patterning. We also demonstrate the assembly of 100 unique arbitrary shapes from a library of these bricks. This proof-of-concept work establishes DNA bricks as a promising method for building structures across scales

We extend the DNA bricks method we developed in the previous chapter to create larger periodic structures, as described in chapter 3. These structures reach up to microns in length and can contain complex repeating units with patterns such as tunnels and channels. We also used two of these crystals as templates for patterning gold nanoparticles in tight arrays and sheets. This work explores in more detail the underlying formation mechanism of DNA brick structures.

We explore, in chapter 4, the design landscape of our DNA bricks to create large scale addressable structures. By modifying the original DNA brick, we are capable of creating a discrete structure that is over 100 times as massive as the original M13 DNA origami. Further, we demonstrate the complexity of these systems by creating complex cavity structures, including ones containing a pattern of the Stanford bunny and interconnected loops.

In chapter 5, we describe the overall contributions of our DNA bricks to the fields of DNA nanotechnology and beyond. We also discuss advances since the development of this work, potential future directions, and enabling applications.

CHAPTER 2

Modular 3D DNA nanostructure assembly

In this chapter, we focus on developing two methods of modular 3D DNA nanostructure assembly. First, we present the concept of short, single-stranded DNA "bricks" oligomers that can self-assemble to a predefined shape. Second, we present a subtractive method of creating shapes by reacting fully complementary oligomers with a pre-formed DNA cuboid to "carve" features into the structure. We demonstrate that the DNA brick system is a modular and simple method for creating unique three-dimensional nanoscale features.

Portions of this chapter has been adapted and partially reproduced with permission from **Yonggang Ke, Luvena L. Ong, William M. Shih, and Peng Yin. "Three-dimensional structures self-assembled from DNA bricks."** ***Science,*** **2012, 338: 1177-1183** [131]. and **Bryan Wei, Luvena L. Ong, Jeffrey Chen, Alexander S. Jaffe, and Peng Yin. "Complex Reconfiguration of DNA Nanostructures."** ***Angewandte Chemie,*** **2014, 126: 7605-7609** [132].

2.1 Abstract

We describe a simple and robust method to construct complex three-dimensional (3D) structures by using short synthetic DNA strands that we call "DNA bricks." In one-step annealing reactions, bricks with hundreds of distinct sequences self-assemble into prescribed 3D shapes. Each 32-nucleotide brick is a modular component; it binds to four local neighbors and can be removed or added independently. Each 8-base pair interaction between bricks defines a voxel with dimensions of 2.5 by 2.5 by 2.7 nanometers, and a master brick collection defines a "molecular canvas" with dimensions of 10 by 10 by 10 voxels. By selecting subsets of bricks from this canvas, we constructed a panel of 102 distinct shapes exhibiting sophisticated surface features, as well as intricate interior cavities and tunnels.

2.2 Introduction

Self-assembly of nucleic acids (DNA and RNA) provides a powerful approach for constructing sophisticated synthetic molecular structures and devices [11–13, 17, 18, 20, 24, 33–35, 39, 45, 48–51, 54, 55, 63, 64, 67–69, 72, 73, 77, 114, 133–136]. Structures have been designed by encoding sequence complementarity in DNA strands in a manner such that, by pairing up complementary segments, the strands self-organize into a prescribed target structure under appropriate physical conditions [11]. From this basic principle, researchers have created diverse synthetic nucleic acid structures [134–136] such as lattices [17, 20, 24, 33, 45, 114], ribbons [63], tubes [24, 63, 64, 114], finite two-dimensional (2D) and three-dimensional (3D) objects with defined shapes [17, 18, 35, 39, 45, 48–51, 54, 55, 64], and macroscopic crystals [34]. In addition to static structures, various dynamic systems have been constructed [13], including switches [77], walkers [68, 72, 73], circuits [67–69], and triggered assembly systems [68].

Additionally, these dynamic systems have been combined with DNA structural assembly methods to create reconfigurable and/or reversible structures via toehold mediated strand displacement [75, 81–83]. For example, DNA origami boxes [49] and clamshells [78] can be reconfigured from a closed to an open state, catenane can be derived from DNA origami Möbius strip [82] and fractal patterns in origami structures can be changed [83]. As DNA and RNA can be interfaced with other functional molecules in a technologically relevant fashion, synthetic nucleic acid structures promise diverse applications; researchers are using nucleic acid structures and devices to direct spatial arrangement of functional molecules [24, 86, 114, 124, 137], to facilitate protein structure determination [138], to develop bioimaging probes [124, 137], to study single-molecule biophysics [115], and to modulate biosynthetic and cell-signaling pathways [78, 114].

An effective method for assembling megadalton nanoscale 2D [48] and 3D shapes [49–51, 54, 55] is DNA origami [136], in which a long "scaffold" strand (often a viral genomic DNA) is folded to a predesigned shape via interactions with hundreds of short "staple" strands. However, each distinct shape typically requires a new scaffold routing design, and the synthesis of a different set of staple strands. In contrast, construction from standardized small components (e.g. DNA tiles) that each can be included, excluded, or replaced without altering the rest of the structure – i.e. modular assembly – offers a simpler approach to constructing shapes. In addition, if all components are short strands that can be chemically synthesized, the resulting structures would have greater chemical diversity than DNA origami, which typically contains half biological material (the scaffold) in mass and half synthetic material (the staples). A variety of structures have been assembled using DNA [24, 33, 34, 39, 45, 63, 133, 133] and RNA [17, 18, 114] tiles, including periodic [20, 24, 114] and algorithmic [33] 2D lattices, extended ribbons [63] and tubes [24, 63, 114] 3D crystals [34], polyhedra [18, 39] and finite two-dimensional shapes [17, 45]. However, modular self-assembly of finite-size, discrete DNA structures has generally lacked the complexity that DNA origami can offer.

Only recently have researchers demonstrated finite complex 2D shapes [64] self-assembled from hundreds of distinct single-stranded tiles (SST) [63]. Unlike a traditional multi-stranded tile [17, 20, 24, 33, 34, 39, 45, 114, 133], which is a well-folded, compact structure displaying several sticky ends, an SST is a floppy single-strand DNA composed entirely of concatenated sticky ends. In one-pot reactions, hundreds of SST self-assemble into desired target structures mediated by inter-tile binding interactions; no scaffold strand is required. The simplicity and modularity of this approach allowed the authors to build more than 100 distinct shapes by selecting subsets of tiles from a common 2D molecular "canvas". This latest success has challenged previous thinking that modular components, such as DNA tiles, are not suitable for assembling complex, uniquely addressable shapes [139]. This presumption was largely based on a supposed, technically challenging requirement for perfect strand stoichiometry (i.e. the relative ratio of the strands). Deviations from equality were expected to result in predominating partial structure formation [139]. The surprising success of SST assembly may have bypassed this challenge via putative slow and sparse nucleation followed by fast growth [64], such that a large number of particles complete their formation well before depletion of the component strand pool.

Here we generalize the concept of single-stranded "tiles" to "bricks" and thus extend our modular-assembly method from 2D to 3D. A canonical DNA brick is a 32-nucleotide single-strand with four 8-base binding domains (sticky ends). In simple one-step annealing reactions, prescribed target 3D structures self-assemble robustly from hundreds of unpurified brick strands that are mixed together with no tight control of stoichiometry. The modularity of our method enabled the construction of 102 distinct structures by simply selecting subsets of bricks from a common 3D cuboid "molecular-canvas" consisting of 1000 voxels (see Supplementary Materials found online for ref. [131], fig. S1); each voxel fits 8 base-pairs and measures approximately 2.5 nanometers by 2.5 nanometers by 2.7 nanometers. These structures include solid shapes with sophisticated geometries and surface patterns, and hollow shapes with intricate tunnels and enclosed cavities. We also exploit the modularly inter-connected architecture of the DNA brick structures to develop a subtractive "carving" technique for creating reconfigurable 3D shapes. Additionally, we have constructed structures with alternative packing geometries or using non-canonical brick motifs, demonstrating the method's versatility. The work here thus establishes DNA bricks as a simple, robust, modular, and versatile framework for constructing complex 3D nano-structures using only short synthetic DNA strands. More generally, it demonstrates how complex 3D molecular structures can be assembled from small, modular components mediated strictly by local binding interactions.

2.3 Materials and Methods

Sample preparation

DNA strands were synthesized by Integrated DNA Technology, Inc. (www.idtdna.com) or Bioneer Corporation (us.bioneer.com). To assemble the structures, unpurified DNA strands were mixed to a final concentration of 100 nM or 200 nM per strand (for a structure that contained more than 500 strands, an evaporation step was performed to achieve the desired 200 nM concentration) in 0.5×TE buffer (5 mM Tris, pH 7.9, 1 mM EDTA) supplemented with 10 to 80 mM $MgCl_2$. Sequences of a full set of carving strands which are respectively reverse complementary to the full set of component strands were generated. The DNA sequences for the DNA brick assembly and carving studies can be found in Supplementary Tables S1–S20 in Supplementary Materials II online for ref. [131].

Annealing ramps

The strand mixture was then annealed in a PCR thermo cycler by a fast linear cooling step from 80°C to 60°C over 1 hour, then a 24-hour or 72-hour linear cooling ramp from 60°C to 24°C. The annealing ramps were named according to the length of the second cooling step, as 24-hour annealing or 72-hour annealing.

Agarose gel electrophoresis and sample purification

Annealed samples were then subjected to 2% native agarose gel electrophoresis at 70 volts for 2 hours (gel prepared in 0.5×TBE buffer supplemented with 11 mM $MgCl_2$ and 0.005% (v/v) EtBr) in an ice water bath. The yields of 3D structures were estimated using agarose gel electrophoresis. Fig. 2-6 demonstrates one example of such assays. Annealed samples were subjected to agarose gel electrophoresis to separate the product from free strands and unwanted aggregates. The yield of a product was estimated by comparing the fluorescence intensity of the product band (marked in a red box) to the fluorescence intensity of the 3 kb ladder band (marked in a blue box). Background was subtracted from the fluorescence signal of the band. The intensities were measured using ImageJ software as:

$$\text{Product mass} = \frac{\text{Fluorescence intensity of product band}}{\text{Fluorescence intensity of 3kb ladder}} \times 60 \text{ ng}$$

Percentage yield is then calculated as:

$$\text{Percentage yield} = \frac{\text{Mass of product}}{\text{Mass of all strands}}$$

Then, the target gel bands were excised and placed into a Freeze 'N Squeeze column (Bio-Rad Laboratories, Inc.). The gel pieces were crushed into fine pieces by a microtube pestle in the column, and the column was then centrifuged at 7000 g for 5 minutes. Samples that were extracted through the column were collected for TEM or AFM imaging.

Carving

To assemble the structure of 10H×10H×80B cuboid, component DNA strands were mixed to a roughly equal molar concentration of 200 nM in 0.5×TE buffer (5 mM Tris, pH 7.9, 1 mM EDTA) supplemented with 40 mM $MgCl_2$. The mixture was then annealed in a PCR thermo cycler by cooling from 80°C to 60°C over 2 hours, followed by cooling from 60°C to 25°C over 72 hours. The annealed samples were then subjected to 2% agarose gel electrophoresis (gel prepared in 0.5×TBE buffer supplemented with 10 mM $MgCl_2$ and pre-stained with SYBR safe) in an ice water bath. The target gel band of the cuboid was excised out and put into a Freeze N' Squeeze column (Bio-Rad). The gel pieces were crushed using a microtube pestle in the column and the column was then directly subjected to centrifuge at 700 g for 5 minutes. Purified samples were collected in the eluate, and concentrations were determined by Nanodrop absorption at 260 nm. A set of carving strands which are complementary to the specific set of component strands respectively were added to the annealed sample in equimolar ratio with an incubation at 28°C for 3 hours. The samples after carving were subjected to TEM imaging.

Robot automation for sample preparation

A Python (http://www.python.org/) program was created to aid complex shape design and automate strand mixing by using a liquid handling robot (Bravo, Agilent). For each shape, 4 μL of each strand (10 μM in water) was pipetted and mixed into a final volume of less than 2 mL (the exact volume was determined by the number of constituent strands for the target shape). The mixture was then vacufuge-dried (Savant Speedvac sc110) and resuspended in 200 μL 0.5×TE buffer with 40 mM $MgCl_2$. Each round of robot pipetting accommodated 48 shapes and took three to four days to complete.

TEM imaging.

For imaging, 3.5 μL of agarose-gel-purified or unpurified sample was adsorbed for 4 minutes onto glow-discharged, carbon-coated TEM grids. The grids were then stained for 1 minute using a 2% aqueous uranyl formate solution containing 25 mM NaOH. Imaging was performed using a JEOL JEM-1400 operated at 80 kV.

AFM imaging

AFM images were obtained using an SPM Multimode with Digital Instruments Nanoscope V controller (Veeco). Five μL of purified sample was applied onto the surface of a freshly cleaved mica chip and left for approximately 2 minutes to allow for adsorption. Forty μL of 0.5×TE (10 mM $MgCl_2$) was then added onto the mica surface. The AFM tips used were the short and thin cantilevers in the SNL-10 silicon nitride cantilever chip (Veeco Probes).

2.4 Results

2.4.1 Design of DNA-brick structures and a 3D "molecular canvas"

In our design, a DNA brick is a 32-nucleotide strand that we conceptualize as four consecutive 8-nucleotide domains (Fig. 2-1A). Each DNA brick bears a distinct nucleotide sequence. All DNA bricks adopt an identical shape when incorporated into the target structure: two 16-nucleotide antiparallel helices joined by a single phosphate linkage. The two domains adjacent to the linkage are designated as "head" domains and the other two are designated as "tail" domains. A DNA brick with a tail domain bearing sequence "a" can interact productively with a neighboring brick with a complementary "a*" head domain in a stereospecific fashion. Each pairing between bricks defines three parallel helices packed to produce a 90° dihedral angle (Fig. 2-1B, top); this angle derives from the approximate 3/4 right-handed helical twist of 8 base-pairs of DNA.

We introduce a Lego-like model to depict the design in a simple manner (Fig. 2-1B, bottom). The model intentionally overlooks the detailed helical structure and strand polarity but preserves the aspect ratios and some of the orientational constraints on interactions between DNA bricks: the two protruding round plugs, pointing in the same direction as the helical axes, represent the two tail domains; the two connected cubes with recessed round holes represent the two head domains. A brick must adopt one of two classes of orientation, horizontal or vertical (Fig. 2-1B). The two bricks connect to form a 90° angle via hybridization, represented as the insertion of a plug into a hole. An insertion is only allowed between a plug and a hole that carry complementary sequences with matching polarity (which is not graphically depicted in the current model for expositional simplicity). In fig. S2, we present a more detailed Lego-like model that explicitly tracks the polarity of the DNA bricks and their stereospecific interaction pattern.

Structural periodicities of the design are illustrated in a 6H(helix)×6H(helix)×48B(bp) cuboid structure (Figs.2-1C, D). Bricks can be grouped into 8-base-pair layers that contain their head domains. Bricks follow a 90° counterclockwise rotation along successive 8-base-pair layers resulting in a repeating unit with consistent brick orientation and arrangement every four layers. For example, the first and fifth 8-base-pair layers in Fig. 2-1D share the same arrangement of bricks. Within an 8-base-pair layer, all bricks share the same orientation and form a staggered arrangement to tile the layer. On the boundary of each layer, some DNA bricks are bisected to half-bricks, representing a single helix with two domains. The cuboid is self-assembled from DNA bricks in a one-step reaction. Each brick carries a unique sequence that directs it to fit only to its predesigned position. Because of its modular architecture, a predesigned DNA brick structure can be used for construction of smaller custom shapes assembled from subsets of DNA bricks (Fig. 2-1E). See figs. S3 and S4 for detailed strand diagrams for the DNA brick structures.

3D "molecular canvas"

The Lego-like model can be further abstracted to a 3D model that contains only positional information of each 8-base-pair duplex. A 10H×10H×80B cuboid is conceptualized as a 3D "molecular canvas" that contains 10×10×10 voxels. Each voxel fits an 8-base-pair duplex and measures 2.5 nm×2.5 nm×2.7 nm (Fig. 2-1F). Based on the 3D canvas, a computer program first generates a full set of DNA bricks, including full-bricks and half-bricks that can be used to build a prescribed custom shape. Using 3D modeling software, a designer then needs only to define the target shapes by removing unwanted voxels from the 3D canvas – a process resembling 3D sculpting. Subsequently, the computer program analyzes the shape and automatically selects the correct subset of bricks for self-assembly of the shape.

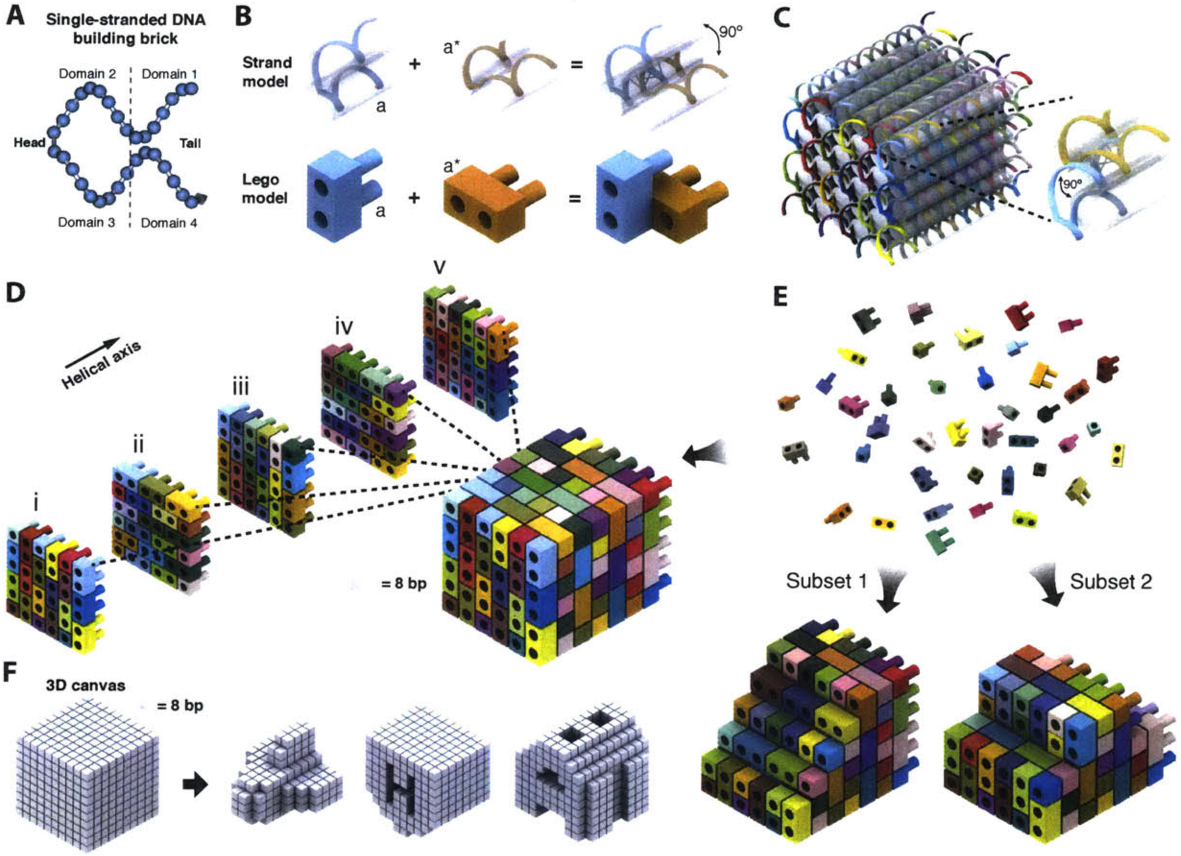
A
Single-stranded DNA building brick
Domain 2
Domain 1
Head
Tail
Domain 3
Domain 4
B
Strand model
Lego model
a
a*
90°
C
90°
D
Helical axis
i
ii
iii
iv
v
= 8 bp
E
Subset 1
Subset 2
F
3D canvas
= 8 bp

Figure 2-1: Design of DNA brick structures. (**A**) A 32nt four-domain single-stranded DNA brick. Each domain is 8nt in length. The connected domains 2 and 3 are "head" domains; domains 1 and 4 are "tail" domains. (**B**) Each two-brick assembly forms a 90° dihedral angle via hybridization of two complementary 8nt-domains "a" and "a*". (**C**) A molecular model that shows the helical structure of a 6H×6H×48B cuboid 3D DNA structure. Each strand has a unique sequence. The inset shows a pair of bricks. (**D**) A Lego-like model of the 6H×6H×48B cuboid. Each brick has a unique sequence, as indicated by a distinct color. Half-bricks are present on the boundary of each layer. (**E**) The 6H×6H×48B cuboid is self-assembled from DNA bricks. The bricks are not interchangeable during self-assembly because of the distinct sequence of each brick. Using the 6H×6H×48B as a 3D "molecular canvas", a smaller shape can be designed using a subset of the bricks. (**F**) Intricate 3D shapes designed from a 10×10×10 voxel "3D canvas", where each voxel is 8bp (2.5 nm×2.5 nm×2.7 nm).

2.4.2 Optimization and characterization of DNA-brick cuboid structures

Using the above design strategy, we constructed a wide range of DNA brick structures. We first constructed 3D cuboid structures of a variety of sizes and aspect ratios (Fig. 2-10).

Random sequence design

The sequences of DNA bricks were designed by random assignments of base pairs (A-T, C-G) to 3D structures. We first tested two versions of a 6H×6H×64B cuboid, with either random sequences or specially designed sequences (designed by smoothing binding energy, minimizing undesired secondary structure, and reducing sequence symmetry), and observed comparable self-assembly yields (fig. S5). We also tested three sets of random sequences using a 4H×12H×120B cuboid and again observed similar assembly yields (Fig. 2-2. More analysis and discussion on domain similarity of random sequence design can be found in fig. S7 and S8). Thus, random sequences were applied to all subsequent designs.

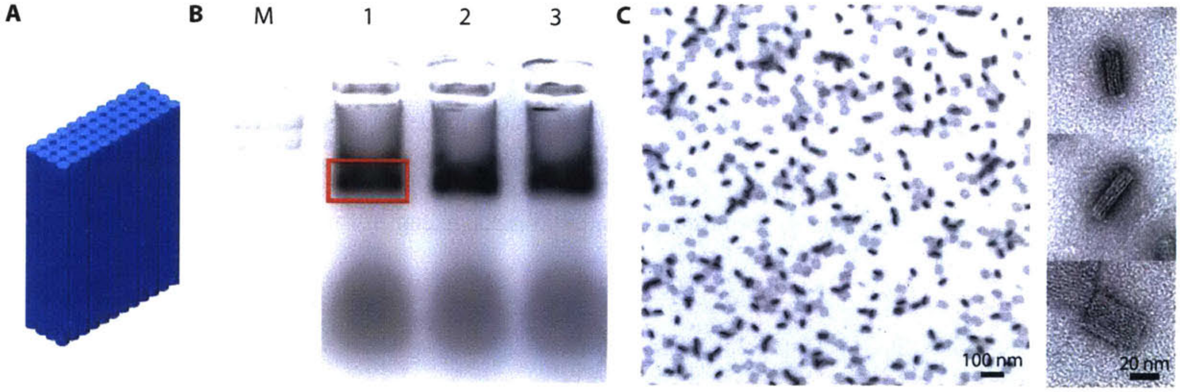

Figure 2-2: Comparison of the self-assembly of 3D structures using three sets of random sequences. (**A**) A 4H×12H×120B cuboid was used for this experiment. (**B**) Agarose gel assaying self-assembly of the 4H×12H×120B cuboid. Lane M shows 1kb ladder. Lanes 1 to 3 show the 4H×12H×120B cuboid designed with three different sets of random sequences. All samples were self-assembled using a 72-hour annealing protocol with 40 mM $MgCl_2$. (**C**) TEM images of the 4H×12H×120B cuboid extracted from the band marked in (**B**).

Protector bricks

Including unpaired single-strands at the ends of DNA duplexes has proven to be effective for mitigating unwanted aggregation that results from blunt-end stacking [48]. An 8-nucleotide single-stranded domain protruded out from every 5' or 3' end of all DNA duplexes in our 3D structure designs (Fig. 2-1C). The sequences of these 8-nucleotide domains were replaced with eight continuous thymidines to further prevent undesired non-specific binding interactions between exposed single-stranded domains. DNA bricks with modified head or tail poly-T domains are named "head protectors" or "tail protectors," respectively.

Boundary bricks

A 16-nucleotide half-brick could be merged with a preceding 32-nucleotide full-brick along the direction of its helix, to form a 48-nucleotide strand (Figs. 2-3,2-4 and S9–11). We observed a 1.4-fold improvement in assembly yield at 40 mM $MgCl_2$ for a 6H×6H×64B cuboid when this 48-nucleotide boundary-strand design was implemented, possibly reflecting accelerated nucleation of target structure formation. Hence, this merge strategy was applied to all our 3D structures.

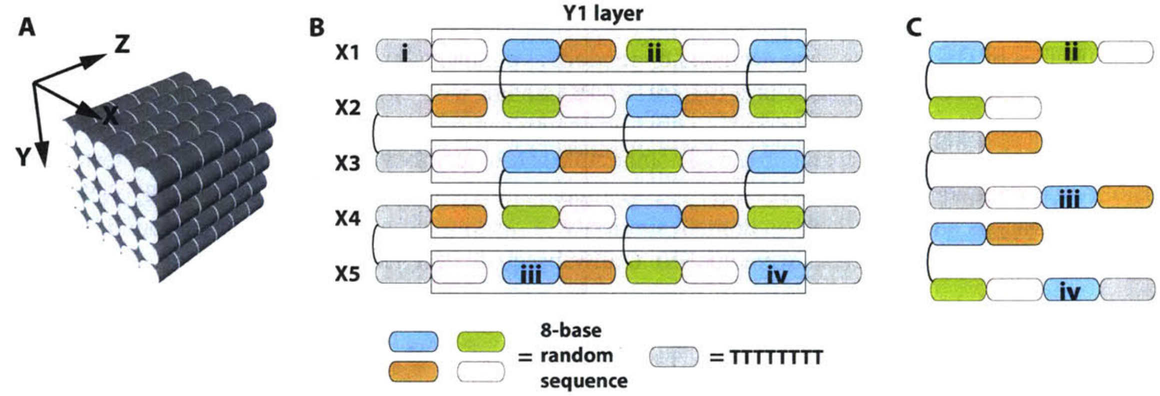

Figure 2-3: Design of 48nt boundary bricks. (**A**) A cylinder model of a 5H×5H×48B cuboid. (**B**) The Y1-layer contains five helices – X1, X2, X3, X4, X5. Only X-bricks in the Y1-layer are shown. i, ii, iii, iv are 16nt boundary bricks. (**C**) Most of these short 16nt boundary bricks can be connected with the 32nt bricks on their left (Z- direction) to form 48nt boundary bricks, except for the ones at the very left end of the structure.

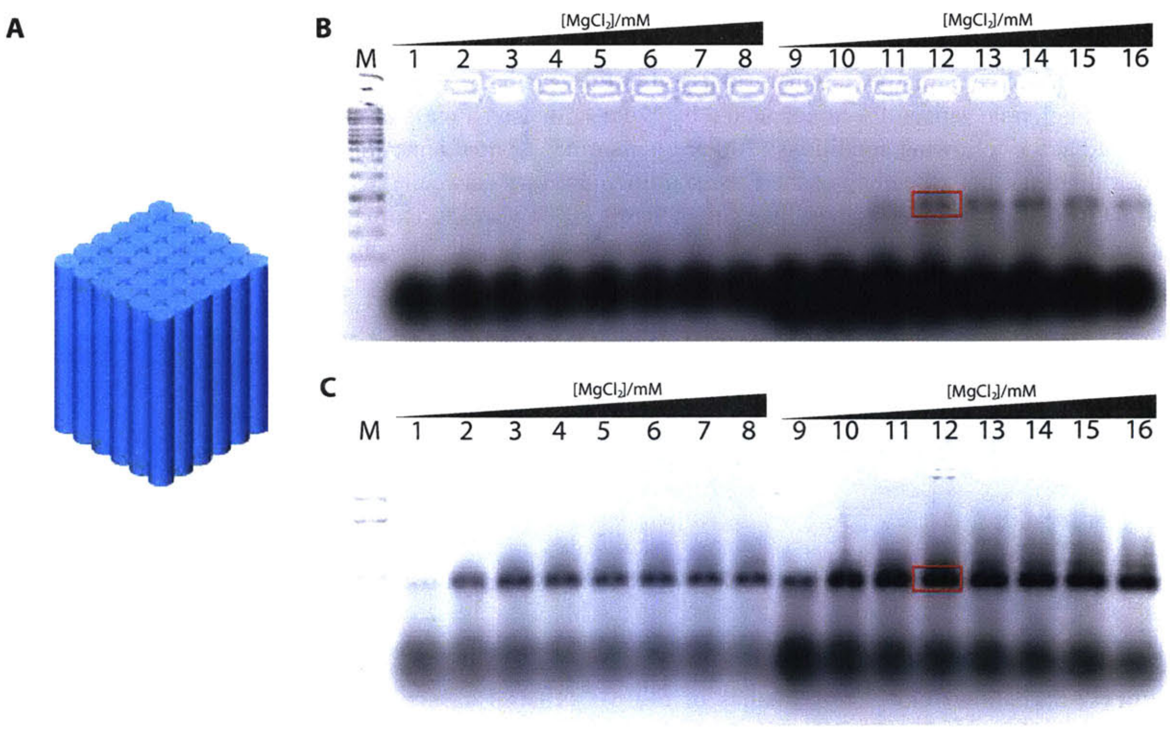
A
B
[MgCl$_2$]/mM
[MgCl$_2$]/mM
M 1 2 3 4 5 6 7 8 9 10 11 12 13 14 15 16
C
[MgCl$_2$]/mM
[MgCl$_2$]/mM
M 1 2 3 4 5 6 7 8 9 10 11 12 13 14 15 16

Figure 2-4: A 6H×6H×64B cuboid with 48nt or 16nt boundary bricks. (**A**) A 6H×6H×64B cuboid is used to test the 16nt short boundary strands and 48nt long boundary strands. The design using 16nt boundary strands is named as a 6H×6H×64B-S cuboid. The design using 48nt boundary strands is named as a 6H×6H×64B cuboid. All samples were annealed using a 72-hour annealing protocol. (**B**) Agarose gel assaying the self-assembly of a 6H×6H×64B-S cuboid. Lane M shows 1kb ladder. Lanes 1 to 8 show a 6H×6H×64B-S cuboid assembled at 100 nM concentration with 10, 20, 30, 40, 50, 60, 70, 80 mM $MgCl_2$. Lanes 9 to 16 show a 6H×6H×64B-S cuboid assembled at 200 nM concentration with 10, 20, 30, 40, 50, 60, 70, 80 mM $MgCl_2$. 20 μL sample was loaded into each lane from 1 to 16. (**C**) Agarose gel assaying self-assembly of a 6H×6H×64B cuboid. Lane M shows 1kb ladder. Lanes 1 to 8 show a 6H×6H×64B cuboid assembled at 100 nM concentration with 10, 20, 30, 40, 50, 60, 70, 80 mM $MgCl_2$. Lanes 9 to 16 show 6H×6H ×64B cuboid assembled at 200 nM concentration with 10, 20, 30, 40, 50, 60, 70, 80 mM $MgCl_2$. 20 μL sample was loaded into each lane from 1 to 16. Fluorescence intensities of the two bands in red boxes are used to compare yields of two designs.

Assembly and characterization of the 6H×10H×128B cuboid

For a detailed characterization study, we constructed a 6H×10H×128B cuboid (Fig. 2-10A). It consists of 459 strands (7,680 base-pairs, with a comparable molecular weight to an M13-based DNA origami, see figures 2-5, S13 for design details). Unpurified DNA strands were mixed together at nominally equal ratios without careful adjustment of stoichiometry. To determine the optimal assembly conditions, we tested two annealing ramps (24-hour annealing and 72-hour annealing), two strand concentrations (100 and 200 nM per strand), and eight MgCl2 concentrations (10, 20, 30, 40, 50, 60, 70, 80 mM). Equal amounts of each sample (2 pmol per strand) were then subjected to EtBr-stained 2% agarose gel electrophoresis (Fig. 2-6). The best gel yield (about 4% as calculated by Yield = Measured mass of product/Mass of all strands) was achieved at the following conditions: 200 nM per strand, 72-hour annealing, 40 mM MgCl2 (Fig. 2-6). It is worth noting that efficiency of the EtBr staining may vary between the double-stranded 3kb ladder and our 3D structures. Therefore, the above gel yield reflects only an approximate estimate for the incorporation ratio of the monomer strands (also see discussion in [64]). Nonetheless, this assay is useful for comparing self-assembly results between structures and for screening optimal annealing conditions of 3D structures.

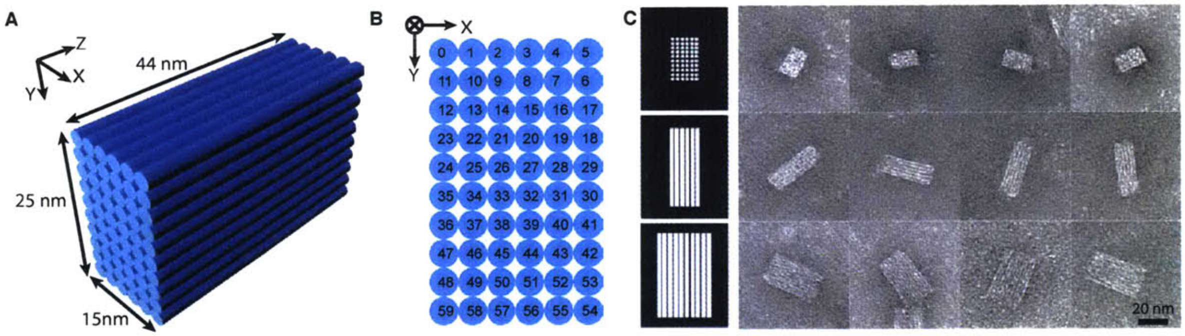

Figure 2-5: Design and TEM images of the 6H×10H×128B cuboid. (**A**) A cylinder model of a 6H×10H×128B cuboid. (**B**) The X–Y cross-section, looking down the Z+ direction of a 6H×10H×128B cuboid. The helices are numbered from 0 to 59 for strand editing in caDNAno. (**C**) Computer-generated projection views (left) and TEM images (right) of a 6H×10H×128B cuboid.

For comparison, 4% to 14% gel yield was reported for 3D DNA origami with similar size and aspect ratios (e.g. the 10H×6H×98B and other origami cuboids in [140]). It is worth noting that the origami gel yield was estimated as Yield = (Scaffold strands incorporated into product/Total scaffold strands); the loss of excessive staple strands (normally 5- to 10-fold more than the scaffold strand) was not taken into account. For DNA bricks, the optimal 40 mM MgCl2 was higher than the optimal MgCl2 concentration for 3D origami folding, which typically is below 30 mM [51]. Column-purified DNA bricks product (50% recovery efficiency, Fig. 2-10B) migrated as a single band on agarose gel and appeared under transmission electron microscopy (TEM) with expected morphology (Fig. 2-10C) and measured dimensions of 0.34 nm (± 0.01 nm SD) per base pair and 2.5 nm (± 0.2 nm SD) per helix width.

The percentage of intact structures observed by TEM were estimated for gel-purified structures. The particles in TEM images were categorized as "good", "minor defect", or "major defect": good – no obvious damage; minor defect – one small damage, often on the edges; major defect – more than one small defect or completely broken structures. The percentage of intact particles was determined as a ratio of the good particles over total counted particles and was estimated at 55%. Most minor defects occurred at the locations close to the helix ends of structures, possibly indicating that strands at these locations were prone to

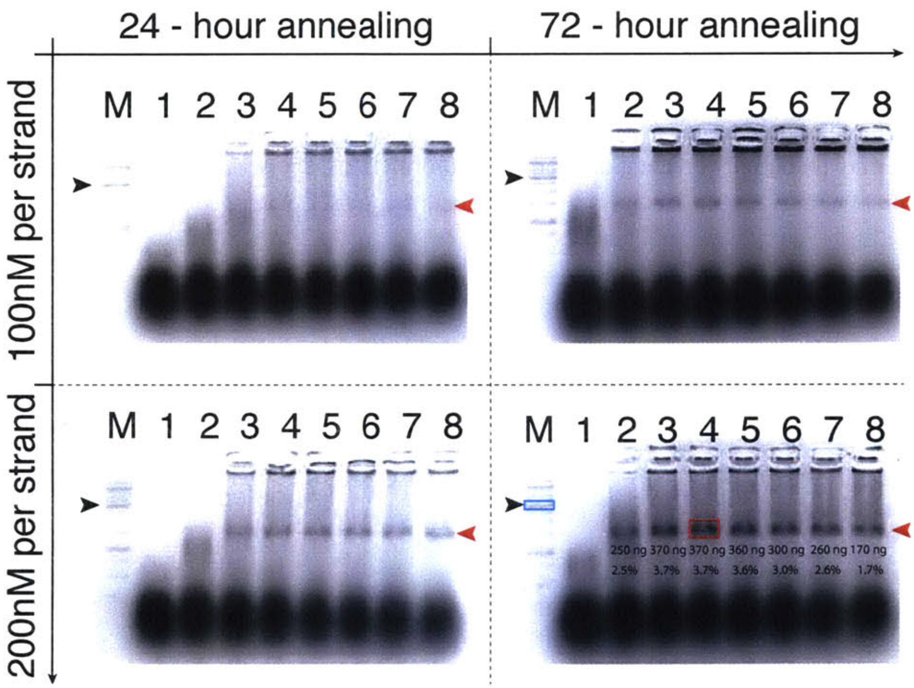

Figure 2-6: Optimization of assembly conditions of the 6H×10H×128B cuboid. Assembly conditions for the 6H×10H×128B cuboid. Agarose gel electrophoresis shows that the maximum assembly yield was achieved when strands (200 nM each) were annealed for 72 hours with 40 mM $MgCl_2$. For each agarose gel, lane M contains the 1 kb ladder, lanes 1 to 8 contain 6H×10H×128B cuboids annealed with ascending $MgCl_2$ concentrations from 10 to 80 mM (10 mM interval). The band in the blue box indicates the 3000bp ladder band corresponding to 60 ng DNA. This band was used as a standard to measure the yield of products. The product band formed with 40 mM $MgCl_2$ is marked in a red box. Both the absolute mass value and the percentage yield are shown below each product band.

dissociation (Fig. 2-7). This percentage is related to the stability of purified structures and is comparable to the previously reported percentages of 3D square-lattice DNA origami (27% for a 6H×12H× 80B cuboid, 59% for an 8H×8H×96B cuboid) [52].

TEM analysis of the purified 6H×10H×128B cuboid

Special designs can be applied to increase the assembly yield of the 6H×12H× 80B cuboid. "Head protectors" and "tail protectors" appeared especially unstable because half of their 8-nucleotide domains are unpaired. By merging "head protectors" of the 6H×10H×128B cuboid with their neighboring strands (figs. S17, S18), a modified version 6H×10H×128B-M cuboid was obtained and showed 190% improvement in gel assembly yield and 17% improvement in the percentage of intact structures under TEM over the standard 6H×10H×128B cuboid (fig. S19). Thus, 3D structures can be further stabilized using special design rules such as this merging strategy. However, this modification requires deletions of crossovers between helices, which may potentially create global or local deformations, and was not used for constructions in the remainder of the paper.

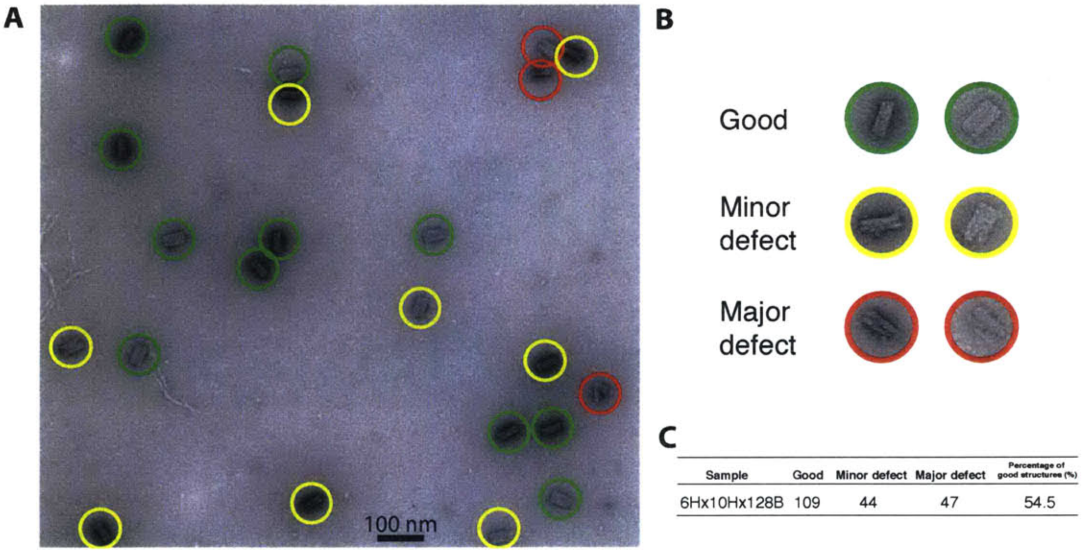

Sample	Good	Minor defect	Major defect	Percentage of good structures (%)
6Hx10Hx128B	109	44	47	54.5

Figure 2-7: TEM analysis of the purified 6H×10H×128B cuboid. (**A**) A representative TEM image of the purified 6H×10H×128B cuboid. Particles circled in green were categorized as "good" particles with no visible defect. Particles circled in yellow that showed minor defects were categorized as "minor defect" particles. Particles circled in red that showed major defects or were even broken were categorized as "major defect" particles. (**B**) Examples of "good", "minor defect", and "major defect" particles of the purified 6H×10H×128B cuboid. (**C**) Statistics of "good", "minor defect", and "major defect" structures.

Assembling a 4H×4H×128B cuboid at different concentrations

In figure 2-6, we tested two concentrations (100 nM and 200 nM) for the assembly of the 6H×10H×128B cuboid and observed higher yield at 200 nM. In this section, we studied whether the yield of DNA-brick structures can be further improved with even higher concentration (e.g. 1 μM) of strands. However, as such high concentration for large structures (e.g the 6H×10H×128 cuboid) is practically challenging (cloudy precipitates at high concentrations were observed during annealing), a small object (4H×4H×128B cuboid) was used for the test. As shown figure 2-8 (also in Fig. 2-6), in the 0.1 – 0.8 μM range, higher concentration resulted in higher yield, consistent with our model in discussion and hypothesis above. The yield dropped slightly at 1 μM concentration, presumably due to precipitation (a cloudy sample was observed at this concentration).

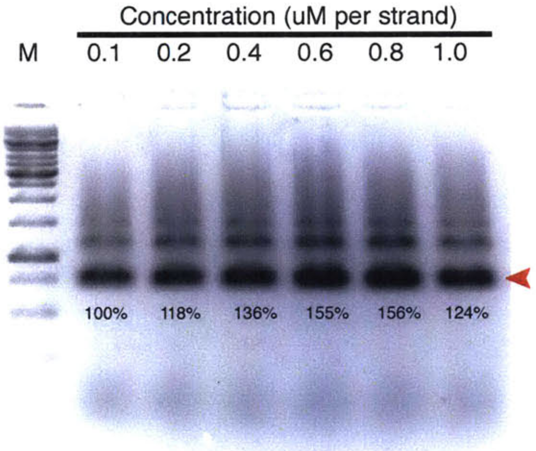

Figure 2-8: Assembling a 4H×4H×128B cuboid at different concentrations. Agarose gel electrophoresis of 4H×4H×128B annealed at 0.1, 0.2, 0.4, 0.6, 0.8, and 1.0 μM (per strand) concentrations. Structures were self-assembled in 0.5× TE buffer with 40 mM $MgCl_2$ using a 24-hour annealing ramp. 1 pmol (per strand) of sample was loaded into each lane. Lane M shows 1kb ladder. The 0.1 μM sample was used as a standard to measure the yield of annealing products (red arrow).

Agarose gel electrophoresis and TEM images of 6H×10H×64B cuboid dimers

Besides the major monomer product bands on agarose gels, weaker slow-migrating bands were also observed for some structures. We speculated that these bands corresponded to dimers, trimers, and other multimers that were caused by non-specific interactions. We annealed the 6H×10H×64B cuboid, purified and imaged the band directly above the monomer band (Fig. 2-9). We observed mostly dimers in the images. In addition, we also saw a small amount of monomers that likely resulted from detached dimers.

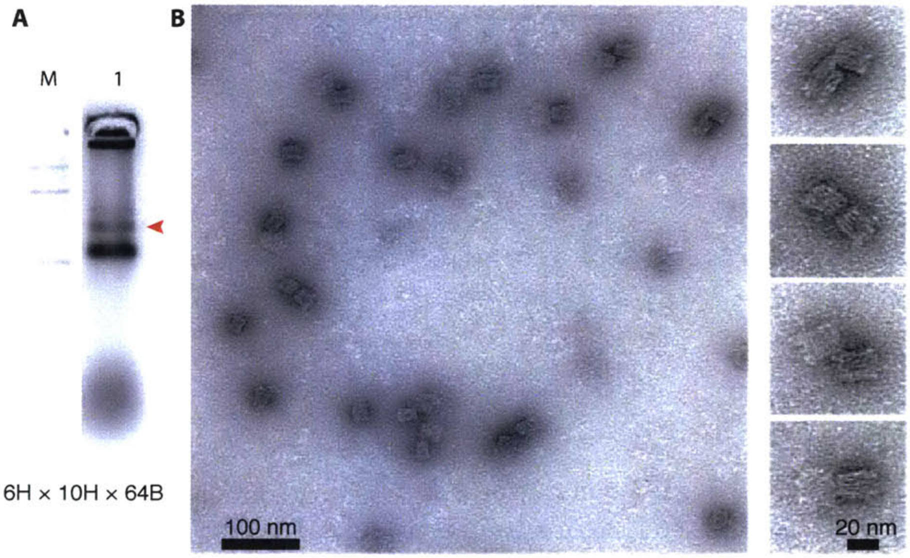

Figure 2-9: Agarose gel electrophoresis and TEM images of 6H×10H×64B dimers. (**A**) Agarose gel electrophoresis of a 6H×10H×64B cuboid. The structure was assembled in 0.5×TE buffer with 40 mM $MgCl_2$ using a 72-hour annealing ramp. The concentration of each strand was 200 nM. 10 μL of sample was loaded into each lane. Lane M shows 1kb ladder. The dimer band is denoted with the red arrow. (**B**) TEM images of purified 6H×10H×64B dimers.

2.4.3 Structures of different sizes

Eighteen distinct cuboid structures that contain 9, 16, 36, 60, 96, and 144 helices were designed, annealed using the optimal conditions previously identified for the 6H×10H×128B cuboid self-assembly, and characterized by gel and TEM (Fig. 2-10D, 2-17). Additional TEM images are shown in figs. S21–S27. Measured dimensions of intact particles for each structure agree with the designs (Fig. 2-1). Gel yields varied from less than 1% to about 80% (Figs. 2-17C, 2-1). For structures with the same number of helices, smaller cuboids exhibited higher assembly yields. The highest yield (80%) was observed for the smallest object, the 3H×3H×64B cuboid; the lowest yields (< 1%) were observed for the 8H×12H×120B, 4H×24H×120B, and 12H×12H×48B cuboids. The biggest DNA objects constructed in this paper are an 8H×12H×120B cuboid (formed by 728 strands) and a 4H×24H×120B cuboid (formed by 710 strands), which are identical in molecular weight (24,576-nucleotide, 8-megadalton, 60% more massive than an M13-based DNA origami). Increasing the concentration for the brick strands helped to increase the yield for a small cuboid, 4H×4H×128B (Fig. 2-8). In some cases, higher molecular weight bands can be detected above the product band; these bands are likely multimers caused by non-specific interactions between assembled products. For example, for the 6H×10H×64B structure, TEM revealed an upper band contained dimers of the cuboids (Fig. 2-9). Cuboids with 32-base-pair (32B) helices were also tested but failed to assemble (fig. 2-17). This is likely due to the fact that these cuboids contained only one crossover between each pair of neighboring helices, and hence were less stable.

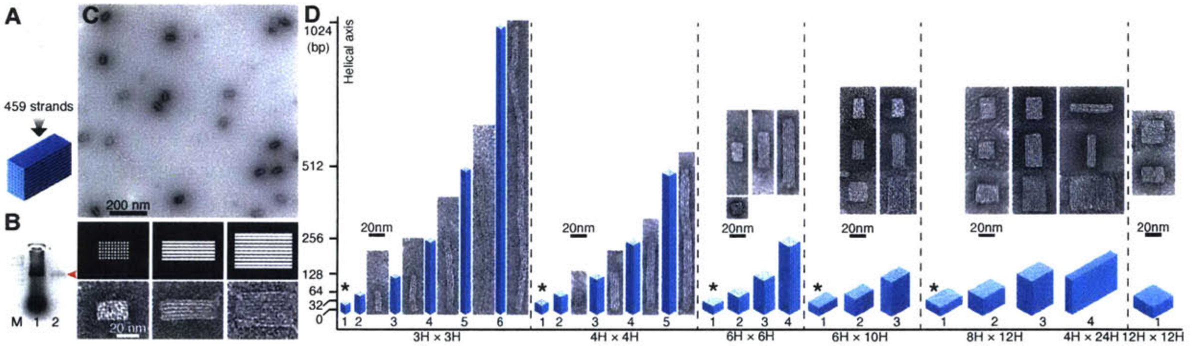

Figure 2-10: Cuboid DNA-brick structures. (**A**) 3D structures were self-assembled from DNA bricks via a one-step thermal annealing process. (**B**) Agarose gel electrophoresis showing 50% purification efficiency of 6H×10H×128B cuboid. Lane M contains the 1 kb ladder. Lanes 1 and 2 contain unpurified and purified 6H×10H×128B cuboid, respectively. The red arrow points to the 6H×10H×128B cuboid product band. (**C**) TEM images of purified 6H×10H×128B cuboid. Zoomed-in images show three different projection views. Corresponding computer-generated projection views are shown on the right. (**D**) Designs and TEM images of cuboids of a variety of dimensions. 3D cylinder models are drawn proportionally to their relative dimensions. The cross-sections of each group are shown above their 3D cylinder models. "⋆"s indicate designs measuring 32 bp in height that failed self-assembly. Gel analysis and cuboid measurements can be found in figures 2-17 and 2-1 in the supplementary section below.

2.4.4 Complex shapes made from a $10\times10\times10$ voxel 3D canvas

Using the $10\times10\times10$ voxel 3D canvas (Fig. 2-1F, Fig. 2-12A, fig. S31), we next constructed 102 distinct shapes (Fig. 2-12), demonstrating the modularity of the DNA brick strategy.

DNA bricks and derivatives

Any brick in the 3D canvas can become either a boundary half brick (i.e. exposed at the edges of a layer and bisected, Fig. 2-1D), a protector brick (i.e. located in the first or last layer along Z-axis), or even both at same time, in a custom shape design. Thus, modified versions of each brick were generated with all combinations of domain-deletion (i.e. bisect to a half-brick), polythymidine-sequence-substitution (i.e. change to protector bricks), and boundary-brick-merger (i.e. change to 48-nucleotide boundary bricks) to accommodate the possibilities (Fig. 2-11, note that two types of strands with low occurring frequency and four types of strands with only one binding domain were excluded in our implementation). Figure 2-11 describes the four-domain bricks and their derivatives used for making the 3D canvas. Self-assembly of discrete DNA structures is often compromised by unwanted aggregation that occurs when a structure contains (1) unpaired single-stranded domains, or (2) unprotected blunt ends of DNA duplexes. Different types of strands shown in **C** to **E** are designed to avoid these two situations by changing the DNA sequence of any unpaired single-stranded domain to eight consecutive Ts. This strategy leads to fourteen total types of strand derivatives, to cover all possibilities when one, two, or three voxels are removed for a custom shape design. If all fifteen types of bricks (**B** to **E**) are included, any custom shape can be designed with 8bp (1 voxel) resolution.

Of the fourteen derivatives, only eight of them are actually implemented in our designs and experiments. The other six types of derivatives (labeled with "*" in **D** and **E**) are excluded. The two removed derivatives (where the two separate voxels are located diagonally) in **D** are expected to occur rarely for designed shapes. The four removed derivatives in **E** consist of only one 8nt random-sequence domain, and their incorporation in the DNA structures is expected to be relatively unstable. We have redesigned two shapes (shapes 45, 55) by incorporating more than one hundred "one voxel" derivatives for each shape. Neither modified shape self-assembled successfully (no product bands detected on agarose gels; data not shown). Based on the above experiments, we choose not to include such one-domain binders in our canvas design. It is worth noting that as these 6 derivatives only occur at the end of a helix that is on the boundary of a shape, their exclusion is not expected to significantly affect the design space for the shapes.

We also included two types of 48nt "boundary bricks" (following the strategy in Fig. 2-3) to improve the self-assembly yield of the shapes. All together, for each strand, a total of $(9+2) = 11$ original and derivatives were created for our design.

Each strand is named by the positions of the voxels it occupies (Fig. 2-11G). The voxel information of strands is used to select strands that form the shape using the program in Fig. 2-18. Overall, a master collection of 4,455 strands (with a total of 138,240 nucleotides) were generated by a computer program to guarantee that a designed shape could be assembled with head/tail protector bricks and 48-nucleotide boundary bricks. Custom shapes were assembled via selecting subsets of the master collection without synthesizing new strands.

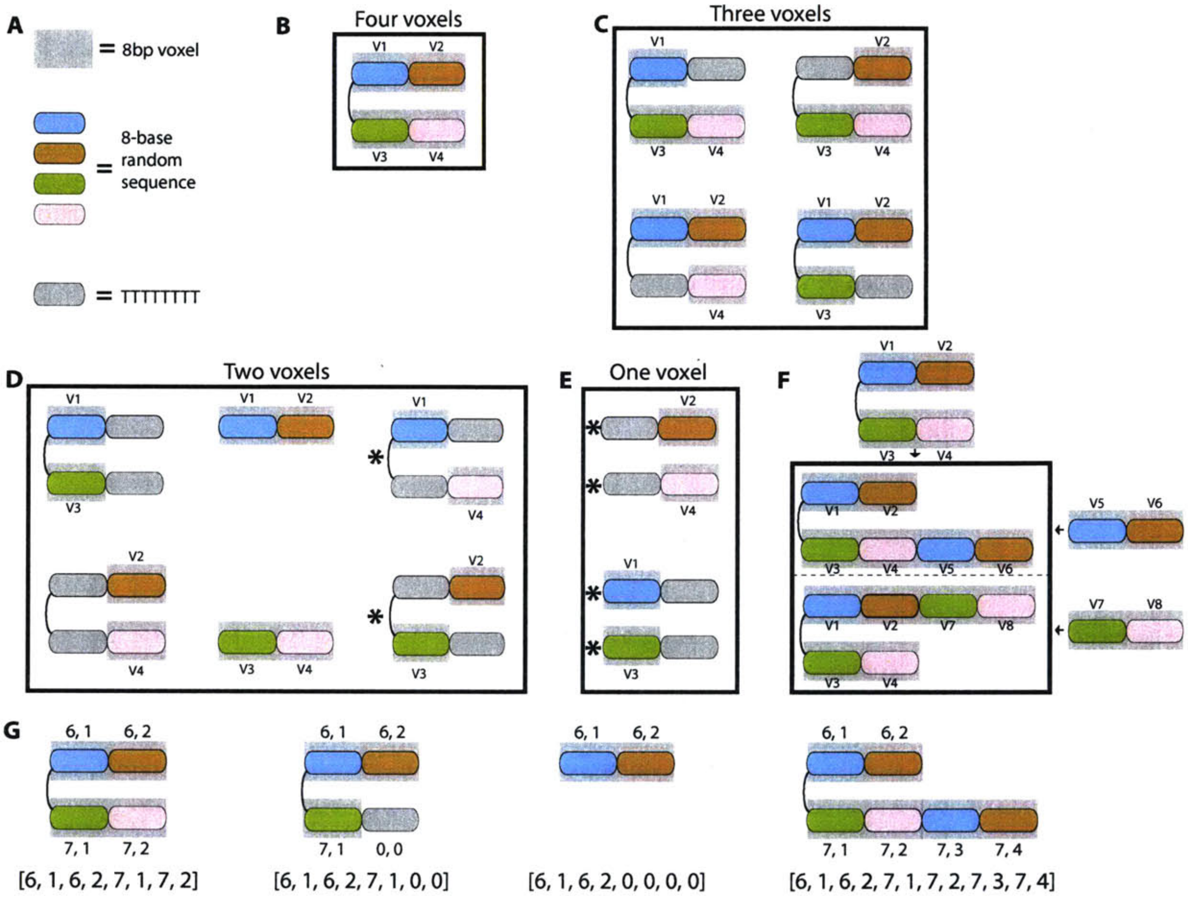
A
= 8bp voxel
8-base random sequence
= TTTTTTTT
B
Four voxels
V1
V2
V3
V4
C
Three voxels
D
Two voxels
*
E
One voxel
F
V5
V6
V7
V8
G
6, 1
6, 2
7, 1
7, 2
0, 0
7, 3
7, 4
[6, 1, 6, 2, 7, 1, 7, 2]
[6, 1, 6, 2, 7, 1, 0, 0]
[6, 1, 6, 2, 0, 0, 0, 0]
[6, 1, 6, 2, 7, 1, 7, 2, 7, 3, 7, 4]

Figure 2-11: DNA bricks and derivatives for making the 3D canvas. (**A**) Symbols used in this figure. (**B**) A typical 32nt brick with four 8nt random-sequence domains. Each 8nt domain is located within an 8bp voxel – V1, V2, V3, or V4. V1 and V2 are on the same helix. V3 and V4 are on another adjacent helix. (**C**) to (**F**) Other types of bricks derived from the strand with four 8nt random-sequence domains. (**C**) When one of the four 8bp voxel is removed, the 8nt domain corresponding to that 8bp voxel is changed to eight consecutive Ts. (**D**) When two of the four 8bp voxels are removed, the two 8nt domains corresponding to those 8bp voxels are either changed to eight consecutive Ts or deleted. The latter case happens if the two removed 8bp voxels are from the same helix. The symbol "*" indicates a derivative that was omitted in our experimental implementation. (**E**) When three of the four 8bp voxels are removed, the two 8nt domains that reside within the two removed voxels on the same helix are deleted. The other 8nt domain that resides within the third removed voxel is changed to eight consecutive Ts. (**F**) For each strand shown in **B**, two types of 48nt boundary strands are created. (**G**) Each strand is labeled by the positions of the voxels that it occupies. Each pair of numbers represent one voxel. The first number indicates the helix number as in caDNAno designs, and the second number indicates the voxel position in the helix. The numbers (0, 0) indicate either a domain with eight consecutive Ts or an empty domain.

Automated design process

By rendering the 3D canvas using 3D modeling software, we can edit voxels and visualize a shape using a graphical user interface (Fig. 2-12B). Then, the voxel information of multiple shapes is interpreted by a custom program to generate a list of strands involved in the formation of each shape. This list is subsequently processed to direct an automated liquid-handling robot to select DNA strands from source plates and pipette them to the wells of a product plate, mixing strands for many shapes in a high throughput manner (Fig. 2-12C). The strands will be subsequently annealed in separate test tubes to produce the desired structures (Fig. 2-12D). The complete design workflow is shown in figures 2-18, 2-19. To utilize existing computational tools previously developed by other researchers, we can also convert shapes to caDNAno files [140]. Each shape's conformation then can be simulated using CanDo [141], a software tool for computing 3D structures of DNA origami (fig. S35).

Using the 3D canvas and following the automated design process, we successfully constructed 102 distinct shapes (gels in figures 2-20, 2-21; TEM images of shapes 1-100 in Fig. 2-12E; raw TEM images for all the shapes in fig. S38-S54).

Shapes 1–17

The basic design constraints were studied using a group of shapes containing two 4H×10H×80B blocks connected by a middle "connecting block" (shapes 2–17). The connecting blocks were two-voxel wide along X-axis and systematically designed to possess decreasing numbers of voxels along Y-axis (shapes 2–9) or Z-axis (shapes 10–17). Eliminating voxels along the X-axis should have the same effect as eliminating voxels along the Y-axis because of the shape symmetry. Agarose gel electrophoresis revealed that, in both systems, as the connector became overly thin, the gel yields for the intact structures decreased and partial structures (putative unconnected 4H×10H×80B blocks) became more prominent (e.g. in lanes for shapes 8, 9, 15-17 in figure 2-20). However, reducing the number of voxels along the Z-axis appeared to decrease the yield more significantly than along the Y-axis. Shape 9, which contained only a 2-voxel connection along the Y-axis, gave 6% gel yield. In contrast, the yield for shape 17 (2-voxel along the Z-axis) dropped to 1%. Overall, these observations suggest safe design criteria of at least two continuous voxels along the X-axis or Y-axis (2 helices) and three Z-axis voxels (24 base-pairs) for stable features. However, as demonstrated in following experiments, smaller features (e.g. two Z-axis voxels, shapes 33–37; one X-axis or Y-axis voxel, shapes 64–74) can still stably exist in certain shapes where these features are presumably reinforced by other voxels in close proximity.

Solid shapes 18–31

A number of solid shapes were designed including Z-direction extrusions of simple geometric shapes (shapes 18-23) and more intricate objects (shapes 24-31; also see shape 102 in fig. S54). Gel yields and TEM images of these objects provided more knowledge of the design space of our methodology. For example, shapes 26 and 27, which both contained 3-helix thick appendages anchored only on one edge, were occasionally found without these protrusions or with them but containing defects (data not shown). Thus, such thin features, though obeying our design criteria, appeared to be less stable than the better-supported or thicker features.

Closed-cavity shapes 32–42

Previously, a few examples of 3D DNA origami with closed cavities were demonstrated, including a box [49], a tetrahedron [50], a sphere and an ellipsoid [55]. Here we created a series of "empty boxes" with different sizes of cuboid cavities (shapes 32–37) as well as more intricate cavity shapes (e.g. square ring, cross, and triangle; shapes 38–42).

Open-cavity shapes 43–62

We constructed shapes with a single open-cavity (i.e. tunnel) of varying width, depth, and geometry (shapes 43–53) and multiple-parallel cavities (shapes 54–56). Shapes with non-crossing perpendicular tunnels (shape 57), turning and branching tunnels (shape 58), and crossing tunnels (shapes 59, 60; also see shape 101 in fig. S54) were also demonstrated. Furthermore, we constructed tunnel-containing cuboids with modified outer surfaces to create varying external views from different angles, as demonstrated by shapes 60–62.

Features-on-solid-base shapes 63–100

Sophisticated features were designed on a solid base, including a full set of 10 Arabic numerals (shapes 65–74) and 26 lowercase letters for the English alphabet (shapes 75–100). Two concentric ring structures (shapes 63, 64) and the numerals (shapes 65–74) contained features as thin as one voxel (2.5 nm), suggesting that the design criteria (e.g. thin structures tend to fail) are contingent on the surrounding environment of a particular feature. These shapes also highlight the capacity of creating extruded features that would otherwise be unattainable via 2D assembly [64].

For most shapes, assembly yields were between a few percent and 30% (Figs. 2-20, 2-21 ; by comparison, yields of five 3D DNA origami structures were reported as 7% to 44% [51]). Only five shapes had assembly yields higher than 30%; three shapes had assembly yields lower than 1%.

In spite of our success in making a variety of intricate 3D shapes, some shapes exhibited undesired properties. For example, shapes 60–62 only showed less than 1% of intact particles in TEM images; some fine features of a shape (e.g. the two wings of shape 27) could be damaged or even completely missing if the shape was extracted from an agarose gel band. We also observed four failed designs that did not produce clear product bands on agarose gels (fig. S55A). Two features-on-solid-base designs showed strong bands on agarose gels (fig. S55B), and were of the expected size in TEM images. However, their features were not clearly resolved under TEM, suggesting that the shapes may have formed but the features were too subtle to be visualized.

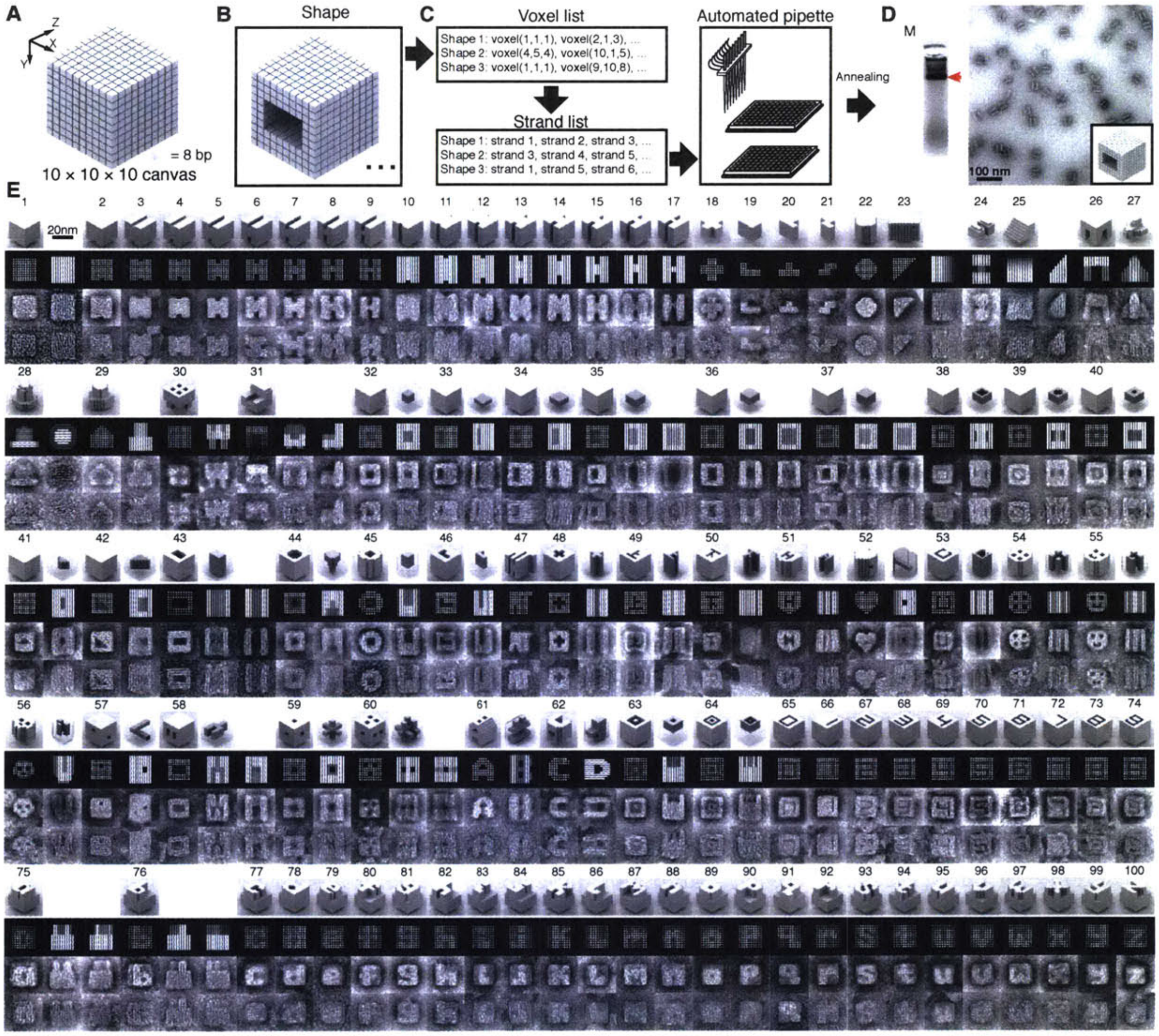
A
Z
X
Y
= 8 bp
10 × 10 × 10 canvas
B
Shape
C
Voxel list
Shape 1: voxel(1,1,1), voxel(2,1,3), ...
Shape 2: voxel(4,5,4), voxel(10,1,5), ...
Shape 3: voxel(1,1,1), voxel(9,10,8), ...
Strand list
Shape 1: strand 1, strand 2, strand 3, ...
Shape 2: strand 3, strand 4, strand 5, ...
Shape 3: strand 1, strand 5, strand 6, ...
Automated pipette
Annealing
D
M
100 nm
E
20nm
1 2 3 4 5 6 7 8 9 10 11 12 13 14 15 16 17 18 19 20 21 22 23 24 25 26 27
28 29 30 31 32 33 34 35 36 37 38 39 40
41 42 43 44 45 46 47 48 49 50 51 52 53 54 55
56 57 58 59 60 61 62 63 64 65 66 67 68 69 70 71 72 73 74
75 76 77 78 79 80 81 82 83 84 85 86 87 88 89 90 91 92 93 94 95 96 97 98 99 100

Figure 2-12: Shapes made from a 3D "molecular canvas". (**A**) A 10×10×10 voxel 3D canvas. (**B**) Shapes are designed by editing voxels using 3D modeling software. (**C**) A computer program recognizes the voxel composition of each shape and generates a list of strands that are needed to form that shape. The list then is used to direct an automated liquid handling robot to mix strands. (**D**) After annealing, the shapes are characterized by agarose gel electrophoresis and TEM imaging. Lane M contains the 1 kb ladder. The product band is indicated by the red arrow. Gel electrophoresis analysis of all structures can be found in figures 2-20 and 2-21 in the supplementary section. (**E**) Models and TEM images of shapes. The top row for each shape depicts a 3D model, followed by a computer-generated projection view, an image averaged from 6 different particles visualized using TEM, and a representative raw TEM image. In a number of cases, multiple projections are presented. Some shapes with cavities or tunnels are depicted with additional transparent 3D views that highlight the deleted voxels. For example, the top-right model of shape 32 shows the enclosed cuboid cavity.

2.4.5 Shapes made by carving the 10×10×10 voxel 3D canvas

We have also developed a carving method for shape reconfiguration and formation. For simplicity, we depict the carving of a 2D SST structure in figure 2-13, and 3D carving occurs analogously. A complete DNA canvas is first formed. Removal (i.e. "carving") of a component strand (red) is achieved by introducing a "carving strand" (salmon) that is fully complementary to the component strand (Fig. 2-13a, b). Note that unlike previous strand-displacement work, our scheme does not use an external toehold [77] (The detailed molecular mechanism will be discussed later). Displacement of multiple component strands with corresponding carving strands can be used to reconfigure the canvas to a prescribed shape (Fig. 2-13c, d). Moreover, because each component strand can be modularly removed, it is possible to create a combinatorially large number of distinct shapes. Experimental demonstrations with 2D structures have demonstrated that the removal of one component strand reveals a newly exposed toehold on a neighboring strand, allowing us to remove connected regions of component strands without the need to modify them with predesigned external toeholds [132]. It is worth noting the method applies only to SST/brick-based structures but not origami based structures because the method relies on the modular architecture.

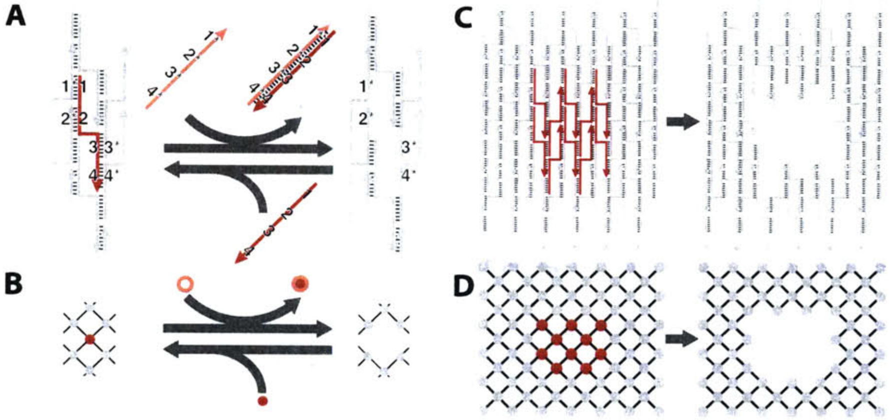

Figure 2-13: Schematics of structural reconfiguration from a 2D SST canvas. (**A**) A strand diagram of strand displacement based SST structural reconfiguration and (**B**) the associated interaction graph. The strand/node to be displaced is highlighted in red with four domains 1, 2, 3 and 4 complementary to domains 1*, 2*, 3* and 4* of the neighboring strands, respectively. When introduced to the system, a full complementary strand 4*-3*-2*-1*, in salmon, forms a duplex with the red target component strand to displace the target off the canvas. (**C**) A strand diagram of strand displacement for an 8 helix (H)×10 turns (T) canvas and (**D**) the associated interaction graph. Strands or nodes highlighted in red, as shown on the left, depict the subset of component strands to be displaced. The carved structure is shown on the right.

We applied this carving method to 3D DNA brick cuboids. Using a 10 helix×10 helix×80 base-pair structure (Fig. 2-14A, top) that we reported previously [131], we tested multiple carving patterns. We used a reaction temperature of 28°C, since 3D structures contain 8-nt binding domains and typically assembly isothermally around 35°C. The successful results of carving a corner off (Fig. 2-14B, top) or a tunnel through (Fig. 2-14C, top) a cuboid, and carving the cuboid into two halves (Fig. 2-14D, top) are shown in agarose gel electrophoresis (Fig. 2-22) and Transmission Electron Microscopy (TEM) (Fig. 2-14, bottom). Because of the limited thermal stability and the limited accessibility of majority of the component strands, the structural reconfigurations of 3D DNA structures are much more difficult to realize in comparison to the 2D counterpart and obtaining fine features is even more challenging. Since finding a temperature high enough for fast strand displacement but low enough (<30°C) to maintain structural stability is challenging, we were only able to realize a few cases of successful carving with coarse resolution.

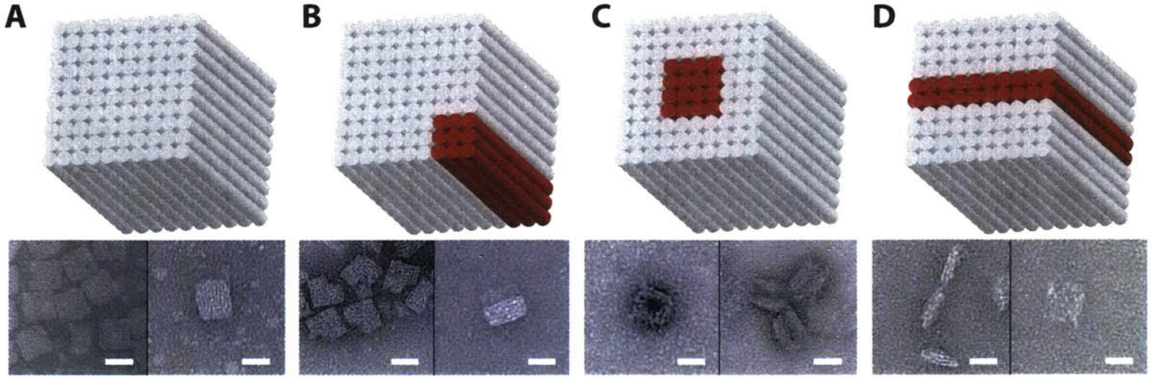

Figure 2-14: Structural reconfiguration from a 3D cuboid. Top panel, cylinder model of the cuboid (red cylinders denote the ones to be displaced); bottom panel, TEM images (scale bar: 20 nm) (**a**) Cuboid before structural reconfiguration. (**b**) Carving a corner from the cuboid. (**c**) Carving a tunnel through the cuboid. (**d**) Carving the cuboid into two halves. Gel electrophoresis analysis of these structures can be found in figure 2-22 in the supplementary section.

2.4.6 Generality of DNA brick self-assembly

To explore the generality of the DNA brick assembly framework, we constructed structures with brick motifs other than the 32-base canonical brick motif. These structures include those with alternative lattice geometries that have been previously demonstrated by DNA origami [48, 51, 53].

Single-layer (2D) structures

Conceptually, a single-layer structure can be constructed by "extraction" of a layer from a 3D brick structure (Fig. 2-15A, also see fig. S56 for comparison with a 2D single-stranded tile rectangle design (26)). A 30H×1H×126B rectangle was intentionally modified to be 10.5 base pairs per turn instead of 10.67 base pairs per turn (for 3D design), in order to get a relatively flat structure (fig. S57). Gel yield was estimated to be 18% (Fig. 2-23A), comparable to 2D single-stranded tile structures [64]. TEM (Fig. 2-15B) and AFM (Fig. 2-15C) revealed expected rectangle structures. Based on AFM images, the dimensions were measured as 0.31 nm (± 0.01 nm SD) per base-pair and 2.6 nm (± 0.3 nm SD) per helix width.

3D honeycomb-lattice structures

We then created 10.8-base-pair/turn (33.3° twist per base-pair) honeycomb-lattice (HC) and hexagonal-lattice (HL) DNA structures. Four types of four-domain DNA strands were designed for honeycomb-lattice structures (Figs. 4D, E). A 6H×6H×84B-HC structure was successfully constructed and characterized (Fig. 2-15F, fig. S59). Particles in TEM images were measured to be 13 nm (± 0.9 nm SD)×22 nm (± 1.0 nm SD)×29 nm (± 1.2 nm SD). Assembly yield was estimated to be 30% (Fig. 2-23B).

3D hexagonal-lattice DNA structures

Two types of strands are used to build a hexagonal-lattice structure: a linear strand with multiple 9-nucleotide domains and an 18-nucleotide strand with two 9-nucleotide domains that are connected by a crossover (Figs. 4G, H). A 6H×7H×108B-HL structure was constructed and characterized (Fig. 2-15I, fig. S61). Particles in TEM images were measured to be 13 nm (± 0.8 nm SD)×18 nm (± 1.1 nm SD)×35 nm (± 2.2 nm SD). Assembly yield was estimated to be 26% (Fig. 2-23C).

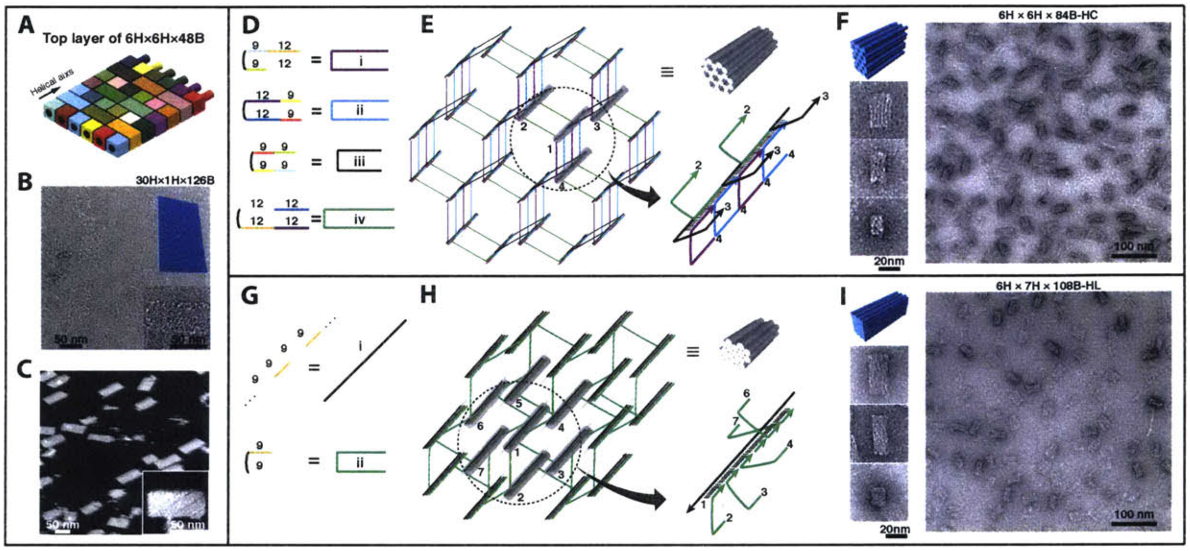

Figure 2-15: Generality of DNA brick self-assembly. (**A–C**) depict the design of single-layer DNA structures. (**A**) DNA bricks of the top layer of the 6H×6H×64B cuboid that is described in Fig. 2-1D, with the crossovers to the layer below removed. (**B**) TEM images of a 30H×1H×126B rectangle. Top-right inset shows the model of the design. Bottom-right inset contains a zoomed-in image of the structure. (**C**) AFM images of the 30H×1H×126B rectangle. Inset contains a zoomed-in image of the structure. (**D–F**) depict the design of 3D honeycomb-lattice DNA structures. (**D**) The four types of strands used for honeycomb-lattice DNA self-assembly. Numbers in the left panel indicate the number of bases in a domain. (**E**) Strand diagram of an 84bp 3D honeycomb-lattice structure. The right-bottom image depicts an enlarged image of the circled helix bundle. Strand colors match those described in the right side of **D**. Numbers indicate DNA helices. (**F**) TEM images of a 6H×6H×84B-HC 3D hexagonal-lattice DNA structure. Zoomed-in images of different projection views are shown on the left. (**G–I**) depict the design of 3D hexagonal-lattice DNA structures. (**G**) The two types of strands used for hexagonal-lattice DNA self-assembly. Numbers in the left panel indicate the number of bases in a domain. (**H**) Strand diagram of a 54bp 3D hexagonal-lattice structure. The right-bottom image depicts an enlarged image of the circled helix bundle. Strand colors match those described on the right side of **G**. Numbers indicate DNA helices. (**I**) TEM images of a 6H×7H×108B-HL 3D hexagonal-lattice DNA structure. Zoomed-in images of different projection views are shown on the left. Gel electrophoresis analysis of the three structures can be found in figure 2-23 in the supplementary section.

Other brick motifs

We also constructed a 6H×10H×64B cuboid that arranges brick strands in an alternating fashion between layers (Figs. 2-16, S64), and two 6H×6H×64B cuboids that implement two other brick motif designs (figs. S65, S66). In contrast to the "unidirectional" design in which all the bricks point towards the same direction (Fig. 2-16A, identical to fig. S3C), bricks can also be designed to point to opposite directions in a 3D structure. Fig. 2-16B depicts an alternating-brick design in which bricks in odd numbered layers (numbered from top most row and the leftmost column) point in the Z- direction, and bricks in even numbered layers point in the Z+ direction. We successfully constructed a 6H×6H×64B-A cuboid using the alternating-brick design (agarose gel electrophoresis, Fig. 2-16D; TEM imaging, Fig. 2-16E). For the other two brick motifs, one design is based on "chopping" the scaffold of a DNA origami to short strands (fig. S65A). The other adopts standardized motifs that are each 32-nucleotide long and has two crossovers (fig. S65B). These designs further demonstrate the versatility of DNA brick self-assembly.

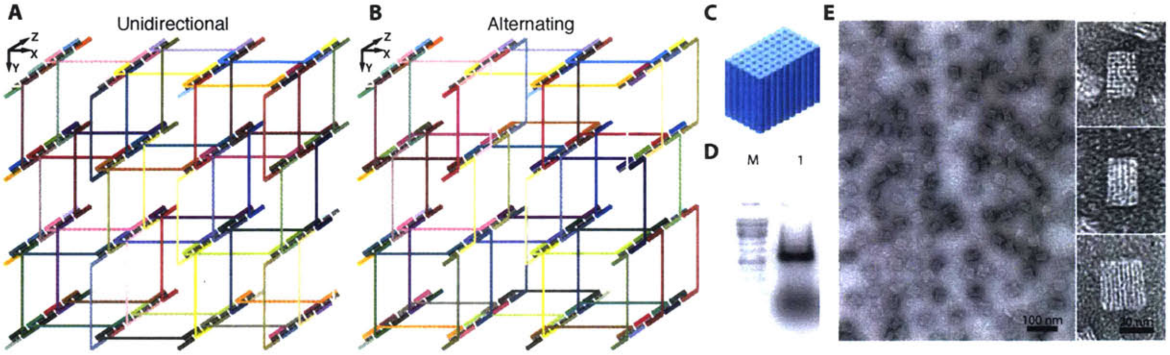

Figure 2-16: Design with alternating bricks. (**A**) Strand diagram of a 4H×4H×64B cuboid unidirectional-brick design. (**B**) Strand diagram of a 4H×4H×64B-A cuboid alternating-brick design. (**C**) A 6H×10H×64B-A cuboid was used to test the alternating-brick design strategy. (**D**) Results of agarose gel electrophoresis. Lane M shows 1kb ladder. Lane 1 shows the 6H×10H×64B-A cuboid. The structures were self-assembled in 0.5×TE buffer with 40 mM $MgCl_2$, using 72-hour annealing ramp. Concentration of each strand is 200 nM. A bright band corresponding to the product was extracted from the gel. (**E**) TEM images of 6H×10H×64B-A cuboid after agarose gel purification.

2.5 Discussion

DNA bricks provide a simple, modular, and robust framework for assembling complex structures from short strands. Simplicity. A canonical brick is a standardized 32-nucleotide single strand composed of four 8-nucleotide binding domains; bricks interact via simple local binding rules. Modularity. With no scaffold present, an assembly of bricks has a modular architecture; each brick can be added or removed independently. Robustness. The assembly process is robust to variations in sequence composition (random sequences are used), strand synthesis (unpurified strands suffice) and stoichiometry (no tight control is required). Together, the simple and standardized motif, modular architecture, and robust performance permit straightforward automation of the design and construction process. A software tool takes as input a 3D shape specification and directs a liquid-handling robot to select and mix pre-synthesized brick strands to form the shape. Using a 1000-voxel canvas, 102 diverse shapes were rapidly prototyped. These shapes demonstrate a new level of geometrical sophistication, as exemplified by the intricate tunnel and cavity features.

Additionally, the modularity of the approach enabled us to develop a second method of forming structure. This subtractive carving technique may initially appear to be thermodynamically unfavorable, since a component strand in the canvas structure that is fully paired with its neighbors has the same designed number of hybridized bases as when it is bound to its fully complementary carving strand (after carving). However, carving a component strand off may help to alleviate the electrostatic repulsion that results from the closely packed neighboring DNA duplexes in the canvas structure [48, 64] and release the mechanical stress that might be accrued at the crossover points [142], thereby favoring the reaction. Further, carving can potentially enable us to create features that would otherwise be difficult to form in an additive manner. For example, small fragile features that are difficult to form in an assembly reaction may be more effectively formed through carving a stable cuboid. Additionally, the dynamic nature of this system by which structures can be reconfigured to new forms through the introduction of triggering species suggest that carving may provide an intriguing platform to explore the rich interplay between structure, dynamics, and computation.

The DNA brick framework is not restricted to the canonical 32-nucleotide motif and can be generalized to include various other motifs (Fig. 2-15), enabling the construction of 3D structure with diverse lattice packing geometries. In addition, previously demonstrated single-stranded tiles [63, 64] can be viewed as a special case of bricks where each pair of neighboring bricks form a 180° angle. For comparison, in hexagonal-, square-, and honeycomb-lattice structures, neighboring bricks form 60°, 90°, and 120° angles, respectively. These different angles are achieved by changing the domain lengths of bricks. Furthermore, neighboring bricks may be merged into a longer strand, which may facilitate nucleation or strengthen structurally weak positions. The DNA brick (and single-stranded tile) method differs from previous multi-stranded tiles in that each brick monomer is a floppy single-strand and only folds into a brick-like shape when incorporated into the assembly. It also differs from DNA origami by not using a scaffold strand. However, DNA origami can also be related to the brick framework, where half of the bricks are concatenated into a long scaffold (fig. S65A). The successes of constructions that use only short strands (as in bricks) and those that includes a long scaffold (as in origami) together suggest a full spectrum of motif possibilities with strands of diverse lengths: longer strands may provide better structural support, and shorter ones finer modularity and features; the eclectic use of both may lead to the most rapid progression towards greater complexity.

The DNA brick structures constructed here are still far below the size limit allowed by sequence uniqueness. Making the conservative assumption (by neglecting the contribution of cooperativity) that every domain must display a different sequence, a structure using canonical 32-nucleotide, 4-domain bricks could potentially reach a size of 8-nucleotide×48 (524,288 nucleotides). In our experiments, the assembly process appeared to tolerate (sparse) identical domains (fig. S8), further expanding the potential obtainable size.

Further exponential increase in size could potentially be achieved by using bricks with longer domains, or by encoding algorithmic growth patterns [33] in the assembly. However, in practice, low yields were already observed for larger designs (up to 24,576 nucleotides attempted thus far). Solving this challenge may require improvements in structure and sequence design, enzymatic synthesis for higher-quality strands, optimized thermal or isothermal [143] annealing conditions, and a detailed understanding and perhaps explicit engineering of the kinetic assembly pathways [33, 68, 143] of DNA brick structures.

The DNA brick structure, with its modular architecture, sophisticated geometry control, and synthetic nature, will further expand the range of applications and challenges that nucleic acid nanotechnology has already started to address, e.g. to arrange technologically relevant guest molecules into functional devices [24, 86, 114, 124, 137], to serve as programmable molecular probes and instruments for biological studies [115, 124, 137], to render spatial control for biosynthesis of useful products [114], to function as smart drug delivery particles [78], and to enable high-throughput nanofabrication of complex inorganic materials for electronics or photonics applications [24, 86]. The modularity of the brick structure may facilitate rapid prototyping of diverse functional nano-devices. Its sophisticated and refined geometrical control may enable applications that require high precision arrangements of guest molecules. As the brick structure is composed entirely of short synthetic strands (i.e. no biologically-derived scaffold), it is conceivable to make bricks using synthetic informational polymers other than the natural form of DNA. Such polymers may include L-DNA, DNA with chemically modified backbones or artificial bases, chemically synthesized or in vitro (or even in vivo) transcribed RNA. This material diversity may potentially produce nanostructures with not only prescribed shapes but also designer (bio-)chemical properties (e.g. nuclease resistance, reduced immunogenicity) that would be useful for diverse applications requiring the structure to function robustly in complex environments, e.g. in living cells or organisms.

2.6 Acknowledgments

DNA bricks

The authors would like to thank Mingjie Dai for technical assistance; Erik Winfree and Bryan Wei for discussions; Danielle Pastuszak for assistance in draft preparation. This work is supported by Wyss Institute and ONR Grant N000014091118 to William M. Shih, ONR Young Investigator Program Award N000141110914, ONR Grant N000141010827, NSF CAREER Award CCF1054898, NIH Director's New Innovator Award 1DP2OD007292, and Wyss Institute Faculty Startup Fund to Peng Yin, Yonggang Ke, William Shih, and Peng Yin conceived the project; Yonggang Ke designed the experiments and wrote the computer programs; Yonggang Ke and Luvena Ong performed the experiments and analyzed data; all authors wrote the manuscript together.

Carving

We thank David Zhang and Yonggang Ke for discussion; Michelle K. Vhudzijena for technical assistance. This work is supported by an Office of Naval Research (ONR) Young Investigator Program Award (N000141110914), ONR grants (N000141010827 and N000141310593), a National Science Foundation (NSF) Faculty Early Career Development Award (CCF1054898), an NSF Expedition in Computing Award (CCF1317291), NSF grants (CCF1162459, CMMI1333215), a National Institutes of Health (NIH) Director's New Innovator Award (1DP2OD007292) and a Wyss Institute for Biologically Engineering Faculty Startup Fund to Peng Yin. Luvena Ong acknowledges support from NSF through a Graduate Research Fellowship.

2.7 Author Contributions

This work could not have been possible without Yonggang Ke and Bryan Wei. Yonggang developed the concept of DNA bricks and took the lead in characterizing the method. He wholly contributed to figures 2-2, 2-3, 2-4, and 2-8. For the carving work, Bryan Wei designed the complementary carving strands used in figure 2-14 and 2-22.

2.8 Supplementary Data

Select supplementary data are included below. Strand diagrams, gel electrophoresis analysis, and cited supplementary figures can be found online at `http://science.sciencemag.org/content/338/6111/1177` and `http://onlinelibrary.wiley.com/doi/10.1002/ange.201402437/abstract` respectively for the modular assembly and carving of 3D DNA brick structures.

2.8.1 Analysis of different sized DNA brick cuboids

TEM and agarose gel electrophoresis of 3H×3H, 4H×4H, 6H×6H, 6H×10H, 8H×12H, 4H×24H, and 12H×12H cuboids

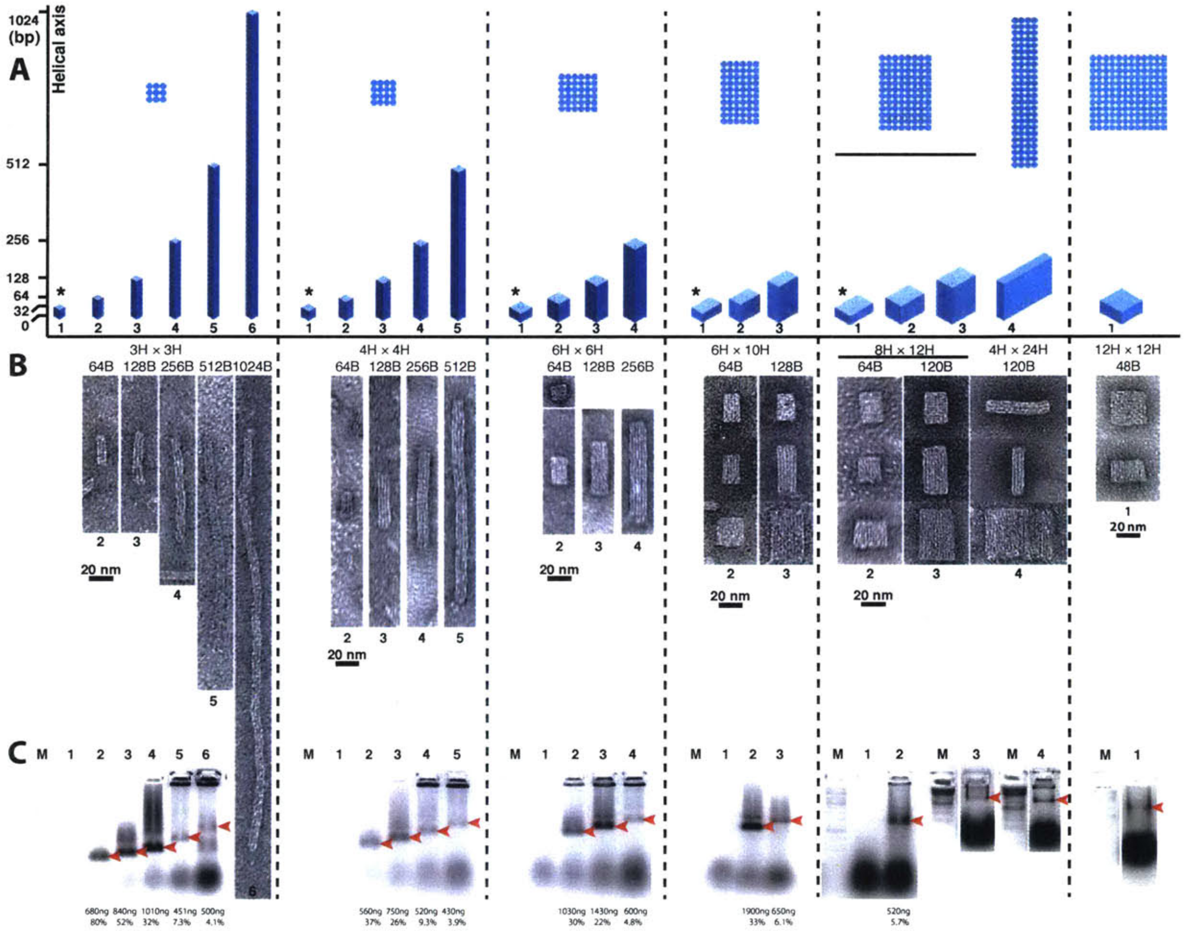

A
B
C
1024 (bp)
Helical axis
512
256
128
64
32
0
*
3H x 3H
64B 128B 256B 512B 1024B
4H x 4H
64B 128B 256B 512B
6H x 6H
64B 128B 256B
6H x 10H
64B 128B
8H x 12H
64B 120B
4H x 24H
120B
12H x 12H
48B
20 nm
M 1 2 3 4 5 6
M 1 2 3 4 5
M 1 2 3 4
M 1 2 3
M 1 2 M 3 M 4
M 1
680ng 840ng 1010ng 451ng 500ng
80% 52% 32% 7.3% 4.1%
560ng 750ng 520ng 430ng
37% 26% 9.3% 3.9%
1030ng 1430ng 600ng
30% 22% 4.8%
1900ng 650ng
33% 6.1%
520ng
5.7%

Figure 2-17: TEM and agarose gel electrophoresis of 3H×3H, 4H×4H, 6H×6H, 6H×10H, 8H×12H, 4H×24H, and 12H×12H cuboids. (**A**) Designs of cuboids with a variety of dimensions. 3D cylinder models are drawn proportionally to their relative dimensions. The cross-sections of each group are shown above their 3D cylinder models. The "⋆"s indicate designs measuring 32bp in height that failed self-assembly. (**B**) TEM images of purified cuboids in **A**. (**C**) Agarose gel electrophoresis for cuboids. For each group, lane M contains the 1 kb ladder; other lanes are labeled with numbers in accordance with their designs in **A**. Products (indicated by red arrows) were purified for TEM imaging. Structures were self-assembled in 0.5×TE buffer with 40 mM $MgCl_2$ using a 72-hour annealing ramp. The concentration of each strand was 200 nM. 10 μL of sample was loaded into each lane. The 3000bp band corresponding to 60 ng DNA was used as a standard to measure the yield of annealing products, indicated by red arrows. Below each product band, both the absolute mass value and the percentage yield are shown, using the method described in figure 2-6 and in the methods section. Note that the yields of 8H×12H×120B, 4H×24H×120B, and 12H×12H×120B cuboids are lower than 1%. Figure 2-17 is a more complete version of Fig. 2-10.

Statistics of 3H×3H, 4H×4H, 6H×6H, 6H×10H, 8H×12H, 4H×24H, and 12H×12H cuboids

Structure	No. of strands	No. of nucleotides	Measured X dimension	Measured Y dimension	Measured Z dimension	Gel yield
3H×3H×64B	33	1296	9±0.3	9±0.3	24±0.4	80%
3H×3H×128B	57	2448	9±0.2	9±0.2	45±0.8	52%
3H×3H×256B	105	4752	8±0.2	8±0.2	86±1.2	32%
3H×3H×512B	201	9360	8±0.3	8±0.3	170±2	7.3%
3H×3H×1024B	393	18576	8±0.4	8±0.4	240±10	4.1%
4H×4H×64B	62	2304	11±0.4	11±0.4	22±0.3	37%
4H×4H×128B	110	4352	10±0.4	10±0.4	46±0.6	26%
4H×4H×256B	206	8448	11±0.5	11±0.5	84±1.1	9.3%
4H×4H×512B	398	16640	9±0.3	9±0.3	170±3	3.9%
6H×6H×64B	147	5184	15±0.7	15±0.7	22±0.4	30%
6H×6H×128B	267	9792	16±0.6	16±0.6	43±0.8	22%
6H×6H×256B	507	19008	15±0.6	15±0.6	86±1.0	4.8%
12H×12H×48B	486	16128	31±1.2	31±1.2	16±0.2	N/A
6H×10H×64B	251	8640	16±0.5	24±1.2	22±0.3	33%
6H×10H×128B	459	16320	15±0.6	26±1.0	44±0.7	6.1%
8H×12H×64B	408	13824	22±0.8	29±1.3	22±0.3	5.7%
8H×12H×120B	728	24576	21±0.7	30±1.4	41±0.6	N/A
4H×24H×120B	710	24576	11±0.3	57±2.6	41±0.6	N/A

Table 2-1: Statistics of 3H×3H, 4H×4H, 6H×6H, 6H×10H, 8H×12H, 4H×24H, 12H×12H cuboids in Fig. 2-10. The number of strands used, the number of nucleotides, the measured dimensions, and the gel yields are listed for each structure.

Dimensions of intact particles were measured. For low yield samples (3H×3H×1024B cuboid, 8H×12H ×120B cuboid, 4H×24H×120B cuboid, and 12H×12H×48B cuboid), analysis was done on only 10 to 20 particles. For all other samples, the measurement was performed over 50 particles.

2.8.2 Custom shapes made from a 3D molecular canvas

Workflow of designing 3D shapes

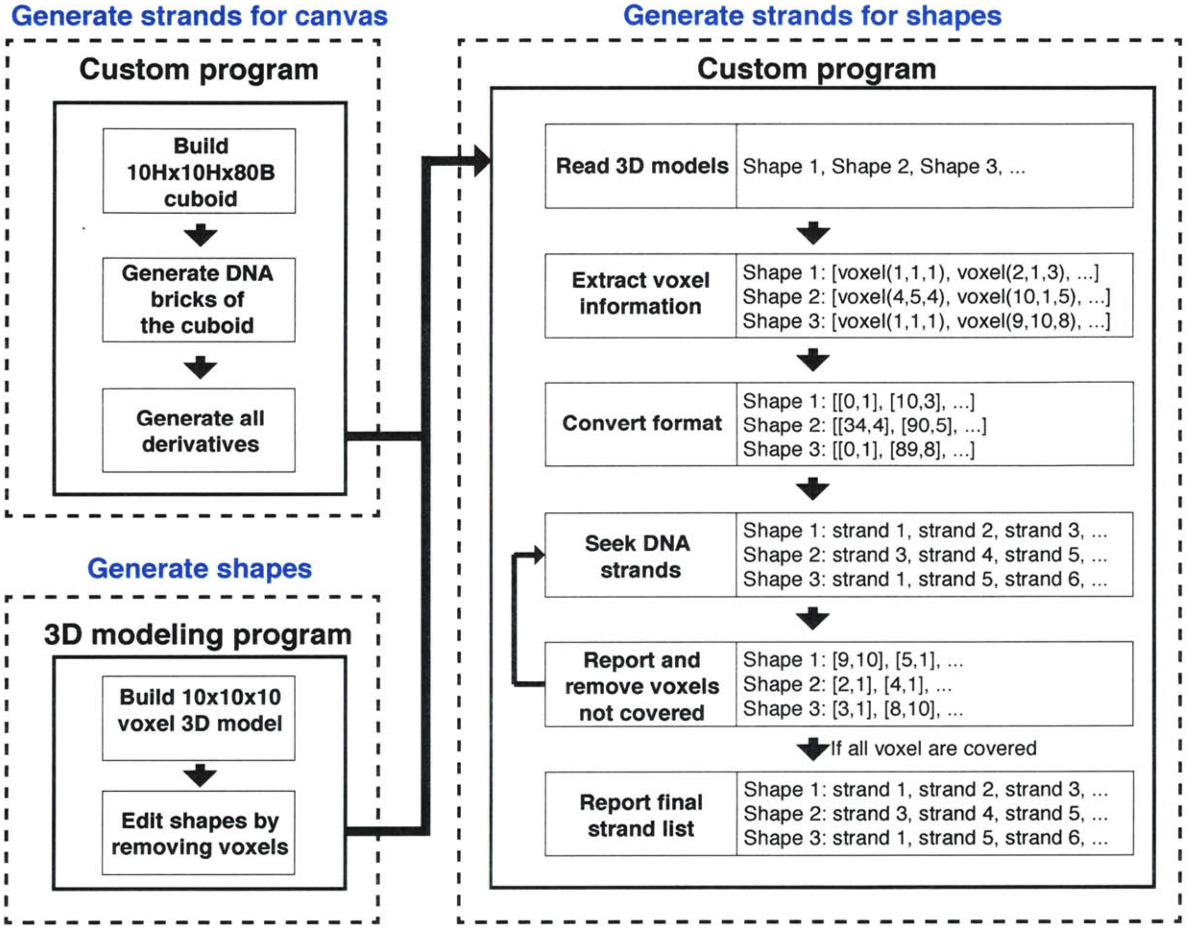
Generate strands for canvas
Custom program
Build 10Hx10Hx80B cuboid
Generate DNA bricks of the cuboid
Generate all derivatives
Generate shapes
3D modeling program
Build 10x10x10 voxel 3D model
Edit shapes by removing voxels
Generate strands for shapes
Custom program
Read 3D models
Shape 1, Shape 2, Shape 3, ...
Extract voxel information
Shape 1: [voxel(1,1,1), voxel(2,1,3), ...]
Shape 2: [voxel(4,5,4), voxel(10,1,5), ...]
Shape 3: [voxel(1,1,1), voxel(9,10,8), ...]
Convert format
Shape 1: [[0,1], [10,3], ...]
Shape 2: [[34,4], [90,5], ...]
Shape 3: [[0,1], [89,8], ...]
Seek DNA strands
Shape 1: strand 1, strand 2, strand 3, ...
Shape 2: strand 3, strand 4, strand 5, ...
Shape 3: strand 1, strand 5, strand 6, ...
Report and remove voxels not covered
Shape 1: [9,10], [5,1], ...
Shape 2: [2,1], [4,1], ...
Shape 3: [3,1], [8,10], ...
If all voxel are covered
Report final strand list
Shape 1: strand 1, strand 2, strand 3, ...
Shape 2: strand 3, strand 4, strand 5, ...
Shape 3: strand 1, strand 5, strand 6, ...

Figure 2-18: Workflow of designing 3D shapes.

The shapes are designed with a combination of custom software and commercial 3D modeling software. The complete workflow of the design process (Fig. 2-18) is described below:

Generate all DNA strands

(1) Build 3D canvas using a custom program. We used a $10\times10\times10$ voxel canvas in this paper (Fig. 2-12A).

(2) A custom program generates strands and their derivatives (Fig. 2-11) for self-assembly of custom shapes that can be made from a $10\times10\times10$ voxel 3D canvas. All sequences and their corresponding voxel information are then stored in a single text file, ALL-strand.txt. A total of 4,455 strands (138,240nt) were generated for making custom shapes.

Build 3D model and edit shapes

(3) Build a 3D model containing all 10×10×10 voxels using a commercial 3D modeling software (we used Strata^{TM} 3D, http://www.strata.com). Each voxel is represented by a small sphere (Fig. 2-19A) and can be edited independently (Fig. 2-19B). The small sphere voxels are easy to edit in comparison with the cube voxels used for the final illustration of shapes. The conversion between sphere-voxels and cube-voxels can be done by a custom program (or simply using the "search and replace" function of a text editing software). Commercial modeling software packages provide convenient tools to remove/add voxels and visualize the shapes from different angles.

(4) Design shapes by removing voxels from a 10×10×10 voxel 3D canvas, as shown in figure 2-19B. In this step, the shapes are designed with single voxel (8bp) resolution. Each shape is stored in a separate file with its voxel information.

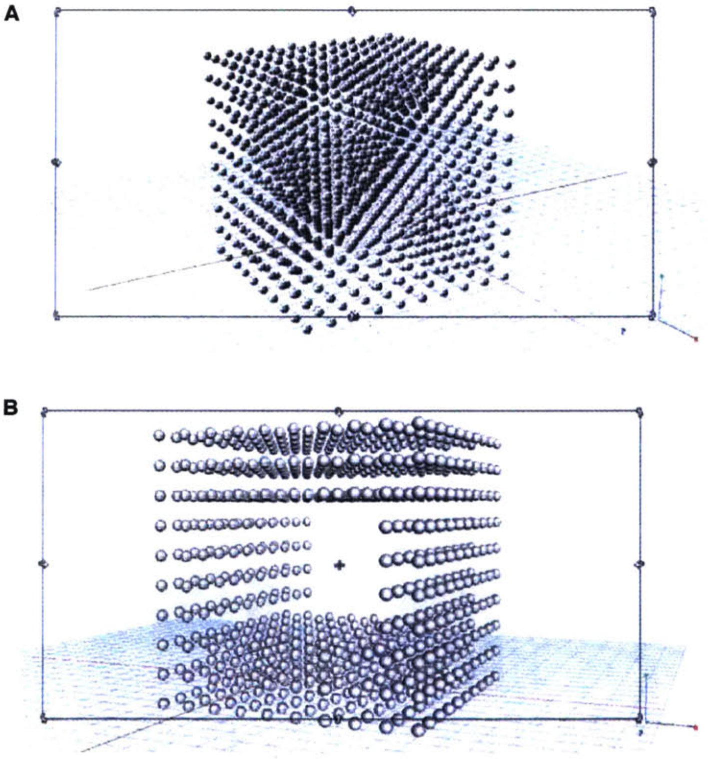

Figure 2-19: 3D-shape-editing interface. **(A)** A 10×10×10 voxel 3D canvas. Each sphere represents one voxel. **(B)** Shape editing is performed by removal of unwanted voxels.

Generate strands for each shape based on its voxel information

(3) Our custom program reads the voxel file. Based on the voxel information of the shape, the program searches the sequence file ALL-strand.txt and generates a list of strands for assembly of the designed shapes. The program first searches for only the 32nt and 16nt bricks to generate the shapes. Then the program determines whether any pairs of 32nt bricks and 16nt bricks can be merged to form a 48nt

"boundary" brick (Fig. 2-11F). If so, the program will substitute the 32nt brick and 16nt brick with a 48nt "boundary" brick.

(4) Because of our strand design described in figure 2-11, some voxel may not be covered by our strands in ALL-strand.txt due to the six removed strand types. During this search process, the program will automatically remove the voxels that cannot be covered and rerun the brick-seeking process. As only a small number of voxels (at the end of helices on the boundary of a shape) will be removed from a shape, the deletions are expected to only cause marginal change to the overall appearance of the designed shapes.

(5) The program finishes searching strands and generates a list of strands for assembling the designed shapes.

2.8.3 Agarose gels of shapes

Agarose gel electrophoresis of shapes 1–17

Shapes 1–17 were designed to explore basic rules of designing shapes from a 3D canvas. Shape 1 is a cuboid that contains all 10×10×10 voxels. Shapes 2–9 are two 4H×10H×80B blocks connected by a 2H×9H×80B, a 2H×8H×80B, a 2H×7H×80B, a 2H×6H×80B, a 2H×5H×80B, a 2H×4H×80B, a 2H×3H×80B, or a 2H×2H×80B block. Shapes 10–17 are two 4H×10H×80B blocks respectively connected by a 2H×10H×72B, a 2H×10H×64B, a 2H×10H×56B, a 2H×10H×48B, a 2H×10H×40B, a 2H×10H×32B, a 2H×10H×24B, or a 2H×10H×16B block, respectively.

Agarose gel electrophoresis revealed that, in both systems, as the connector became overly thin, the gel yields for the intact structures decreased and partial structures (putative unconnected 4H×10H×80B blocks) became more prominent (e.g. in lanes for shapes 8, 9, 15-17 in figure 2-20). However, reducing the number of voxels in the Z-axis appeared to decrease the yield more significantly than in the Y-axis. Shape 9, which contained only a 2-voxel connection along the Y-axis, gave 6% gel yield. In contrast, the yield for shape 17 (2-voxel in Z-axis) dropped to 1%. It is worth noting that TEM still detected some intact structures for shape 17. It is conceivable that a fraction of complete structures may fall apart during agarose gel electrophoresis.

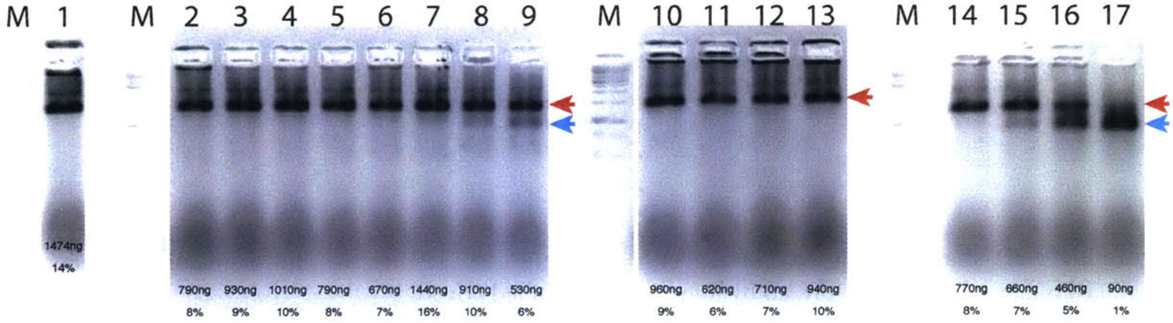

Figure 2-20: Agarose gel electrophoresis of shapes 1–17 from (Fig. 2-12E). Lane M shows 1kb ladder. Lanes 1–17 show shapes 1–17, respectively. The red arrows point to slow migrating bands that correspond to complete shapes. The blue arrows point to faster migrating bands that correspond to putative broken shapes. Yield of each intact shape (red arrow) is labeled under each lane.

Agarose gel electrophoresis of shapes 18–100

Yields are estimated using the method described in figure 2-6 and in the methods section. Most shapes have yields between a few percent and 30%.

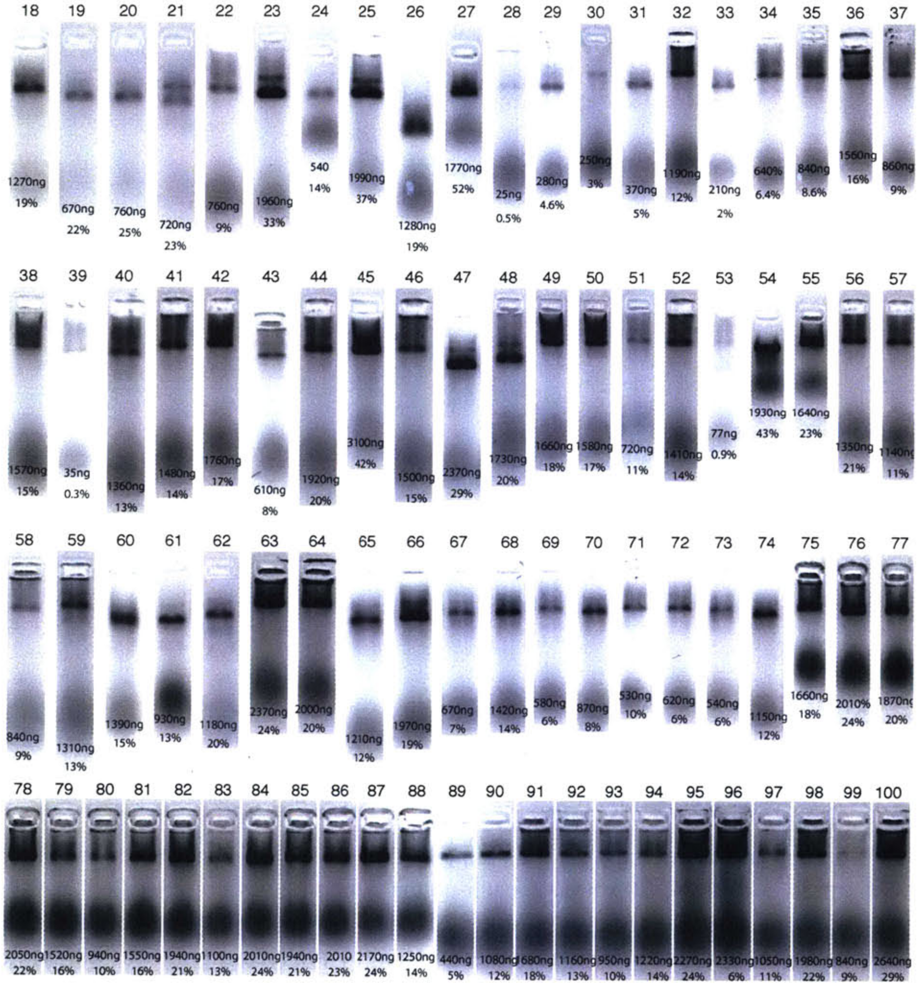
18 1270ng 19%
19 670ng 22%
20 760ng 25%
21 720ng 23%
22 760ng 9%
23 1960ng 33%
24 540 14%
25 1990ng 37%
26 1280ng 19%
27 1770ng 52%
28 25ng 0.5%
29 280ng 4.6%
30 250ng 3%
31 370ng 5%
32 1190ng 12%
33 210ng 2%
34 640% 6.4%
35 840ng 8.6%
36 1560ng 16%
37 860ng 9%
38 1570ng 15%
39 35ng 0.3%
40 1360ng 13%
41 1480ng 14%
42 1760ng 17%
43 610ng 8%
44 1920ng 20%
45 3100ng 42%
46 1500ng 15%
47 2370ng 29%
48 1730ng 20%
49 1660ng 18%
50 1580ng 17%
51 720ng 11%
52 1410ng 14%
53 77ng 0.9%
54 1930ng 43%
55 1640ng 23%
56 1350ng 21%
57 1140n 11%
58 840ng 9%
59 1310ng 13%
60 1390ng 15%
61 930ng 13%
62 1180ng 20%
63 2370ng 24%
64 2000ng 20%
65 1210ng 12%
66 1970ng 19%
67 670ng 7%
68 1420ng 14%
69 580ng 6%
70 870ng 8%
71 530ng 10%
72 620ng 6%
73 540ng 6%
74 1150ng 12%
75 1660ng 18%
76 2010% 24%
77 1870n 20%
78 2050ng 22%
79 1520ng 16%
80 940ng 10%
81 1550ng 16%
82 1940ng 21%
83 1100ng 13%
84 2010ng 24%
85 1940ng 21%
86 2010 23%
87 2170ng 24%
88 1250ng 14%
89 440ng 5%
90 1080ng 12%
91 680ng 18%
92 1160ng 13%
93 950ng 10%
94 1220ng 14%
95 2270ng 24%
96 2330ng 6%
97 1050ng 11%
98 1980ng 22%
99 840ng 9%
100 2640ng 29%

Figure 2-21: Agarose gel electrophoresis of shapes 18–100. Both the mass yield and the percentage yield of each shape are shown under each lane.

2.8.4 3D carving

Figure 2-22 shows the results of native agarose gel electrophoresis for the 3D carved structures from the cuboid. The carved samples from gel-purified cuboid after annealing were subjected to TEM imaging shown in fig. S39 to fig. S41 in the supplementary of [132].

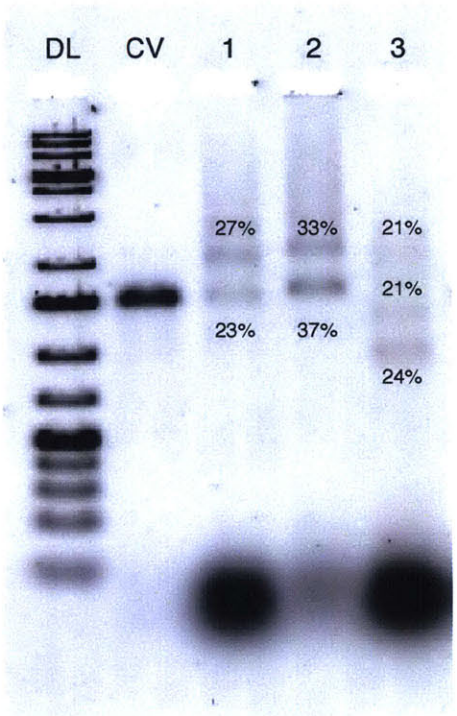

Figure 2-22: Agarose gel electrophoresis analysis for 3D carving. DL: 1 kb DNA ladders; CB: the plain cuboid. 1: carved structure 1 (a corner off); 2: carved structure 2 (a tunnel through); 3: carved structure 3 (cut in halves). Numbers above and below bands indicate the yield of the band relative to the total intensity of the lane. Mixtures containing 200 nM of each component strand were annealed in 0.5× TE buffer supplemented with 40 mM $MgCl_2$ from 90°C to 25°C over 72 hours. The target band was extracted and purified by centrifugation, with the concentration estimation by the measurement of ultraviolet absorption at 260 nm. A specific set of carving strand was added to the purified canvas sample with molar ratio between component strands and carving strands to be 1:1 and the carving sample was incubated in 27°C for 3 hours. Then, a 10 μL sample (mixed with 2 μL 6× bromophenol blue loading dye) was loaded into a 2% native agarose gel and subjected to electrophoresis in an ice water bath with 0.5× TBE running buffer (supplemented with 10 mM $MgCl_2$).

2.8.5 Generality of modular DNA-brick self-assembly

Agarose gel electrophoresis of other modular DNA brick assemblies

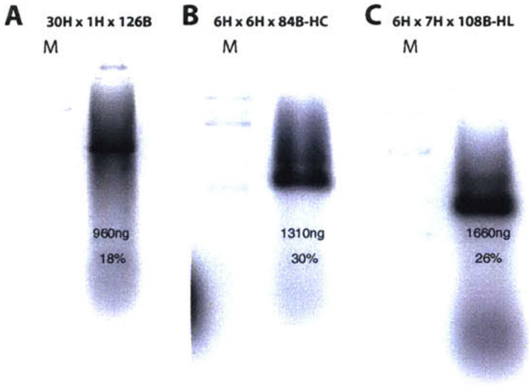
A
30H x 1H x 126B
M
960ng
18%
B
6H x 6H x 84B-HC
M
1310ng
30%
C
6H x 7H x 108B-HL
M
1660ng
26%

Figure 2-23: Agarose gel electrophoresis of other modular DNA brick assemblies. A 2% agarose gel was run on **(A)** the 30H×1H×126B rectangle, **(B)** the 6H×6H×84B-HC, and **(C)** the 6H×7H×108B-HL cuboid. Yield is labeled beneath the sample lane. The sample was self-assembled under the following conditions: 200 nM per strand, 0.5×TE buffer with 40 mM $MgCl_2$, 72-hour annealing ramp. 10 μL of sample was loaded to the gel.

CHAPTER 3

DNA Brick Crystals with Prescribed Depth

In chapter 2, we focused on addressing a challenge in nanotechnology of creating arbitrary 3D nanoscale patterns in a simple and modular manner through self-assembly of DNA bricks. We are capable of creating patterns across roughly a 25 nm by 25 nm by 25 nm volume. Many applications require larger surface coverage. Thus, in this chapter, we focus on extending our technology to create large scale periodic structures using our DNA bricks approach.

This chapter has been adapted and partially reproduced with permission from **Yonggang Ke*, Luvena L. Ong*, Wei Sun*, Jie Song, Mingdong Dong, William M. Shih, and Peng Yin. "DNA Brick Crystals with Prescribed Depth."** ***Nature Chemistry,*** **2014, 6: 994-1002** [144].

3.1 Abstract

The ability to assemble functional materials with precise spatial arrangements is important for applications ranging from protein crystallography to photovoltaics. Here, we describe a general framework for constructing two-dimensional crystals with prescribed depths and sophisticated three-dimensional features. The crystals are self-assembled from single-stranded DNA components called DNA bricks. We demonstrate the experimental construction of DNA brick crystals that can grow to micrometer size in their lateral dimensions with precisely controlled depths up to 80 nm. They can be designed to pack DNA helices at angles parallel or perpendicular to the plane of the crystal and to display user-specified sophisticated three-dimensional nanoscale features, such as continuous or discontinuous cavities and channels.

3.2 Introduction

The production of two-dimensional materials, particularly crystals with prescribed depths and intricate three-dimensional (3D) features, provides an enabling platform for nanofabrication. For example, these two-dimensional (2D) crystals could be integrated with inorganic nanomaterials for developing complex nanoelectronics [145] and photonics systems [146, 147]. Although thin film structures have been created using either electron/ion beam lithography [147] or self-assembly of block co-polymers [148, 149], fabricating two-dimensional materials that simultaneously achieve precisely tunable thickness, and prescribed complex surface and internal features (e.g. channels or pores) with sub-5 nm resolution remains challenging [147, 150–152].

A promising route to address this challenge is structural DNA nanotechnology [11]. DNA has been used to create complex discrete shapes [11, 35, 38, 39, 48, 49, 51, 54, 55, 59, 60, 64, 65, 131, 133, 153, 154] and extended periodic crystals [20, 24–26, 30, 33, 34, 63, 155–159], including ribbons [63], tubes [24, 30, 63, 156], two-dimensional crystals [20, 24–26, 30, 33, 59, 155, 157–159], and three-dimensional crystals [34]. DNA structures can serve as scaffolds for precise patterning of functional moieties (for example gold nanoparticles) for electronics and photonics applications [86, 156, 160]. However, in contrast to current organic polymeric films [161], the two-dimensional DNA crystals are typically restricted to a single-layer of DNA helices with about 2 nm depth. A three-dimensional crystal has been reported previously, but it grows in all three dimensions with no control in depth and uses a small triangular repeating unit [34]. One major categorical gap in constructing atomically precise DNA structures – and, more generally, synthetic molecular structures – is the lack of a general framework for making complex two-dimensional crystals crystals with precisely controlled depth and sophisticated three-dimensional features. Successful construction of such structures could enable a wide range of applications ranging from nanoelectronics and plasmonics to biophysics and molecular diagnosis.

Using single-stranded DNA bricks [63, 64, 131], we describe here a simple, robust, and general approach to engineer complex micrometre-sized two-dimensional crystals with prescribed depths and complex three-dimensional features with nanometre resolution. In previous reports [20, 24–26, 30, 33, 34, 155–159], DNA crystals are typically formed via a two-stage hierarchical process, in which individual strands first assemble into a discrete building block (often known as a DNA tile) and individual tiles then assemble into crystals. In contrast, DNA brick crystals grow non-hierarchically, and the growth of DNA crystals from short, floppy, single-stranded DNA bricks does not involve the assembly of pre-formed discrete multi-stranded building blocks with well-defined shapes. During the brick crystal growth, assembly and disassembly occur via relatively weak intermolecular interactions involving the addition or subtraction of a single short strand at a time.

We constructed a total of 32 DNA brick crystals. These crystals can grow up to several micrometers in their lateral dimensions with a prescribed depth up to 80 nm, and display sophisticated user-specified nanometre-scale three-dimensional features, including intricate cavities, channels, and tunnels (fig. S1 in the supplementary materials of ref. [144]). Additionally, the non-hierarchical nature of the assembly permits isothermal formation of the crystals. We illustrated the scaffolding utility of these crystals by functionalising them with parallel arrays and layers of tightly-packed (1-2 nm spaced) gold nanoparticles.

3.3 Materials and Methods

Sample preparation

DNA strands were synthesized by Integrated DNA Technology, Inc. (www.idtdna.com). To assemble the structures, unpurified DNA strands were mixed in an equimolar stoichiometric ratio to the highest possible concentration from a 100 μM stock in 0.5×TE buffer (5 mM Tris, pH 7.9, 1 mM EDTA) supplemented with 40 mM $MgCl_2$.

Annealing ramps and isothermal assembly

The strand mixture was then annealed in a PCR thermo cycler using a fast linear cooling step from 80°C to 60°C over 1 hour, then a 72-hour or 168-hour linear cooling ramp from 60°C to 24°C. The annealing ramps were named according to length of the second cooling step, as 72-hour annealing or 168-hour annealing. Most ZX-crystals were folded using the 72-hour annealing, except the ZX-96H×64B-cross-tunnels which used the 168-hour annealing. All XY-crystals were folded with the 168-hour annealing. For isothermal assembly of DNA crystals, the sample solution was incubated at 33°C for up to 48 hours.

DNA modification of 10-nm gold nanoparticles

Conjugation of thiolated DNA onto 10-nm gold nanoparticles was achieved following previously reported protocol [162]. In a typical experiment, 20 μL 2.5 μM phosphine-coated 10-nm gold nanoparticle was mixed with 0.5 μL 2 M $NaNO_3$ and 0.65 μL 100 μM thiolated DNA in 0.25× TBE buffer. The reaction solution was incubated at room temperature for 36 hours in the dark. After that, the reaction solution was loaded into 1% agarose gel containing 0.5× TBE buffer. The electrophoresis was running at 95 V for 1 hour in a gel box on an ice-water bath. The purple band was recovered by pestle crushing, followed by centrifugation for 3 min at 10,000 rpm at room temperature using "Freeze 'N Squeeze" DNA Gel Extraction spin columns (Bio-Rad). Recovered DNA-modified gold nanoparticles were stored at 4°C in the dark for further use. The sequence for the thiolated DNA was: 5′-AAAAAAAAAA-/3ThioMC3-D/.

Gold nanoparticle decoration of DNA crystals

To 15 μL 400 mM NaCl solution, 0.8 μL (ZX-4H×6H×96B-channel crystal) or 0.6 μL (XY-4H×4H×64B-cuboid crystal) DNA samples were added. Then 0.2 uL 95 nM 10 nm gold nanoparticles were introduced. After pipetting for 50 times, the reaction mixture was left at room temperature for three hours in the dark.

TEM imaging

For imaging, 2.5 μL of annealed sample were adsorbed for 2 minutes onto glow-discharged, carbon-coated TEM grids. The grids were then stained for 10 seconds using a 2% aqueous uranyl formate solution containing 25 mM NaOH. Imaging was performed using a JEOL JEM-1400 TEM operated at 80 kV.

Cryo-EM imaging

A 5 μL droplet of the crystal sample was added onto the positively-charged carbon grids, blotted 5.5 s, and plunge-frozen in liquid ethane using a Vitrobot (FEI). Grids were then loaded into a Titan Krios transmission electron microscope (FEI), which was operated at 300 kV with nominal –3-μm defocus using a dose of 1.5 e/^{2}. The specimen was tilted $\sim$2° increments over a total angular range of ±60°. All of the images were kept by using automated data acquisition software. 3D reconstructions from the above tilt series were performed with the weighted back-projection method and further analysis of tomograms was done using IMOD software [163].

Annealing and melting curves

500 nM of strands were folded following the annealing ramp protocol listed above in the presence of 0.3× SYBR Green I using the Eppendorf Master cycler realplex 4 PCR. Samples were read once during the first cooling step and four times during the second cooling step. Following annealing, the same samples were melted at the rate of 0.2°C/min. 9 μL samples were removed during the annealing or melting for TEM and gel electrophoresis analysis.

Agarose gel electrophoresis

Annealed samples were subjected to 1.5 or 2 percent native agarose gel electrophoresis for 2 hours (gel prepared in 0.5×TBE buffer supplemented with 10 mM $MgCl_2$ and 0.005% (v/v) EtBr) or 1× SYBR Safe in an ice water bath.

AFM imaging

AFM images were obtained using a MultiMode VIII SPM (Bruker) equipped with a liquid cell. 2 μL of sample was applied onto the surface of highly ordered pyrolytic graphite (HOPG), which was pretreated with ultraviolet-ozone for 30 seconds. The 50 μL of TAE buffer (12.5 mM Mg^{2+}, 5 mM Ni^{+}) was added into the liquid cell. And images were collected using silicon nitride cantilevers (Olympus).

3.4 Results

3.4.1 Design and assembly of DNA brick crystals

The crystal design is based on previous discrete three-dimensional DNA brick structures [131]. A DNA brick is a 32-nucleotide (nt) strand with four 8-nt binding domains, and can be modeled as a Lego-like brick (Fig. 3-1A). In a one-step annealing reaction, DNA bricks – each with a distinct sequence – assemble into a prescribed structure by binding to their designated neighbors. Implementing "connecting" bricks between discrete structures yields DNA brick crystals. The design strategy is illustrated using a 6H (helix)×6H (helix)×24B (basepair) cuboid structure that can be programmed to grow along three orthogonal axes (Fig. 3-1B). To achieve homo-multimerization along the z axis (parallel to helical axes), the domains in the first layer are modified to be complementary to the domains in the last layer. Growth along the x axis or y axis is achieved by including brick that each have two domains bound to one face of the cuboid and the other two domains bound to the opposing face (see fig. S2 for detailed strand connection patterns). The crystals are designed to form via non-hierarchical growth, with individual bricks (rather than pre-formed multi-brick blocks) directly incorporated into the crystal (Fig. 3-1C).

We constructed four groups of crystals: (1) Z-crystals: one-dimensional "DNA-bundle" crystals extending along the z axis (Fig. 3-1D); (2) X-crystals: one-dimensional crystals extending along the x axis; (3) ZX-crystals: two-dimensional 'multilayer' crystals extending along the z axis and the x axis (Fig. 3-1E); (4) XY-crystals: two-dimensional "DNA-forest" crystals extending along the x axis and y axis (Fig. 3-1F). Using different designs of repeating units, DNA crystals with prescribed depths and features, such as pores, channels, and tunnels, can be made (Fig. 3-1G–I). Here we define a 'channel' as a surface-exposed cavity extending across multiple repeating units, a "pore" as a hole across a single repeating unit, and a "tunnel" as a series of concatenated pores. A crystal is named as "[the growth direction(s)]-[the dimensions of the repeating-unit]-[the shape of the unit]". For instance, an "XY-6H×6H×24B-cuboid" crystal is a two-dimensional XY-crystal with a cuboid-shaped 6H×6H×24B repeating unit. Like discrete DNA brick structures [131], the sequences for DNA brick crystals were randomly generated. All crystals used 10.67 base-pair (bp)/turn reciprocal twist density which is slightly under-wound compared to the 10.5 bp/turn of natural B-form DNA.

Each crystal was assembled by mixing 100 nM of each unpurified DNA brick strand in 40 mM $MgCl_2$, without careful adjustment of strand stoichiometry. After 72-hour or 168-hour one-pot annealing, assembled crystals were imaged using transmission electron microscopy (TEM), cryo-electron microscopy (cryo-EM), or atomic force microscopy (AFM) without further purification. See Methods for details.

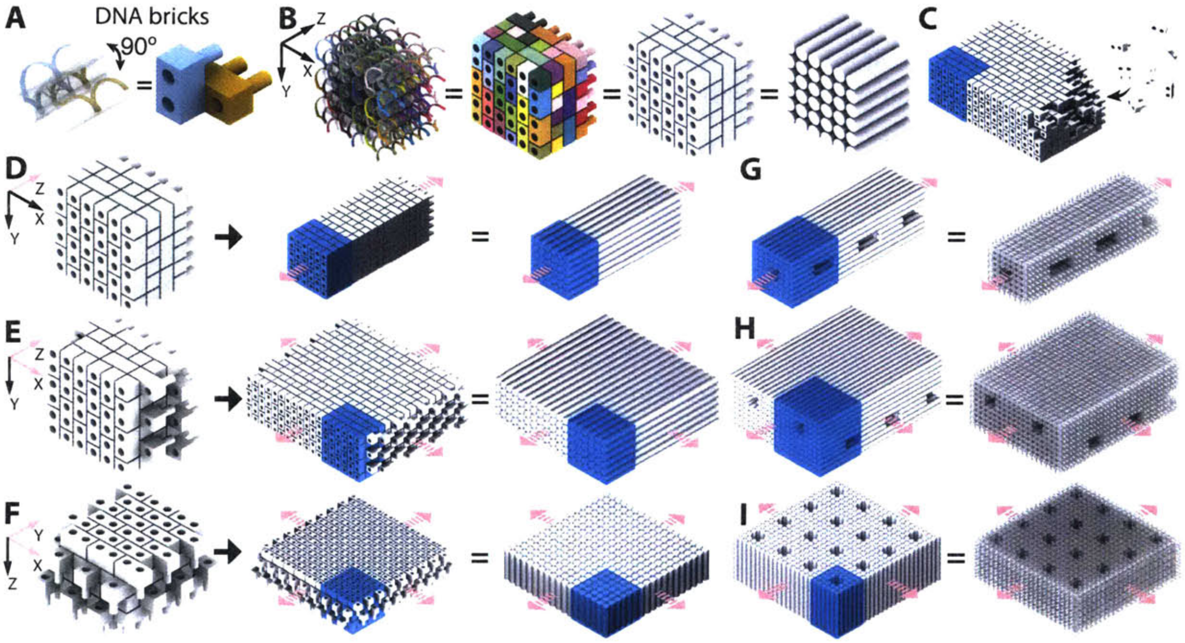

Figure 3-1: Design of DNA brick crystals. **(A)** A strand (left) and a brick (right) model showing two 32-nt DNA bricks that form a 90° angle. **(B)** Models of a 6H (helix)×6H (helix)×24B (basepair) cuboid with increasing levels of abstraction: a strand (leftmost) and a brick model where colors distinguish brick species, a brick model with all bricks colored grey, and a model where cylinders representing DNA double-helices. **(C)** Individual DNA strands, rather than pre-assembled multi-brick blocks, are directly incorporated into the growing crystal. **(D)** to **(F)** Brick and cylinder models of a 1D Z-crystal (**D**), a 2D ZX- crystal (**E**), and a 2D XY-crystal (**F**) designed from the 6H×6H×24B cuboid. **(G)** to **(I)** Cylinder and DNA-helix models of crystals with pores and tunnels. **(G)** A Z-crystal with a tunnel and periodic pores. **(H)** A ZX-crystal with two groups of parallel tunnels. **(I)** An XY-crystal with periodic pores. Repeating units of the crystals are denoted using blue-colored boxes. Pink arrows indicate the directions of crystal growth.

3.4.2 One-dimensional DNA-bundle crystals (Z-crystals)

Both solid Z-crystals (Fig. 3-2A–F) and Z-crystals with tunnels (Fig. 3-2G–I) were successfully constructed.

Solid Z-crystals with different cross-sectional shapes

We first constructed three solid Z-crystals with distinct square-shaped cross-sections (6H×6H×32B, 8H×8H×32B, and 10H×10H×32B; Fig. 3-2A–C). We then demonstrated crystals with more complex cross-sections: a Z-8H×8H×128B-spiral crystal with a surface helical channel along the z axis (Fig. 3-2D), a Z-43H×32B-triangle crystal (Fig. 3-2E), and a Z-44H×32B-hexagon crystal (Fig. 3-2F). The spiral channel was clearly visible in the TEM image of the Z-8H×8H×128B-spiral crystal. However, many broken structures were also observed for this spiral crystal (fig. S6).

Z-crystals with tunnels

Three Z-crystals with tunnels were tested (Fig. 3-2G–I). The cross-section of the Z-56H×32B-tunnel is an 8H×8H square with a 2H×4H rectangle removed from the center (Fig. 3-2G). The Z-108H×32B-tunnel has a 12H×12H square cross-section with a 6H×6H hole (Fig. 3-2H). The Z-60H×64B-tunnel crystal contains a 2H×2H tunnel along the z axis and 8H×2H×24B pores that intersect the 2H×2H tunnel every 64bp along the z axis (Fig. 3-2I). TEM images of the Z-60H×64B-tunnel showed many splintered structures containing only half of the designed DNA helices, likely reflecting the weakening effect of the periodic 8H×2H×24B pores on the connections between the top and bottom halves of the structures along the y axis.

All Z-crystals displayed a global right-handed twist, which likely resulted from the stress generated by the underwound design [52, 54]. Zoomed-out TEM images of Z-crystals are included in fig S3–11.

3.4.3 One-dimensional X-crystals

We constructed two 1D-crystals that extended along the x axis: an X-6H×6H×64B-cuboid crystal (Fig. 3-2J) and an X-32H×64B-pore crystal (Fig. 3-2K). Both appeared well-formed and grew up to a few hundred nanometers in length in TEM images. See fig. S12 for larger images.

3.4.4 Two-dimensional DNA-multilayer crystals (ZX-crystals)

Solid ZX-crystals (Fig. 3-3A–D), ZX-crystals with channels, pores, and tunnels (fig. S3E-H), and an offset ZX-crystal (Fig. 3-3I) were successfully constructed.

Solid ZX-crystals

Four solid ZX-crystals were designed from 4H×32B units that contained 4, 6, 10, and 20 layers of helices, respectively (Fig. 3-3A-D). The thickness of each ZX-crystals was directly measured at the crease where the crystal folded over onto itself in TEM images. The thicknesses of the 4, 6, 10, and 20-layer ZX-crystals were measured to be approximately 10, 15, 25 and 50 nm, respectively, proving all layers of the crystals were completely formed and that the width of each DNA helix was about 2.5 nm in diameter.

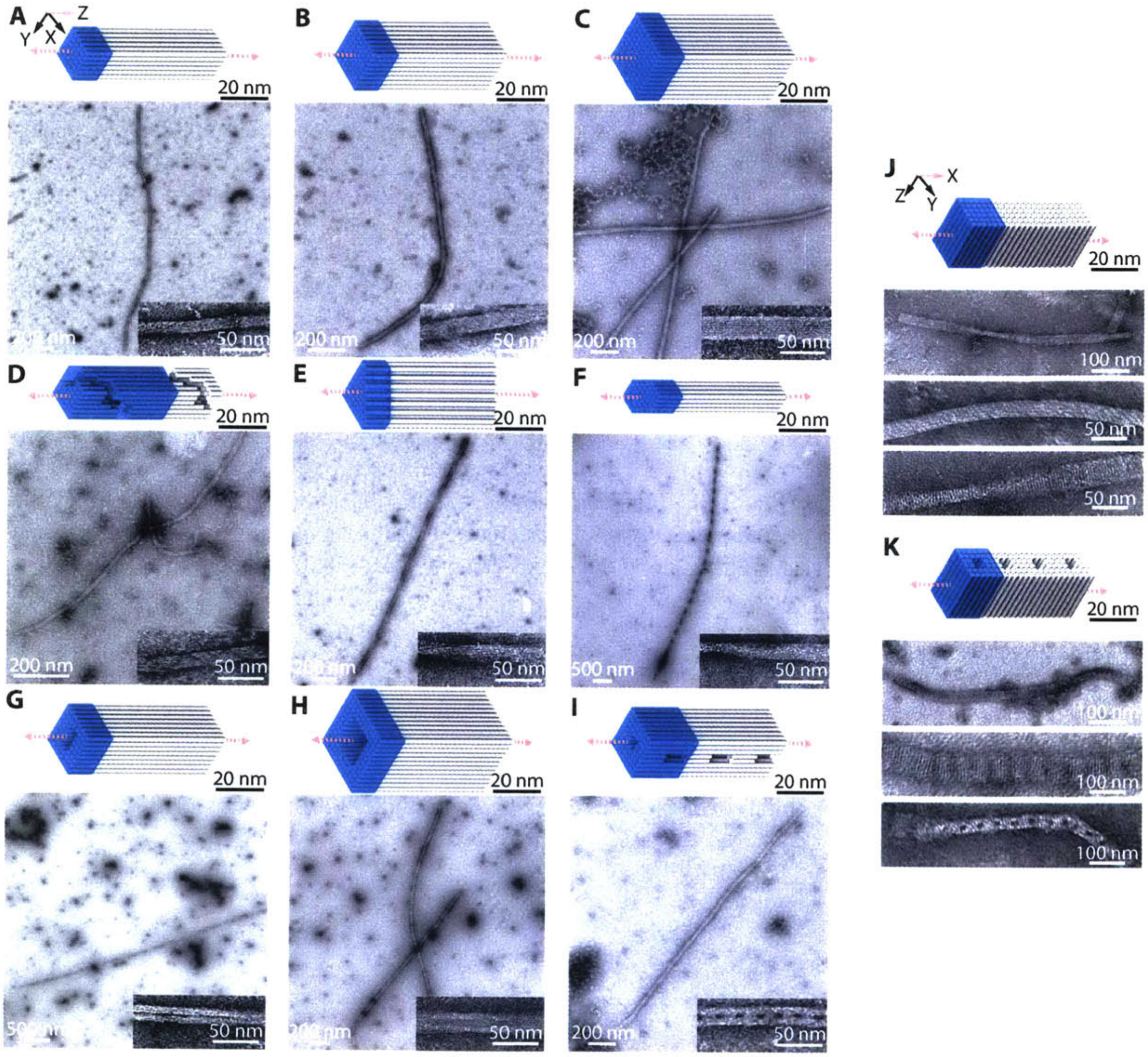
A
Z
Y
X
20 nm
200 nm
50 nm
B
20 nm
200 nm
50 nm
C
20 nm
200 nm
50 nm
D
20 nm
200 nm
50 nm
E
20 nm
200 nm
50 nm
F
20 nm
500 nm
50 nm
G
20 nm
500 nm
50 nm
H
20 nm
200 nm
50 nm
I
20 nm
200 nm
50 nm
J
X
Z
Y
20 nm
100 nm
50 nm
50 nm
K
20 nm
100 nm
100 nm
100 nm

Figure 3-2: One-dimensional DNA crystals. **(A)** to **(I)**, Z-crystals with cylinder models and TEM images. **(A)** to **(C)**, Z-crystals with solid cross-sections: 6H×6H **(A)**, 8H×8H **(B)**, and 10H×10H **(C)** Z-crystals. **(D)** to **(F)**, Z-crystals with different cross-sectional shapes: an 8H×8H Z-crystal with right-handed spiral channel **(D)**, a 43H Z-crystal with triangle-shaped cross-section **(E)**, and a 44H Z-crystal with hexagon-shaped cross-section **(F)**. **(G)** to **(I)**, Z-crystals with porous cross-sections: an 8H×8H Z-crystal with a 2H×4H tunnel **(G)**, a 12H×12H Z-crystal with a 6H×6H tunnel **(H)**, and an 8H×8H Z-crystal with a 2H×2H tunnel and perpendicular 8H×2H×24B pores **(I)**. **(J)** and **(K)**, cylinder models (top) and TEM images (bottom) of X-crystals of an X-6H×6H×64B-cuboid crystal **(J)** and a 6H×6H X-crystal with 2H×2H pores **(K)**. Unit cells of crystals are denoted using blue-colored boxes. See figs. S3–12 for more TEM images.

ZX-crystals with channels, pores, and tunnels

We first designed three ZX-crystals from a 6H×6H×32B cuboid unit (Fig. 3-3E-G). Four helices were removed from the cuboid to generate ZX-32H×64B-channel (Fig. 3-3E). The second design, ZX-32H×64B-cross-channel, was obtained by further removing a perpendicular 2H×32B channel from ZX-32H×64B-channel (Fig. 3-3F). The third design, ZX-6H×6H×64B-pore, contained a 2H×4H×32B vertical pore along the y axis in each cuboid unit (Fig. 3-3G). This design yielded narrow and long crystals. The most complex ZX-crystal design is the ZX-96H×64B-cross-tunnel crystal (Fig. 3-3H). Its repeating unit can be considered as a 10H×10H×64B cuboid with a 2H×2H×64B pore along the z axis and with a 10H×2H×24B pore along the x axis. In this structure, the design contained two types of parallel tunnels separated by two layers of DNA. These tunnels appeared perpendicular when viewed from the ZX projection.

Offset 2D ZX-crystal

We constructed a ZX-crystal that extended 6H×6H×64B-cuboid repeating units along the z axis and x axis using an "offset-register" scheme: the crystal's z axis extension was shifted 4H along the x axis; the crystal's x axis extension was shifted 32B along the z axis (Fig. 3-3I). In this offset-ZX-6H×6H×64B-cuboid crystal design, the crystal's Z-axis extension is shifted 4 duplexes along the X-axis; the crystal's X-axis extension is shifted 32 bp along the Z-axis (Fig. 3-3I). It is worth noting that the offset connections need to obey the following rules due to the periodicities of DNA-brick structures: shifting along the X-axis or Y-axis can occur only in two-helices intervals; shifting along the Z-axis can only occur in 32-bp intervals.

General observations

All ZX-crystals showed a small amount of right-handed twist, which also likely arose from the 10.67 bp/turn under-wound design. As a result, we observed that the crystals sometimes appeared twisted and folded on top of themselves in TEM images. We also observed that all ZX-crystals grew faster along the z axis than the x axis, consistent with observations from previous crystal growth studies [20]. See figs. S13–21 for more TEM images.

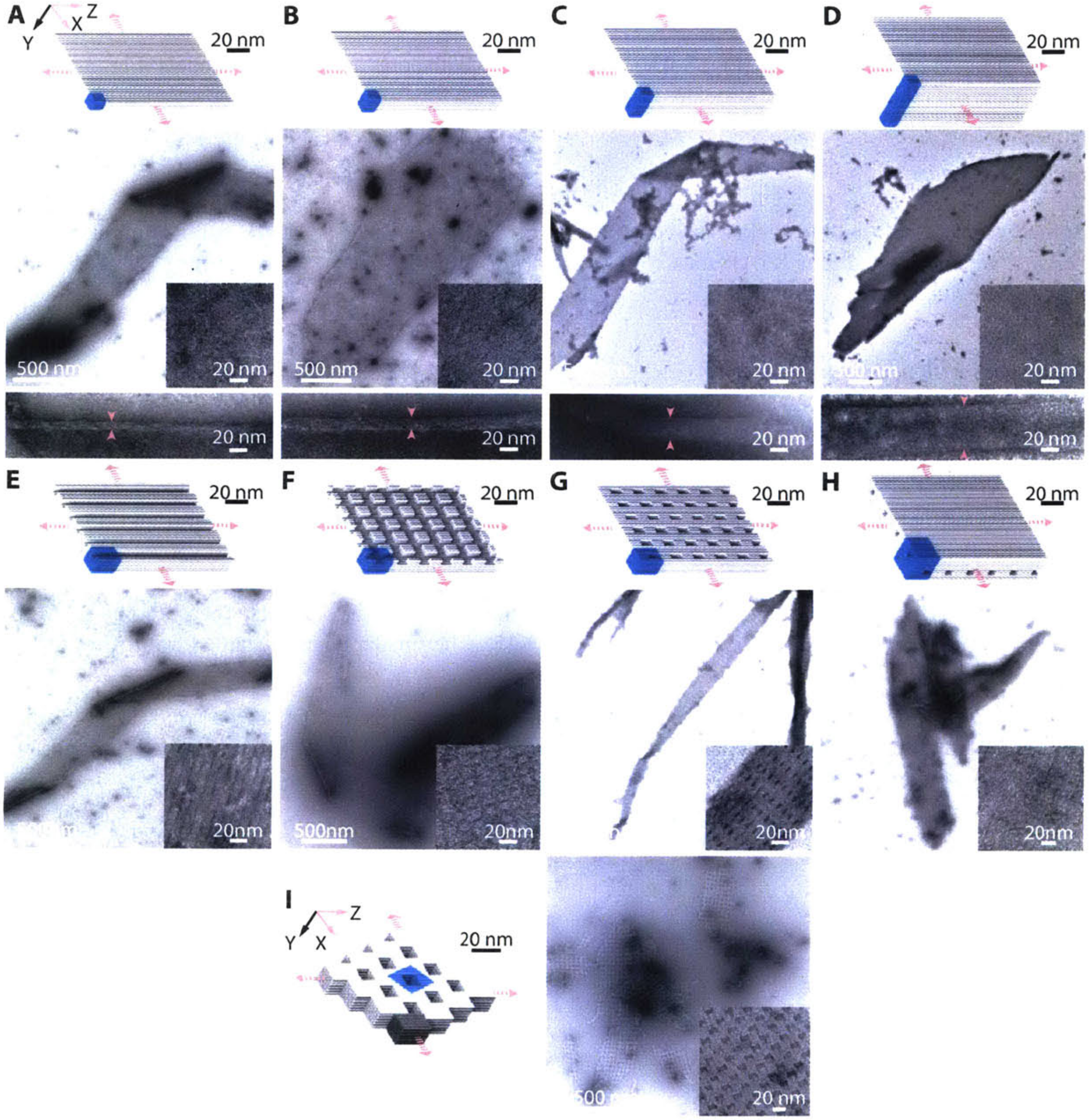
A
Y
X
Z
20 nm
B
20 nm
C
20 nm
D
20 nm
500 nm
20 nm
500 nm
20 nm
20 nm
500 nm
20 nm
20 nm
20 nm
20 nm
20 nm
E
20 nm
F
20 nm
G
20 nm
H
20 nm
20nm
500nm
20nm
20nm
20nm
I
Y
X
Z
20 nm
20 nm

Figure 3-3: Two-dimensional multilayer ZX-crystals. Cylinder models (top) and TEM images (bottom) are shown for each crystal. **(A)** to **(D)** Solid ZX-crystals: 4-layer (**A**), 6-layer (**B**), 10-layer (**C**), and 20-layer (**D**), solid ZX-crystals. Arrows indicate the positions for the thickness measurement of the crystals. **(E)** to **(H)** ZX-crystals with channels, pores, and tunnels: 6-layer crystal with 2H×2H parallel channels (**E**), 6-layer crystal with two groups of crossing channels – 2H×2H channels that run parallel to the DNA helical axis and 2H×32B channels that run perpendicular to the DNA helical axis (**F**), 6 layer crystal with 2H×6H×32B pores (**G**), and 10 layer crystal with two groups of non-contacting tunnels – 2H×2H tunnels parallel to the DNA helical axis and 2H×24B tunnels perpendicular to DNA helical axis (**H**). In **H**, the two groups of tunnels are separated by two layer of DNA helices. **(I)**, An offset-ZX-6H×6H×64B-cuboid ZX-crystal. The dark grey part represents a 6H×6H×64B-cuboid repeating unit. Unit cells of crystals are denoted using blue-colored boxes. See Supplementary figs. S13–21 for more TEM images.

3.4.5 Two-dimensional DNA-forest crystals (XY-crystals)

We constructed solid XY-crystals (Fig. 3-4A–D), XY-crystals with pores and surface channels (Fig. 3-4E–I), and XY-crystals that form a tube structure (Fig. 3-4J).

Solid XY-crystals

Solid XY-crystals of variable thicknesses constructed (Fig. 3-4A–D). Using a 4H×4H cuboid unit of various heights, we constructed four XY-crystals with 64B (21 nm), 128B (42 nm), 192B (63 nm), and 256B (84 nm) designed thickness.

XY-crystals with pores and channels

XY-32H×64B-pore and XY-32H×128B-pore crystals were constructed (Fig. 3-4E, H). Both designs contained periodic 2H×2H pores separated by 4H in each dimension. The two crystals resemble 21 and 42 nm porous membranes, respectively. Cryo-EM imaging was applied to these two crystals (Fig. 3-14). Based on 3D reconstruction data, their depths were measured to be 26±2 nm (32H×64B-pore) and 45±3 nm (32H×128B-pore), respectively (Fig. 3-4G, H), in good agreement with the theoretical values (21 nm and 42 nm). The slight discrepancy is likely because theoretical estimations did not account for the single-stranded poly-T at the ends of the duplex. The depth of these two crystals were also measured by AFM to be approximately 16 nm and 36 nm, respectively (Fig. 3-15). The smaller depths obtained from AFM likely reflects the compression of the crystal by the cantilever.

An XY-4H×8H×96B-channel crystal was constructed (Fig. 3-4G). It contained a solid 64B (42 nm) base and parallel channels. The channels are 4H (10 nm) in width and 32B (21 nm) in height, and are separated by 4 layers of helices.

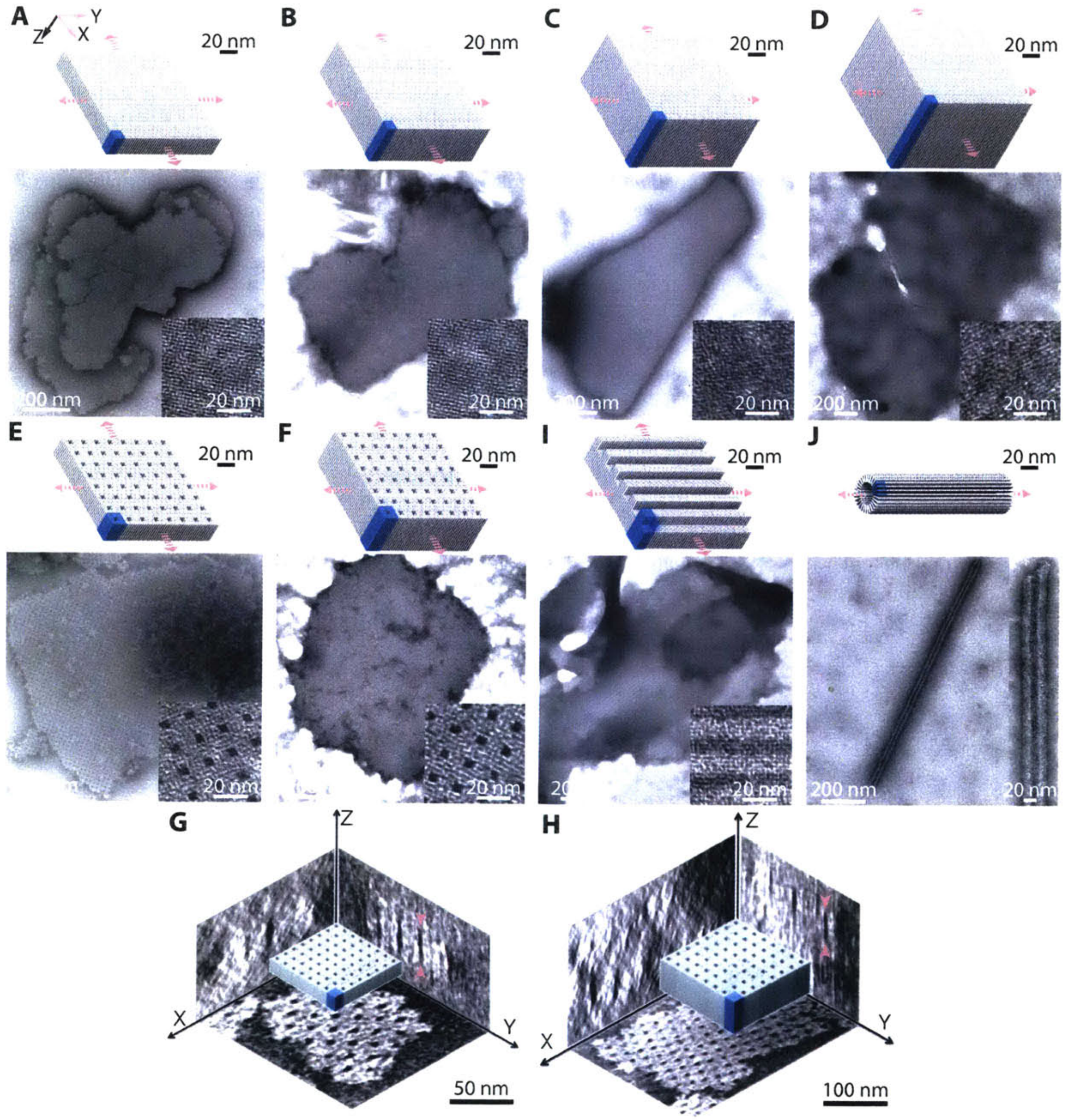
A
Z
X
Y
20 nm
200 nm
20 nm
B
20 nm
20 nm
C
20 nm
20 nm
D
20 nm
200 nm
20 nm
E
20 nm
20 nm
F
20 nm
20 nm
I
20 nm
20 nm
J
20 nm
200 nm
20 nm
G
Z
X
Y
50 nm
H
Z
X
Y
100 nm

Figure 3-4: Two-dimensional DNA-forest XY-crystals. Cylinder models (top) and TEM images (bottom) are shown for each crystal. **(A)** to **(D)**, Solid XY-crystals: 64B (**A**), 128B (**B**), 192B (**C**), and 256B (**D**) solid XY-crystals designed from a 4H×4H cuboid. **(E)** and **(F)**, XY-crystals with pores: a 32×64B-pore XY-crystal with 2H×2H×64B parallel pores (**E**) and a 32H×128B-pore XY-crystal with 2H×2H×128B parallel pores (**F**). **(G)** and **(H)**, Cryo-EM 3D reconstruction images showing the three projections of the XY-32H×64B-pore crystal (**G**) and the XY-32H×128B-pore crystal (**H**). Arrows indicate the positions for thickness measurements. **(I)**, A 96B XY-crystal with 4H×32B parallel channels. **(J)**, A tube crystal formed by 32B helices with helical axis perpendicular to the tube axis. Unit cells of crystals are denoted using blue-colored boxes. See figs. S25–34 for more TEM images.

A tube-shaped XY-crystal

An XY-4H×4H×32B-tube crystal (Fig. 3-4H, 3-5A) was designed using the same strategy as the other XY-crystals. However, this thin XY-crystal (32 bp, or 10.6 nm) forms a tube structure instead of a flat 2D crystal. These tubes are narrow and can grow to several micrometers in length (Fig. 3-5B). The inner diameters of tubes are about 14 to 20 nm, and the outer diameters are about 34–40 nm. Annealing the XY-4H×4H×32B-tube at higher $MgCl_2$ concentration produced tubes with larger diameters, presumably due to a greater reduction in repulsion between negatively-charged DNA helices. At 60 mM $MgCl_2$, we observed many tubes with diameters between 140 and 300 nm (Fig. 3-5C).

We hypothesize the tube formation is due to the uneven distribution of connections between helices (Fig 3-5D). Because helices in the XY-4H×4H×32B-tube are relatively short, there is only one connection between each pair of neighboring helices. The connections are evenly distributed along the Y-axis. However, along the X-axis, half of the connections are located in the middle of the structure, and the other half are positioned at one side of the structure Figs. 3-5E. Therefore, we hypothesize that the spacing between helices on the end with fewer connections can expand to form a crystal with a tube-like structure.

To further test our hypothesis that the tube formation is caused by the asymmetric distribution of crossovers, we designed an XY-4H×4H×32B-cuboid crystal in which the DNA bricks are arranged in an alternating fashion between layers [131] (Fig. 3-5F, fig. S65 for strand diagram). Connections between helices in this design were symmetrically distributed along both the x axis and y axis (Fig. 3-5F). This alternating design produced only flat crystal structures (Fig. 3-5G). Additionally, the thicker 64, 128, 192, and 256B XY-crystals with non-alternating designs had 2, 4, 6, and 8 connections between each pair of neighboring helices, respectively. No visible curvature was observed for these designs in TEM images (figs. S28–31).

General observations

Unlike the ZX-crystals, the XY-crystals did not show global right-handed twist. The lack of global twist can be explained by the following analysis. For simplicity, assuming an XY-crystal forms a perfect cylinder containing n helices. The overall twist in radians of the cylinder is $\theta = TL/JG$, where T is the applied torque resulting from the underwound design, L is helix length, G is the modulus rigidity of a helix, and J is the torsion constant. The first three parameters can be considered as constants. The torsion constant J for a cylinder as a function of cross-sectional (XY-plane) radius can be approximated as $\pi r^4/2$ (r^4 is proportional to n^2), where r is the circular cross-sectional radius. Thus, θ is inversely proportional to n^2. As an XY-crystal grows to include a large number of helices, its global twist θ rapidly becomes negligible.

As both growth directions (x axis and y axis) for an XY-crystal is perpendicular to the DNA helical axis, the XY-crystal grew in an isotropic fashion and did not exhibit any apparent directional preference. Because crystal growth along the x axis or y axis is slower than growth along z axis (as discussed for ZX-crystals), the 72-hour annealing often produces either no XY-crystals or XY-crystals smaller than one hundred nanometers in the lateral dimensions. Therefore, we used a 168-hour annealing ramp for all XY-crystals.

XY-crystals provide a particularly attractive platform for DNA-directed guest molecule assembly: the surface of an XY-crystal can be considered as a "breadboard" [48] on which guest molecules can be conveniently attached to the ends of DNA helices at 2.5 nm resolution in the lateral plane.

See figs. S25–34 for more TEM images of XY-crystals.

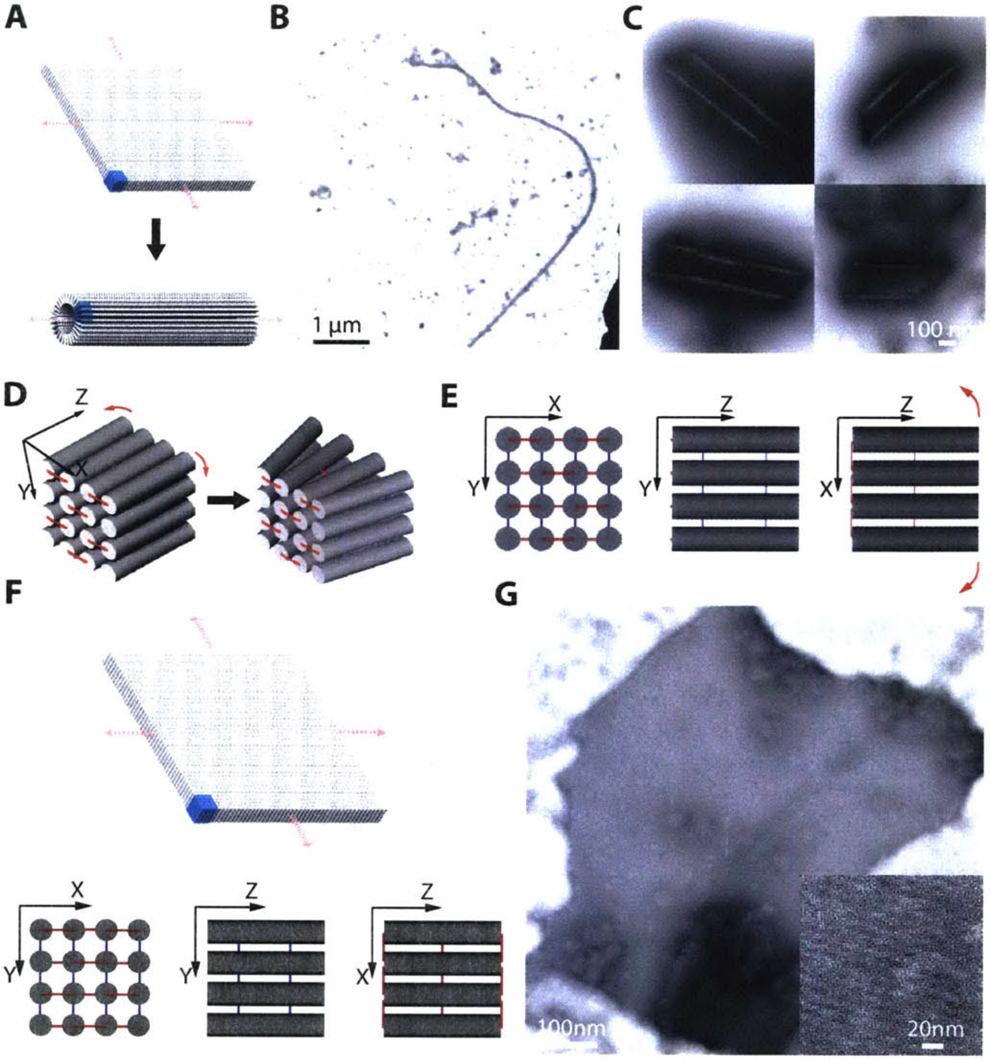

Figure 3-5: Formation mechanism of the XY-4H×4H×32B-tube crystal. **(A)** Top, a two-dimensional XY-4H×4H×32B-cuboid DNA-forest crystal design. Bottom, the structure instead forms a tube. Unit cells of crystals are denoted using blue-colored boxes. **(B)** TEM image of the XY-4H×4H×32B-cuboid crystal annealed in the presence of 40 mM $MgCl_2$. **(C)** TEM images of the XY-4H×4H×32B-cuboid crystal annealed in the presence of 60 mM $MgCl_2$. **(D)** A 4H×4H×32B-cuboid repeating unit expands in the X-direction while traversing along the Z-axis. **(E)** Projection views of a 4H×4H×32B-cuboid repeating unit. In the ZX-plane projection view, the crossovers are asymmetrically distributed along the Z-axis: half of the crossovers are located at the middle-point of the cuboid, and the other half are located at the left end of the cuboid. **(F)** Top, a two-dimensional XY-4H×4H×32B-cuboid DNA-forest crystal design using alternating DNA-bricks. Bottom, Projection views of a 4H×4H×32B-cuboid repeating unit assembled from alternating DNA-bricks. In the ZX-plane projection view, the crossovers are symmetrically distributed along the Z-axis with crossovers present at both ends of the helices. **(G)** TEM images of the XY-4H×4H×32B-cuboid crystal using alternating DNA-bricks.

3.4.6 Crystal growth mechanism

The non-hierarchical growth mechanism of DNA brick crystals is verified by the following experiments: (1) Analysis of the boundaries of DNA brick crystals based on high-resolution TEM images revealed that these crystals lack well defined, complete structural repeating units on their boundaries; (2) Annealing profile of the formation of the crystals revealed a single transition temperature (rather than two or more transition temperatures characteristic of hierarchically formed DNA crystals [30, 157]); (3) Time-lapse analysis of the TEM images and gel electrophoresis of the assembly process revealed the absence of repeating units of designed size.

Boundary analysis

We studied the edge of the XY-32H×64B-pore crystal by counting the number of units that match with that of the designed repeating unit (Fig. 3-6). By selecting structures with a repeating unit containing surface features, we could count each edge unit and analyze whether its shape matched that of the designed repeating unit. In hierarchically-assembled crystals, the designed repeating units are first formed before they are assembled into a crystal. As a result, the edges of the crystal often consist of the shape of the designed repeating unit (e.g. >90% of the edges of a previously reported hierarchically-assembled crystal [30, 157] (Fig. 3-6D, E). In contrast, only 2% of the edges of the XY-32H×64B-pore brick crystal match that of the designed shape (Fig. 3-6C), consistent with a non-hierarchical assembly mechanism. Structures grown in a hierarchical manner would first form the monomer before assembling these units together, resulting in a uniform boundary defined by the shape of the repeating unit. In contrast, non-hierarchical assembly would have a single stage growth where individual component strands would be added to the growing crystal, resulting in an arbitrarily-shaped boundary.

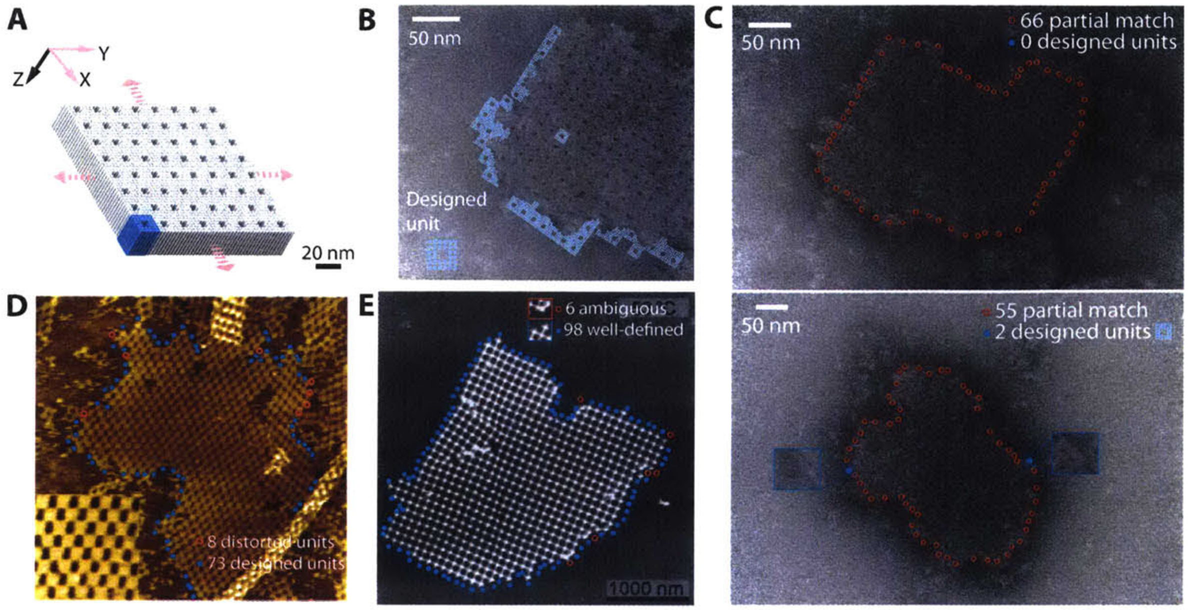
A
Y
Z
X
20 nm
B
50 nm
Designed unit
C
50 nm
66 partial match
0 designed units
50 nm
55 partial match
2 designed units
D
8 distorted units
73 designed units
E
6 ambiguous
98 well-defined
1000 nm

Figure 3-6: Boundary analysis of the XY-32H×64B-pore crystal and of hierarchically assembled 2D lattices. The boundaries of different crystals and lattices were analyzed for whether the edges matched the designed repeating unit. Each edge unit is marked with a blue dot if it matches the shape of designed unit or a red circle if it does not. A XY-32H×64B-pore crystal was selected for analysis because the final crystal structure clearly shows the repeating unit. **(A)** Schematic of the XY-32H×64B-pore crystal. **(B)** TEM image of the XY-32H×64B-pore crystal with an overlay depicting how the boundary is analyzed. The designed repeating unit is shown in the lower left and in the center of the crystal. Each light blue dot represents a DNA helix. The frame outlining the structure edge shows where the boundary would be if its shape matched that of the designed repeating unit. **(C)** Boundary analysis of XY-32H×64B-pore crystal showed that 98% of the total 123 counted units did not match that of the designed unit. The insets outlined in blue depict the edge where it matches that of the designed repeating unit. **(D)** A hierarchically assembled 2D lattice image obtained from Ke, et al. *J. Am. Chem. Soc.* 128, 4414-4421 (2006)[30] showed that 9.9% of all counted edge units were distorted. **(E)** A hierarchically assembled 2D lattice image obtained from Liu, et al. *Angew. Chem. Int. Ed.* 50, 264 (2011)[157] showed that 6% of all counted edge units were ambiguous in matching. An example of each is shown in the insets with a color-matched border.

Annealing curve

To study the annealing profile of the brick crystals, we assembled the ZX-4H×20H×32B and XY- 32H×64B-pore crystals in the presence of SYBR Green I (Fig. 3-7A and 3-8A). The derivative of the fluorescence with respect to temperature was obtained by subtracting two fluorescent intensities obtained one degree apart. For both these structures, a single sharp transition peak was observed for the 3-day annealing curves. For the ZX-crystal, this peak was located around 40°C (Fig. 3-7B), while the XY-crystal had its transition around 30°C (Fig. 3-8B). For hierarchical assembly systems (e.g. lattices formed from multi-stranded tiles), two or more characteristic transition temperatures are typically observed [157]: the lowest transition temperature corresponds to the formation/melting of lattice from the pre-formed tile monomers, and the higher ones correspond to the formation/melting of tile monomers from component strands. In contrast, our results are consistent with a non-hierarchical assembly mechanism, in which there is a single stage where individual strands are added directly into the growing structure without forming a well-defined multi-stranded monomer unit first.

Time-lapse analysis with gel electrophoresis and TEM

Time-points before, at, and after the transition temperature were sampled for both the above two ZX- and XY-crystals to confirm the lack of well-formed, discrete repeating units. Gel electrophoresis showed no intermediate band between the well and monomers (fig. 3-7D, 3-8D), as expected. To further confirm the lack of a well-defined, discrete intermediate structural unit, these time-points were also imaged under TEM. At 60, 43, and 40°C for the ZX-crystal, although some structures were observed, they were randomly sized and shaped and did not match the uniform pattern of the designed crystal (Fig. 3-7E, insets). At 30°C, crystal structures were observed. For the XY-crystal, these small (approximately 100 nm) amorphous clusters were also observed at 60, 40, 32, and 30°C. Starting at 28°C, the designed crystal structure was observed (Fig. 3-8E, inset). At 25°C, well-formed crystals were observed, but they were heavily stacked on top of one another. Overall, TEM imaging showed no uniformly sized and shaped discrete structures (Fig. 3-7E), further confirming the non-hierarchical growth mechanism.

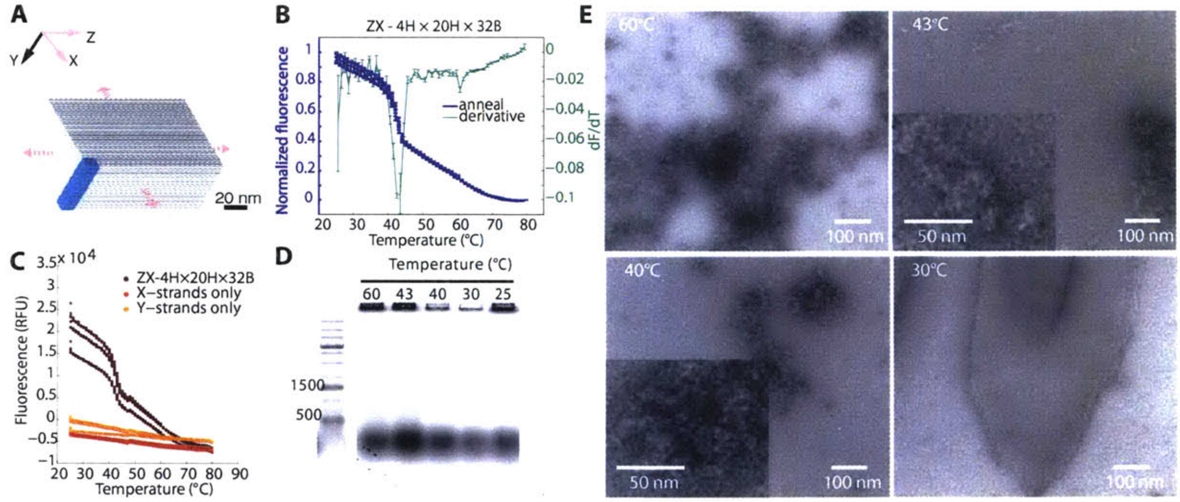

Figure 3-7: Annealing and time-lapse analysis of the ZX-4H×20H×32B crystal. **(A)** Schematic of the ZX-4H×20H×32B crystal. **(B)** Normalized and averaged annealing curves (blue) of the ZX-4H×20H×32B crystal obtained over a 3-day anneal. Controls contain only the x-strands or the y-strands of the structure. The averaged sum of these signals was used as a baseline measurement, and final signals were normalized to fluorescence at 25°C and 80°C. The derivative of the normalized fluorescence over temperature was also calculated (green). **(C)** Raw annealing curves of ZX-4H×20H×32B obtained over a 3-day anneal and used for calculation **B.** **(D)** 2% agarose gel electrophoresis was performed on samples taken at different temperatures along the annealing curves in **B.** **(E)** TEM images of these sample annealing time points obtained in **d.** Insets depict zoomed-in images of the observed structure.

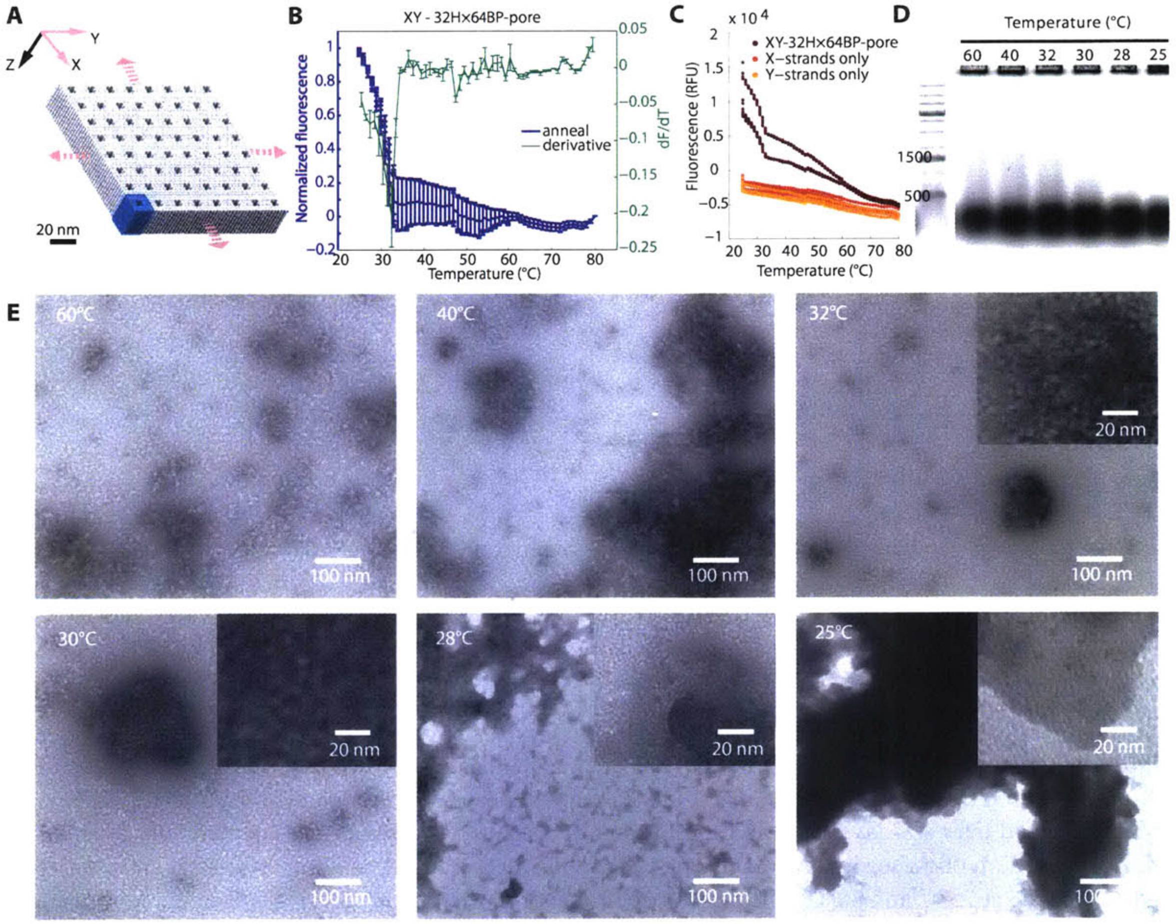

Figure 3-8: Annealing and time-lapse analysis of the XY-32H×64B-pore crystal. **(A)** Schematic of the XY-32H×64B-pore crystal. **(B)** Normalized and averaged annealing curve (blue) of the XY-32H×64B-pore crystal obtained over a 3-day anneal. Controls contain only the x-strands or the y-strands of the structure. The averaged sum of these signals was used as a baseline measurement, and final signals were normalized to fluorescence at 25°C and 80°C The derivative of the normalized fluorescence over temperature was also calculated (green). **(C)** Raw annealing curves of the XY-32H×64B-pore crystal obtained over a 3-day anneal and used for calculating **B**. **(D)** 2% agarose gel electrophoresis was performed on samples taken at different temperatures along the annealing curves in **B**. **(E)** TEM images of these sample annealing time points obtained in **D**. Insets depict zoomed-in images of the observed structure.

Isothermal assembly

The single transition temperature of the DNA brick crystallization suggests that these crystals should be able to assemble isothermally. Annealing curves for the ZX-6H×4H×96B crystal was obtained by assembling the crystal in the presence of SYBR Green I (Figs. 3-9B,C), 3-9C depicts the raw fluorescent data for the ZX-6H×4H×96B crystal for the curves in figure 3-9B. Signal was directly averaged to obtain the reported fluorescent trace. The derivative of the fluorescence with respect to temperature was obtained by subtracting two fluorescent intensities obtained one degree apart. These curves allowed us to find the peak transition temperature for isothermal folding.

Thus, we assembled a ZX-6H×4H×96B-cuboid crystal isothermally at the observed annealing transition temperature of 33°C (Fig. 3-9C). Time-points were sampled during this annealing process and analyzed by gel electrophoresis (Fig. 3-9D), which showed no discrete monomer band. As a control, a 6H×4H×96B cuboid was also folded and analyzed on the gel (Fig. 3-9D, lane D). Time-lapse TEM images further supported the non-hierarchical assembly mechanism: structures around 100 nm in size appeared after 4 hours and rapidly grew to micron-sized structures by 48 hours (Fig. 3-9E).

Thus, we assembled a ZX-6H×4H×96B-cuboid crystal isothermally at the observed annealing transition temperature of 33°C (Fig. 3-9C). Gel electrophoresis showed no discrete monomer band during annealing (Fig. 3-9D). Time-lapse TEM images further supported the non-hierarchical assembly mechanism: structures around 100 nm in size appeared after 4 hours and rapidly grew to micron-sized structures by 48 hours (Fig. 3-9E).

3.4.7 Yield and quality analysis

We analyzed three parameters to study how well formed our crystals are: (1) crystal deposition density and (2) strand depletion ratio to approximate yield of the brick crystals and (3) defect analysis to determine the quality of the structures formed.

Deposition density analysis

The ZX-6H×4H×96B crystal was formed isothermally for 2 days (Fig. 3-9). The sample was then diluted four times and deposited on a TEM grid to determine structure deposition density. Four randomly selected 40 μm x 32 μm regions were counted for the number of structures present (Fig. 3-10A). We found more than 300 individual crystals larger than 200 nm×100 nm in each region (Fig. 3-10B). This results in a deposition density higher than 0.23 crystal per μm^2. Because the structures aggregate together, precise counting is challenging and the reported density is an under-estimate of the total structures present within the selected regions (Fig. 3-10C). Although deposition density does not provide a direct measure for the yield, the large number of structures counted suggests that crystallization of these DNA structures occurs relatively easily.

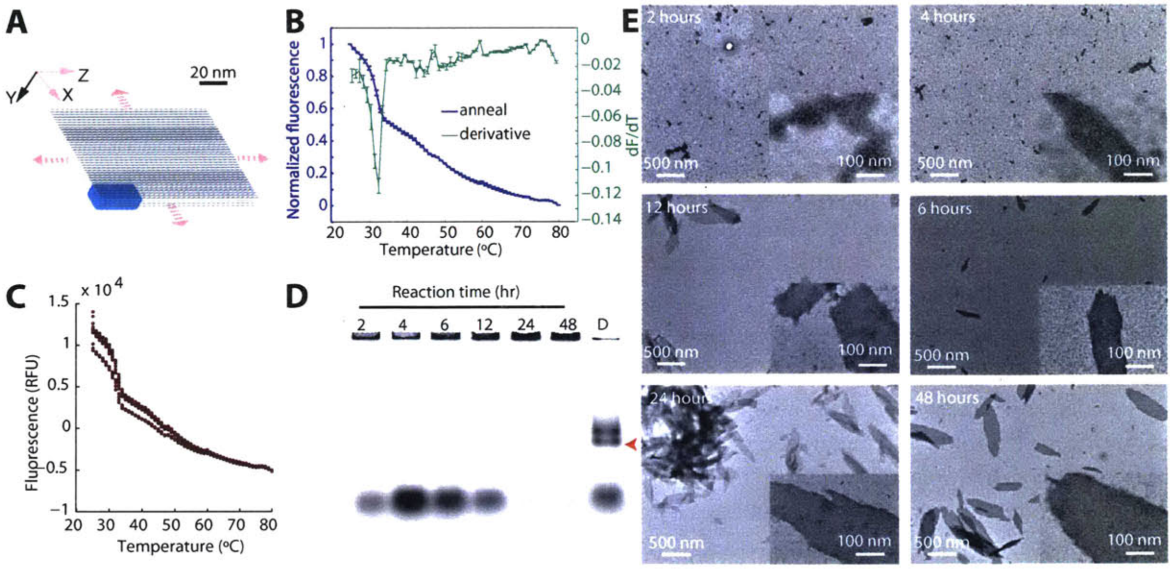

Figure 3-9: Isothermal assembly and time-lapse analysis of the ZX-6H×4H×96B crystal. **(A)** Schematic of the ZX-6H×4H×96B crystal. **(B)** Normalized and averaged annealing curve (blue) of the ZX-6H×4H×96B crystal obtained over a 3-day anneal. These signals were normalized to fluorescence at 25°C and 80°C and averaged. **(C)** Raw annealing curves of ZX-6H×4H×96B crystal obtained over a 3-day anneal and used for calculating **B**. 500 nM of each strand was folded in the presence of 0.3× SYBR Green I. **(D)** 1.5% agarose gel electrophoresis was performed on samples taken at different times after the reaction was initiated for a 33°C isothermal annealing protocol. Red arrow denotes the location of the band for a discrete 6H×4H×96B cuboid. **(E)** TEM images of the time-lapse samples obtained in **D**. Insets depict zoomed-in images of the observed structure.

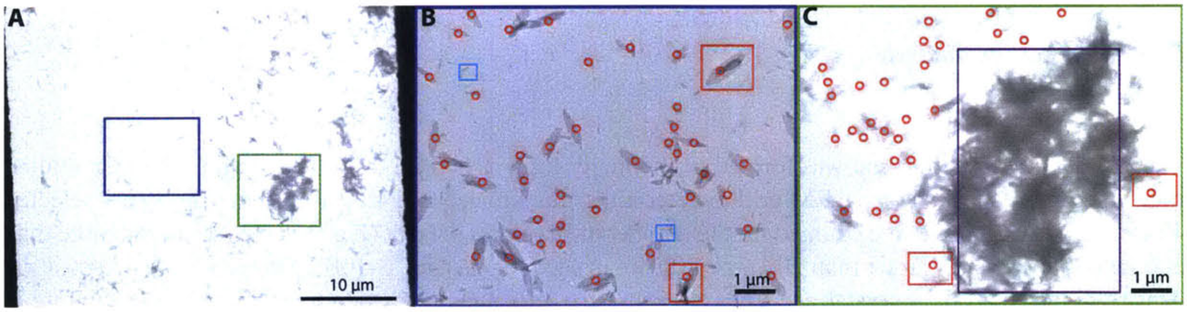

Figure 3-10: Deposition density analysis of the ZX-6H×4H×96B crystal. **(A)** Large-field-of-view TEM images of the ZX-6H×4H×96B crystal assembled under isothermal conditions at 33°C for 48 hours. The sample was diluted four times before deposition on TEM grids. **(B)** Zoomed-in view of the inset outlined in blue in **A**. Each red circle indicates one counted crystal. The crystal structures that appeared smaller than 200 nm×100 nm, such as those outlined in light blue, were not counted. Aggregation prevents accurate counting of the crystals on the surface. A few structures were stacked (e.g. those outlined in red), and each stack of crystals was counted only as one crystal. **(C)** Zoomed-in view of the inset outlined in green in **A** showing how structures were counted when there was heavy aggregation. The main aggregate, outlined in purple, was excluded from counting. Some smaller clear structures on the edges were counted (red).

Strand depletion analysis

Another metric to estimate the formation yield is the brick strand depletion ratio. We labeled strands with fluorescein (FAM) and rhodamine (TAM) on two neighboring helices in a ZX-6H×6H×64B crystal for Förster Resonance Energy Transfer (FRET) experiments (Fig. 3-11). A discrete 6H×6H×64B cuboid (see fig. S75 for strand diagram) and the ZX-6H×6H×64B cuboid crystal was labelled with both FAM and TAM labels or just the FAM or TAM label (Fig. 3-11A,C). In our case, the FAM label is the donor dye (D), while the TAM label is the acceptor (A).

FRET efficiency measurement using the discrete cuboid. We first measured the FRET efficiency using the discrete cuboid (Fig. 3-11A). 2% gel electrophoresis was performed on the discrete 6H×6H×64B cuboid and scanned in the donor channel (Fig. 3-11B). The intensity of the band was measured for each of the samples. The FRET quenching efficiency of this structure was estimated by applying these intensities to the equation: $E = 1 - \frac{I_{DA} - I_A}{I_D}$, where I represents the intensity at the donor wavelength. Note that the FRET efficiency calculated here assumes that in the dual-labeled sample every structure with a donor dye also contains the acceptor dye. Additionally, it is assumed that the background acceptor leakage observed in the dual-labelled structure has the same intensity value as the structure with the acceptor only. The FRET efficiency is measured to be 89%.

Bulk fluorescence quenching of the brick crystal. We next measured fluorescence quenching on the ZX-6H×6H×64B cuboid crystal (Fig. 3-11D). The raw fluorescence signals were normalized as follows: $\frac{F_D}{F_{D,80^oC}}$ for the sample containing donor dye only and $\frac{F_{DA} - F_A}{F_{DA,80^oC} - F_{A,80C}}$ for the sample with both labels (Fig. 3-11E). Here, F_A represents the raw fluorescent signal from the sample containing TAM and the signal was normalized to that at 80°C. These normalized signals were then used to calculate the percentage of quenching: $Q = 1 - \frac{F_{DA}}{F_D}$ (Fig. 3-11F). The final sample quenching was found to be 71%.

Strand depletion ratio. By assuming that the bulk fluorescence quenching observed on the crystals is due only to FRET quenching, we can approximate the strand deletion ratio by $Y = \frac{Q}{E}$, where Q is the bulk quenching and E is the FRET efficiency. Using this method, the estimated strand depletion ratio for the brick crystal is 80%. Note that this measurement likely represents an overestimate for the crystal formation yield because it does not account for potential quenching between the dye pairs on different repeating units or any quenching observed from random strand aggregation instead of the target structure formation.

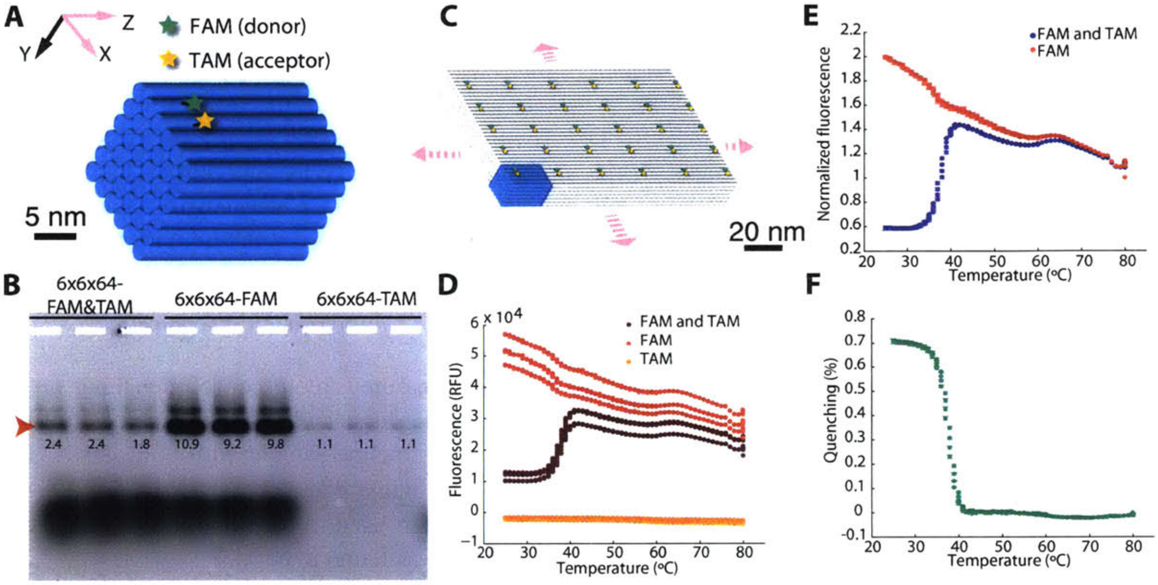

Figure 3-11: Strand depletion analysis of the ZX-6H×6H×64B cuboid crystal. **(A)** Schematic of the 6H×6H×64B cuboid with the locations of the donor and acceptor dye labels denoted by the stars. The green star represents the donor FAM dye and the yellow star represents the acceptor TAM dye. **(B)** 2% gel electrophoresis of the 6H×6H×64B cuboid assembled for 3 days at 100 nM per strand with the presence of both donor and acceptor labels, donor only, or acceptor only. The gel was not stained and scanned using the donor channel only. The red arrow points to the location of the folded structure, and the values below denote the measured intensity of that band. **(C)** Schematic of the ZX-6H×6H×64B cuboid crystal with the locations of the donor and acceptor dyes labeled. Because the ZX-crystal uses a repeating unit that is the same size as the discrete cuboid structure, the relative locations of the dye labels are the same on each monomer. **(D)** Raw donor fluorescence signals of the ZX-crystal assembled at 100 nM per strand for 3 days in the presence of donor and acceptor labels, donor only, or acceptor only. **(E)** Normalized fluorescent signal in the donor channel of the ZX-crystal. The acceptor signal is subtracted for the traces with both labels. All traces are normalized to the signal at 80°C. **(F)** The percentage of quenching observed from the dual-labeled structure relative to that with the donor only labeled structure from **e**. N = 3. Error bars represent standard deviation from the mean.

Defect analysis

To roughly determine the quality of the crystals, we counted the number of defective pores in a XY-32H×64B-pore crystal (Fig. 3-12). A pore was considered defective if it was either missing from its expected location or was enlarged by 2 nm or more than 10% of the designed dimensions (see examples in figure 3-12D). A 9% defect rate of the pores in the XY-32H×64B-pore crystal was observed. The enlarged pores could be caused by missing strands in the structure. Additionally, the crystal surface is often observed to be rather rough, possibly as a result of stacking between structures or non-specific sticking of other strands. From the images, it appeared that such non-specific interactions caused certain materials/structures to adhere on the surface of the crystal and thus fill or block the designed pores. As a result, our estimated defect rate is likely an overestimate due to debris adhering to the crystal surface causing false positives in the analysis.

3.4.8 Patterning gold nanoparticles

Gold nanoparticles have been previously arranged into discrete patterns [86, 160, 164] and single-layer periodic patterns [156] using DNA structures as templates. However, it remains challenging to form close-packed periodic patterns, especially multi-layer patterns, of gold nanoparticles. This challenge is addressed here using DNA crystals. We constructed two close-packed gold nanoparticle superstructures on DNA brick crystals: (1) parallel lines of gold particles arranged on a ZX-4H×6H×96-channel crystal (fig. S44) spaced on average 2 nm apart (Fig. 3-13A, B), and (2) parallel gold-nanoparticle monolayers, with each particle spaced on average 1 to 2 nm apart, on an XY-4H×4H×64-cuboid (Fig. 3-13C-E).

The design and TEM images of the ZX-4H×6H×96-channel crystal is shown in figs. S44 and S76. A channel is two-helix (5 nanometers) in depth, and 32-bp (10.6 nanometers) in width. Neighboring parallel channels are separated by 64-bp (21.2 nm) distance along the Z-axis. Gold nanoparticles functionalized with poly-A (ten consecutive adenine bases) DNA strands were arranged on the DNA crystals. Within the channels, every helix-end displays a poly-T (ten consecutive thymidine bases) single-stranded DNA for capturing gold nanoparticles. Gold nanoparticles were successfully arranged into parallel lines consistent with our design. Within each line, a single chain of close-packed gold nanoparticles was observed. The average distance between particles with a line is about 2 nanometers, except for some locations with clear defects (Fig. 3-13B).

Two parallel gold-nanoparticle monolayers were assembled on the XY-4H×4H×64-cuboid crystal in Fig. 3-4C. The crystals display poly-T sequences at each helix-end on both surfaces for capturing 10-nanometer gold nanoparticles functionalized with poly-A strands (Fig. 3-13D, inset). The average distance between particles appeared to be about 1 to 2 nanometers (Fig. 3-13D). The structures sometimes curved on the edges (Fig. 3-13E). The edge-to-edge distance between the two monolayers of gold nanoparticles were measured to be about 25 nm, consistent with the designed crystal thickness.

Aligning gold nanoparticles into micron-scale ordered arrays is required in diverse plasmonic applications. In particular, nanoparticle arrays with sub-2-nm face-to-face spacing are expected to exhibit strong plasmonic coupling [165]. With DNA nanostructures as templates, gold nanoparticles have been arranged into chiral[86], linear[95, 166], and branched patterns[167, 168]. However, most of these structures are discrete sub-100 nm structures, which lack long-range ordering at the micron scale. In addition, decreasing the interparticle spacing down to 2 nm is also challenging. DNA crystals provide a unique solution towards these challenges. By varying the surface distribution of poly-T binding sites, gold nanoparticles were programmed with different 2D patterns at micron scale, from close-packing patterns to arrays of gold nanoparticle chains with 20-nm inter-chain spacing. The periodicity of poly-T binding sites is 2.5 nm on

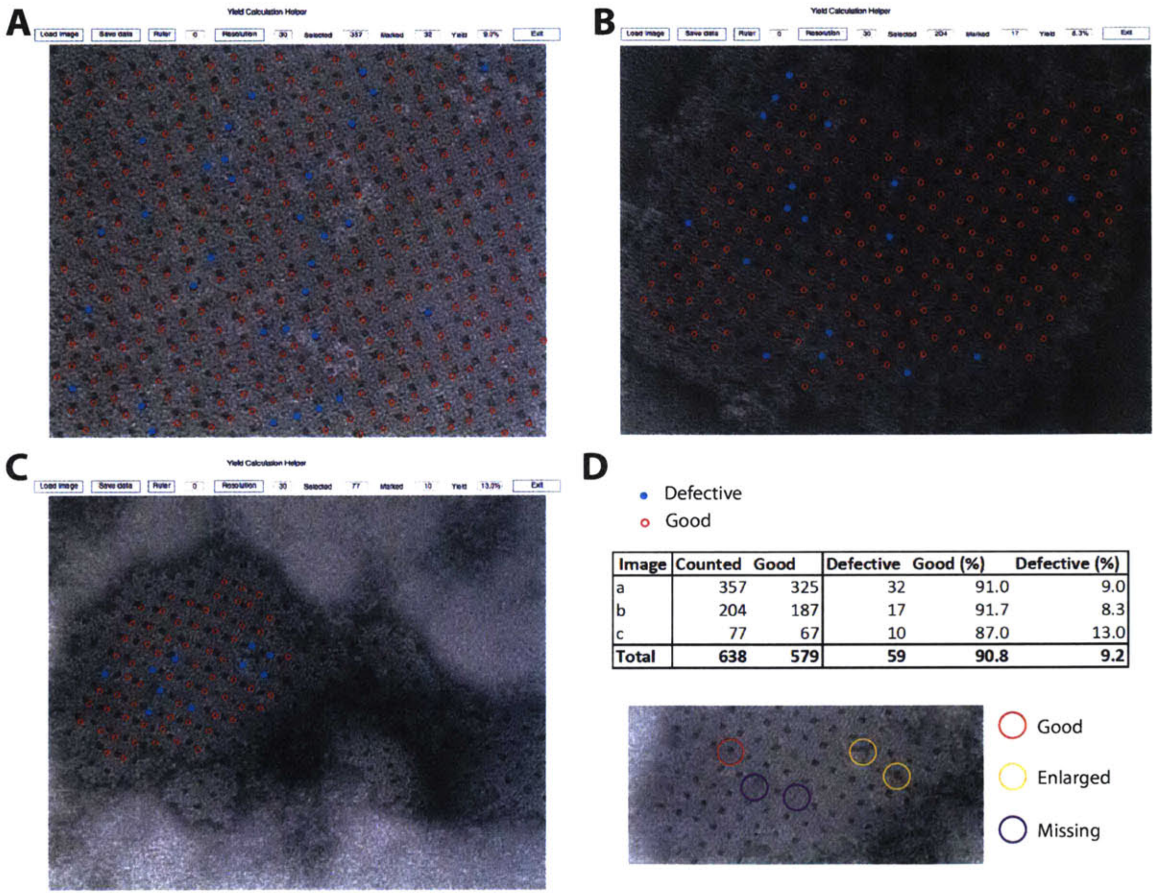
A
Yield Calculation Helper
Load image
Save data
Ruler
Resolution
Exit
B
Yield Calculation Helper
Load image
Save data
Ruler
Resolution
Exit
C
Yield Calculation Helper
Load image
Save data
Ruler
Resolution
Exit
D
● Defective
○ Good
Good
Enlarged
Missing

A: Ruler 0 Resolution 30 Selected 357 Marked 32 Yield 9.0%

B: Ruler 0 Resolution 30 Selected 204 Marked 17 Yield 8.3%

C: Ruler 0 Resolution 30 Selected 77 Marked 10 Yield 13.0%

Image	Counted	Good	Defective	Good (%)	Defective (%)
a	357	325	32	91.0	9.0
b	204	187	17	91.7	8.3
c	77	67	10	87.0	13.0
Total	**638**	**579**	**59**	**90.8**	**9.2**

Figure 3-12: Defect analysis of the XY-32H×64B-pore crystal. Pores in the XY-32H×64B-pore crystal were counted and categorized to be either "present/good" or "missing/defective" depending on whether the TEM images showed a pore of approximately the correct dimensions and in the correct location **(A-C)**. Present pores are marked with a red circle, while the defective ones are indicated with a blue-filled red circle. **(D)** Analysis statistics and methodology. A total of 638 pores were counted, and 91% of them are "good". The image shows how the pores were categorized as either good (red) or defective (enlarged pores [yellow] or missing pores [purple]).

DNA crystals, which produced an inter-particle spacing around 2 nm.

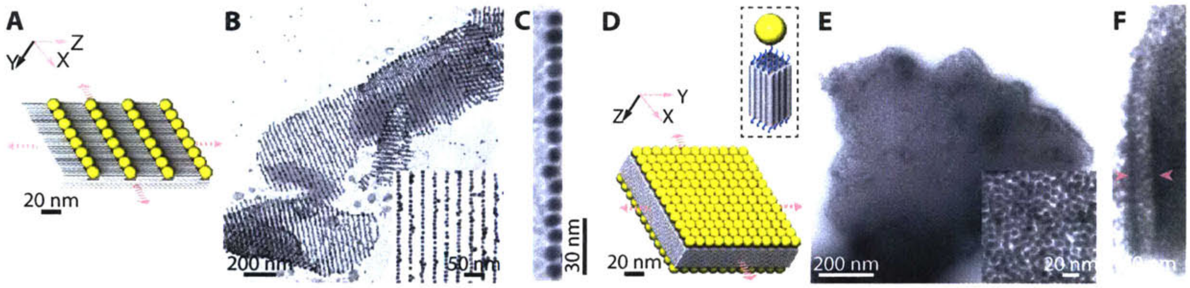

Figure 3-13: Gold nanoparticles patterned using DNA brick crystals. **A** to **C**, Model (**A**) and TEM images (**B, C**) of parallel lines of 10-nanometer gold nanoparticles closely packed on a ZX-4H×6H×96-channel crystal. (**C**), Zoomed-in TEM image of a single chain of gold nanoparticles. **D** to **e**, Model (**D**) and TEM images (**E, F**) of close-packed gold nanoparticle monolayers formed on the top and bottom surfaces of an XY-4H×4H×64B-cuboid crystal. Inset shows the single-stranded poly-T extensions on each end of the helix and a 10 nm gold nano particle occupying a 4H×4H surface. **F**, A crystal displays curvatures on the edge. Pink arrows indicate the curved positions where the two gold nanoparticle monolayers can be seen.

3.5 Discussion

Crystallization of increasingly large macromolecular complexes can be challenging. Traditionally the process is hierarchical, i.e. the complexes incorporate into the crystal as pre-formed monomeric units [20, 24–26, 30, 33, 34, 155–159]. However, the homogeneity of complex monomers is often difficult to ensure, and the addition of a defective monomer can compromise the growth of a well-ordered crystal. Furthermore, the kinetics of joining large monomers can be slow because of their size, especially in the case when they repel each other due to like charges. Finally, effective crystallization is thought to require error correction that involves near-equilibrium incorporation and dissociation of monomers to erase defects on the path to the lowest energy state. Therefore, if the strength of the interaction between monomers is too strong, which is more likely for large structures, irreversible rather than reversible self-assembly may dominate, resulting in defective crystals.

In contrast, our DNA brick framework explores a non-hierarchical route to crystallization that achieves reversible assembly of rapidly diffusing subcomponents without sacrificing the complexity of the larger repeating unit in the final crystals. Using a modular strategy that utilizes standardized components – such as our DNA bricks – a repeating unit can contain thousands of base pairs, enabling the implementation of designs bearing intricate features. Although we define a repeating unit for ease of design, there is no difference between bricks within each repeating unit and those that connect the repeating units, hence bricks can be added to or subtracted from the growing crystal one at a time. A corollary is that the boundary where one repeating unit begins and the next one ends is arbitrary.

Microscale two-dimensional DNA brick crystals with prescribed depth and three-dimensional nanoscale features provide a new platform for developing diverse applications. In biophysics, host-guest two-dimensional DNA crystals could facilitate cryo-electron microscopic imaging and 3D reconstruction of protein structures [105]. Thicker two-dimensional crystals are more rigid and resistant to dynamic thermal fluctuations, providing better translational alignment of proteins; their 3D cavities could potentially hold the guest molecule in a specific conformation, providing better orientational alignment within each unit cell. In photovoltaics, bottom-up self-assembly of nanomaterials, such as nanowires [169], provides a promising route to producing high efficiency photovoltaic devices. DNA brick crystals may prove useful for self-assembling 3D nanomaterials with nanometer precision, thus achieving enhanced cooperation effects and energy conversion efficiency for photovoltaic devices. In nanofabrication, these two-dimensional DNA crystals may serve as etching masks for fabricating diverse inorganic materials based devices and circuits, providing better shape programmability than current block copolymer based masks [149].

3.6 Acknowledgments

This work is supported by an ONR Young Investigator Program Award N000141110914, ONR Grants N000141010827, N000141410610, N000141310593, an ARO Grant W911NF1210238, an NSF CAREER Award CCF1054898, an NSF Expedition in Computing Award CCF1317291, NSF Grants CCF1162459, CMMI1333215, CMMI1334109, CMMI1344915, an NIH Director's New Innovator Award 1DP2OD007292, and a Wyss Institute Faculty Startup Fund to Peng Yin, and by a Wyss Institute Faculty Grant, ARO MURI grant W911NF1210420, ONR Grants N000014091118 and N000141010241, and an NIH Director's New Innovator Award 1DP2OD004641 to William Shih. Luvena Ong is supported by a NSF Graduate Research Fellowship. Jie Song acknowledges AUFF founding from Aarhus University and Niels Bohr Foundation from The Royal Danish Academy of Science. Mingdong Dong acknowledges financial support from the Danish National Research Foundation, and the Villum Foundation.

3.7 Author contributions

Yonggang Ke, Wei Sun, and I equally contributed to the work described in this chapter. Yonggang Ke conceived of this project and contributed to the design of all the crystals. Wei Sun performed the experiments involving deposition density, isothermal assembly and gold-nanoparticle patterning demonstrated in figures 3-10, 3-9, and 3-13. Jie Song obtained the cryo-EM and AFM images in figures 3-14 and 3-15.

3.8 Supplementary Materials

Select supplementary data are included below. Strand diagrams, gel electrophoresis analysis, and cited supplementary figures can be found online at `http://www.nature.com/doifinder/10.1038/nchem.2083`.

3.8.1 Cryo-EM images of the XY-32H×64B-pore crystal and the XY-32H×128B-pore crystal

Cryo-EM images and 3D reconstruction date analysis of the 32H×64B-pore crystal (figs. 3-14A and 3-14C) and the 32H×128B-pore crystal samples (figs. 3-14B and 3-14D). The crystal samples were frozen in amorphous ice for imaging. 3D reconstruction was performed after data collection, and three planes (XY, XZ, YZ) were extracted from 3D reconstruction date for measurement of crystal thickness. The depths of the 32H×64B-pore crystal and the 32H×128B-pore crystal were measured to be 26×2 nm and 45±3 nm, respectively. These values were slightly larger than the theoretical values of the two crystals (21 nm and 42 nm, respectively). This is likely due to the fact that the theoretical estimations of crystal depths did not take the single-stranded poly-T (at the $5'$ and $3'$ ends of each duplex) into consideration.

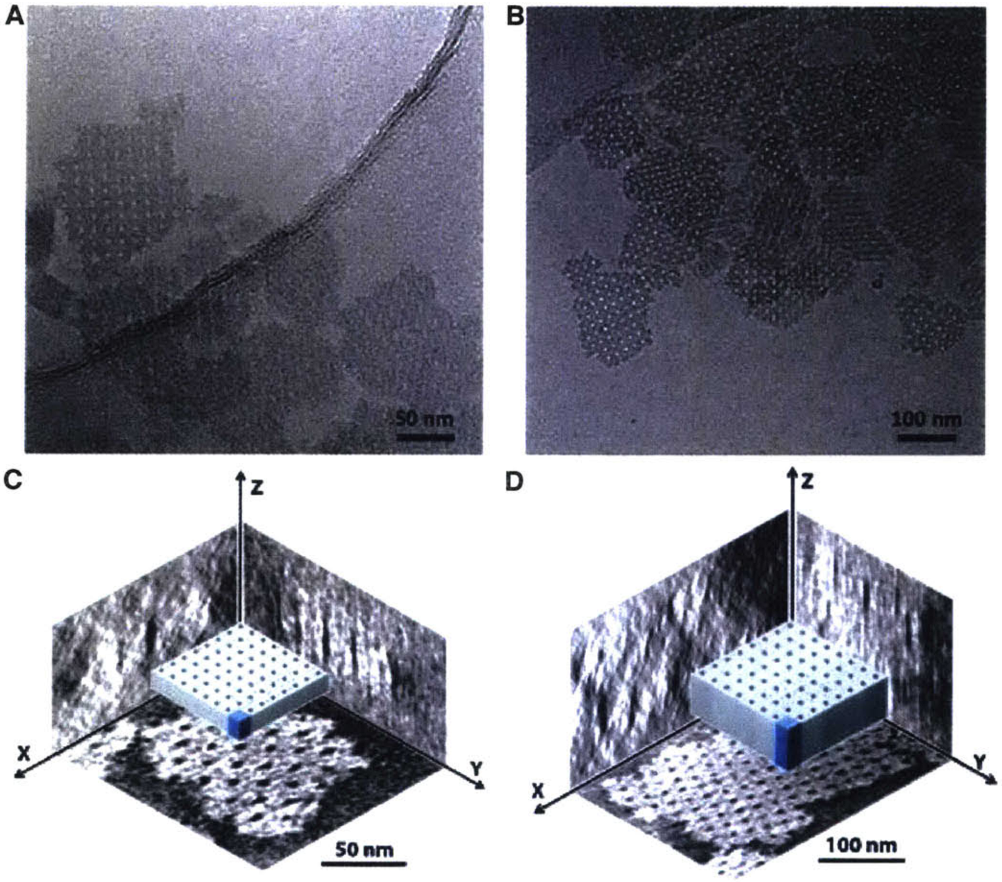

Figure 3-14: Cryo-EM images of the XY-32H×64B-pore crystal and the XY-32H×128B-pore crystal **(A)** A representative Cryo-EM image of the XY-32H×64B-pore crystal. **(B)** A representative Cryo-EM image of the XY-32H×128B-pore crystal. **(C)** Cryo-EM 3D reconstruction images showing the three projection views of a single XY-32H×64B-pore crystal. The 3D model is used to approximately denote the projection views of the crystal. **(D)** Cryo-EM 3D reconstruction images showing the three projection views of a single XY-32H×128B-pore crystal. The 3D model is used to approximately denote the projection views of the crystal.

3.8.2 AFM images of the XY-32H×64B-pore crystal and the XY-32H×128B-pore crystal

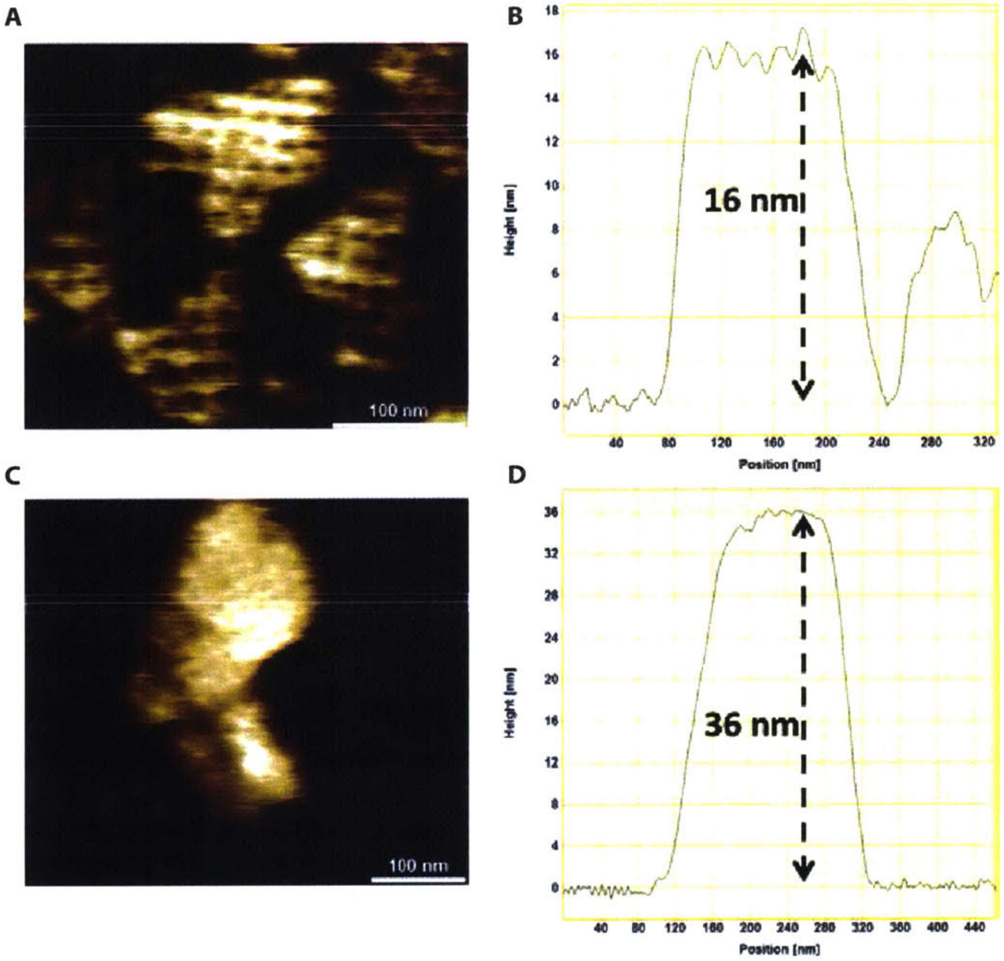

Figure 3-15: AFM images of the XY-32H×64B-pore crystal and the XY-32H×128B-pore crystal (A) A representative AFM image of the XY-32H×64B-pore crystal. **(B)** Height-profile shows the depth of the XY-32H×64B-pore crystal. **(C)** A representative AFM image of the XY-32H×128B-pore crystal. **(D)** Height-profile shows the depth of the XY-32H×128B-pore crystal.

CHAPTER 4

Towards large scale DNA assemblies

In the previous chapters, we demonstrated the assembly of complex 3D discrete and periodic DNA nanostructures using the 8 nucleotide (nt) DNA brick approach. While we are able to extend our patterning capabilities to cover surfaces of over 1 micron in size, our addressability remains limited to the size of the unique building block. In this chapter we focus on developing and optimizing a modified version of the DNA bricks that enables us to create patterns uniquely over 100 nanometers in all three dimensions.

4.1 Abstract

DNA self-assembly provides an effective "bottom-up" approach for producing complex user-prescribed nanostructures. In 2006, DNA origami brought bottom-up nanotechnology from the kilodalton scale to the megadalton scale by enabling practical construction of fully addressable megadalton-size nanostructures (typically 5 megadalton using an M13 virus scaffold, composed of $\sim$200 unique strands totaling $\sim$15,000 nucleotides). Using a new DNA brick motif, we report here practical construction of gigadalton-size nanostructures using commercially available, unpurified short DNA strands through simple one-pot isothermal reaction, and demonstrate a fully addressable 0.5 gigadalton cuboid (100 times larger and more complex than DNA origami). The structure is self-assembled from over 30,000 unique components (i.e. DNA strands), and contains 1.7 million nucleotides (comparable to the entire genome of a simple bacteria). We also demonstrate one-pot assembly of a 1 gigadalton tetramer cuboid composed of four identical 262-megadalton cuboid monomers. Such addressability across scales enables even more intricate patterning to be encoded within our structures, which we show through the assembly of complex cavity structures using these super massive canvases. DNA bricks thus help bring bottom-up nanotechnology and synthetic molecular self-assembly from megadalton scale to gigadalton scale by enabling the construction of complex discrete 3D gigadalton nanostructures with user-specified dimensions and shapes.

4.2 Introduction

The emergence of unique properties and interesting and useful phenomena at the nanoscale motivates the development of technologies to more precisely manipulate materials at such small scale. "Top-down" approaches such as lithography [146] can successfully manufacture objects with nanoscale features, but typically have limited throughput, require multiple steps, and often have limited resolution along the vertical axis [149]. "Bottom-up" methods such as molecular self-assembly where inter- or intra-molecular interactions specify the overall final structure, have arisen as promising alternative approaches to create high-resolution features in a parallel, high throughput manner [148].

DNA self-assembly has been of particular interest due to the programmability and addressability of the structure. By specifying suitable complementarity between strand segments, diverse structures have been assembled, including discrete 2D [48, 64, 154] and 3D structures [49, 51, 54, 55, 131, 154], wireframe polyhedra [18, 35, 38–40, 60, 170], 1D ribbons [24] and tubes [24, 30, 68, 156], algorithmic [33] and periodic 2D lattices [17, 20, 41, 114, 171, 172], depth-defined 2D crystals [144], and 3D crystals [34].

A perpetual challenge in bottom up nanotechnology has been creating fully addressable discrete structures with ever-increasing complexity. Scaffolded DNA origami represents a major landmark as the first practical method to construct discrete structures with complex user-prescribed shapes on the megadalton (MDa) scale [48, 49, 51, 54, 55, 61, 126, 153, 154]. These structures are typically constructed using an M13 virus scaffold strand and ~200 short synthetic DNA staple strands (approximately 5 megadalton in total mass), which are programmed to self-assemble into controlled patterns across 100 nm in two dimensions or ~20 nm in three dimensions. While typical M13 DNA origami has a mass of ~5 MDa, 2D DNA origami structures composed of non-repetitive components and with masses as large as 33 MDa [173] have been reported. Additionally, fully addressible 2D structures as large as 44 MDa have been produced by reusing origami monomers and assembling hierarchically via multiple steps, and symmetric 3D prism structures with 60 MDa mass were produced in one pot reaction by hierarchical assembly of twelve 5 MDa origami tripod monomers [58–61, 174, 175].

A number of challenges arise to further scale up DNA structures. While 2D DNA origami larger than the typical 5 MDa structures (e.g. 33 MDa [173]) have been created, generating these longer scaffolds is still practically difficult [173, 176–178], Notably, these longer scaffold strand based methods have not been used to construct 3D objects, which may both reflect the relatively early development stage of the methods, but possibly also the difficulty to fold a very long scaffold strand into complex 3D rather than 2D patterns.

In our previous work, we reported a method to bypass the scaffold synthesis and folding challenge: in the DNA brick method, hundreds of short DNA brick strands (each composed of four concatenated 8-nt binding domains) self-assemble into complex 2D [64] and 3D shapes [131] without the assistance of a central organizational scaffold. Because these DNA brick structures are entirely composed of short DNA strands that can be chemically synthesized, commercially purchased, and used without purification or careful adjustment of stoichiometry, this approach in principle offers more potential for facile scaling up. However, DNA bricks face alternative challenges for scaling up. In particular, increased system complexity will result in a massive number of component species, which could cause undesired spurious interactions to result in partially assembled structures rather than complete products. Additionally, as the strands will assemble at necessarily lowered concentration per species (due to the increased number of components) with reduced incorporation speed, the overall yield could be substantially decreased. In practice, reported 3D DNA brick assembly has only generated structures up to 8 MDa in size [131]. Lower yields and increased portions of unincorporated strands were observed during assembly of larger DNA brick structures.

Here, we used a non-canonical DNA brick motif composed of four 13-nt binding domains to address challenges in assembling large, fully addressable DNA structures that contain a massive number of distinct component strands (e.g. over 10,000 species). Compared with our previous 8-nt domain bricks, the new 13-nt bricks have substantially increased sequence diversity (see figure 4-1 for detailed analysis of sequence design space) and binding strength, and thus should facilitate sustained growth kinetics and assembly yield when a large number of unique components are required to interact and assemble in one-pot, and the concentration of each component species is necessarily lowered. In practice, in one-pot isothermal assembly (Table 4-2), massive discrete 3D structures with prescribed size and shape were constructed. For example, a cuboid was assembled from 33,511 unique DNA brick strands, contained ~1.7 million nucleotides (comparable to the size of an entire genome of some simple bacteria [179]), and had a mass of ~0.54 gigadalton (GDa), which is 100 times larger than M13 DNA origami. Additionally, a 1 GDa tessellation structure was assembled from four identical 262 MDa cuboids. With these larger canvases, we are also capable of assembling more complex shapes. We have developed a software that enable facile design of these large-scale structures to sequence import. Further, we have demonstrated the successful assembly of XYZ different complex 3D structures

By enabling the practical construction of gigadalton sized discrete 3D structures with user specified dimensions and shapes, DNA bricks represent a 100-fold "leap" in complexity compared to current 3D origami structures, and thus help bring bottom-up nanotechnology and synthetic biomolecular self-assembly from megadalton scale to gigadalton scale.

4.2.1 Sequence space

We wanted to analyze the sequence uniqueness of structures formed using randomly assigned domains. For the 8-nt design, we have a total of $\frac{4^8-4^4}{2}+4^4=32,896$ unique domains. The 4^4 subtraction results from the presence of palindromic sequences. In contrast, 13-nt designs have a total of $\frac{4^{13}}{2}=33,554,432$ unique domains. To compare the sequence design space of the different motifs, we applied the birthday paradox theory to estimate the probability of encountering a single match when a certain number of domains are used (Fig. 4-1A, eq. 4.1). For this calculation, we assume that the frequency differences for the 8-nt domains are negligible. From our estimates, we find that the 8-nt domains reach a 50% probability of having a match when structures are sized at roughly 200 domains. This limit is at roughly 6,500 domains for 13-nt brick structures.

$$p(N)=1-e^{\frac{-N^2}{2d}} \tag{4.1}$$

We additionally simulated random sequences and analyzed the number of matches for structures of different sizes. We tested 1000 simulations for structures of each size to obtain averages and standard deviations (Fig. 4-1B). We found that out of 1400 randomly domains assigned (the size of the largest previously published 8-nt brick structure) would contain on average 30 repeated domains. In contrast, 13-nt domains would contain on average no repeated domains. A 0.5 GDa 13-nt brick structure would contain 60 repeats. For all of these situations, the fraction of repeats of the total domains used comprise of less than 1% of the total number of domains in the structure. Structures assembled using the 13-nt approach can contain over 8000 domains before an average of one repeat is encountered, substantially expanding the sequence design space.

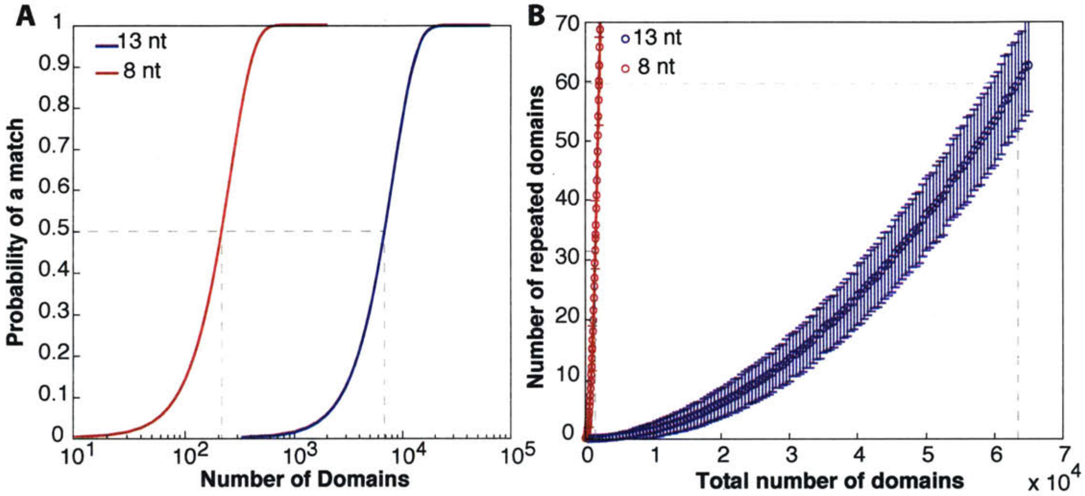

Figure 4-1: Domain sequence match analysis for varying numbers of randomly assigned domains. (A) Estimated probabilities of achieving at least a single matching domain given a specified number of random domains. Grey dotted lines highlight the number of domains necessary to reach a 50% probability of having a match. **(B)** Simulated averages of total number of domains with repeated sequences, n = 1,000. Error bars represent standard deviation. Grey lines denote the largest fully addressable structures formed using 8-nt and 13-nt domains. The largest structure formed using 8-nt domains contained a total of 1,440 domains, which confers to roughly 30 reused sequences. The largest number of 13-nt domains used was 63,480 unique domains, which has roughly 60 matches.

4.2.2 Thermodynamic analysis of brick interaction

We wanted to better understand the underlying thermodynamic and kinetics of the brick interactions. We used the nearest-neighbor models to study the energy of the binding interaction of two brick strands. By estimating an average base-stacking energy, we can calculate and estimate the melting temperature. From SantaLucia and Hicks, we find that the average $\Delta H_{bs} = -8.2$, $\Delta H_{init} = 0.2$, $\Delta H_{sym} = 2.2$, $\Delta H_{dangles} = -2.5$, $\Delta S_{bs} = -22$, $\Delta S_{init} = -5.7$, $\Delta S_{sym} = 6.9$, and $\Delta S_{dangles} = 6.9$ [15]. These average values of ΔH are in units of kcal/mol, while ΔS is in cal/mol. We can then use equation 4.2 to calculate the average ΔG for a hybridization, where n is the number of base-stacks present.

$$\Delta G = n\Delta H_{bs} + \Delta H_{init} + \Delta H_{sym} + 3\Delta H_{dangles} - T(n\Delta S_{bs} + \Delta S_{init} + \Delta S_{sym} + 3\Delta S_{dangles} + \Delta S_{salt}) \tag{4.2}$$

where

$$\Delta S_{salt} = 0.368n\ ln([Na^{+}] + 3.3\sqrt{[Mg^{2+}]}) \tag{4.3}$$

We can estimate the melting temperatures in Celcius of these structures by equation 4.4.

$$T_m = \frac{1000\Delta H}{\Delta S + R\ ln([strands]/4)} - 273.15 \tag{4.4}$$

Various domain lengths and their energies are listed in table 4-1. Melting temperatures are estimated at 5 nM strand concentration. Generally, we observe that the melting temperatures of 8-bp of hybridization is far below that of 13-bp and 18.5-bp (basically the average of the 18.5-nt domain). Additionally, the melting temperature differences between two hybridized domains and one hybridized domain is roughly 10°C higher for the 8-nt domains than for the 13-nt domains. As the domain lengths increase, the melting temperature differences between two versus one hybridized domains shrinks. Previous models of the DNA brick system have suggested that the nucleation barrier for assembly is composed of structures where each monomer contains two hybridized domains [180]. This additional 5 bp of hybridization from 8-nt to 13-nt would increase the stability of the interaction by approximately 10 kcal/mol to allow for more stable formation and interaction at low component concentrations (table 4-1).

4.2.3 Brick design

This modular DNA-brick approach enables fast, facile design of structures with custom-prescribed sizes and shapes. Our computer program allowed us to quickly design structures that contain millions of nucleotides. When incorporated in a structure, our DNA brick adopts a U-shape arrangement with four binding domains distributed evenly across two anti-parallel helices connected by a single crossover. Each DNA brick interacts with an adjacent DNA brick through one binding domain via Watson-Crick base-pairing (Fig. 4-10B, 4-2). This 13-bp duplex confers roughly 1.25 turns of the helix and a 90° dihedral angle between two strands (Fig. 4-2B).

Hybridization Length	$MgCl_2$ **(mM)**	ΔH **(kcal/mol)**	ΔS **(e.u.)**	T_m(°C) **@5 nM**	T_m **(°C) @100 nM**
8	40	-62.5	-175.8	16.9	25.1
16	40	-128.1	-352.0	53.0	58.1
13	20	-103.5	-287.0	42.6	48.4
26	20	-210.1	- 576.7	67.1	70.4
13	40	-103.5	- 285.5	44.1	50
26	40	-210.1	- 573.5	68.9	72.2
18.5	40	-148.6	-407.4	58.5	62.9
37	40	-300.3	-817.2	76.9	76.9

Table 4-1: Average melting temperatures at 5 nM strand concentration and energies. Values derived from the SantaLucia and calculations are performed following equations 4.2 – 4.4.

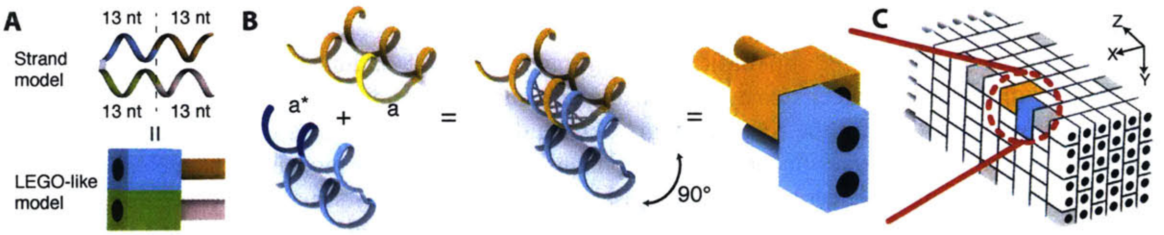

Figure 4-2: Detailed schematic for the 13-nt domain brick structure. (A) The top panel shows a strand model for the basic component of the structure. Each brick can be divided into 13-nt domains. A Lego-like model is shown in the bottom panel with corresponding colors to match the strand model. **(B)** Two strands interact via hybridization of 13 base pairs, marked by complementary domains a and a*, to form a 90° dihedral angle. **(C)** DNA brick model of a 6H × 6H × 91B cuboid with a pair of interacting bricks highlighted.

4.3 Materials and Methods

Sample preparation

Chemically synthesized DNA oligomers were purchased from Integrated DNA Technologies, inc (www.idtdna.com). Strands were adjusted to concentrations of 2–100 nM per strand in 0.5×TE buffer (5 mM Tris, pH 8, 1 mM EDTA) containing 10 – 80 mM $MgCl_2$. For some of the larger structures, strands were evaporated using the vacuum centrifuge (Thermo Scientific, Savant SPD131DDA Speedvac concentrator) before being added to the folding buffer. To anneal the structures, samples were subjected to either a thermal ramp or an isothermal folding protocol. For the 3-day thermal ramp, samples were cooled from 80 to 60°C over 1 hour and from 60 to 25°C over 3 days. For a linear annealing ramp, samples were cooled from 80 to 25°C at the rate of 2 hr/°C. For the isothermal folding, samples were subjected to a denaturation step at 80°C for 10 minutes before being held at the optimal temperature for 5 – 7 days. Cuboids and their optimal folding temperature at 5 nM are listed in Table 4-2. Structures are named by the number of helix (H) × H × base-pairs (B) formed. Optimal temperatures at other strand concentrations can be obtained from the gels shown in figure 4-9. Note that samples were analyzed on the gel immediately after annealing was completed to avoid aggregation of the structures upon cooling.

Structure	**Temperature** (°C)
10H×10H×156B	49.1
14H×14H×208B	50.3
20H×20H×260B	51.4
30H×30H×260B	51.4
36H×36H×312B	50.7
40H×40H×338B	50.7
46H×46H×390B	49.3

Table 4-2: Optimal formation temperature for isothermal assembly of different sized cuboids at 5 nM strand concentration.

Shape design and library preparation

Structures were designed using our in-house Nanobricks software. Oligomers were selected from a library of strands and concentrated to 5 nM per strand in 0.5×TE buffer (5 mM Tris, pH 8, 1 mM EDTA) containing 20 mM $MgCl_2$. Structures were annealed for either 6 or 7 days in a narrow annealing ramp between 52.5° and 51° or isothermally. Structures were characterized using 0.5% agarose gel electrophoresis that was run at 80V for 1 hour at room temperature and 1 hour on an ice water bath.

Agarose gel electrophoresis and purification

Samples were subjected to 0.3-2% agarose gel electrophoresis at 80V for 2 hours on an ice water bath. Gels were prepared with 0.5×TBE buffer containing 10 mM $MgCl_2$ and with a 1:10,000 to a 1:20,000 dilution of SYBR Safe loading dye. Quantification of band intensities and percentages were obtained using the TotalLab Quant v12.2 software with the rubber band background subtraction and detecting a fixed edge width when measuring the signals or manually using ImageJ. Band intensity percentages describe the target band intensity compared to that of the entire lane. Since using this method will consider roughly 70% of the total peak intensity, the reported percentages may be an underestimate of the total amount of target structures present. For purification, target bands were excised and crushed into fine pieces in Freeze 'N Squeeze tubes (Bio-Rad Laboratories, inc.) and centrifuged at 100–250 g for 5–10 minutes. Flow-through was collected and analyzed on the TEM.

TEM imaging

To visualize the samples, 2.5 – 7 μL of purified samples were deposited on glow-discharged, formvar/carbon coated grids (Electron Microscopy Sciences) for 5 minutes. Samples were then stained for 1–60 seconds with 2% uranyl formate solution containing 25 mM NaOH and subsequently imaged using the JEOL JEM-1400 TEM operated at 80 kV.

4.4 Results

Using a new DNA brick design that contains four concatenated 13-nucleotide (nt) domains (fig. 4-2), we demonstrated facile assembly of eight three-dimensional cuboids of increasing scale: 10H (helix) by 10H (helix) by 156B (base pair) cuboid (or 10H×10H×156B for short), 14H×14H×208B, 20H×20H×260B, 30H×30H×260B, 36H×36H×312B, 40H×40H×338B, 46H×46H×390B, and 72H×72H×312B cuboids, which respectively have masses of 10.1, 26.5, 67.6, 152.1, 262.8, 351.8, 536.4, and 1051.2 MDa. The first seven cuboids are uniquely addressable (Fig. 4-10, grey), while the discrete 1 GDa structure is tessellated from a 262.8 MDa cuboid (Fig. 4-10, D to F). As a benchmark for comparison, we designed an 8H×8H×104B DNA origami cuboid using an M13 phage derived p7560 scaffold (Fig. 4-10A, blue).

DNA bricks were computationally designed using a previous algorithm [131] and a custom software package, and purchased commercially as unpurified strands. Structures were then assembled in one-pot reaction isothermally. TEM imaging of native agarose gel purified structures showed expected morphologies (Fig. 4-10A). The 536.4 MDa, 46H×46H×390B cuboid was the largest fully addressable DNA structure demonstrated, over 100 times as massive as an M13-scaffolded DNA origami structure [48]. It contained 33,511 unique strands and measures over 100 nm in length in each dimension.

4.4.1 Design optimization

In a square-lattice DNA structure, a DNA brick contains four single-stranded domains, and two neighboring DNA bricks form a 90° dihedral angle. In B-form DNA duplex, a full helical turn corresponds to 10.5 base pairs. Thus a DNA brick domain should contain roughly $10.5 \times (0.5n + 0.25)$ nucleotides, where n is a non-negative integer. To select an optimal design strategy for massive DNA structure assembly, we tested two new brick designs: (1) 13-nt brick that contains four 13-nt domains, and (2) 18.5-nt brick that contains two 18-nt and two 19-nt domains, and compared them with the canonical DNA brick design composed of four 8-nt domains (referred to as 8-nt brick [131]).

Comparison of 6H×6H×(8-domain) structure with domains of length 8-nt, 13-nt, and 18.5-nt

We tested 3D structures that contain the same number of binding domains to compare assembly efficiencies. Cuboids were designed to have 6H×6H cross-section and measure eight x-bp in length, where $x = \{8, 13, 18.5\}$ is the length of the domain of different bricks to be tested. The cuboids were then assembled from 8-nt DNA bricks, 13-nt DNA bricks, or 18.5-nt DNA bricks in 10–80 mM $MgCl_2$ using a linear annealing ramp and compared for assembly efficiency (Fig. 4-3). After annealing, DNA structures were analyzed on gel electrophoresis. Because the dye intercalation scales with the number of nucleic acids present, the larger 13-nt and 18.5-nt structures showed darker staining. Intensity percentages of the DNA structures were measured by comparing the intensity of the target band with that of the entire lane. The 13-nt brick structures had the highest gel intensity percentages of approximately 30% across all salinities tested. In contrast, the 8-nt structures contained more unreacted monomers. The 18.5-nt brick design with longer domains (and hence stronger inter-domain interactions) did not produce increased band intensity percentages, but instead showed more unwanted products (more aggregation and intermediates) besides target bands, possibly resulting from strand incorporation errors for the 18.5-nt structures due to the presence of truncated oligomers in the unpurified strand pools.

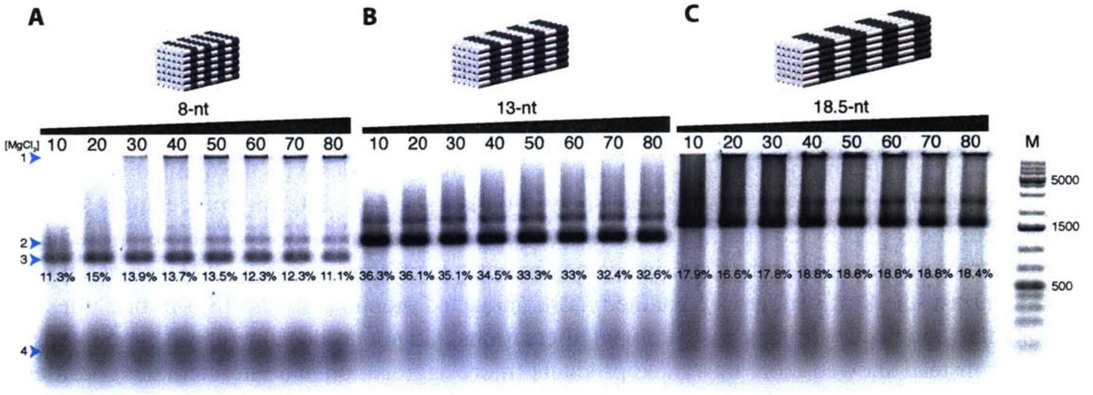

Figure 4-3: Gel electrophoresis of a 6H×6H×(8-domain) structure with domains of length 8-nt, 13-nt, and 18.5-nt. Cylinder models of the structures are depicted in the top panel. The banding pattern distinguishes the different domains along the helical axis. Structures were annealed at 100 nM strand concentration using a linear annealing ramp in the presence of 10–80 mM $MgCl_2$. Samples were assayed on a 2% agarose gel. A 1kb ladder was run on lane M. Blue arrows point to the different types of structures observed: **1** aggregates, **2** dimers, **3** target structure, **4** unreacted bricks. Numbers listed indicate the target band intensity percentages.

Comparison of assembly efficiency across different reaction times

We next compared formation rates between different designs by monitoring intensity percentages of product bands during 72-hour isothermal annealing reactions (Fig. 4-4). We assembled different cuboids using domains of length 8-nt, 13-nt, and 18.5-nt at 100 nM strand concentration. The strand number was controlled by designing structures containing the same number of voxels (6×6×8). Additionally, a 6H×6H×104B cuboid was tested using 8-nt and 13-nt domains. The parameters of each structure assembled is listed in figure 4-4A. Temperature of formation was selected to be at or near the optimal annealing temperature. Agarose gel electrophoresis was used to analyze the band intensity percentages for the different structures at different time points (Fig. 4-4B). In general, the assembly of 8-nt bricks, 13-nt bricks and 18.5-nt bricks all exhibited three distinct phases: (1) a lag period when no product is formed, (2) a rapid increase in target formation, and (3) a plateau in growth near equilibrium.

Cuboids composed of 8-nt bricks with boundary strands [131] and 18.5-nt bricks assembled comparably, while 13-nt brick structures assembled the fastest kinetically and showed highest yields after 72 hours. Structures composed of 13-nt bricks begin to appear starting after 5 minutes of assembly. In contrast, 8-nt and 18.5-nt structures formed comparably, with structures appearing after 10-70 minutes of reaction. The larger 6H×6H×104B 8-nt brick cuboids appeared at 70 minutes, as opposed to 10 minutes required for the smaller 6H×6H×64B 8-nt brick cuboids. In absence of boundary strands, 8-nt brick structures formed rather slowly and inefficiently with structures appearing on the gel after 70 minutes. Although structures appeared starting at 70 minutes, minimal additional assembly was achieved over longer reaction times. Additional analysis to determine the rate of percentage change (i.e. derivative of **(B)**) reveals that structure completion occurs the fastest at the onset of formation and slows down after the initial formation events (Fig. 4-4B). Overall, these studies support our hypothesis of delayed nucleation growth mechanism, with fast growth occurring initially.

A

Marker	Structure	Domain Length(nt)	Number of strands	Boundary strands	$MgCl_2$ (mM)	Temperature (°C)
▲	6Hx6Hx64B	8	189	no	40	29
○	6Hx6Hx64B	8	145	yes	40	34.5
○	6Hx6Hx104B	8	222	yes	40	36.5
○	6Hx6Hx104B	13	189	no	40	53.8
▲	6Hx6Hx104B	13	189	no	20	52
○	6Hx6Hx148B	18/19	189	no	40	65.8

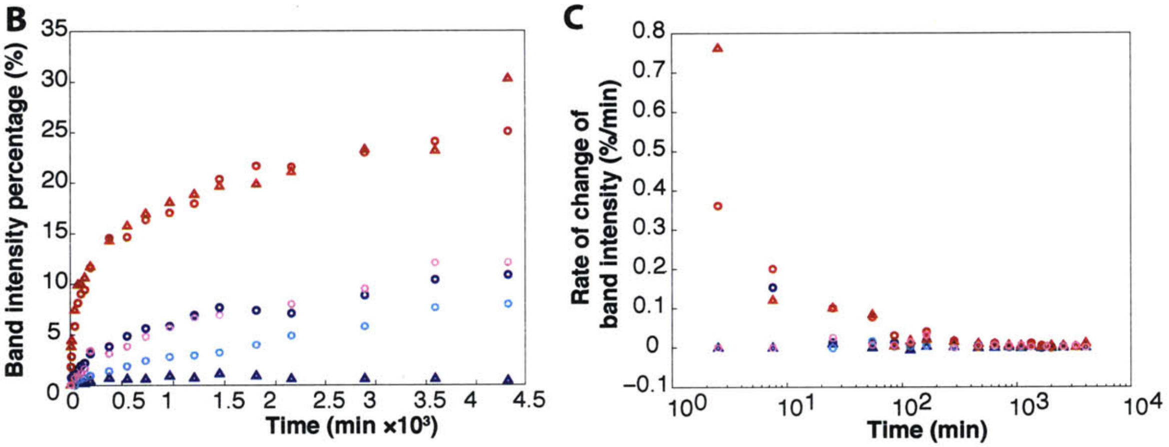

Figure 4-4: Cuboids were assembled isothermally at their optimal temperatures and subjected to 2% agarose gel electrophoresis with 10 mM $MgCl_2$. **(A)** Table listing the structure assembly conditions for each structure and whether boundary strands were used in the design. Boundary strands are half-strands that are connected to the previous full strand to further stabilize its incorporation [131]. These boundary strands were used previously in the 8-nt domain designs. To understand how salt concentrations affect assembly kinetics, we included a condition where a lower $MgCl_2$ was used. **(B)** Band intensity percentages for each structure was plotted against reaction time on a linear scale. **(C)** The rate of change in band intensity percentage (i.e. Δ intensity / Δ time) at given time points.

Stability comparison

Further, we compared a 6H × 6H × 104B structure assembled using our original 8-nt bricks with one using the new 13-nt brick motif and found that 13-nt brick structures assembled with higher percentages and also showed higher thermal stability (Fig. 4-5) . Following 3-day annealing, the gel intensity percentages were compared. 13-nt brick structures showed intensity percentages up to 40%, while 8-nt bricks showed intensity percentages of only around 12.6% (Fig. 4-5). This difference is consistent with the trends we observed in figure 4-4, where the 13-nt brick structures assemble much faster and with higher yields than the 8-nt brick structures. Although the structures were designed with the same global morphology and molecular weight, structures assembled using the 13-nt brick migrated on the gel at a slower pace. This could be attributed to the lower crossover density in these structures, resulting in expansion of the overall structure size.

Purified 8-nt and 13-nt 6H×6H×104B structures were compared for post-folding thermal stability at varying temperatures. The 13-nt structure was found to be stable up to 48°C, while the 8-nt structure began to fall apart around 37°C (Fig. 4-5E–F). Interestingly, the 13-nt structure shows a presence of increased higher molecular-weight products, possibly resulting from increased dimerization that occurs upon the loss of strands at the surface of the structures.

Annealing and melting curves further demonstrated that the 13-nt brick structures assembled around 50-53°C at 5-100 nM strand concentration, while the 8-nt bricks were found to fold around 35°C at 100 nM strand concentration(Fig. 4-5G–H), in agreement with what was found previously for DNA crystal formation [144]. The formation temperatures fall between the melting temperatures of one and two hybridized domains (Table 4-1) as expected. Hysteresis is observed for the annealing and melting temperatures of both structures. The melting temperature for the 8-nt structure was around 48°C, while that of the 13-nt structure was around 62°C.

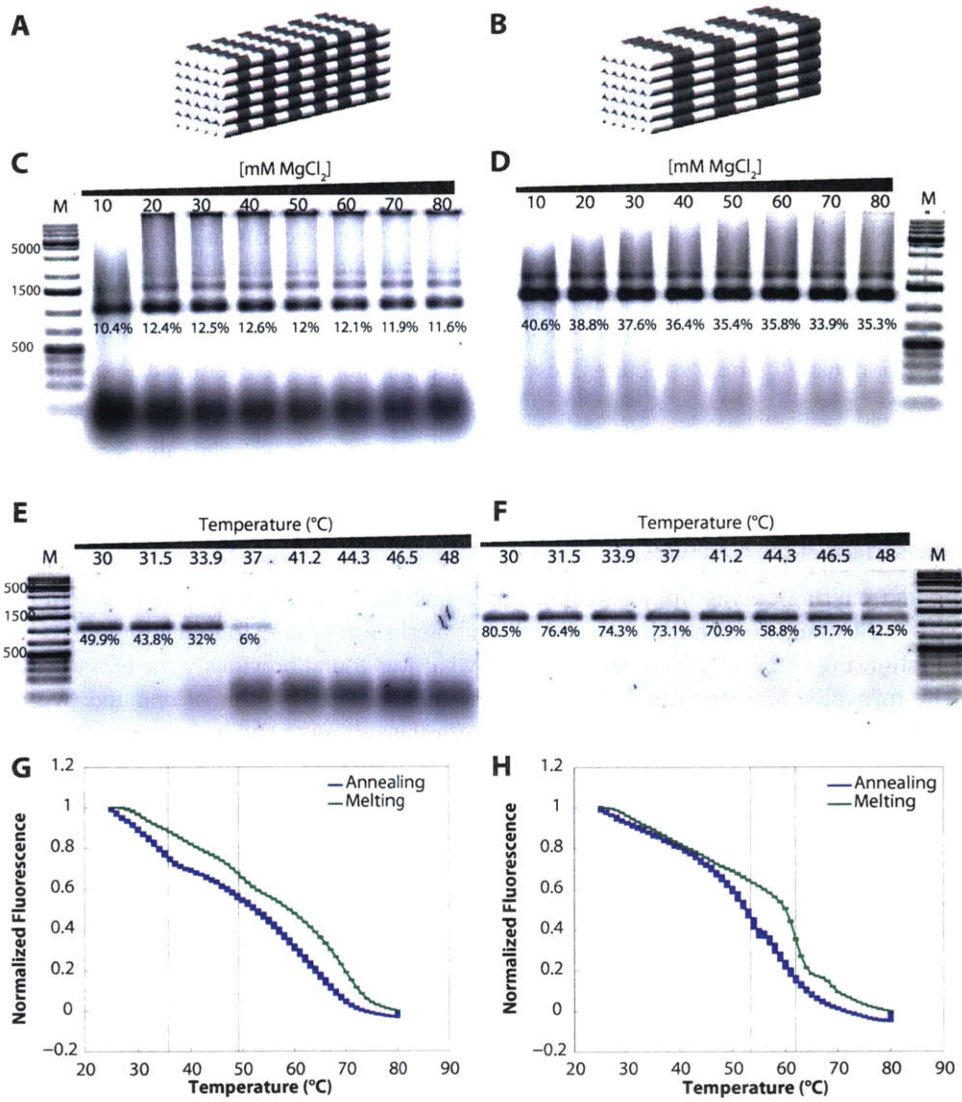

Figure 4-5: Characterization of a 6H×6H×104B structure composed of 8-nt versus 13-nt DNA bricks. A 6H×6H×104B cuboid containing 8-nt (**A, C, E, G**) and 13-nt (**B, D, F, H**) DNA bricks was designed and characterized. **(A) – (B)** Cylinder representations of the cuboid designs. Banding patterns indicate the length of the designed binding domain. **(C) – (D)** Assembly efficiency of cuboids. Structures were annealed at 100 nM strand concentration using a 3-day 2-stage linear annealing ramp in the presence of 10–80 mM $MgCl_2$ and assayed on a 2% agarose gel. **(E) – (F)** Thermal stability of purified structures. Structures were annealed at 100 nM using a 3-day 2-stage linear annealing ramp in the presence of 20 (13-nt) or 40 (8-nt) mM Mg^{2+}. Target bands were purified from a 2% agarose gel and adjusted to 2.6 nM/strand. Following, the structures were subjected to a higher temperature (30-48°C) over 24 hours and assayed on a 2% agarose gel. A 1kb ladder was run on lane M. Numbers indicate the percentage of the target band intensity. **(G) – (H)** Annealing/Melting curves of the structures. Structures were were folded using a 1-day linear annealing ramp and a 30 minute melting curve at 100 nM strand concentration in the presence of 0.3×SYBR Green I and 20 (13-nt) or 40 (8-nt) mM Mg^{2+}. Fluorescence signal was normalized to the those at 80°C and 25°C. The black vertical lines delineate the melting and annealing temperatures.

Variations of the 13-nt DNA bricks

We also tested different versions of the 13-nt DNA bricks, including one with alternating crossover direction and another in which the 26-nt half strands are merged with an adjacent full length strand (Fig. 4-6). The 13-nt brick structure with disjoint bricks oriented in the same direction gave the highest yields. As a result, the 13-nt unidirectional brick motif was selected for assembling large structures.

4.4.2 Variants of the 13-nt 6H×6H×104B structure

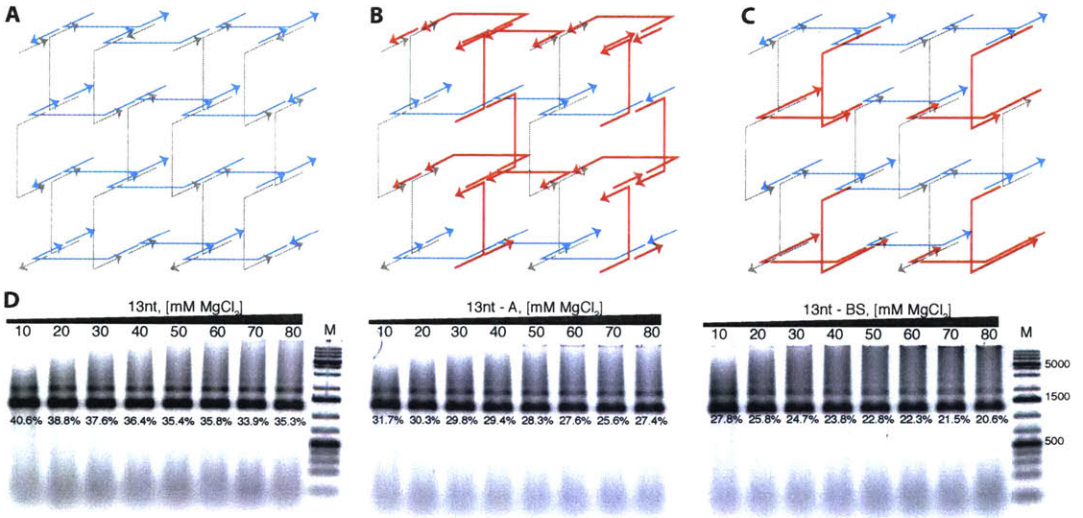
A
B
C
D
13nt, [mM MgCl$_2$]
10 20 30 40 50 60 70 80 M
40.6% 38.8% 37.6% 36.4% 35.4% 35.8% 33.9% 35.3%
13nt - A, [mM MgCl$_2$]
10 20 30 40 50 60 70 80
31.7% 30.3% 29.8% 29.4% 28.3% 27.6% 25.6% 27.4%
13nt - BS, [mM MgCl$_2$]
10 20 30 40 50 60 70 80 M
27.8% 25.8% 24.7% 23.8% 22.8% 22.3% 21.5% 20.6%
5000
1500
500

Figure 4-6: Gel electrophoresis of a 6H×6H×104B structure with varying connection patterns of 13-nt DNA bricks. The cuboid was folded using a 3-day 2-stage annealing ramp in varying concentrations with MgCl$_2$ (10–80 mM). Three different connection patterns were used: **(A)** uni-directional 13-nt DNA bricks, **(B)** alternating 13-nt DNA bricks, and **(C)** uni-directional 13-nt DNA bricks with boundary strands. Percentages below the band indicate the target band intensity ratio.

4.4.3 Assembly optimization

Annealing conditions are crucial for assembly of massive DNA brick structures. We tested both folding protocol, buffer conditions, and folding times on a number of different structures.

Annealing ramp optimization

We tested a number of folding conditions with the 67.6 MDa structure to obtain an optimal protocol. First, we annealed 5 nM strands at 10–80 mM magnesium in a linear folding ramp, and gel electrophoresis showed the sharpest band at 20 mM $MgCl_2$. Subsequently, we annealed the structures isothermally at 20 mM $MgCl_2$ and found that structures formed well in roughly a 2°C window (Fig. 4-7).

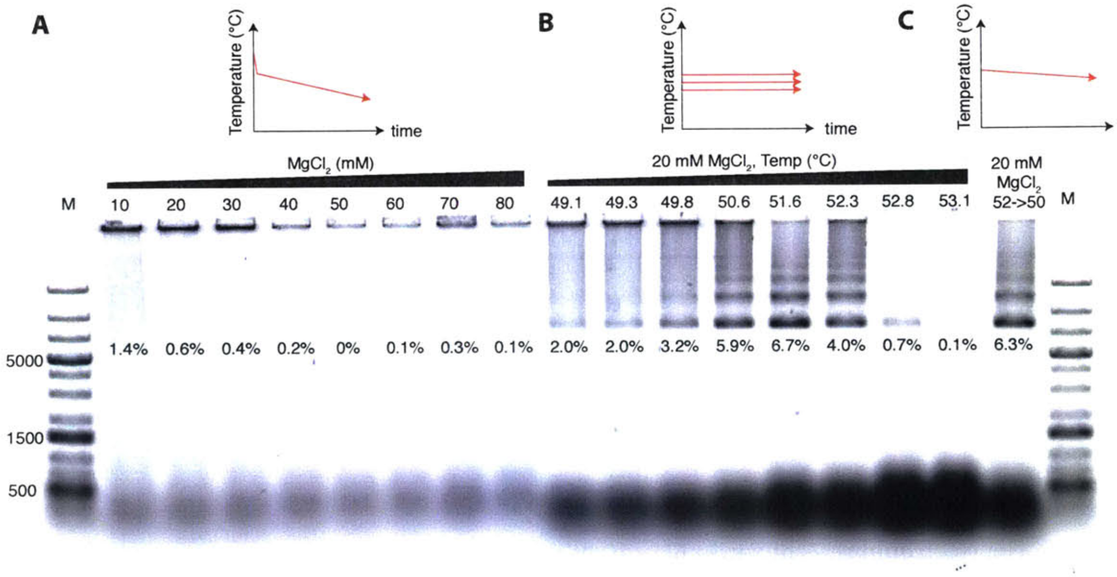
A
B
C
Temperature (°C)
time
Temperature (°C)
time
Temperature (°C)
time
MgCl$_2$ (mM)
20 mM MgCl$_2$, Temp (°C)
20 mM MgCl$_2$ 52->50
M
10
20
30
40
50
60
70
80
49.1
49.3
49.8
50.6
51.6
52.3
52.8
53.1
M
1.4%
0.6%
0.4%
0.2%
0%
0.1%
0.3%
0.1%
2.0%
2.0%
3.2%
5.9%
6.7%
4.0%
0.7%
0.1%
6.3%
5000
1500
500

Figure 4-7: Annealing ramp optimization. The 20H×20H×260B cuboid at 5 nM strand concentration was subjected to varying annealing conditions. **(A)** Structures were annealed at varying $MgCl_2$ concentrations in a two-stage thermal annealing ramp with a fast cooling step from 80°C to 60°C over 40 minutes followed by a slow cooling step from 60°C to 25°C over 72 hours. **(B)** Cuboids were annealed at 20 mM $MgCl_2$ over 72 hours isothermally. **(C)** Cuboids were subjected to a slow, narrow annealing ramp between 52 and 50°C over 72 hours. Lane M contains a 1 kb plus DNA ladder. Numbers below the band indicate the band intensity percentages.

Reaction time optimization

A narrow annealing ramp using the similar strand concentrations and optimal salinity also showed roughly the same intensity percentage of 6% as that of the optimal formation temperature. We selected to use isothermal assembly conditions. Structure assembly times were varied, and reactions were found to near equilibrium in 5-7 days. With shorter reaction times, the structures showed lower yields (Fig. 4-8).

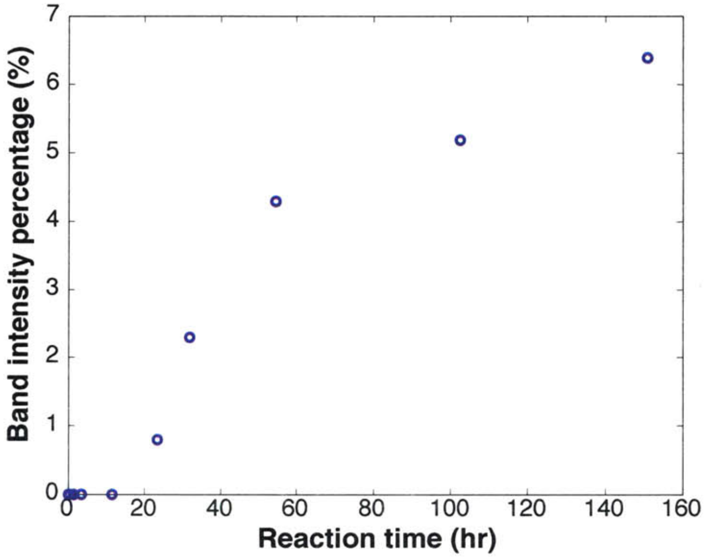

Figure 4-8: Assembly efficiency of the 30H×30H×260B cuboid across different reaction times. 30H×30H×260B cuboids were assembled at 30 nM strand concentration isothermally at 53°C in 10 mM $MgCl_2$ for varying amounts of times. Target band intensity percentages were analyzed using 2% agarose gel electrophoresis.

Formation temperature range

To further characterize these large, complex structures, we compared the temperature window for assembly of each of the cuboids. Structures were annealed isothermally for 5 days at temperatures from 45–55°C using identical reactions conditions (5 nM strand concentrations and in the presence of 20 mM $MgCl_2$) and assayed on gel electrophoresis. We found that as the complexity of the structure increases, the range of temperatures at which the structures form becomes narrower (Fig. 4-9). For the smallest 10.2 MDa structure, structures were capable of forming across roughly a 5°C range, while the largest 512 MDa structure formed only within a <1°C window. This narrowing window observation fits with our our expectation, as more complex structures have increased sequence diversity and larger component numbers that could limit efficient nucleation to a smaller window of reaction conditions. This narrowing window may restrict the size of structures that can be formed in a relevant time scale using this DNA brick method. Also note that while the absolute intensity percentages may vary between different gels, the relative band intensities and the narrowing temperature trend observed between the gels are still valuable for understanding underlying mechanisms driving structure formation.

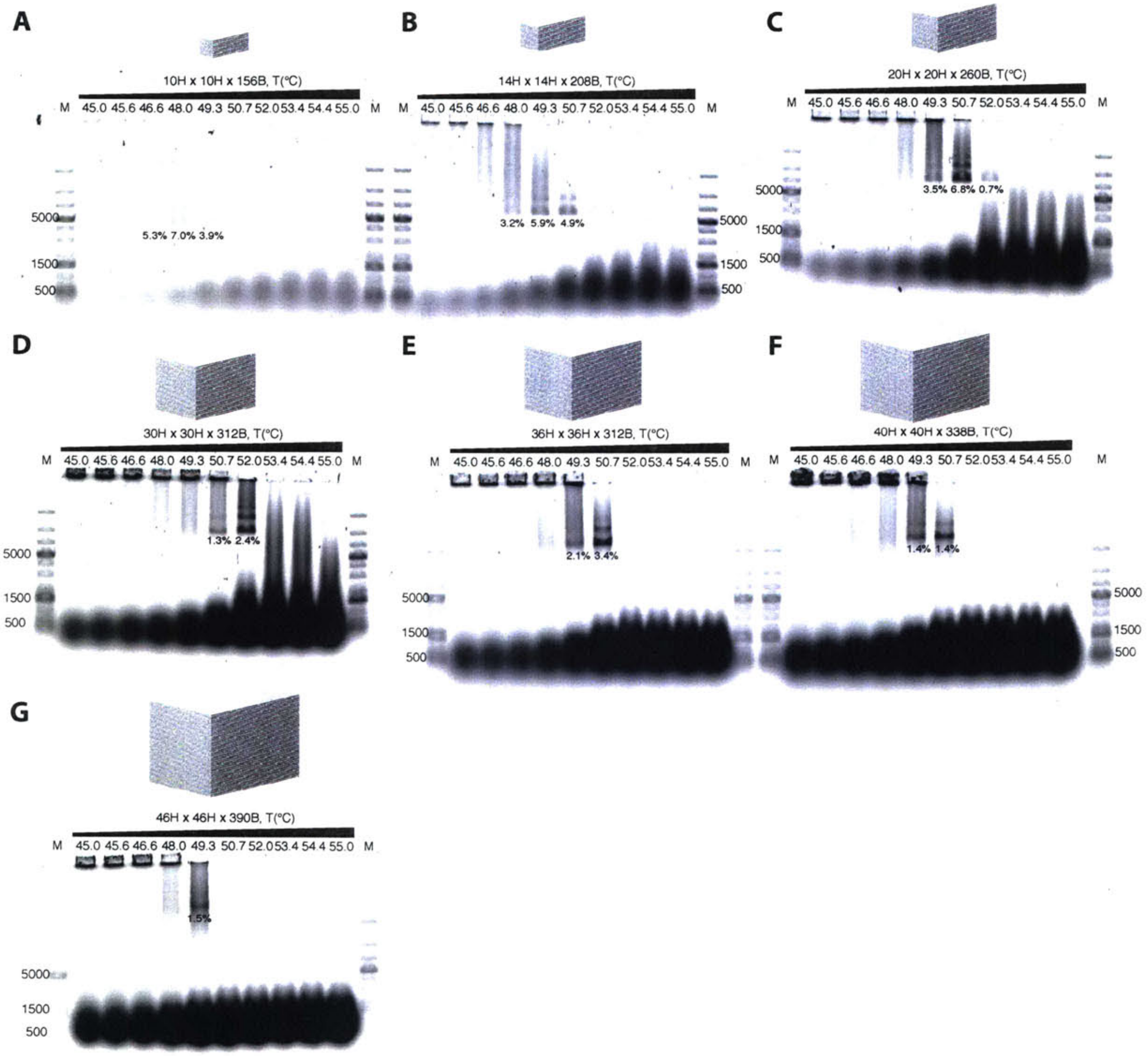
A
10H x 10H x 156B, T(°C)
M 45.0 45.6 46.6 48.0 49.3 50.7 52.0 53.4 54.4 55.0 M
5.3% 7.0% 3.9%
5000
1500
500
B
14H x 14H x 208B, T(°C)
M 45.0 45.6 46.6 48.0 49.3 50.7 52.0 53.4 54.4 55.0 M
3.2% 5.9% 4.9%
5000
1500
500
C
20H x 20H x 260B, T(°C)
M 45.0 45.6 46.6 48.0 49.3 50.7 52.0 53.4 54.4 55.0 M
3.5% 6.8% 0.7%
5000
1500
500
D
30H x 30H x 312B, T(°C)
M 45.0 45.6 46.6 48.0 49.3 50.7 52.0 53.4 54.4 55.0 M
1.3% 2.4%
5000
1500
500
E
36H x 36H x 312B, T(°C)
M 45.0 45.6 46.6 48.0 49.3 50.7 52.0 53.4 54.4 55.0 M
2.1% 3.4%
5000
1500
500
F
40H x 40H x 338B, T(°C)
M 45.0 45.6 46.6 48.0 49.3 50.7 52.0 53.4 54.4 55.0 M
1.4% 1.4%
5000
1500
500
G
46H x 46H x 390B, T(°C)
M 45.0 45.6 46.6 48.0 49.3 50.7 52.0 53.4 54.4 55.0 M
1.5%
5000
1500
500

Figure 4-9: Range of temperature formation. Agarose gel electrophoresis was used to analyze the formation of 13-nt brick structures assembled isothermally for 5 days at 5 nM strand concentration in the presence of 1× TE buffer with 20 mM $MgCl_2$. Structures tested include **(A)** 10H×10H×156B, **(B)** 14H×14H×208B, **(C)** 20H×20H×260B, **(D)** 30H×30H×312B, **(E)** 36H×36H×312B, **(F)** 40H×40H×338B, and **(G)** 46H×46H×390B cuboids. **(A)-(D)** used a 0.5% agarose gels, while **(E)-(G)** used a 0.3% agarose gel. A 1kb ladder was run on lane M.

4.4.4 Structure characterization

Using optimized conditions, seven large DNA brick structures ranging from 10.1 to 536 MDa were annealed isothermally in one-pot reactions (Fig. 4-10A, in grey). As a benchmark, a 4.3 MDa origami structure was assembled using a three-day annealing ramp in 10 mM $MgCl_2$ (Fig. 4-10A, in blue). Gel electrophoresis analysis showed that the brick structures formed at intensity percentages ranging from 1 – 20%, depending on the size of the overall structure and strand concentration used. For all structures, an optimal formation temperature based on strand intensity percentages was observed. Purified structures had expected dimensions and morphologies under transmission electron microscopy (Fig. 4-10B). However, with larger structure size, some broken structures were observed. These defective structures may result from incomplete assembly of structures or from damage occurring during gel purification or the TEM deposition processes.

The dimensions of 100 distinct 36H×36H×312B 262.8 MDa cuboids were measured from the TEM images (Fig. 4-15). The length along the helical axis was 104.5 nm, which is close to our expected length of 103 nm calculated from a length of 0.33 nm per base pair. The distance measured across the helices was 102.1 nm on particles lying laterally and 99.2 nm on those lying helically. These measurements result in an average helix diameter of 2.8 nm, which is comparable but slightly larger than 2.5 nm helix diameter measured in previous square-lattice 8-nt brick structures [50, 131, 144]. The large helix diameter is perhaps due to the lower crossover density in 13-nt brick structures. In addition, the thickness of the structure may contribute to the larger lengths since the drying and staining processes may flatten the cuboids, widening the measurements.

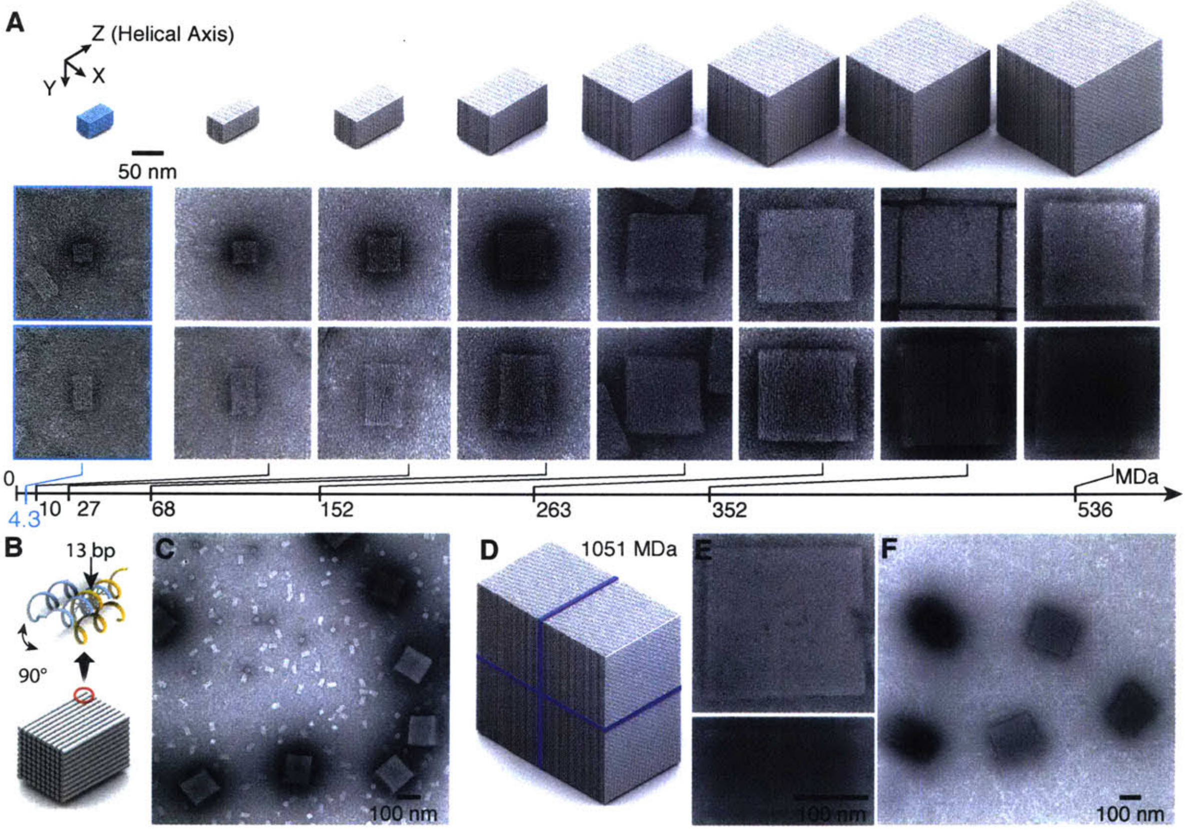

Figure 4-10: Assembly of DNA cuboids across scales. **(A)** Top row shows cylindrical models of DNA cuboids, where a cylinder represents a DNA double helix. TEM images from different projections are shown in the middle (helical direction) and bottom (lateral) rows. Molecular weight of each structure is indicated on the scale axis under the bottom row. A M13-scaffolded DNA origami cuboid with dimensions of 8H×8H×104B and mass of 4.3 MDa is colored blue (leftmost column). The grey-colored DNA brick cuboids are 10, 27, 68, 152, 263, 352, and 536 MDa in mass, and have respective dimensions of 10H×10H×156B, 14H×14H×208B, 20H×20H×260B, 30H×30H×260B, 36H×36H×312B, 40H×40H×338B, and 46H×46H×390B. **(B)** Each DNA brick strand binds to a neighboring strand via a 13 base pair interaction. **(C)** TEM image of 536.4 MDa brick cuboids in comparison with 4.3 MDa origami cuboid. **(D)** Cylindrical model of a 1051 MDa cuboid composed of four identical 263 MDa cuboids. This 1 gigadalton cuboid measures 72H×72H×312B. **(E)** TEM images of the helical (top) and lateral (bottom) projections of the 1051 MDa cuboid. **(F)** Wide-field TEM image of the 1051 MDa cuboid.

4.4.5 Design Software

We have developed custom software to facilitate the design of large DNA nanostructures using the DNA bricks methodology. Existing nucleic acid design software [51] includes robust tools for designing small DNA tile and origami structures. While these software can be adapted to design some DNA brick structures, the process is not optimized for large 3D brick structures. Particularly, the user interface focuses on editing on the strand-level through an "unfolded" 2D representation of the 3D structure, making complex shape design and positional editing difficult for large structures. We thus address these challenges by developing a streamlined software, named Nanobricks, capable of editing at three levels. First, the user draws, imports, or programs a 3D shape by placing "voxels" that represent domains (Fig. 4-11A). Second, the software uses a "translation scheme" to convert the shape into associating DNA brick strands. (Fig. 4-11B). Finally, the software designs sequences for or applies an existing set of sequences to the strands (Fig. 4-11C). The output is a set of sequences to be chemically synthesized and combined in the laboratory. To facilitate each of these three steps, the software also contains numerous other features to add, remove, or modify features on the voxel and strand level (Fig. 4-11D-F). Additionally, Nanobricks is capable of outputting file formats compatible with other DNA structure design software.

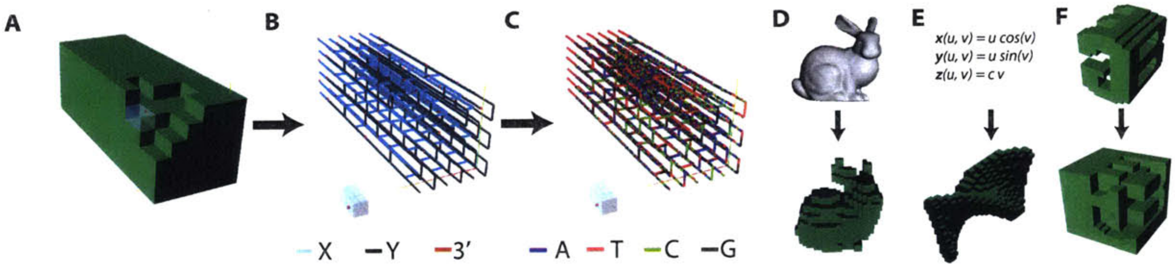

Figure 4-11: Process flow diagram and features of Nanobricks, a DNA brick shape design software. **(A)** Voxels are added through a 3D user interface to create the desired shape. **(B)** Voxels can be translated to strands, where X strands are depicted in blue, Y strands in black, and 3' ends in red. **(C)** Sequences can be applied to these strands from a previous source or by assigning random sequences. **(D)** A 3D file of the Stanford bunny (top panel) can be imported into the software and approximated into voxels (bottom panel). **(E)** A helicoid (equations shown on top) can be mathematically scripted in the software to include voxels that satisfy the equations (bottom panel). **(F)** Shapes can be designed using a number of tools, including an invert option. Top panel shows the inner cavity of a structure. Bottom panel shows cutouts of the inverted shape.

4.4.6 Shape Design

We used different tools in our software to design 22 different shapes, primarily complex cavities, from a 30H×30H×20B canvas (Fig. 4-12 and 4-16). Because we used the original cuboids as our canvases without ordering additional modified strands with polyT replacing unused voxels, each structure would be missing several strands. As a result, features shown from our original design that are 4 voxels thick would actually contain strands that cover 3 voxels. Thus, our designs were made to be a bit more conservative to account for these differences. Our previous studies that used a 10×10×10 voxel canvas was limited in feature patterning. Only a few channels or simple shapes could be patterned by this small voxel number. By using our new DNA bricks approach, we can create substantially more massive structures with more than 60 times the number of voxels of the original canvas. By using a 30×30×20 voxel canvas here with just 18 times more voxels, we are already capable of patterning far more intricate features. Further, the larger canvas sizes can help stabilize fragile features by providing surrounding structural support for our intricate cavities. Additionally, the increased patterning volume allows for more stable cavity structures, as these voids may suffer from rigidity issues due to the thin structural features that arise from stretching limited material across the larger volumes.

Generally, the shapes were designed in one of three methods: importing, mathematical scripting, and hand designing. Nanobrick's powerful editing functions and 3D display interface allowed for easy manipulation of the 18000 voxels. We used the software to converted several different 3D designs from open source websites to voxelized approximations (Fig. 4-12A–D). Additionally, scripting capabilities allowed for design complex mathematical cavities, including a Möbius strip and a helicoid, by identifying whether voxels were located within a given mathematical formula (Fig. 4-12F–J). A few notable designs that we independently created includes a structure with a cavity that threads through itself and two interconnected loop cavities (Fig. 4-12E, K–O).

Structures were folded at 5 nM strand concentration for 6 or 7 days. Surprisingly, these large structures tolerated the presence of free single-stranded ends and were able to form with target gel intensity band percentage between 1.4 and 5.1% (Fig. 4-17). Imaging of unpurified samples of shapes that were difficult to purify using gel electrophoresis (< 2%) also showed the expected design. For each of the categories, we describe the process and relevant shapes below. Through these designs, we tested our system limitations and demonstrate an unprecedented level of 3D feature complexity on the nanoscale.

Feature resolution testing

We gradually introduced finer and finer features to the top surface of a cuboid canvas containing a 26H×26H×52B cavity (Fig. 4-16). When features are less than 3 helices, they prove to be difficult to form due to the fragility of the structure and the increased number of missing strands. As there are an odd number of helices in the features, there is an increased ratio of half strands which are thereby missing from the reaction stocks.

Because our readout for these studies is the contrast change resulting from different layer thicknesses, we can only validate structural designs that are visible via TEM. A few other thin channels were tested for their visibility. The interconnected loop cavities of Shape L show that TEM contrast is most visible if features are least 3 voxels thick along the helical direction and at least 2 helices thick.

3D model import

We used different 3D models to design a few complex cavities. These structures demonstrate the type of complex features that can be patterning only with larger scales. Previously, our attempts in creating very defined cavities and features were limited due to the small canvas size. While we had the possibility of creating geometric patterns such as triangles and rectangles, it was difficult to create fine features. With the increase in voxel number, we have been able to accommodate cavities including a teddy bear (Shape A), a bunny (Shape C), and even words to spell out 'LOVE' (Shape B). The previous 3D DNA brick structures could only hold one letter or character at a time. Now the increased size allows not only for words to be created but also for control over lettering thickness.

Mathematical scripting

We also are able to rapidly design a number of mathematically inspired cavities, including Shape F's helicoid cavity, Shape G's twisted Möbius strip, Shape H's hyperboloid, and Shape J's roman surface, by using the scripting function of Nanobricks.

Hand-designed shapes

Remaining shapes were made by combination of Nanobricks scripting to easily control voxel deposition and hand placement of voxels. Two particularly complex structures include a interconnected loop cavities (Shape L) and a cavity that penetrates into itself (Shape K). Such structures may be difficult to self-assemble because such intricate features require a large enough canvas to accommodate the different cavities. Additionally, the numerous cavities may require the appropriate growth mechanism and kinetics for bricks to add to a growing structure in such a way that the internal forms are not excluded.

Overall, these larger structures demonstrate unique features and designs that have previously been unachievable in a 3D structure in a single-pot reaction. Generally, this involves diversity of fine features spread across a large volume. One would expect growth of such cavity structures to be difficult because different parts of the structure could potentially nucleate and grow separately, making it difficult to form one contiguous structure. Further, the increased voxel number allows for formation of structures stable enough to provide 3 different projections that show 3 different letters (Fig. 4-12E). Before only 2 letters were possible and these designs were very fragile and formed with low yields. Additionally, words with detailed lettering thickness is possible and the presence of numerous parallel intersecting and non-intersecting channels.

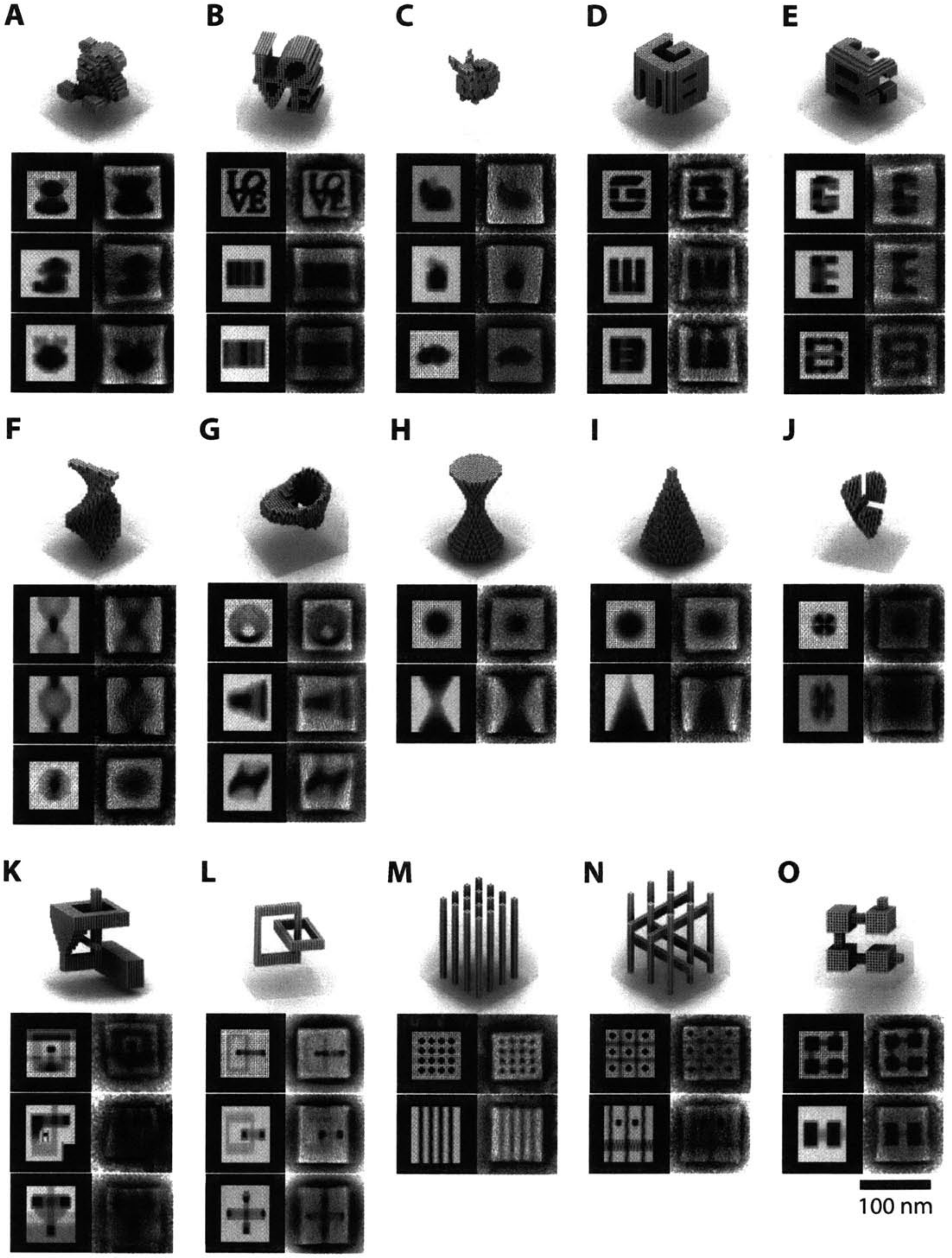

Figure 4-12: Complex shapes from a 30H × 30H × 20H canvas. For each design, the top diagram depicts a 3D visual of the designed shape. left panel shows the respective shape projections. Right panel shows averaged TEM images from at least six particles. For some of these shapes (e.g. O), the two lateral projections are difficult to distinguished, so they were averaged together. Gel electrophoresis analysis of these shapes are shown in figure. 4-17.

4.4.7 Discrete symmetric structures

Multimers from a 6H×6H×104B

Due to the symmetry present in these structures, symmetric multimer structures can be created by connecting strands across different symmetric planes by exploiting symmetric connection strategies [181] (Fig. 4-13). We first used a relatively small 6H×6H×104B cuboid to test the different homo-multimeric designs. Specifically, via simple one-pot isothermal annealing, we successfully demonstrated the formation of head-to-head dimers (Fig. 4-13A–D), tail-to-tail dimers (Fig. 4-13E–H), side-to-side dimers Fig. 4-13I–L), and side-to-side tetramers (Fig. 4-13M–Q).

We first used a small 6H×6H×104B cuboid to test the different one-pot homo-multimeric designs. The design of these structures is analogous to the previously assembled DNA crystals [144] in that complementarities are specified across different planes of helices. In contrast to the periodic structures, these multimeric structures are designed to grow to a designed and prescribed structure size based upon their starting unit and connection pattern. We explored the formation of dimers and tetramers using a number of different approaches. We then applied these approaches to a larger cuboid to create gigadalton-sized structures.

Head-to-head dimers were created by removing the protecting head strands and connecting the remaining quartered strands in a symmetric manner across a plane parallel to the helical axis (Fig. 4-13A–D). Tail-to-tail dimers were similarly created by removing the protecting tail strands and connecting the remaining half strands in a symmetric manner across a plane parallel to the helical axis (Fig. 4-13E–H). Side-to-side dimers were created by connecting half strands within the same face of a structure such that the dimerized product results in two stacked cuboids that are shifted out of phase in the helical direction (Fig. 4-13I–L). To create rotationally symmetric structures, we connected half-strands on two adjacent faces together. The resulting expected product would be a strained tetramer where each strand is connected to another in a rotational manner (Fig. 4-13M–Q). A potential byproduct can result by creating products with no strain where two cuboids are not connected (indicated by the arrow in figure 4-13N).

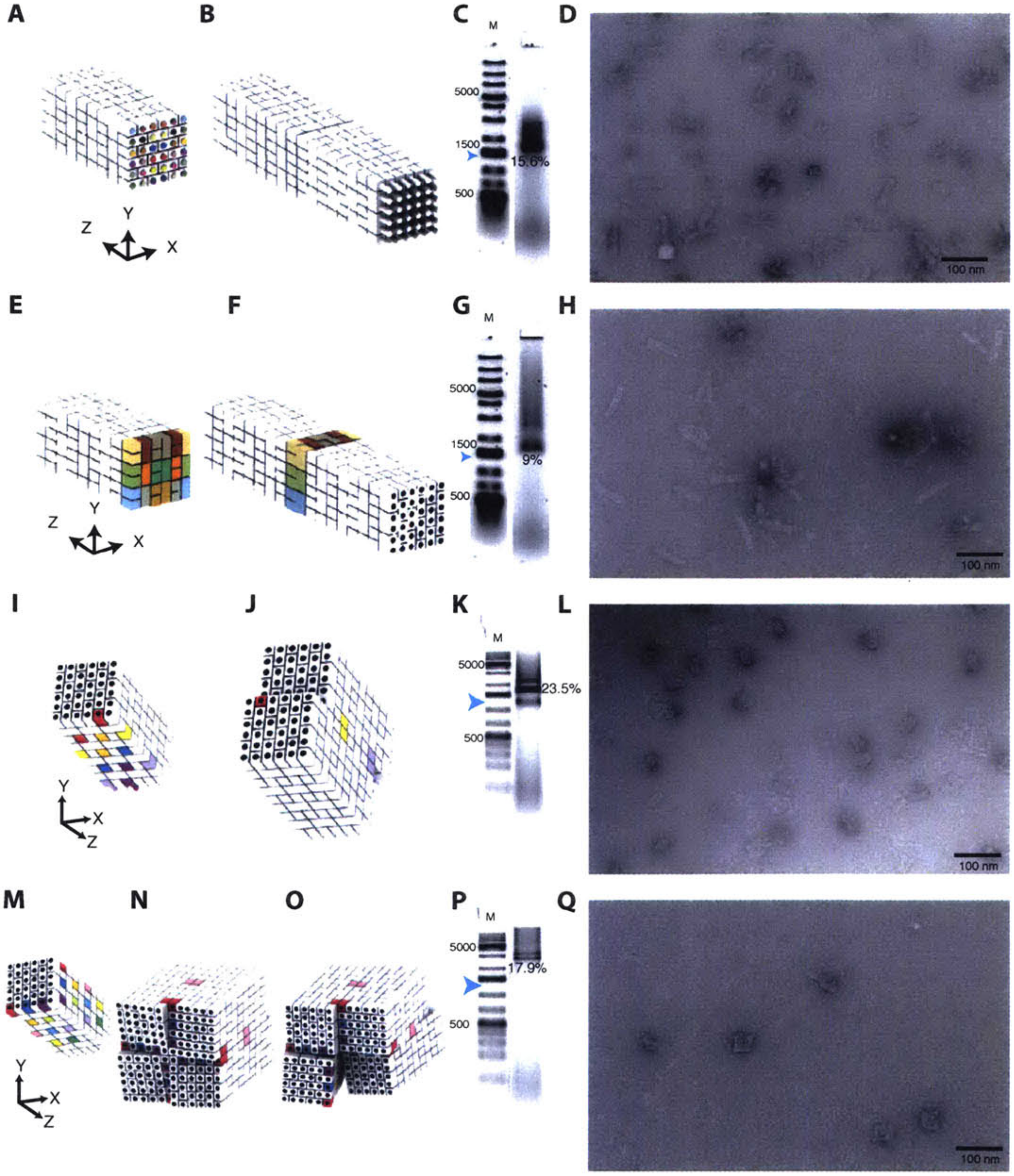
A
B
C
M
5000
1500
500
15.6%
D
100 nm
Z
Y
X
E
F
G
M
5000
1500
500
9%
H
100 nm
Z
Y
X
I
J
K
M
5000
500
23.5%
L
100 nm
Y
X
Z
M
N
O
P
M
5000
500
17.9%
Q
100 nm
Y
X
Z

Figure 4-13: Detailed design schematic and results for the 6H×6H×104B multimerized structures. In the models, the repeating units (left) and the expected final designs (right) are shown. The matching colors indicate connected bricks. 2% agarose gel was used to analyze the multimers which were formed at 200 nM/unit and 100 nM/connector strand for dimer structures or at 400 nm/strand for the tetramer in the presence of 20 mM $MgCl_2$ using a 3-day two-stage annealing ramp **(C)**, **(G)**, **(K)**, **(P)**. Blue arrow points to the expected location of a single 6H×6H×104B cuboid structure. Lane M contains a 1 kb DNA ladder. Numbers listed indicate the target band intensity percentages. TEM images were obtained for all structures **(D)**, **(H)**, **(L)**, **(Q)**. Multimers consist of **(A)–(D)** 6H×6H×104B head-to-head dimer, **(E)–(H)** 6H×6H×104B tail-to-tail dimer, **(I)–(L)** 6H×6H×104B side-to-side dimer, and **(M)–(Q)** 6H×6H×104B side-to-side tetramer. Note that the formation of this structure would result in a strained structure **(N)** and unconnected byproducts can form **(O)**.

Gigadalton tetrameric cuboid

We next applied the side-to-side tetramer design to assemble a 1 gigadalton tessellation structure, which measures 72H×72H×312B and contains four identical 262.8 MDa monomeric units. Specifically, by taking advantage of the C4 symmetry present in the plane perpendicular to the DNA helical axis, we designed strands that connected one face of the structure parallel to the helical axis with an adjacent face of the same orientation. This connection pattern resulted in a final structure that is sized four times that of the unique unit and with each unit tessellated in a rotationally symmetric pattern (Figs. 4-10D-F, 4-14). Similar to other brick structures, this gigadalton structure was formed via simple isothermal one-pot annealing reaction. The gel electrophoresis produced a distinct product band with ~1% yield (Fig. 4-14). The band was purified and imaged under TEM (Fig. 4-10D-F). While a number of structures were broken, the many intact particles showed expected dimensions. Occasionally, some structures appeared to form the beginnings of a pentamer (data not shown).

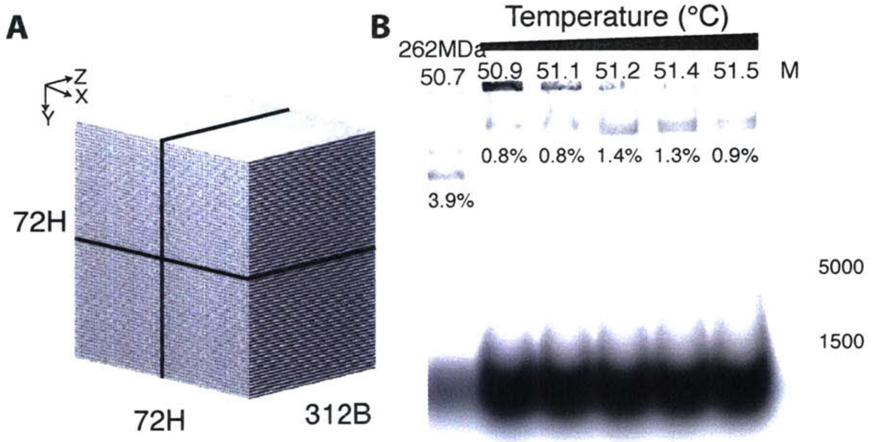

Figure 4-14: Gel electrophoresis of a tetramer comprised of 36H×36H×312B units. A 0.3% agarose gel was used to analyze the tetramer which was formed at 20 nM/strand concentration in the presence of 20 mM $MgCl_2$ using a 5-day isothermal annealing protocol. Lane M contains a 1 kb DNA ladder. Numbers listed indicate the target band intensity percentages.

4.5 Discussion

We have demonstrated the assembly of massive DNA nanostructures up to the gigadalton scale. Previous fully addressable 3D DNA structures were typically 5-8 MDa [51, 131]. The 0.5 GDa 46H×46H×390B fully addressable cuboid is over 100 times more massive and bridge two orders of magnitude in length to form structures with an overall 100 nm length in each of the three dimensions and a feature resolution of $2.8 \times 2.8 \times 4.4$ nm^3. To the best of our knowledge, this 0.5 GDa structure is the largest designed monodisperse self-assembled nanostructure with the highest information density, containing 33,511 unique components and 1,684,336 nt of sequence. By mass, these structures are larger than most viruses that lack an envelope [182, 183] – note that these viral particles consist of only 1 to 200 unique proteins that are repeated to create a symmetrical capsid rather than an asymmetrical addressable structure. Additionally, the sequence complexity of our system is now comparable to the information content of genomes in the simplest bacteria [179].

We also demonstrate that highly complex cavities and features can be encoded into subsets of our brick libraries. Traditionally, such massive structures and complex cavities are difficult to design due to software limitations and difficult to assemble due to limited structural scalability and rigidity. Through our custom software Nanobricks, we can manipulate voxels and strands *in situ* and use the scripting tools to automate complex or repetitive tasks, enabling facile design of shapes from an 18,000 voxel canvas. Surprisingly, even though some structures contains rather fragile features, the thousands of bricks required to form the shapes were able to self-assemble within a week, as confirmed by TEM analysis. Our ability to assemble these larger canvases enables us to design more complex shapes than demonstrated on smaller structures.

The 13-nt bricks appeared capable of mitigating reduced kinetics associated with necessarily decreased component concentration in assembly of large DNA structures with a massive number of distinct components. While the detailed mechanism of brick structure formation remains to be dissected, our results are consistent with the hypothesized assembly mechanism of delayed nucleation followed by fast growth [131, 180, 184]. When domains were increased from 8-nt to 13-nt, the structure were observed to form more rapidly. Additionally, researchers have further found that binding heterogeneity circumvents the emergence of multiple dominant competing nuclei [180]. The component heterogeneity is further enhanced in our 13-nt brick design because the range of accessible binding energies becomes wider with longer domains due to the larger sequence space.

With the existing structures, we have achieved 100 nm of complete addressability with 2.8-4.4 nm of precision in 3D. By creating DNA crystals [144], forming porous structure [60], or developing hierarchical assembly methods [59, 61], we may potentially move towards multidimensional patterning and gain addressability across even larger length scales. With these growing length scales, we could consider creating new biological [78, 119, 126], photonic [86, 124, 160], and nanofabrication [102] applications, such as 3D photonic waveguides [146] and optical metamaterials [185]. The high information density of these gigadalton-sized structures could also facilitate the emerging effort to use DNA as long term information storage systems [186].

4.6 Acknowledgments

The authors thank Nandhini Ponnuswamy, Rasmus Sørensen, Jaeseung Hahn, Juanita Lara, Leo Chou, Nicolas Garreau de Loubresse, Hiroshi Sasaki, and Sinem Saka for experimental help. The authors thank Matthew Beatty and Jerry Chang for the assistance in designing Nanobricks. The authors also thank Bryan Wei, Wei Sun, Cameron Myhrvold, and William Shih for insightful discussions. The work was funded by Office of Naval Research grants N000141010827, N000141310593, and N000141410610, Army Research Office grant W911NF1210238 (Peng Yin); Emory Biomedical Engineering Department Startup Fund, Emory Winship Cancer Institute Billi and Bernie Marcus Research Award (Yonggang Ke). Luvena Ong was funded by an NSF graduate research fellowship.

4.7 Author contributions

Yonggang Ke designed the first 6H×6H×104B structure. Casey Grun and Jocelyn Kishi wholly developed the Nanobricks software described in figure 4-11. Omar Yaghi performed experiments comprising figures 4-10, 4-9, and 4-15. Nikita Hanikel and Bei Wang performed experiments in figure 4-12. Allen Zhu and Jocelyn Kishi assisted with experiments in figure 4-12.

4.8 Supplementary materials

4.8.1 Particle size measurement distribution

The edge lengths for the 36H×36H×312B cuboid were measured in two different TEM projection views: helical (denoted by XY projection) and lateral (denoted by ZX or ZY projection). Because this cuboid is symmetrical, the X- and Y-axes are indistinguishable. The measured lengths are plotted as a histogram in fig 4-15. We expect the distance between bases to be approximately 0.34 nm and between helices to be 2.5 nm, which would respectively give lengths of 106 nm parallel to the helices and 90 nm perpendicular to the helices. The measured length along the helices peaked around 104 nm, which is close to our anticipated length. In contrast, the edge length perpendicular to the helices was measured to be 102 or 99 nm depending on whether the particles lay laterally or helically on the grid surface. This 10 nm discrepancy between the measured and expected lengths may result from electrostatic repulsion between the backbone that makes the lengths between helices to be larger. Additionally, these measurements are within those reported previously where up to 3 nm span between two helices. The distribution of measurements is also much wider for the edge perpendicular to the helical direction, especially when the structures are lying on the grid laterally. This larger variation may result from different compressive responses of the structure to adhesive forces or from surface forces that result during TEM sample deposition, since the structures are more flexible perpendicular to the helices compared to along the helices.

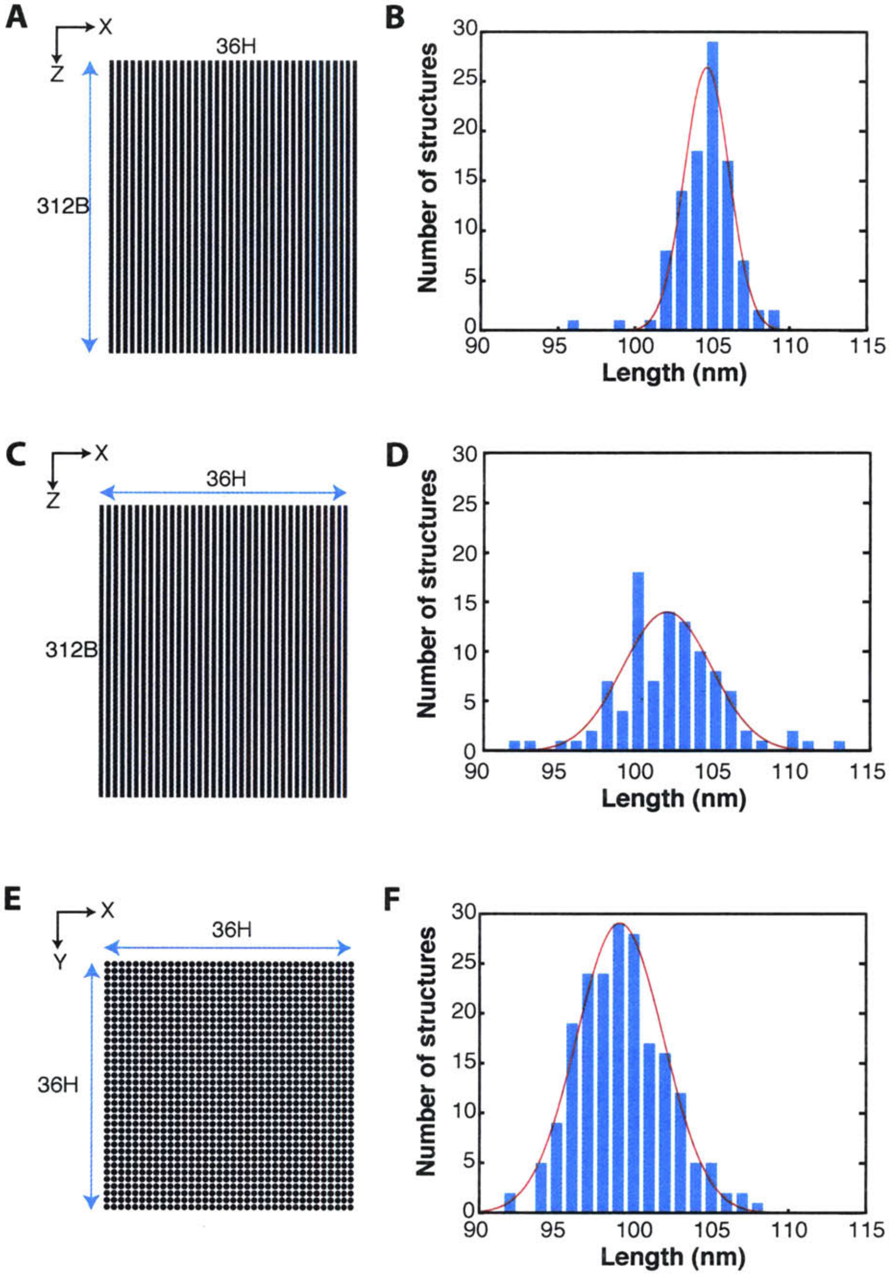

Figure 4-15: Histogram of measured edge lengths for the 36H×36H×312B particles. (A) Lateral projection view of the cuboid, with the measured edge in **(B)** indicated by the blue arrow (n=100). Average length measures 104.5 nm ± 1.8 nm s.d. **(C)** Lateral projection view of the cuboid, with the measured edge in **(D)** indicated by the blue arrow (n=100). Average length measures 102.1 nm ± 3.4 nm s.d. Note that the X and Y axis are equivalent in these diagrams. **(E)** Helical projection view of the cuboid, with the measured edges in **(F)** indicated by the blue arrow (n=200). Average length measures 99.2 nm ± 2.9 nm s.d. All histograms display in the x-axis the length rounded to the nearest nm and the number of structures measured in the y-axis. Red curve shows the gaussian fit of these histograms.

4.8.2 Feature testing of the 30H×30H×260B canvas structure

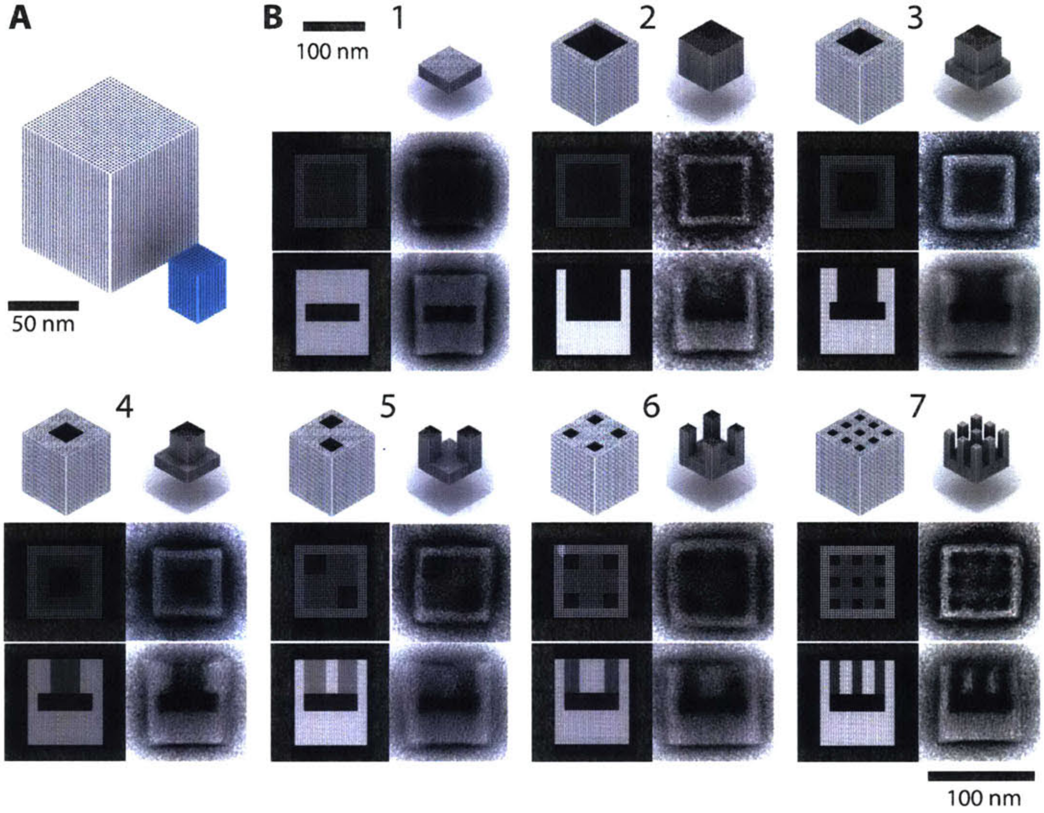

Figure 4-16: Feature testing of the 30H×30H×260B canvas structure. **(A)** A schematic comparing our 30H×30H×260B (152 MDa) canvas structure in grey with an 8H×8H×104B (4.3 MDa) origami-sized structure. **(B)** For each design, the top diagram depicts a 3D visual of the designed shape with both an opaque outer view and a transparent inner view of the cavity structure. Left panel shows the respective shape projections. Right panels depict averaged TEM images from at least six particles. Gel electrophoresis analysis of these shapes are shown in figure. 4-17.

4.8.3 Gel electrophoresis of large shape designs

Band intensity percentages ranged from 1.4 to 5.1 % for the different designs. Often, these seemed to vary depending on the fragility of the structure and the amount of exposed surface. More exposed surfaces give rise to many free single-stranded ends that can non-specifically interact to aggregate the individual particles, making them difficult to separate on gel electrophoresis.

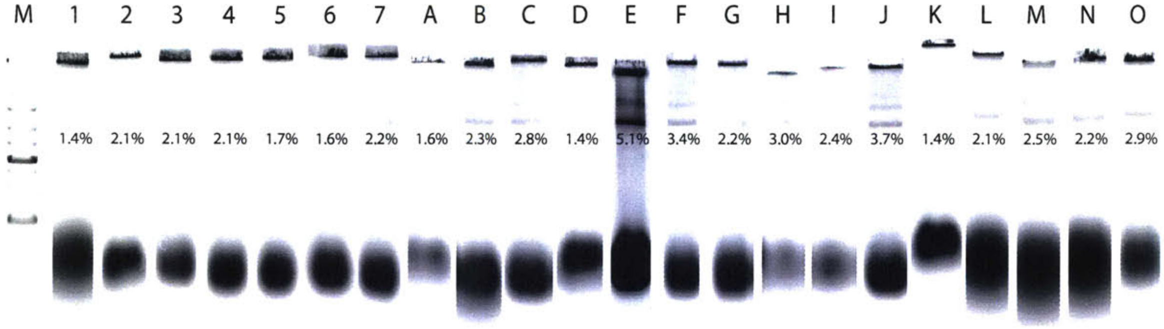

Figure 4-17: Gel electrophoresis of large shape designs. 0.5% agarose gel electrophoresis was used to analyze the shapes that were folded at 5 nM strand concentration for 7 days in a narrow annealing ramp. Representative gel lanes are shown, and lettering corresponds with the shapes found in figure 4-12 and 4-17. Lane M contains a 1 kb DNA ladder. Percentages indicated below target band indicate the band intensity ratios.

4.8.4 3D models of large shapes

Shapes A–D in Figure 4-12 were designed via importation and voxelization of different open source available 3D rendering files.

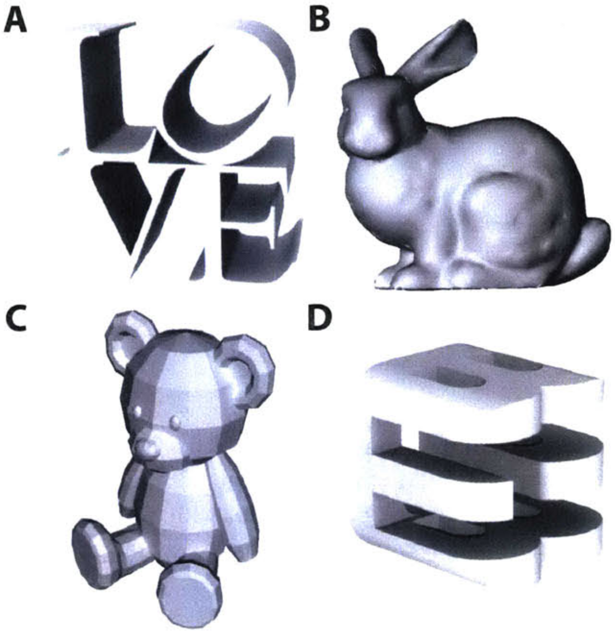

Figure 4-18: 3D view of Shapes A–D (A) Low poly Teddy bear by nonon http://www.thingiverse.com/thing:653095. **(B)** LOVE Sculpture by phineasjw from http://www.thingiverse.com/thing:22952/. **(C)** Stanford bunny from http://graphics.stanford.edu/data/3Dscanrep/. **(D)** Godel Escher Bach shadow cube by WeMeetAgainhttp://www.thingiverse.com/thing:25755/.

CHAPTER 5 Perspectives and Outlook

Efficient 3D nanoscale patterning is a challenging endeavor. While numerous methods have been previously developed to achieve nanoscale patterning, there are often trade-offs for the varying methods. "Top-down" approaches such as lithography provide large surface coverage and often sacrifice high resolution for high throughput [2]. Further, complex 3D patterning requires multiple steps or may be difficult for these top-down approaches [3]. In contrast, traditional "bottom-up" approaches such as block co-polymer self assembly will provide high feature resolution and high throughput but often are limited in material versatility or in its ability to pattern complex 3D features or cavities [5].

Self-assembly of nucleic acids has emerged as a promising approach towards addressing these patterning challenges. Through Watson-Crick base-pairing, nucleic acid strands are programmed to self-assemble. This complementary coding underlies the foundation for the different DNA nanotechnologies. The initial structures assembled from DNA were often accomplished through a tilling approach [20]. These tiling methods typically resulted in large lattice arrays that use few unique strand species and had limited addressability and overall structure complexity [17, 24, 33, 45, 114]. The standard of creating larger discrete structures is to use DNA origami [48]. While this approach is capable of creating a number of complex structure, each independent design requires careful redesign of scaffold routing and staple strands. Further, size and complexity of structures is limited by scaffold length. There has yet to be a technique that would combine the modularity of tilling approaches and the complexity DNA origami to create large, arbitrarily designed 3D nanostructures.

In this thesis, we extend the repertoire of methods available for 3D patterning (Fig. 5-1). We focus on developing the simple and modular DNA bricks approach where unique sequences of single-stranded oligomers assemble in a square-lattice pattern to form either discrete or periodic structures. By selecting to include specific bricks, we can easily create complex 3D patterns in a single-pot reaction. We describe the specific contributions of our work and the potential future applications these DNA brick structures may enable in the sections below.

5.1 Summary

In chapter two, we focused on developing a modular method of assembling 3D DNA nanostructures. These DNA bricks contain four different 8-nt binding domains that basepairs with a neighboring brick. By treating each binding domain as a voxel, a DNA brick cuboid can serve as a molecular patterning canvas. Different shapes are generated by selecting the desired voxels. From this voxel structure, we can determine the strands in the underlying canvas required to form this shape and select the oligomers from a library. Implementing this approach, we demonstrate an unprecedented number of discrete shapes from a single library of strands (Fig. 5-1D). These 100 shapes showcases the simplicity and versatility of our approach for rapidly creating diverse designs. This study is a proof-of-concept work demonstrating that tiling based approaches are capable of creating complex 3D discrete DNA nanostructures. DNA bricks technology not only demonstrates that a modular approach can be used to assemble complex discrete structures, but also liberates us from a dependency on scaffolds from biological sources. Further together with the 2D single-stranded tiling approach, these DNA bricks do not require careful sequence design to avoid undesired interactions, and we are granted nearly complete freedom in sequence design.

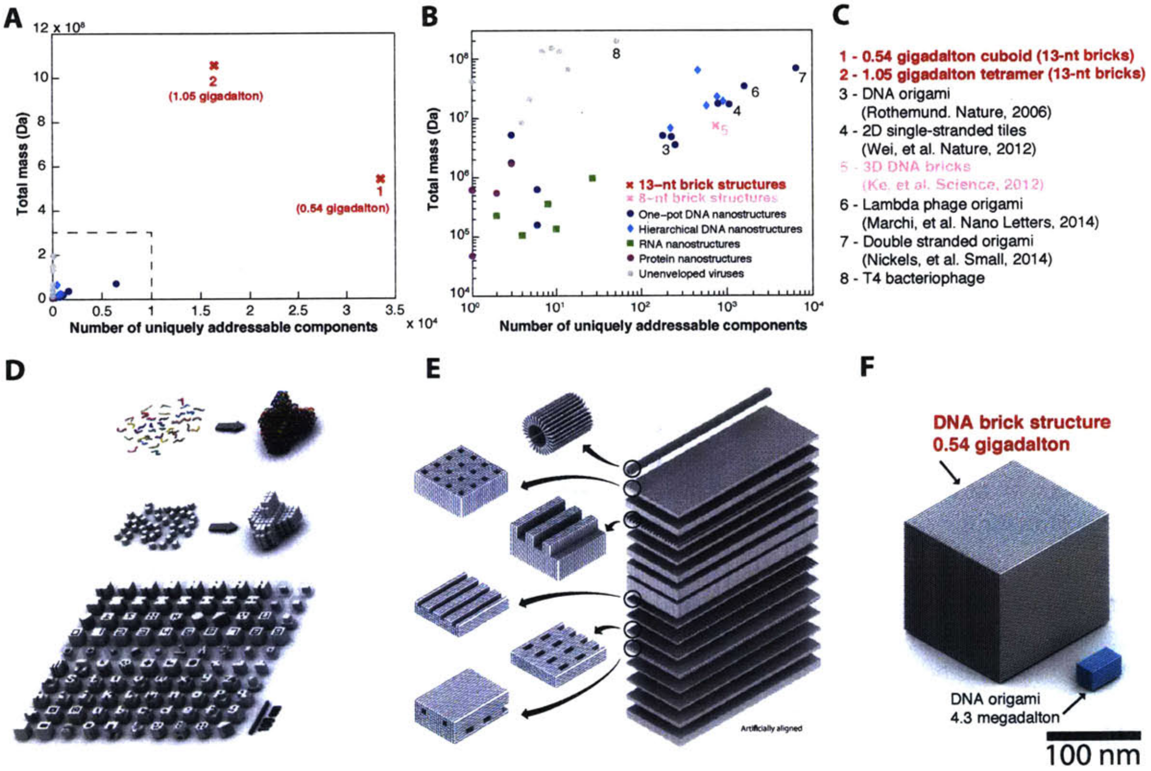

Figure 5-1: Summary of DNA bricks **(A)** Diverse self-assembled nanostructures (DNA, RNA, and protein-based) are compared based on two orthogonal parameters: the number of uniquely addressable components and the total mass of the structure. Non-enveloped viruses are included as a benchmark. **(B)** Zoom-in of the portion highlighted by dotted line in panel A. **(C)** Numbers correspond to the points highlighted in panels A and B. **(D)** Modular DNA bricks and the diverse shape assemblies. **(E)** Schematic of the different depth-defined DNA brick crystals and their patterns **(F)** Comparison of the largest, fully addressable 13-nt DNA brick structure with a standard M13 DNA origami structure.

We extend our DNA brick method from discrete structures to crystal structures in chapter three. Our crystals are designed such that strands would have complementary domains on opposing faces of the repeating unit, enabling growth along any of the three orthogonal axes. Rods and crystals with growth directions parallel and perpendicular to the helical directions were formed. The modular architecture of these crystals allowed for easy patterning of complex tunnels, channels, and pores across scales nearing one micron (Fig. 5-1E), demonstrating the first non-hierarchically assembled complex nucleic acid crystals with defined depths. Altogether, this work highlights the potential directions these crystals enable for applications requiring large surface coverage. We also gain insight to the underlying growth mechanism in structure assembly, supporting our hypothesis of delayed nucleation.

Finally, in chapter four, we expand the addressability of our DNA brick structures by two orders of magnitude from hundreds of components tens of thousands. By modifying the original DNA brick design to contain 13-nt binding domains instead of 8-nt, structures are able to fold with much higher strand incorporation efficiencies. We demonstrate that cuboids up to 0.5 GDa, containing over 30,000 uniquely addressable components, and measuring over 100 nm in each dimension can be assemble in a single-pot annealing reaction (Fig. 5-1F). We used a structure three times smaller to create a number of discrete complex cavity structures. In this work, we have demonstrated a self-assembled structure containing the largest number of unique components, overcoming a number of challenges including low component concentration, slow assembly kinetics, sequence design space and undesired or partial structures. Such extended bottom-up control of the three dimensions serves as a first step towards enabling large coverage for complex component patterning, bringing us closer to bridging top-down and bottom-up fabrication methods.

5.2 Revisiting the promise

DNA nanotechnology has much potential for creating impactful technologies, because nucleic acid nanostructures can fulfill a unique role of offering highly complex 3D patterning of a wide variety of functional materials in a parallelized manner. The development of the DNA bricks platform may enable a number of new applications. In this work, we established a method to easily construct both 3D crystals and large scale (>100 nm in all three dimensions) patterning with relatively high assembly yields. Previously applications were often limited to 2D arrays or within a $25\times25\times25$ nm^3 region. With these DNA brick structures, we can now potentially pattern hundreds to thousands of unique components in a complex 3D space with long range. This capability will allow us to extend existing directions. For example, this work may enable us to create nanoscale patterns at length scales near the wavelength of visible light for developing unique photonics systems. Alternatively, we can scaffold larger or a larger number of independent components to form integrated electronic systems. Biologically, we can use these structures to mimic or study large macromolecular complexes. Integration of more complex functions, such as dynamic systems, will also enable many more technological platforms to emerge. Although much work and development is left to fully achieve these goals, we hope that DNA bricks can help contribute to fulfilling the promise of structural DNA nanotechnology.

5.3 Conclusions

In this work, we establish a foundation for modular complex 3D DNA nanostructure assemblies. However, there remains a number of unsolved challenges in the field of structural DNA nanotechnology. A challenge of the field is to build any arbitrarily sized and shaped structure out of DNA. To work towards this goal, we must gain a stronger understanding of the thermodynamics and kinetics that drive self-assembly of these structures. Experiments performed [144] and previously published theoretical models [180] support our hypothesis of delayed nucleation and growth for both discrete and crystal structures, but we have yet to validate this mechanism. If we can gain insight to the specific growth mechanisms behind these complex structure assemblies, we can then focus our efforts on developing improved structures and improved assembly yields. Along with mechanistic studies, we can also explore the effects of sequence design and optimization on structure assembly.

Structures with skewed aspect ratios, such as long thin rods or packed short helices, remain difficult to assemble. These structures bring up questions on how we can better improve overall structural stability and rigidity. Mechanistic studies described above may aid in our understanding of why such features are difficult to form. Likely different assembly methods or perhaps hybrid methods that combine DNA bricks and origami may be necessary to address such challenges.

Finally, the development of these gigadalton-sized DNA structures brings forth a challenge of how we can synthesize DNA more cheaply and easily. For these large structures containing tens of thousands of unique components, cost of synthesis can hinder development of this platform. Further, these strands need to be sufficiently high quality for correct and efficient structure assembly. Currently, most these structures come from oligomers synthesized by solid-phase chemistry at costs of $\sim$ 10 cents/base at scales of 10-100 nmole [187]. Thus, as we assemble larger and larger structures, the costs also climb. While a number of studies have explored alternative low cost methods of synthesizing oligomers [173, 188], they still have yet to demonstrate appropriate scale and quality for assembling these large structures.

We aspire to disseminate the DNA bricks platform for usage and for further development. Ultimately, we hope that this work and future directions will help bring DNA nanotechnology closer to reaching its potential and closer to creating a number impactful technologies.

References

[1] Z.-Z. Gu, H. Uetsuka, K. Takahashi, R. Nakajima, H. Onishi, A. Fujishima, and O. Sato. Structural color and the lotus effect. *Angewandte Chemie International Edition*, 42:894–897, 2003.

[2] B. D. Gates, Q. Xu, M. Stewart, D. Ryan, C. G. Wilson, and G. M. Whitesides. New approaches to nanofabrication: Molding, printing, and other techniques. *Chemical Reviews*, 105:1171–1196, 2005.

[3] S. Takahashi, K. Suzuki, M. Okano, M. Imada, T. Nakamori, Y. Ota, K. Ishizaki, and S. Noda. Direct creation of three-dimensional photonic crystals by a top-down approach. *Nature Materials*, 8:721–725, 2009.

[4] G. von Freymann, V. Kitaev, B. V. Lotsch, and G.A. Ozin. Bottom-up assembly of photonic crystals. *Chemical Society Reviews*, 42:2528–2554, 2013.

[5] J. Y. Cheng, C. A. Ross, H. I. Smith, and E. L. Thomas. Templated self-assembly of block copolymers: Top-down helps bottom-up. *Advanced Materials*, 18:2505–2521, 2006.

[6] K. Salaita, Y. Wang, and C. A. Mirkin. Applications of dip-pen nanolithography. *Nature*, 2:145–155, 2007.

[7] W. Lu and C. M. Lieber. Nanoelectronics from the bottom up. *Nature Materials*, 6:841–850, 2007.

[8] F. Crick. Central dogma of molecular biology. *Nature*, 227:561–562, 1970.

[9] J. D. Watson and F. H. C. Crick. Molecular structure of nucleic acids. *Nature*, 171:737–738, 1953.

[10] R. E. Franklin and R. G. Gosling. Molecular configuration in sodium thymonucleate. *Nature*, 171: 740–741, 1953.

[11] N. C. Seeman. Nucleic acid junctions and lattices. *Journal of Theoretical Biology*, 99:237–247, 1982.

[12] N. C. Seeman. Nanomaterials based on DNA. *Annual Review of Biochemistry*, 79:65–87, 2010.

[13] D. Y. Zhang and G. Seelig. Dynamic DNA nanotechnology using strand displacement reactions. *Nature Chemistry*, 3:103–113, 2011.

[14] A. Klug and L.C. Lutter. The helical periodicity of DNA on the nucleosome. *Nucleic Acids Research*, 9:4267–4284, 1981.

[15] J. SantaLucia and D. Hicks. The thermodynamics of DNA structural motifs. *Annual Reviews Biophysics Biomolecular Structure*, 33:415–440, 2004.

[16] R. K. Kallenbach, R.-I. Ma, and N. C. Seeman. An immobile nucleic acid junction constructed from oligonucleotides. *Nature*, 305:829–831, 1983.

[17] A. Chworos, I Severcan, A. Y. A. Y. Koyfman, P. Weinkam, E. Emin Oroudjev, H. G. Hansma, and L Jaeger. Building programmable jigsaw puzzles with RNA. *Science*, 306:2068–2072, 2004.

[18] I. Severcan, C. Geary, A. Chworos, N. Voss, E. Jacovetty, and L. Jaeger. A polyhedron made of tRNA. *Nature Chemistry*, 2:772–779, 2010.

[19] L. Jaeger, E. Westhof, and N. B. Leontis. TectoRNA: modular assembly units for the construction of RNA nano-objects. *Nucleic Acids Research*, 29:455–463, 2001.

[20] E. Winfree, F. Liu, L. A. Wenzler, and N. C. Seeman. Design and self-assembly of two-dimensional DNA crystals. *Nature*, 394:539–544, 1998.

[21] C. Mao, W. Sun, and N. C. Seeman. Designed two-dimensional DNA Holliday junction arrays visualized by atomic force microscopy. *Journal of the American Chemical Society*, 121:5437–5443, 1999.

[22] T. H. LaBean, H. Yan, J. Kopatsch, F. Liu, E. Winfree, J. H. Reif, and N. C. Seeman. Construction, analysis, ligation, and self-assembly of DNA triple crossover complexes. *Journal of the American Chemical Society*, 122:1848Ð1860, 2000.

[23] D. Liu, S. H. Park, J. H. Reif, and T. H. LaBean. DNA nanotubes self-assembled from triple-crossover tiles as templates for conductive nanowires. *Proceedings of the National Academy of Sciences of the United States of America*, 101:717–722, 2004.

[24] H. Yan, S. H. Park, G. Finkelstein, J. H. Reif, and T. H. LaBean. DNA-templated self-assembly of protein arrays and highly conductive nanowires. *Science*, 301:1882–1884, 2003.

[25] D. Liu, M. Wang, Z. Deng, R. Walulu, and C. Mao. Tensegrity: Construction of rigid DNA triangles with flexible four-arm DNA junctions. *Journal of the American Chemical Society*, 126:2324–2325, 2004.

[26] Y. He, Y. Chen, H. Liu, A. E. Ribbe, and C. Mao. Self-assembly of hexagonal DNA two-dimensional (2d) arrays. *Journal of the American Chemical Society*, 127:12202–12203, 2005.

[27] F. Mathieu, S. Liao, J. Kopatscht, T. Wang, C. Mao, and N. C. Seeman. Six-helix bundles designed from DNA. *Nano Letters*, 5:661–665, 2005.

[28] D. Reishus, B. Shaw, Y. Brun, N. Chelyapov, and L. Adleman. Self-assembly of DNA double-double crossover complexes into high-density, doubly connected, planar structures. *Journal of the American Chemical Society*, 127:17590–17591, 2005.

[29] B. Wei and Y. Mi. A new triple crossover triangle (txt) motif for DNA self-assembly. *Biomacromolecules*, 6:2528–2532, 2005.

[30] Y. Ke, Y. Liu, J. P. Zhang, and H. Yan. A study of DNA tube formation mechanisms using 4-, 8-, and 12-helix DNA nanostructures. *Journal of the American Chemical Society*, 128:4414–4421, 2006.

[31] P. E. Constantinou, T. Wang, J. Kopatsch, L. B. Israel, X. Zhang, B. Ding, W. B. Sherman, X. Wang, J. Zheng, R. Shaa, and N. C. Seeman. Double cohesion in structural DNA nanotechnology. *Organic & Biomolecular Chemistry*, 4:3414–3419, 2006.

[32] M. N. Hansen, A. M. Zhang, A. Rangnekar, K. M. Bompiani, J. D. Carter, K. V. Gothelf, and T. H. LaBean. Weave tile architecture construction strategy for DNA nanotechnology. *Journal of the American Chemical Society*, 132:14481–14486, 2010.

[33] P. W. K. Rothemund, N. Papadakis, and E. Winfree. Algorithmic self-assembly of DNA Sierpinski triangles. *PLoS Biology*, 2:2041–2053, 2004.

[34] J. P. Zheng, J. Birktoft, Y. Chen, T. Wang, R. J. Sha, P. Constantinou, S. Ginell, C. Mao, and N. C. Seeman. From molecular to macroscopic via the rational design of a self-assembled 3D DNA crystal. *Nature*, 461:74–77, 2009.

[35] J. Chen and N. C. Seeman. The synthesis from DNA of a molecule with the connectivity of a cube. *Nature*, 350:631–633, 1991.

[36] Y. Zhang and N. C. Seeman. Construction of a DNA-truncated octahedron. *Journal of the American Chemical Society*, 116:1661–1669, 1994.

[37] R. P. Goodman, I. A. T. Schaap, C. F. Tardin, C. M. Erben, R. M. Berry, C. F. Schmidt, and A. J. Turberfield. Rapid chiral assembly of rigid DNA building blocks for molecular nanofabrication. *Science*, 310(5754):1661–1665, 2005.

[38] W. M. Shih, J. D. Quispe, and G. F. Joyce. A 1.7-kilobase single-stranded DNA that folds into a nanoscale octahedron. *Nature*, 427:618–621, 2004.

[39] Y. He, T. Ye, M. Su, C. Zhang, A. E. Ribbe, W. Jiang, and C. Mao. Hierarchical self-assembly of DNA into symmetric supramolecular polyhedra. *Nature*, 452:198–201, 2008.

[40] C. Zhang, M. Su, Y. He, X. Zhao, P. A. Fang, A. E. Ribbe, W. Jiang, and C. Mao. Conformational flexibility facilitates self-assembly of complex DNA nanostructures. *Proceedings of the National Academy of Sciences of the United States of America*, 105:10665–10669, 2008.

[41] H. Yan, T. H. LaBean, L. Feng, and J. H. Reif. Directed nucleation assembly of DNA tile complexes for barcode-patterned lattices. *Proceedings of the National Academy of Sciences of the United States of America*, 100:8103–8108, 2003.

[42] R. Schulman and E. Winfree. Synthesis of crystals with a programmable kinetic barrier to nucleation. *Proceedings of the National Academy of Sciences of the United States of America*, 104:15236–15241, 2007.

[43] R. D. Barish, R. Schulman, P. W. K. Rothemund, and E. Winfree. An information-bearing seed for nucleating algorithmic self-assembly. *Proceedings of the National Academy of Sciences of the United States of America*, 106:6054–6059, 2009.

[44] K. Lund, Y. Liu, S. Lindsay, and H. Yan. Self-assembling molecular pegboard. *Journal of the American Chemical Society*, 127:17606–17607, 2005.

[45] S. H. Park, C. Pistol, S.J. Ahn, J. H. Reif, A. R. Lebeck, C. Dwyer, and T. H. Labean. Finite-size, fully-addressable DNA tile lattices formed by hierarchical assembly procedures. *Angewandte Chemie International Edition*, 45:735–739, 2006.

[46] Y. Liu, C. X. Lin, H. Y. Li, and H. Yan. Aptamer-directed self-assembly of protein arrays on a DNA nanostructure. *Angewandte Chemie International Edition*, 44:4333–4338, 2005.

[47] C. X. Lin, Y. Liu, and H. Yan. Designer DNA nanoarchitectures. *Biochemistry*, 48:1663–1674, 2009.

[48] P. W. K. Rothemund. Folding DNA to create nanoscale shapes and patterns. *Nature*, 440:297–302, 2006.

[49] E. S. Andersen, M. Dong, M. M. Nielsen, K. Jahn, R. Subramani, W. Mamdouh, M. M. Golas, B. Sander, H. Stark, C. L. P. Oliveira, J. S. Pedersen, V. Birkedal, F. Besenbacher, K. V. Gothelf, and J. Kjems. Self-assembly of a nanoscale DNA box with a controllable lid. *Nature*, 459:73–76, 2009.

[50] Y. Ke, J. Sharma, M. Liu, K. Jahn, Y. Liu, and H. Yan. Scaffolded DNA origami of a DNA tetrahedron molecular container. *Nano Letters*, 9:2445–2447, 2009.

[51] S. M. Douglas, H. Dietz, T. Liedl, B. Högberg, F. Graf, and W. M. Shih. Self-assembly of DNA into nanoscale three-dimensional shapes. *Nature*, 459:414–418, 2009.

[52] Y. Ke, S. M. Douglas, M. Liu, J. Sharma, A. Cheng, A. Leung, Y. Liu, W. M. Shih, and H. Yan. Multilayer DNA origami packed on a square lattice. *Journal of the American Chemical Society*, 131: 15903–15908, 2009.

[53] Y. Ke, N. V. Voigt, K. V. Gothelf, and W. M. Shih. Multilayer DNA origami packed on hexagonal and hybrid lattices. *Journal of the American Chemical Society*, 134:1770–1774, 2012.

[54] H. Dietz, S. M. Douglas, and W. M. Shih. Folding DNA into twisted and curved nanoscale shapes. *Science*, 325:725–730, 2009.

[55] D. Han, S. Pal, J. Nangreave, Z. Deng, Y. Liu, and H. Yan. DNA origami with complex curvatures in three-dimensional space. *Science*, 332:342–346, 2011.

[56] E. Benson, A. Mohammed, J. Gardell, S. Masich, E. Czeizler, P. Orponen, and B. Högberg. DNA rendering of polyhedral meshes at the nanoscale. *Nature*, 523:441–444, 2015.

[57] F. Zhang, S. Jiang, S. Wu, Y. Li, C. Mao, Y. Liu, and H. Yan. Complex wireframe DNA origami nanostructures with multi-arm junction vertices. *Nature Nanotechnology*, 10:779–784, 2015.

[58] A. Rajendran, M. Endo, Y. Katsuda, K. Hidaka, and H. Sugiyama. Programmed two-dimensional self-assembly of multiple DNA origami jigsaw pieces. *ACS Nano*, 5:665–671, 2011.

[59] S. Woo and P. W. K Rothemund. Programmable molecular recognition based on the geometry of DNA nanostructures. *Nature Chemistry*, 3:620–627, 2011.

[60] R. Iinuma, Y. Ke, R. Jungmann, T. Schlichthaerle, J. B. Woehrstein, and P. Yin. Polyhedra self-assembled from DNA tripods and characterized with 3D DNA-PAINT. *Science*, 344:65–69, 2014.

[61] T. Gerling, K. F. Wagenbauer, A. M. Neuner, and H. Dietz. Dynamic DNA devices and assemblies formed by shape-complementary, non-base pairing 3D components. *Science*, 347:1446–1452, 2015.

[62] Y. Suzuki, M. Endo, and H. Sugiyama. Lipid-bilayer-assisted two-dimensional self-assembly of DNA origami nanostructures. *Nature Communications*, 6:8052, 2015.

[63] P. Yin, R. Hariadi, S. Sahu, H. M. T. Choi, S. H. Park, T. H. LaBean, and J. H. Reif. Programming DNA tube circumferences. *Science*, 321:824–826, 2008.

[64] B. Wei, M. Dai, and P. Yin. Complex shapes self-assembled from single-stranded DNA tiles. *Nature*, 485:623–626, 2012.

[65] B. Wei, M. Dai, C. A. Myhrvold, Y. Ke, R. Jungmann, and P. Yin. Design space for complex DNA structures. *Journal of the American Chemical Society*, 135:18080–18088, 2013.

[66] C. A. Myhrvold, M. Dai, P. A. Silver, and P. Yin. Isothermal self-assembly of complex DNA structures under diverse and biocompatible conditions. *Nano Letters*, 13:4242–4248, 2013.

[67] G. Seelig, B. Yurke, and E. Winfree. Catalyzed relaxation of a metastable DNA fuel. *Journal of the American Chemical Society*, 128:12211–12220, 2006.

[68] P. Yin, H. M. T. Choi, C. R. Calvert, and N. A. Pierce. Programming biomolecular self-assembly pathways. *Nature*, 451:318–322, 2008.

[69] L. Qian and E. Winfree. Scaling up digital circuit computation with DNA strand displacement cascades. *Science*, 332:1196–1201, 2011.

[70] L. Qian, E. Winfree, and J. Bruck. Neural network computation with DNA strand displacement cascades. *Nature*, 475:368–372, 2011.

[71] D. Y. Zhang, A. J. Turberfield, B. Yurke, and E. Winfree. Engineering entropy-driven reactions and networks catalyzed by DNA. *Science*, 318:1121–1125, 2007.

[72] W. B. Sherman and N. C. Seeman. A precisely controlled DNA biped walking device. *Nano Letters*, 4:1203–1207, 2004.

[73] T. Omabegho, R. Sha, and N. C. Seeman. A bipedal DNA brownian motor with coordinated legs. *Science*, 324:67–71, 2009.

[74] C. Mao, W. Sun, Z. Shen, and N. C. Seeman. A DNA nanomechanical device based on the b-z transition. *Nature*, 397:144–146, 1999.

[75] H. Yan, Z. Zhang, X. Shen, and N. C. Seeman. A robust DNA mechanical device controlled by hybridization topology. *Nature*, 415:62–65, 2002.

[76] L. Feng, S. H. Park, J. H. Reif, and H. Yan. A two state DNA lattice actuated by DNA motors. *Angewandte Chemie International Edition*, 42:4342–4346, 2003.

[77] B. Yurke, A. J. Turberfield, A. P. Mills, F. C. Simmel, and J. L. Neumann. A DNA-fuelled molecular machine made of DNA. *Nature*, 406:605–608, 2000.

[78] S. M. Douglas, I. Bachelet, and G. M. Church. A logic-gated nanorobot for targeted transport of molecular payloads. *Science*, 335:831–834, 2012.

[79] R. M. Zadegan, M. D. E. Jepsen, K. E. Thomsen, A. H. Okholm, D. H. Schaffer, E. S. Andersen, V. Birkendal, and J. Kjems. Construction of a 4 zeptoliters switchable 3D DNA box origami. *ACS Nano*, 6:10050–10053, 2012.

[80] A. Banerjee, D. Bhatia, A. Saminathan, S. Chakraborty, S. Kar, and Y. Krishnan. Controlled release of encapsulated cargo from a DNA icosahedron using a chemical trigger. *Angewandte Chemie International Edition*, 52:6854–6857, 2013.

[81] Z. Li, Y. Ke, C. Lin, H. Yan, and Y. Liu. Subtractive assembly of DNA nanoarchitectures driven by fuel strand displacement. *Chemical Communications*, 36:4318–4320, 2008.

[82] D. Han, S. Pal, Y. Liu, and H. Yan. Folding and cutting DNA into reconfigurable topological nanostructures. *Nature Nanotechnology*, 5:712–717, 2010.

[83] F. Zhang, J. Nangreave, Y. Liu, and H. Yan. Reconfigurable DNA origami to generate quasifractal patterns. *Nano Letters*, 12:3290–3295, 2012.

[84] A. E. Marras, L. Zhou, H. J. Su, and C. E. Castro. Programmable motion of DNA origami mechanisms. *Proceedings of the National Academy of Sciences of the United States of America*, 112: 713–718, 2014.

[85] S. Pal, Z. Deng, H. Wang, S. Zou, Y. Liu, and H. Yan. DNA directed self-assembly of anisotropic plasmonic nanostructures. *Journal of the American Chemical Society*, 133:17606–17609, 2011.

[86] A. Kuzyk, R. Schreiber, Z. Fan, G. Pardatscher, E. Roller, A. Högele, F. C. Simmel, A. O. Govorov, and T. Liedl. DNA-based self-assembly of chiral plasmonic nanostructures with tailored optical response. *Nature*, 483:311–314, 2012.

[87] J. Sharma, Y. Ke, C. Lin, R. Chhabra, Q. Wang, J. Nangreave, Y. Liu, and H. Yan. DNA tile directed self-assembly of quantum dots into two-dimensional nanopatterns. *Angewandte Chemie International Edition*, 47:5157 – 5159, 2008.

[88] H. Bui, C. Onodera, C. Kidwell, Y. P. Tan, E. Graugnard, W. Kuang, J. Lee, W. B. Knowlton, B. Yurke, and W. L. Hughes. Programmable periodicity of quantum dot arrays with DNA origami nanotubes. *Nano Letters*, 10:3367–3372, 2010.

[89] R. Schreiber, J. Do, E. Roller, T. Zhang, V. J. Schüller, P. C. Nickels, J. Feldmann, and T. Liedl. Hierarchical assembly of metal nanoparticles, quantum dots and organic dyes using DNA origami scaffolds. *Nature Nanotechnology*, 9:74–78, 2014.

[90] P. K. Dutta, R. Varghese, J. Nangreave, S. Lin, H. Yan, and Y. Liu. DNA-directed artificial light-harvesting antenna. *Journal of the American Chemical Society*, 133:11985–11993, 2011.

[91] T. Zhang, A. Neumann, J. Lindlau, Y. Wu, G. Pramanik, B. Naydenov, F. Jelezko, F. Schüder, S. Huber, M. Huber, F. Stehr, A. Högele, T. Weil, and T. Liedl. DNA-based self-assembly of fluorescent nanodiamonds. *Journal of the American Chemical Society*, 137:9776–9779, 2015.

[92] J. B. Knudsen, L. Liu, A. L. B. Kodal, M. Madsen, Q. Li, J. Song, J. B. Wöhrstein, S. F. Wickham, M. T. Strauss, F. Schüder, J. Vintner, A. Krissanaprasit, D. Gudnason, A. A. Smith, R. Ogaki, A. N. Zelikin, F. Besenbacher, V. Birkedal, P. Yin, W. M. Shih, R. Jungmann, M. Dong, and K. V. Gothelf. Routing of individual polymers in designed patterns. *Nature Nanotechnology*, 10:892–898, 2015.

[93] H. T. Maune, S. Han, R. D. Barish, M. Bockrath, W. A. Goddard, P. W. K. Rothemund, and E. Winfree. Self-assembly of carbon nanotubes into two-dimensional geometries using DNA origami templates. *Nature Nanotechnology*, 5:61–66, 2010.

[94] J. D. Le, Y. Pinto, N. C. Seeman, K. Musier-Forsynth, T. A. Taton, and R. A. Kiehl. DNA-templated self-assembly of metallic nanocomponent arrays on a surface. *Nano Letters*, 4:2343–2347, 2004.

[95] B. Ding, Z. Deng, H Yan, S. Cabrini, R. N. Zuckermann, and J. Bokor. Gold nanoparticle self-similar chain structure organized by DNA origami. *Journal of the American Chemical Society*, 132: 3248–3249, 2010.

[96] R. J. Kershner, L. D. Bozano, C. M. Micheel, A. M. Hung, A. R. Fornof, J. N. Cha, C. T. Rettner, M. Bersani, J. Frommer, P. W. K. Rothemund, and G. M. Wallraff. Placement and orientation of individual DNA shapes on lithographically patterned surfaces. *Nature Nanotechnology*, 4:557 – 561, 2009.

[97] A. Gopinath and P. W. K. Rothemund. Optimized assembly and covalent coupling of single-molecule DNA origami nanoarrays. *ACS Nano*, 8:12030–12040, 2014.

[98] A. M. Hung, C. M. Micheel, L. D. Bozano, L. W. Osterbur, G. M. Wallraff, and J. N. Cha. Large-area spatially ordered arrays of gold nanoparticles directed by lithographically confined DNA origami. *Nature Nanotechnology*, 5:121–126, 2010.

[99] J. J. Funke and H. Dietz. Placing molecules with Bohr radius resolution using DNA origami. *Nature Nanotechnology*, 10:47–52, 2016.

[100] V. J. Schüller, S. Heidegger, N. Sandholzer, P. C. Nickels, N. A. Suhartha, S. Endres, C. Bourquin, and T. Liedl. Cellular immunostimulation by CpG-sequence-coated DNA origami structures. *ACS Nano*, 5:9696–9702, 2011.

[101] J. Liu, Y. Geng, E. Pound, S. Gyawall, J. R. Ashton, J. Hickey, A. T. Woolley, and J. N. Harb. Metallization of branched DNA origami for nanoelectronic circuit fabrication. *ACS Nano*, 22:2240–2247, 2011.

[102] W. Sun, E. Boulais, Y. Hakobyan, W. Wang, A. Guan, M. Bathe, and P. Yin. Casting inorganic structures with DNA molds. *Science*, 346:1258361, 2014.

[103] Z. Jin, W. Sun, Y. G. Ke, C. J. Shih, G. L. C. Paulus, Q. H. Wang, B. Mu, P. Yin, and M. S. Strano. Metallized DNA nanolithography for encoding and transferring spatial information for graphene patterning. *Nature Communications*, 4:1663, 2013.

[104] S. Surwade, F. Zhou, B. Wei, W. Sun, A. Powell, C. O' Donnell, P. Yin, and H. Liu. Nanoscale growth and patterning of inorganic oxides using DNA nanostructure templates. *Journal of the American Chemical Society*, 135:6778–6781, 2013.

[105] D. N. Selmi, R. J. Adamson, H. Attrill, A. D. Goddard, R. J. C. Gilbert, A. Watts, and A. J. Turberfield. DNA-templated protein arrays for single-molecule imaging. *Nano Letters*, 11:657–660, 2011.

[106] S. M. Douglas, J. J. Chou, and W. M. Shih. DNA-nanotube-induced alignment of membrane proteins for NMR structure determination. *Proceedings of the National Academy of Sciences of the United States of America*, 104:6644–6648, 2007.

[107] X. Bai, T. G. Martin, S. H. W. Scheres, and H. Dietz. Cryo-EM structure of a 3D DNA-origami object. *Proceedings of the National Academy of Sciences of the United States of America*, 109:20012–20017, 2012.

[108] M. Endo, K. Tatsumi, K. Terushima, Y. Katsuda, K. Hidaka, Y. Harada, and H. Sugiyama. Direct visualization of the movement of a single T7 RNA polymerase and transcription on a DNA nanostructure. *Angewandte Chemie International Edition*, 51:8778–8782, 2012.

[109] A. Udomprasert, M. N. Bongiovanni, R. Sha, W. B. Sherman, T. Wang, P. S. Arora, J. W. Canary, S. L. Gras, and N. C. Seeman. Amyloid fibrils nucleated and organized by DNA origami constructions. *Nature Nanotechnology*, 9:537–541, 2014.

[110] O. I. Wilner, Y. Weizmann, R. Gill, O. Lioubashevski, R. Freeman, and I. Wilner. Enzyme cascades activated on topologically programmed DNA scaffolds. *Nature Nanotechnology*, 4:249–254, 2009.

[111] J. Fu, M. Liu, Y. Liu, N. W. Woodbury, and H. Yan. Interenzyme substrate diffusion for an enzyme cascade organized on spatially addressable DNA nanostructures. *Journal of the American Chemical Society*, 134:5516–5519, 2012.

[112] J. Fu, Y. R. Yang, A. Johnson-Buck, Y. Liu, N. G. Walter, N. W. Woodbury, and H. Yan. Multi-enzyme complexes on DNA scaffolds capable of substrate channeling with an artificial swinging arm. *Nature Nanotechnology*, 9:531–536, 2014.

[113] Z. Zhao, J. Fu, S. Dhakal, A. Johnson-Buck, M. Liu, T. Zhang, N. W. Woodbury, Y. Liu, N. G. Walter, and H. Yan. Nano-caged enzymes with enhanced catalytic activity and increased stability against protease digestion. *Nature Communications*, 7:10619, 2016.

[114] C. J. Delebecque, A. B. Lindner, P. A. Silver, and F. A. Aldaye. Organization of intracellular reactions with rationally designed RNA assemblies. *Science*, 333:470–474, 2011.

[115] N. D. Derr, B. S. Goodman, R. Jungmann, A. E. Leschziner, W. M. Shih, and S. L. Reck-Peterson. Tug-of-war in motor protein ensembles revealed with a programmable DNA origami scaffold. *Science*, 338:662–665, 2012.

[116] R. F. Hariadi, M. Cale, and S. Sivaramakrishnan. Myosin lever arm directs collective motion on cellular actin network. *Proceedings of the National Academy of Sciences of the United States of America*, 111:4091–4096, 2013.

[117] R. F. Hariadi, R. F. Sommese, and S. Sivaramakrishnan. Tuning myosin-driven sorting on cellular actin networks. *eLife*, 4:e05472, 2015.

[118] R. F. Hariadi, R. F. Sommese, A. S. Adhikari, R. E. Taylor, S. Sutton, J. A. Supdich, and S. Sivaramakrishnan. Mechanical coordination in motor ensembles revealed using engineered artificial myosin filaments. *Nature Nanotechnology*, 10:696–700, 2015.

[119] A. Shaw, V. Lundin, E. Petrova, F. Fördös, E. Benson, A. Al-Amin, A. Herland, A. Blokzijl, B. Högberg, and A. Teixeira. Spatial control of membrane receptor function using ligand nanocalipers. *Nature Methods*, 11:841–846, 2014.

[120] D. Y. Zhang, S. X. Chen, and P. Yin. Optimizing the specificity of nucleic acid hybridization. *Nature Chemistry*, 4:208–214, 2012.

[121] M. Rudchenko, S. Taylor, P. Pallavi, A. Dechkovskaia, S. Khan, V. P. Butler, S. Rudchenko, and M. Stojanovic. Autonomous molecular cascades for evaluation of cell surfaces. *Nature Nanotechnology*, 8:580–586, 2013.

[122] Y. Benenson, B. Gil, U. Ben-Dor, R. Adar, and E. Shapiro. An autonomous molecular computer for logical control of gene expression. *Nature*, 429:423–429, 2004.

[123] Y. Li, Y.T.H. Cu, and D. Luo. Multiplexed detection of pathogen DNA with DNA-based fluorescence nanobarcodes. *Nature Biotechnology*, 23:885–889, 2005.

[124] C. Lin, R. Jungmann, A. M. Leifer, C. Li, D. Levner, G. M. Church, W. M. Shih, and P. Yin. Submicrometer geometrically encoded fluorescent barcodes self-assembled from DNA. *Nature Chemistry*, 4:832–839, 2012.

[125] N.A.W. Bell, C.R. Eng, M. Ablay, G. Divitni, C. Ducati, T. Liedl, and U.F. Keyser. DNA origami nanopores. *Nano Letters*, 12:512–517, 2012.

[126] M. Langecker, V. Arnaut, T. G. Martin, J. List, S. Renner, M. Mayer, H. Dietz, and F. C. Simmel. Synthetic lipid membrane channels formed by designed DNA nanostructures. *Science*, 338:932–936, 2012.

[127] X. Liu, Y. Xu, T. Yu, C. Clifford, Y. Liu, H. Yan, and Y. Chang. A DNA nanostructure platform for directed assembly of synthetic vaccines. *Nano Letters*, 12:4254–4259, 2012.

[128] H. Lee, A. K. R. Lytton-Jean, Y. Chen, K. T. Love, A. I. Park, E. D. Karagiannis, A. Sehgal, W. Querbes, C. S. Zurenko, M. Jayaraman, C. G. Peng, K. Charisse, A. Borodovsky, M. Manoharan, J. S. Donahoe, J. Truelove, M. Narendorf, R. Langer, and D. G. Anderson. Molecularly self-assembled nucleic acid nanoparticles for targeted in vivo siRNA delivery. *Nature Nanotechnology*, 7: 389–393, 2012.

[129] Y. Amir, E. Ben-Ishay, D. Levner, S. Ittah, A. Abu-Horowitz, and I. Bachelet. Universal computing by DNA origami robots in a living animal. *Nature Nanotechnology*, 9:353–357, 2014.

[130] S. D. Perrault and W. M. Shih. Virus-inspired membrane encapsulation of DNA nanostructures to achieve in vivo stability. *ACS Nano*, 8:5132–5140, 2014.

[131] Y. Ke, L. L. Ong, W. M. Shih, and P. Yin. Three-dimensional structures self-assembled from DNA bricks. *Science*, 338:1177–1183, 2012.

[132] B. Wei, L. L. Ong, J. Chen, A. S. Jaffe, and P. Yin. Complex reconfiguration of DNA nanostructures. *Angewandte Chemie International Edition*, 126:7605–7609, 2014.

[133] T. J. Fu and N. C. Seeman. DNA double-crossover molecules. *Biochemistry*, 32:3211–3220, 1993.

[134] C. Lin, Y. Liu, S. Rinker, and H. Yan. DNA tile based self-assembly: Building complex nanoarchitectures. *ChemPhysChem*, 7:1641–1647, 2006.

[135] N. B. Leontis, A. Lescoute, and E. Westhof. The building blocks and motifs of RNA architecture. *Current Opinion in Structural Biology*, 16:279–287, 2006.

[136] W. M. Shih and C. Lin. Knitting complex weaves with DNA origami. *Current Opinion in Structural Biology*, 20:276–282, 2010.

[137] H. M. T. Choi, Trinh Chang, J.Y., Padilla L. A., S. E. J. E., Fraser, and N. A. Pierce. Programmable in situ amplification for multiplexed imaging of mRNA expression. *Nature Biotechnology*, 28:1208–1212, 2010.

[138] M. J. Berardi, W. M. Shih, S. C. Harrison, and J. J. Chou. Mitochondrial uncoupling protein 2 structure determined by NMR molecular fragment searching. *Nature*, 476:109–113, 2011.

[139] P. W. K. Rothemund and E. S. Andersen. Nanotechnology: The importance of being modular. *Nature*, 485:584–585, 2012.

[140] S. M. Douglas, A. H. Marblestone, S. Teerapittayanon, A. Vazquez, G. M. Church, and W. M. Shih. Rapid prototyping of 3d DNA-origami shapes with caDNAno. *Nucleic Acids Research*, 37:5001–5006, 2009.

[141] C. E. Castro, F. Kilchherr, D. Kim, E. L. Shiao, T. Wauer, P. Wortmann, M. Bathe, and H. Dietz. A primer to scaffolded DNA origami. *Nature Methods*, 8:221–229, 2011.

[142] Prabal K Maiti, Tod A Pascal, Nagarajan Vaidehi, and William A Goddard. The stability of Seeman JX DNA topoisomers of paranemic crossover (PX) molecules as a function of crossover number. *Nucleic Acids Research*, 32:6047–6056, 2004.

[143] R. Schulman, B. Yurke, and E. Winfree. Robust self-replication of combinatorial information via crystal growth and scission. *Proceedings of the National Academy of Sciences of the United States of America*, 109:6405–6410, 2012.

[144] Y. Ke, L. L. Ong, W. Sun, J. Song, M. Dong, W. M. Shih, and P. Yin. DNA bricks crystals with prescribed depths. *Nature Chemistry*, 6:994–1002, 2014.

[145] N. A. Melosh, A. Boukai, F. Diana, B. Gerardot, A. Badolato, P. M. Petroff, and J. R. Heath. Ultrahigh-density nanowire lattices and circuits. *Science*, 300:112–115, 2003.

[146] M. H. Qi, E. Lidorikis, P. T. Rakich, S. G. Johnson, J. D. Joannopoulos, E. Ippen, and H. I. Smith. A three-dimensional optical photonic crystal with designed point defects. *Nature*, 429:538–542, 2004.

[147] N. Liu, M. Hentschel, T. Weiss, A. P. Alivisatos, and H. Giessen. Three-dimensional plasmon rulers. *Science*, 332:1407–1410, 2011.

[148] C. B. Tang, E. M. Lennon, G. H. Fredrickson, E. J. Kramer, and C. J. Hawker. Evolution of block copolymer lithography to highly ordered square arrays. *Science*, 322:429–432, 2008.

[149] A. Tavakkoli K. G., K W Gotrik, A F Hannon, A Alexander-Katz, C A Ross, and K K Berggren. Templating three-dimensional self-assembled structures in bilayer block copolymer films. *Science*, 336:1294–1298, 2012.

[150] N. Liu, H. Guo, L. Fu, S. Kaiser, H. Schweizer, and H. Giessen. Three-dimensional photonic metamaterials at optical frequencies. *Nature Materials*, 7:31–37, 2008.

[151] E. W. Edward, M. F. Montague, H. H. Solak, C. J. Hawker, and P. F. Nealey. Precise control over molecular dimensions of block-copolymer domains using the interfacial energy of chemically nanopatterned substrates. *Advanced Materials*, 16:1315–1319, 2004.

[152] S. O. Kim, B. H. Kim, D. Meng, D. O. Shin, C. M. Koo, H. H. Solak, and Q. Wang. Novel complex nanostructure from directed assembly of block copolymers on incommensurate surface patterns. *Advanced Materials*, 19:3271–3275, 2007.

[153] J.-P. J. Sobczak, T. G. Martin, T. Gerling, and H. Dietz. Rapid folding of DNA into nanoscale shapes at constant temperature. *Science*, 338:1458–1461, 2012.

[154] D. Han, S. Pal, Y. Yang, S. Jiang, J. Nangreave, Y. Liu, and H. Yan. DNA gridiron nanostructures based on four-arm junctions. *Science*, 339:1412–1415, 2013.

[155] J. Malo, J. C. Mitchell, C. Venien-Bryan, J. R. Harris, H. Wille, D. J. Sherratt, and A. J. Turberfield. Engineering a 2d protein-DNA crystal. *Angewandte Chemie International Edition*, 44:3057–3061, 2005.

[156] J. Sharma, R. Chhabra, A. Cheng, J. Brownell, Y. Liu, and H. Yan. Control of self-assembly of DNA tubules through integration of gold nanoparticles. *Science*, 323:112–116, 2009.

[157] W. Liu, H. Zhong, and N. C. Seeman. Crystalline two dimensional DNA origami arrays. *Angewandte Chemie International Edition*, 50:264–267, 2011.

[158] U. Majumder, A. Rangnekar, K. V. Gothelf, J. H. Reif, and T. H. LaBean. Design and construction of double-decker tile as a route to three-dimensional periodic assembly of DNA. *Journal of the American Chemical Society*, 133:3843–3845, 2011.

[159] T. Wang, D. Schiffels, S. M. Cuesta, D. K. Fygenson, and N. C. Seeman. Design and characterization of 1d nanotubes and 2d periodic arrays self-assembled from DNA multi-helix bundles. *Journal of the American Chemical Society*, 134:1606–1616, 2012.

[160] G. P. Acuna, F. M. Möller, P. Holzmeister, S. Beater, B. Lalkens, and P. Tinnefeld. Fluorescence enhancement at docking sites of DNA-directed self-assembled nanoantennas. *Science*, 338:506–510, 2012.

[161] S. Park, D. H. Lee, J. Xu, B. Kim, S. W. Hong, U. Jeong, T. Xu, and T. P. Russell. Macroscopic 10-terabit-per-square-inch arrays from block copolymers with lateral order. *Science*, 323:1030–1033, 2009.

[162] J. Sharma, R. Chhabra, C. S. Anderson, K. V. Gothelf, H. Yan, and Y. Liu. Toward reliable gold nanoparticle patterning on self-assembled DNA nanoscaffold. *Journal of the American Chemical Society*, 130:7820–7821, 2008.

[163] J. R. Kremer, D. N. Mastronarde, and J. R. McIntosh. Computer visualization of three dimensional image data using IMOD. *Journal of Structural Biology*, 116:71–76, 1996.

[164] F A Aldaye and H F Sleiman. Sequential self-assembly of a DNA hexagon as a template for the organization of gold nanoparticles. *Angewandte Chemie International Edition*, 45:2204–2209, 2006.

[165] S. F. Tan, L. Wu, J. K. Yang, P. Bai, M. Bosman, and C. A. Nijhuis. Quantum plasmon resonances controlled by molecular tunnel junctions. *Science*, 343:1496–1499, 2014.

[166] Z. Deng, Y. Tian, S. H. Lee, A. E. Ribbe, and C. Mao. DNA-encoded self-assembly of gold nanoparticles into one-dimensional arrays. *Angewandte Chemie International Edition*, 44:3582–3585, 2005.

[167] J. Sharma, R. Chhabra, Y. Liu, Y. G. Ke, and H. Yan. DNA-templated self-assembly of two-dimensional and periodical gold nanoparticle arrays. *Angewandte Chemie International Edition*, 45: 730–735, 2006.

[168] J. Zhang, Y. Liu, Y. Ke, and H. Yan. Periodic square-like gold nanoparticle arrays templated by self-assembled 2D DNA nanogrids on a surface. *Nano Letters*, 6:248–251, 2006.

[169] X. N. Dang, H. J. Yi, M. H. Ham, J. F. Qi, D. S. Yun, R. Ladewski, M. S. Strano, P. T. Hammond, and A. M. Belcher. Virus-templated self-assembled single-walled carbon nanotubes for highly efficient electron collection in photovoltaic devices. *Nature Nanotechnology*, 6:377–384, 2011.

[170] K.A. Afonin, E. Bindewald, A.J. Yaghoubian, N. Voss, E. Jacovetty, B.A. Shapiro, and L. Jaeger. In vitro assembly of cubic RNA-based scaffolds designed in silico. *Nature Nanotechnology*, 5:676–682, 2010.

[171] S. H. Park, P. Yin, Y. Liu, J. H. Reif, T. H. LaBean, and H. Yan. Programmable DNA self-assemblies for nanoscale organization of ligands and proteins. *Nano Letters*, 5:729–733, 2005.

[172] C. Geary, P. W. K. Rothemund, and E. S. Andersen. A single-stranded architecture for co-transcriptional folding of RNA structures. *Science*, 345:799–804, 2014.

[173] A. N. Marchi, I. Saaem, B. N. Vogen, S. Brown, and T. H. LaBean. Towards larger DNA origami. *Nano Letters*, 14:5740Ð5747, 2014.

[174] Z. Zhao, Y. Liu, and H. Yan. Organizing DNA origami tiles into larger structures using preformed scaffold frames. *Nano Letters*, 11:2997–3002, 2011.

[175] T. Wang, R. Sha, R. Dreyfus, M. Leunissen, C. Maass, D. J. Pine, P. M. Chaikin, and N. C. Seeman. Self-replication of information-bearing nanoscale patterns. *Nature*, 478:225–228, 2011.

[176] H. Zhang, J. Chao, D. Pan, H. Liu, Q. Huang, and C. Fan. Folding super-sized DNA origami with scaffold strands from long-range PCR. *Chemical Communications*, 48:6405–6407, 2012.

[177] Y. Yang, D. Han, J. Nangreave, Y. Liu, and H. Yan. DNA origami with double-stranded DNA as a unified scaffold. *ACS Nano*, 6:8209–8215, 2012.

[178] P. C. Nickels, Y. Ke, R. Jungmann, D. M. Smith, M. Leichsenring, W. M. Shih, T. Liedl, and B. Högberg. DNA origami structures directly assembled from intact bacteriophages. *Small*, 10:1765–1769, 2014.

[179] B. Leuf, K. R. Frischkorn, K. C. Wrighton, H. N. Holman, G. Birarda, B. C. Thomas, A. Singh, K. H. Williams, C. E. Siegerist, S. G. Tringe, K. H. Downing, L. R. Comolli, and J. F. Banfield. Diverse uncultivated ultra-small bacterial cells in groundwater. *Nature Communications*, 6:6372, 2015.

[180] W. M. Jacobs, A. Reinhardt, and D. Frenkel. Rational design of self-assembled pathways for complex multicomponent structures. *arXiv*, 1:1502.0135, 2015.

[181] Y. Liu, Y. Ke, and H. Yan. Self-assembly of symmetric finite-size DNA nanoarrays. *Journal of the American Chemical Society*, 127:17140–17141, 2005.

[182] H. Liu, L. Jin, S. B. S. Koh, I. Atanasov, S. Schein, L. Wu, and Z. H. Zhou. Atomic structure of human adenovirus by cryo-EM reveals interactions among protein networks. *Science*, 329:1038–1043, 2010.

[183] R. E. F. Matthews. A classification of virus groups based on the size of the particle in relation to genome size. *Journal of General Virology*, 27:135–149, 1975.

[184] A. Reinhardt and D. Frenkel. Numerical evidence for nucleated self-assembly of DNA brick structures. *Physical Review Letters*, 112:238103, 2014.

[185] A. Álu and N. Engheta. Three-dimensional nanotransmission lines at optical frequencies: A recipe for broadband negative-refraction optical metamaterials. *Physical Review B*, 75:024304, 2007.

[186] G. M. Church, Y. Gao, and S. Kosuri. Next-generation digital information storage in DNA. *Science*, 337:1628, 2012.

[187] S. Kosuri and G. M. Church. Large-scale de novo DNA synthesis: technologies and applications. *Nature Methods*, 11:499–507, 2014.

[188] T. L. Schmidt, B. J. Beliveau, Y. O. Uca, M. Theilmann, F. Da Cruz, C.-T. Wu, and W. M. Shih. Scalable amplification of strand subsets from chip-synthesized oligonucleotide libraries. *Nature Communications*, 6:8634, 2015.

Oh, hello! You've made it to the end. I guess you're probably thinking what I'm thinking...

It's time to go play with Legos!! :)